

# UC Berkeley

## UC Berkeley Electronic Theses and Dissertations

### Title

Delivery of Therapeutically Relevant Cargo to Mammalian Cells Using Cell-Permeant Miniature Proteins

### Permalink

<https://escholarship.org/uc/item/8203b48k>

### Author

Knox, Susan Laura

### Publication Date

2021

Peer reviewed|Thesis/dissertation

Delivery of Therapeutically Relevant Cargo to Mammalian Cells Using Cell-  
Permeant Miniature Proteins

By

Susan L. Knox

A dissertation submitted in partial satisfaction of the

requirements for the degree of

Doctor of Philosophy

in

Chemistry

in the

Graduate Division

of the

University of California, Berkeley

Committee in charge:

Professor Alanna Schepartz, Chair

Professor Matthew B. Francis

Professor Randy Schekman

Summer 2021

Delivery of Therapeutically Relevant Cargo to Mammalian Cells Using Cell-  
Permeant Miniature Proteins

© Copyright 2021

by

Susan L. Knox

## Abstract

### Delivery of Therapeutically Relevant Cargo to Mammalian Cells Using Cell-Permeant Miniature Proteins

by

Susan L. Knox

Doctor of Philosophy in Chemistry

University of California, Berkeley

Professor Alanna Schepartz, Chair

Despite the growing interest in protein-based therapeutics, one of the major limitations towards their development is the fact that proteins cannot simply diffuse into the cell interior. Instead, most proteinaceous cargo must be taken up via the biological process of endocytosis. Proteins become engulfed by the endocytic vesicle that travels into the cell and many of these protein cargoes remained trapped within endosomes. While some protein therapeutics, such as Cerezyme and Fabrazyme, take advantage of this entrapment to exhibit their functions within the endocytic pathway, the inability to access the cytosol and other organelles within the cell prevents development of intracellular-targeting proteins. A number of delivery vehicles have been proposed, including liposomes, nanoparticles, polymers, and cell-penetrating peptides (CPPs). Unfortunately, each of these techniques must be optimized for their respective cargo and target and may still suffer from overall low cytosolic delivery. Cell-permeant miniature proteins (CPMPs) provide a promising solution as they reach the cytosol intact at high concentrations, have a defined mechanism, and can deliver protein cargo.

Here, I describe progress from the evaluation of CPMPs alone to delivery of therapeutically relevant proteins and enzymes in both mammalian cells and mice. First, I present a summary of CPMP development, from designing miniature proteins that installed structural elements of traditionally flexible CPPs, to describing mechanistic details of endosomal uptake and escape, to delivering enzymatic cargo to the liver of mice. Next, I describe fluorescence correlation spectroscopy (FCS) in conjunction with flow cytometry experiments for monitoring proteins in live cells and evaluating endosomal escape. This methodology is followed by FCS studies that establish diffusion properties of free dye and CPMPs to assess whether intact CPMPs reach the cytosol of Saos-2 cells. The following chapter illustrates that among a panel of CPPs and CPMPs, the CPMP ZF5.3 is a superior delivery vehicle for a model cargo in multiple cell lines. Next, I describe the development and use of ZF5.3 conjugated to argininosuccinate synthetase (ZF-AS), an enzyme involved in an inborn error of metabolism. ZF-AS was the first ZF5.3-containing molecule to participate in animal studies to evaluate clinical utility of CPMPs. To continue improving cellular delivery of therapeutically relevant proteins, I describe functional and cellular uptake studies in

which ZF5.3 is appended to the well-studied endonuclease Cas9 and initial development towards ZF5.3 conjugates of NS1, a monobody that binds Ras proteins with high affinity. Finally, I conclude with remarks on CPMP-mediated delivery. Together, these projects demonstrate that the CPMP ZF5.3 is a superior delivery vehicle compared to canonical and cyclic CPPs, illustrate ZF5.3-mediated delivery of three protein cargos, and support further ZF5.3 clinical development as a tool for protein-based therapeutics.

## Table of Contents

<b>ACKNOWLEDGMENTS</b> .....	<b>v</b>
<b>CHAPTER 1: Cell-Permeant Miniature Proteins: Development and Applications....</b>	<b>1</b>
1.1 INTRODUCTION .....	2
1.2 INTRODUCING STRUCTURE TO CPPs .....	3
1.3 A TRANSLATABLE MOTIF THAT PROMOTES ENDOSOMAL ESCAPE .....	4
1.3.1 <i>Methods for Measuring Endosomal Escape</i> .....	4
1.3.2 <i>A Motif that Promotes Access to the Cytosol</i> .....	6
1.3.3 <i>Summary</i> .....	7
1.4 A PORTAL INTO THE CELL .....	7
1.4.1 <i>Cellular Uptake</i> .....	7
1.4.2 <i>Endosomal Escape</i> .....	8
1.5 APPLICATIONS .....	11
1.5.1 <i>Stapled Peptides</i> .....	11
1.5.2 <i>Beta Peptides</i> .....	11
1.5.3 <i>Delivery of Protein Cargo</i> .....	12
1.5.4 <i>Enzyme Replacement Strategy</i> .....	13
1.6 CONCLUSIONS .....	14
1.7 FIGURES .....	16
1.8 REFERENCES .....	18
<b>CHAPTER 2: Quantification of Protein Delivery Using Fluorescence Correlation Spectroscopy</b> .....	<b>28</b>
2.1 ABSTRACT .....	29
2.2 INTRODUCTION .....	29
2.2.1 <i>Motivations for improving the delivery of intact, active proteins to the cytosol and nucleus</i> .....	29
2.2.2 <i>FCS is a unique and useful tool for quantifying protein delivery</i> .....	30
2.2.3 <i>Introduction to FCS</i> .....	30
2.3 EQUIPMENT AND MATERIALS .....	31
2.3.1 <i>Synthesis of fluorophore-tagged CPPs and CPMPs</i> .....	31
2.3.2 <i>Preparation of fluorophore-tagged CPP- or CPMP-protein fusions</i> .....	32
2.3.3 <i>Cell Culture Work</i> .....	33
2.3.4 <i>Flow Cytometry</i> .....	33
2.3.5 <i>FCS</i> .....	33
2.4 METHODS .....	34
2.4.1 <i>Cellular Treatment</i> .....	34
2.4.2 <i>Flow cytometry of cells treated with a fluorophore-tagged CPP- or CPMP-protein fusion</i> .....	36
2.4.3 <i>FCS of cells treated with fluorophore-tagged CPP- or CPMP-protein fusions</i> .....	36
2.5 ANALYSIS .....	38
2.6 THEORY/CALCULATION .....	38
2.6.1 <i>Introduction</i> .....	38
2.6.2 <i>Theory</i> .....	39

2.6.3 Calculations.....	40
2.7 CONCLUSIONS.....	42
2.8 FIGURES.....	43
2.9 TABLES.....	45
2.10 REFERENCES.....	45
<b>CHAPTER 3: Diffusion of Free Dyes and Cell-Permeant Miniature Proteins Using Fluorescence Correlation Spectroscopy .....</b>	<b>53</b>
3.1 ABSTRACT .....	54
3.2 INTRODUCTION .....	54
3.3 METHODS .....	55
3.3.1 Cell Preparation for Flow Cytometry and Fluorescence Correlation Spectroscopy .....	55
3.3.2 Flow Cytometry .....	55
3.3.3 Fluorescence Correlation Spectroscopy (FCS).....	55
3.3.4 Peptide Diffusion Times using FCS .....	56
3.3.5 Calculation of Diffusion Coefficients of Dyes and Peptides .....	56
3.4 RESULTS AND DISCUSSION.....	56
3.4.1 Diffusion of Free Dyes In Vitro and In Cellulo .....	56
3.4.2 Diffusion Times of CPMPs and CPPs at 37 °C.....	58
3.5 CONCLUSIONS.....	59
3.6 FIGURES .....	60
3.7 TABLES.....	62
3.8 REFERENCES .....	63
<b>CHAPTER 4: Comparison of Cellular Uptake Using Various Cell-Permeant Miniature Proteins and Cell-Penetrating Peptides .....</b>	<b>65</b>
4.1 ABSTRACT .....	66
4.2 INTRODUCTION .....	66
4.3 METHODS .....	67
4.3.1 Cell Culture .....	67
4.3.2 Flow Cytometry .....	67
4.4 RESULTS AND DISCUSSION.....	67
4.5 CONCLUSIONS.....	68
4.6 FIGURES .....	69
4.7 REFERENCES .....	70
<b>CHAPTER 5: Cytosolic Delivery of Argininosuccinate Synthetase Using a Cell- Permeant Miniature Protein.....</b>	<b>72</b>
5.1 ABSTRACT .....	73
5.2 INTRODUCTION .....	73
5.3 RESULTS AND DISCUSSION.....	74
5.3.1 Expression, purification, and characterization of AS and ZF-AS .....	74
5.3.2 ZF-AS fusion proteins are catalytically active .....	75
5.3.3 Evaluation of uptake by Saos-2 cells using flow cytometry and confocal microscopy .....	76

5.3.4 Evaluation of cytosolic trafficking of AS <sup>Rho</sup> and ZF-AS <sup>Rho</sup> using fluorescence correlation spectroscopy (FCS).....	77
5.3.5 Evaluation of uptake by SK-HEP-1 cells using flow cytometry and confocal microscopy .....	78
5.3.6 Evaluation of cytosolic trafficking of AS <sup>Rho</sup> and ZF-AS <sup>Rho</sup> in SK-HEP-1 cells using FCS.....	78
5.3.7 Endotoxin Analysis and Removal.....	79
5.3.8 Delivery to Healthy Mice .....	80
5.4 CONCLUSIONS.....	80
5.5 METHODS .....	81
5.5.1 Materials.....	81
5.5.2 Equipment .....	83
5.5.3 Sequences of Expressed Proteins .....	83
5.5.4 Expression and Purification of Proteins .....	85
5.5.5 Determination of Oligomerization State .....	89
5.5.6 Circular Dichroism (CD) Analysis.....	90
5.5.7 Plasma Stability.....	90
5.5.8 Activity Assay .....	91
5.5.9 Activity of AS and ZF-AS in Mouse Liver Homogenate.....	95
5.5.10 Cell Culture and Assays.....	96
5.5.11 Endotoxin Analysis.....	98
5.5.12 Quantification of Endogenous [AS] in C57BL/6 Mouse Liver.....	100
5.5.13 Dosing of ZF-AS into C57BL/6 Mice .....	101
5.5.14 Enzyme-Linked Immunosorbent Assays for Determination of [ZF-AS] in Mouse Serum and Liver .....	102
5.6 FIGURES .....	104
5.7 TABLES.....	131
5.8 ACKNOWLEDGEMENTS .....	133
5.9 REFERENCES .....	133
<b>CHAPTER 6: Cellular Delivery of Cas9 Using ZF5.3 .....</b>	<b>140</b>
6.1 ABSTRACT .....	141
6.2 INTRODUCTION .....	141
6.3 MATERIALS AND METHODS.....	142
6.3.1 Sequences of Proteins .....	142
6.3.2 Materials.....	144
6.3.3 Expression and Purification of Cas9, ZF5.3-Cas9, Cas9-ZF5.3 .....	145
6.3.4 In Vitro Activity Assay.....	146
6.3.5 Non-Specific Labeling of Cas9 Proteins.....	146
6.3.6 Cell Culture and Assays.....	147
6.4 RESULTS .....	148
6.4.1 Purification of Cas9 Conjugates.....	148
6.4.2 In Vitro Cleavage Assay.....	148
6.4.3 Non-specific Labeling of Cas9 Conjugates .....	149
6.4.4 Evaluation of Overall Uptake via Confocal Microscopy and Flow Cytometry .....	149
6.4.5 Evaluation of Cas9 via FCS .....	150

6.5 CONCLUSIONS.....	151
6.6 FIGURES .....	152
6.7 REFERENCES .....	156
<b>CHAPTER 7: Towards Cellular Delivery of Ras-Binding NS1 Using ZF5.3 .....</b>	<b>159</b>
7.1 ABSTRACT .....	160
7.2 INTRODUCTION .....	160
7.3 METHODS .....	161
7.3.1 <i>Protein Sequences</i> .....	161
7.3.2 <i>Primers for pET32a Vector Linearization</i> .....	161
7.3.3 <i>Polymerase Chain Reaction (PCR) to Delete ZF5.3 from pET32a_ZF5.3-NS1-His<sub>6</sub>-Cys</i> .....	162
7.3.4 <i>Gibson Assembly</i> .....	162
7.3.5 <i>Protein Expression and Purification</i> .....	162
7.3.6 <i>Peptide Synthesis</i> .....	163
7.3.7 <i>Tyrosinase Reactions</i> .....	165
7.3.8 <i>TEV Protease Cleavage</i> .....	165
7.3.9 <i>Maleimide Labeling</i> .....	165
7.4 RESULTS AND DISCUSSION.....	166
7.5 CONCLUSIONS.....	169
7.6 FIGURES .....	170
7.7 REFERENCES .....	176
<b>CHAPTER 8: Conclusions .....</b>	<b>179</b>
<b>APPENDIX 1: Probing ZF5.3-Lipid Interactions Using Lipid Strips .....</b>	<b>183</b>
INTRODUCTION .....	184
METHODS .....	184
RESULTS AND DISCUSSION .....	185
CONCLUSIONS .....	187
FIGURES.....	188
REFERENCES .....	190

## Acknowledgments

First, I would like to thank Alanna for the opportunity to work in her lab and her support, whether encouraging me to present at a conference or guiding my scientific writing or writing letters of recommendation or training me to always evaluate proper controls. Through your mentorship, I have grown into an independent scientist and been able to complete my graduate studies studying a topic I am passionate about — therapeutically relevant drug delivery.

In addition to Alanna, I have had amazing scientific mentors over the last decade, starting with Chuck Wysocki. Chuck provided me with my first lab-based opportunity at Monell which confirmed my interest in conducting research. Following, I have worked with a number of individuals who have each contributed towards my career path. Danielle Guarracino first introduced me to Alanna's research in her chemical biology course at The College of New Jersey (TCNJ). While working in Danielle's lab, I discovered my love of peptide-based materials and am ecstatic that I was able to work with them beyond undergrad. At TCNJ, Joe Baker taught me how to study peptides via simulations, which revealed to me the value in computation. Mike Giano contributed to my positive experience at Johnson and Johnson, motivating my decision to pursue a career in industry. Since the first time I met her, Rebecca Wissner continues to inspire me to be a better scientist. Her excitement for science is infectious and I am thankful to have benefited from being trained by her. I am appreciative of all of the advice I have received from my mentors prior to and during graduate school.

Without the support of my parents, I would not be here. They have always encouraged me to pursue my passions, whether learning to play field hockey in middle school, joining the Blawenburg Band, attending graduate school, or moving across the country to finish my Ph.D. Additionally, they advocated for me so that I had the best opportunities available throughout my education. I am so grateful for your love and cannot wait to see you and Steven this summer.

My friends have been constant pillars of encouragement. Aarushi, Angela, and Allie: thank you for motivating me even after you graduated from the lab. To my Yale 'Girl Gang'—Lizzy, Danielle, Julia, and Maddie—thanks for including me in lunches even though I was 3000 miles away! Sara, I am forever grateful that you continue to be my best friend even though I never respond to texts in a timely manner; I am looking forward to being in the same state again for the first time in 5 years! Sarah Smaga and I first connected at Berkeley over our desire for making friends in the Bay Area and instead of making new ones (thanks COVID-19), developed our own friendship. I look forward to our bond strengthening beyond California. Our hiking adventures with Ryan and Penny have been the highlight of the pandemic. Sebastian, I have been so glad to have you as my first ever rotation student, a labmate, and a friend.

Thank you to the past and present members of the Schepartz Lab (especially the protein delivery group) who are always willing to converse about science. I have to specifically call out Jonathan Tyson and Neville Dadina for their synthetic help over the

years. There are many molecules that would have taken longer to make without their assistance. Thank you Karen Wong and Michelle Ferrara for all of the organizational efforts you support. I am also grateful for the passionate individuals I have met through extracurricular organizations such as Open Labs at Yale and the Diversity and Inclusion Focus Groups here at Berkeley which provided an opportunity for balance between research and outside interests.

I am appreciative of my qualifying committees at both Yale (Alanna, Sarah Slavoff, and Scott Miller) and Berkeley (Michelle Chang, Matt Francis, Randy Schekman, and Jon Rittle), and especially thankful for my dissertation committee (Alanna, Matt, and Randy) here at Berkeley.

I would like to recognize the support of my collaborators, including Charles River Laboratories and the Marqusee Lab for their data collection for results in Chapter 5. I am grateful for funding support from the National Institutes of Health Chemical Biology Training Grant at Yale University and the National Science Foundation Graduate Research Fellowship Program.

To my sources of happiness, Peter and Penny, I am grateful for all of your snuggles and pets.

Finally, I have to thank Ryan Davis, although a paragraph cannot express my full gratitude. Ryan has been the most amazing partner throughout my entire graduate school career. Even before we started dating, he was my 'go to' person at Yale functions and parties. I have never doubted his love or support. I appreciate the sacrifices you made so that we could move to California together. Thank you for all of the time and patience you have given me as I said "just one more late night" for the last three years. I love you with all my heart and cannot wait to marry you in September so that I can spend the rest of my life with you as my husband.

## **CHAPTER 1**

### Cell-Permeant Miniature Proteins: Development and Applications

This chapter is based on a manuscript in preparation “Discovery and Application of Genuinely Cell-Permeant Proteins” and has been adapted with permission from all co-authors.

## 1.1 Introduction

Delivery of extracellular proteinaceous cargo into mammalian cells could improve treatment of a wide range of diseases, but crossing the plasma membrane presents a challenge. While small molecules can passively diffuse through the lipid-filled membrane,<sup>1,2</sup> larger cargo cannot, requiring separate means of cellular access. As more biologics are FDA-approved, there is increasing interest in developing new ways to traffic material that cannot passively diffuse through the membrane into cells.

One such material of interest is proteins—investigations of macromolecular uptake into cells began in 1965 when Ryser and Hancock determined that histones and basic amino acids stimulate the uptake of serum albumin into cells.<sup>3</sup> After a lull in interest, Frankel and Pabo and Green and Löwenstein independently concluded in 1988 that Tat, derived from the transactivator of transcription from the HIV-1 virus, induced viral expression when added exogenously to cells.<sup>4,5</sup> After penetratin, another cell penetrating peptide (CPP), was reported in 1994, many groups focused their efforts towards the CPP space and using new constructs to deliver cargo.<sup>6,7</sup>

Since the mid-1990s, thousands of putative CPPs have been identified and developed,<sup>8</sup> including but not limited to supercharged proteins,<sup>9</sup> cyclic peptides,<sup>10–13</sup> hydrocarbon stapled peptides,<sup>14</sup> and miniature proteins.<sup>15–19</sup> The majority of these molecules contain a series of positive residues (either Lys or Arg) that convey cell permeability, possibly through electrostatic interactions with sulfated proteoglycans on the cell surface.<sup>9,20,21</sup> Futaki *et al.* tested this hypothesis through study of Arg-rich sequences, suggesting that RNA-binding proteins should translocate through cell membranes since they are rich in Arg residues.<sup>22</sup> Indeed, the group showed that multiple Arg-rich proteins accumulated in the cytoplasm and nucleus at comparable levels to the minimal transduction sequence of Tat, Tat<sub>(48-60)</sub>.<sup>22</sup> In addition, comparison to polyarginine sequences, from Arg<sub>4</sub> to Arg<sub>16</sub>, showed that Arg<sub>8</sub> was the most efficient of these peptides and could be attached to carbonic anhydrase for delivery into cells.<sup>22</sup> More recently, cyclic peptides have been identified as intracellular delivery tools with improved proteolysis resistance as compared to linear peptides.<sup>23</sup> While two of these macrocycles, CPP9 and CPP12, were reported to have high delivery efficiencies,<sup>12,24</sup> they were unable to deliver protein cargo to cells.<sup>25</sup>

While these studies highlight the ability of a variety of peptides and proteins to internalize into cells, they do not assess localization within the cell. The most common mechanism by which CPPs and other cationic molecules enter cells is through endocytosis, a process that prevents interaction of the entrapped molecules with the cytosol or nucleus.<sup>26</sup> A molecule must escape from the endosome to enter the cell's cytosol and traffic to other regions of the cells. However, many CPPs remain trapped in endosomes where they are degraded or recycled back into extracellular space.<sup>27,28</sup> A peptide-based delivery tool that reliably traffics material to the cytosol would greatly expand the existing druggable space.<sup>29</sup>

Since the mid-2000s, the Schepartz laboratory has contributed to this body of work with the design and implementation of cell-permeant miniature proteins (CPMPs).<sup>15–19,25,30,31</sup> This chapter details the group's efforts to establish a peptide-based drug delivery tool through appending elements of cell-permeability onto a structured scaffold, optimizing cellular uptake, and demonstrating utility through the delivery of protein cargo. One of our CPMPs, ZF5.3, escapes endosomes with unprecedented efficiency,<sup>15,18</sup> and does so *via* a defined and underexploited mechanism using the homotypic fusion and vacuole protein sorting (HOPS) complex.<sup>30</sup> These studies, taken together, establish that cell-permeant miniature proteins not only have increased uptake but also high endosomal escape efficiencies to reach the cytosol,<sup>15–19</sup> have a defined mechanism for cytosolic access,<sup>30</sup> and can deliver protein cargo.<sup>25,31</sup>

## 1.2 Introducing Structure to CPPs

In the mid-2000s, the best CPPs were unstructured variants of oligoarginine peptides containing 8–12 Arg residues (Arg<sub>8–12</sub>)<sup>22</sup> that reached cellular levels equal to<sup>12,22,32</sup> or above<sup>16,18</sup> Tat. Oligoarginines were reported to increase toxicity and decrease stability of proteins to which they are attached,<sup>33,34</sup> and their lack of structure hampered identification of structural determinants of cell permeability. Daniels *et al.* suspected that introduction of structure to CPPs would aid in the identification of cell-permeant properties, improve stability in the protease-rich cellular environment, and decrease toxicity.<sup>16</sup> Similar to cyclic peptides, Arg<sub>n</sub> molecules were thought to form larger macromolecular structures,<sup>8</sup> displaying guanidino groups in favorable conformations for interactions with the cell membrane. However, unlike a cyclic peptide, encodable peptides were appealing so that the tag could be easily appended to protein cargo via genetic fusion.

In the search for a structured, protease-resistant, peptide-based delivery vehicle, Daniels *et al.* first established that type-II polyproline helices (PPII) containing arginine and proline residues (**Figure 1.1**) could convey cell-permeant properties.<sup>16</sup> Several natural proline-rich sequences permeate cells with low efficiency, supporting the use of this scaffold in the initial design effort.<sup>35,36</sup> The short and stable PPII helices containing 3 residues/turn allow incorporation of charged amino acids on one of three distinct faces of the helix.<sup>16</sup> A series of (PRR)<sub>n</sub> and (PPR)<sub>n</sub> variants were evaluated to understand the relationship between number of arginine residues and helicity. The design of these peptide structures resulted in aligned faces of either proline or arginine residues and both series retained helicity from 5–90 °C. Ultimately, the (PPR)<sub>n</sub> series was less cell-permeable than (PRR)<sub>n</sub> molecules as evaluated by flow cytometry and was no longer pursued. (PRR)<sub>5</sub> and (PRR)<sub>6</sub> were similarly permeable to Arg<sub>8</sub>, Arg<sub>10</sub>, and Arg<sub>12</sub>. Live cell confocal microscopy images depicted diffuse cytoplasmic and nuclear staining, while the lack of co-localization with the endocytic marker dextran implied that the peptides reached the cytosol.

To show that well-folded miniature proteins could serve as scaffolds for cell-permeability, the (PRR)<sub>n</sub> motif was grafted into avian pancreatic polypeptide (aPP).<sup>16</sup> The 15 amino acid (aa) sequence (PRR)<sub>5</sub> replaced the 11 aa PPII helix of avian

pancreatic polypeptide<sup>37–43</sup> (aPP, 36 total residues) to create RR5-aPP (**Figure 1.1**). Modifying this construct slightly to remove the 4 aa extension on the N-terminus (named RR3-aPP) resulted in a miniature protein that was most cell-permeable.<sup>16</sup> In addition to high uptake, the RRn-aPP series exhibited melting transitions near 40 °C, correlating well with the transition of aPP itself.<sup>16</sup> This study showed that it was possible to design encodable cell-penetrating peptides retaining PPII helices for uptake into HeLa cells and that these helices could be grafted onto small, structured proteins.<sup>16</sup>

Building upon the observation that additional arginine residues improved cellular access of aPP, a subsequent study enhanced cell permeability by grafting three to five arginine residues in positions that contributed minimally to the protein's stability alongside one native arginine residue in the original PPII helix of aPP.<sup>19</sup> The resulting aPP<sup>4R1</sup>, aPP<sup>5R1</sup>, and aPP<sup>6R1</sup> designs (**Figure 1.1**) contained 4, 5, and 6 arginine residues, respectively on the solvent exposed face of the  $\alpha$ -helix. The secondary structure of aPP<sup>4R1</sup> and aPP<sup>5R1</sup> matched that of aPP by circular dichroism (CD); however, the spectrum for aPP<sup>6R1</sup> indicated that it was less  $\alpha$ -helical, possibly due to helical disruption from the additional Arg residues.<sup>19</sup> Confocal microscopy images indicated that the fluorescence colocalized with dextran and diffuse fluorescence implied either endosomal escape or an alternative, non-endocytic entry pathway.

Next, Smith *et al.* established another generation of cationic miniature proteins that access the interior of cell by grafting 2–4 arginine residues onto PPII helix of the transcription factor YY2 and at the same locations in the PPII helix as aPP (**Figure 1.1**).<sup>19</sup> The constructs <sup>Flu</sup>YY2<sup>4R1</sup> and <sup>Flu</sup>YY2<sup>5R1</sup> were shown to be cell-permeant at similar levels to <sup>Flu</sup>aPP<sup>6R1</sup>.<sup>19</sup> The introduction of multiple arginine residues decreased the  $T_M$ , but did not disrupt folding.<sup>19</sup>

These introductory studies provide evidence that structured peptides containing arginine residues at discrete locations increase cellular permeability as well as endosomal escape (or an alternative entry mechanism for cytosolic access). It is important to be clear that at this point in time, it was not certain where inside the cells these miniature proteins were located due to the limitations in microscopy techniques. Ultimately, these experiments influenced the rational design of a translatable  $\alpha$ -helical motif that promotes endosomal escape.

### 1.3 A Translatable Motif that Promotes Endosomal Escape

#### 1.3.1 Methods for Measuring Endosomal Escape

There are two discrete challenges that molecules face when attempting to access the cell interior: (1) uptake into the endosomal pathway, and (2) endosomal release, or the ability to actually reach the cytosol. To evaluate whether miniature proteins or other CPPs reach the cytosol, it is necessary to design assays that can distinguish between endosomal uptake and escape. Our contributions to assessing endosomal escape are summarized below, and a broader review of assays that measure total cellular uptake and those that determine cytosolic localization is summarized in Deprey *et al.*<sup>29</sup>

As many have noted,<sup>25,29</sup> traditional confocal microscopy struggles to differentiate between cellular delivery and access to organelles within the cell. Fixation methods can alter signal distribution within the cell (e.g. fluorescence moving from endosomes to cytosol due to membrane permeation by harsh reagents) and peptides bound to the cell membrane can result in false positive signals. Our group mitigates these problems by treating cells with trypsin to remove surface bound material before live cell imaging.<sup>15</sup>

To design an assay that provides a readout of cytosolic access, Appelbaum *et al.* and Holub *et al.* built upon two observations (1) dexamethasone (Dex) binds cytosolic glucocorticoid receptor (GR), which can be detected by transcription of luciferase in cell lysate<sup>44</sup> and (2) Dex treatment leads to nuclear accumulation of GR-green fluorescent protein (GR-GFP)<sup>45</sup>. Holub *et al.* improved upon these two independent assays by developing a GR assay called glucocorticoid-induced eGFP induction (GIGI), which utilizes a transient transfection of GR-GFP. In the absence of Dex, GR-GFP is cytosolic and nuclear, but upon addition of Dex, the nuclear GFP signal increases.<sup>15</sup> Two modifications enhanced the initial assay: (1) a variant of GR, GR\*, with improved affinity for Dex and Dex-tagged materials is expressed and (2) instead of encoding luciferase as in Yu *et al.*,<sup>44</sup> eGFP is encoded to allow 6–24 h measurement times and conduct the assay in living cells.<sup>17</sup> Live cell microscopy then determines whether a molecule localized to the cytosol by assessing nuclear accumulation of GR-GFP with peptide-Dex conjugates through calculation of a translocation ratio (TR, the median GFP signal in the nucleus divided by the median signal within 2  $\mu\text{m}$  of the cytosolic region surrounding the nucleus).<sup>15,17</sup> A TR near 1 mean equal intensity in the nucleus and surrounding cytosol. The assay works in multiple cell lines (HeLa, HEK293T, U2OS), but a stable cell line, U2OS(GIGI), was generated to eliminate the transfection step and make the assay high throughput.<sup>17</sup> GIGI is an amplified assay that provides information on cytosolic release and while it can be assessed using adherent cells under the microscope, a cell lysate can also be evaluated by a plate reader. While this assay is amplified, indirect, and qualitative, it is useful for molecules whose cytosolic access is low<sup>29</sup> and provides a good first analysis of endosomal escape of Dex-tagged molecules.<sup>15</sup>

Glucocorticoid-induced eGFP translocation (GIGT) is a nonamplified version of this assay that uses high-content images in live cells and further improves on the Yu *et al.* assay<sup>44</sup> by eliminating the need for transcription and translation (minimizing a time delay), instead directly quantifying translocation of GR\* fusion from cytosol to nucleus in live cells.<sup>17</sup>

To increase the rigor in which delivery into the interior of cells is evaluated, LaRochelle *et al.* were the first to use fluorescence correlation spectroscopy (FCS) in live cells to compare cytosolic concentrations achieved by CPPs and CPMPs.<sup>18,25,30,31,46</sup> FCS directly and absolutely quantifies the material inside the cytosol, whereas other assays only provide comparative measurements.<sup>18,29,46</sup> FCS generates an autocorrelation curve from fluctuations in fluorescence intensity. This curve can be fit to an appropriate model of diffusion to calculate the concentration in various organelles,

the size, and the mobility of the molecules being studied.<sup>46</sup> Previous work using FCS in the CPP field evaluated penetratin and MTS peptide, but high background and pH sensitive dyes limited the technology.<sup>47,48</sup> Using both flow cytometry and FCS measurements, total cellular uptake and cytosolic concentrations can be compared, allowing a fuller picture to be drawn. FCS drawbacks include that protein degradation may be of concern (depending on the protein being studied) and the assays are time consuming, but this technique provides a precise measurement and high-quality data that other endosomal escape assays simply cannot achieve.

Similar to observations comparing flow cytometry data with cytosolic concentrations determined by FCS,<sup>25,31,49</sup> the comparison of cytosolic delivery assessed by a biotin ligase assay using various protein uptake strategies also showed that endosomal uptake does not correlate with cytosolic delivery and that there are cell line-dependent differences.<sup>50</sup> Additional assays continue to be described<sup>51,52</sup> and will no doubt have significant contributions to the screening of putative CPPs and CPMPs.

### 1.3.2 A Motif that Promotes Access to the Cytosol

To evaluate whether Arg-containing miniature proteins reached the cytosol, Appelbaum *et al.* used the GIGI assay.<sup>15</sup> Variants of miniature protein aPP (containing two innate Arg residues near the C-terminus) were designed to carry 1–6 Arg residues at the solvent-exposed  $\alpha$ -helical surface of the hairpin fold. The Arg substitutions did not alter folding in seven out of eight designs as determined by CD (addition of 6 Arg decreased both helicity and  $T_M$ , similar to the observation with aPP<sup>6R1</sup>).<sup>15</sup> aPP containing 4 or 5 Arg and tagged with a rhodamine fluorophore (R) exhibited higher uptake by flow cytometry. Specifically, constructs with five Arg placed on either two (5.2) or three (5.3) faces of the alpha helix—deemed aPP5.2<sup>R</sup> (equivalent to aPP<sup>4R1</sup>) and aPP5.3<sup>R</sup>—were taken up with higher efficiency than Tat<sup>R</sup> or Arg<sub>8</sub><sup>R</sup>. Structurally compared to Tat and Arg<sub>8</sub>, aPP5.2 and aPP5.3 contained twice the mass and one less overall positive charge (7 rather than 8).<sup>15</sup> This study suggested that simply increasing overall charge of protein transduction domains does not correlate with increased uptake into cells.

aPP5.3 was identified as one of only four miniature protein variants containing arginine residues that accessed the cytosol using the GIGI assay.<sup>15,17</sup> GIGI studies revealed that approximately the same amount of aPP5.3<sup>Dex</sup>, Tat<sup>Dex</sup>, and Arg<sub>8</sub><sup>Dex</sup> reach the cytosol due to similar translocation ratios.<sup>15</sup> To establish whether aPP5.3 was intact within cells, whole-cell lysates generated by HeLa cell treatment with streptolysin O (SLO, generates membrane pores but not in cytoplasmic vesicles) were evaluated by HPLC.<sup>15</sup> The analysis indicated no cleavage of aPP5.3<sup>R</sup>, whereas retention times varied for Tat<sup>R</sup> and Arg<sub>8</sub><sup>R</sup>, consistent with observations that unstructured CPPs degrade<sup>53</sup> and supporting the hypothesis that structured peptides would improve cellular stability.<sup>15</sup> This suite of experiments provided motivation to evaluate the translatability of the 5.3 arginine (penta-Arg) motif.

Zinc finger nucleases have been implemented in genome therapies,<sup>54</sup> providing incentive to engineer cell permeability into a zinc finger protein for cell-permeant therapeutic application. CP1 is a zinc finger peptide containing a Cys<sub>2</sub>His<sub>2</sub> zinc binding site.<sup>55</sup> Appelbaum *et al.* grafted the penta-Arg motif onto this peptide to generate ZF5.3. Flow cytometry results showed that ZF5.3<sup>R</sup> experienced higher uptake than Tat<sup>R</sup> and Arg<sub>8</sub><sup>R</sup> in HeLa cells, even at 500 nM (many CPPs require micromolar concentrations to access cells<sup>56,57</sup>).<sup>15,18</sup> As assessed by FCS, ZF5.3 reached the cytosol at delivery efficiencies >70%.<sup>18</sup> For comparison, Tat<sup>R</sup> and Arg<sub>8</sub><sup>R</sup> exhibited delivery efficiencies of 2% and 4%, respectively. Cytosolic fractionation and UPLC analysis of the cytosol showed that the cytosolic fraction comigrated with ZF5.3<sup>R</sup> in buffer and that 70% remained intact (aPP5.3<sup>R</sup> remained 12% intact), supporting the SLO assay that ZF5.3<sup>R</sup> does not degrade within cells.<sup>15,18</sup> FCS experiments indicated penta-Arg-containing miniature proteins reach the cytosol with efficiencies >50%, which is approximately 10-fold higher than those of Tat and Arg<sub>8</sub>, and similar to hydrocarbon-stapled peptides.<sup>18</sup> These results suggest that CPMPs overcome the bottleneck of endosomal escape to reach the cytosol in high quantities.

### 1.3.3 Summary

The ultimate goal of this work was to develop a structured cell penetrating peptide based on the scaffold of miniature proteins. By increasing the number of arginine residues on multiple miniature proteins, the total cellular uptake and cytosolic concentrations also increased. Multiple accounts<sup>25,31,49</sup> support that measuring total cellular uptake (by means of flow cytometry, for example) does **not** correlate with cytosolic concentrations, again, showing that the uptake and endosomal release are two discrete biological pathways. Ultimately, ZF5.3 exhibited the highest delivery efficiency (>70%) and is the best candidate to apply to the delivery of larger cargoes. The levels that ZF5.3 reach in the cytosol rival those of stapled peptides, which have clinical trials in humans.<sup>58</sup> With evidence that CPMPs accesses the cytosol at high nanomolar concentrations, it became interesting to determine the mechanism by which CPMPs enter cells and reach the cytosol.

## 1.4 A Portal into the Cell

It is well appreciated that cargo require 2 discrete steps: (1) uptake and (2) endosomal escape.<sup>25,29–31,49</sup> We have used a variety of techniques to understand how miniature proteins complete these cellular processes.

### 1.4.1 Cellular Uptake

Previous studies show that Tat and Arg<sub>8</sub> bind to cell-surface proteoglycans,<sup>59</sup> which suggests a mechanism of uptake based on direct interaction of CPPs with the cell membrane. To confirm endocytosis was a major pathway for access into the cell as described for other cationic peptides,<sup>56</sup> cell uptake of fluorescein-labeled (Flu) miniature proteins<sup>Flu</sup>aPP<sup>5R1</sup> and<sup>Flu</sup>aPP<sup>6R1</sup> was shown to be temperature- and ATP-dependent.<sup>19</sup> To evaluate the mechanism of subsequent aPP variants, Appelbaum *et al.* compared

incubation of cells at 4 °C and 37 °C.<sup>15</sup> Uptake of miniature proteins aPP5.2 and aPP5.3 improves at 37 °C, similar to Tat and Arg<sub>8</sub> and suggesting that the internalization process is ATP-dependent. When analyzed by confocal microscopy, rhodamine-tagged aPP5.2 and aPP5.3 colocalize with the endosomal marker transferrin-AlexaFluor488,<sup>60,61</sup> with Pearson's R<sub>488,R</sub> values of 0.739 (aPP5.2) and 0.637 (aPP5.3) compared to Pearson's R<sub>488,R</sub> values of 0.779 and 0.661 for Tat and Arg<sub>8</sub>, respectively.<sup>15</sup> These results imply that miniature proteins and canonical CPPs traverse similar pathways of uptake into endosomes.

To evaluate specific modes of endocytic uptake, Appelbaum *et al.* treated cells with inhibitors of various cellular processes before assessment of uptake and cytosolic delivery.<sup>15</sup> Clathrin-mediated endocytosis, pinocytosis, and caveolin-mediated endocytosis all depend on dynamin,<sup>62</sup> which is inhibited by dynasore (prevents GTPase activity such that coated pits necessary for endocytosis do not form)<sup>63</sup> and methyl-β-cyclodextrin (MβCD, depletes cellular cholesterol).<sup>64</sup> Clathrin-coated pit formation requires actin remodeling,<sup>62</sup> which is inhibited by N-ethyl-isopropyl amiloride (EIPA).<sup>65</sup> Actin remodeling is required for some dynamin- and cholesterol-independent endocytic pathways.

Dynasore inhibited uptake of aPP5.3<sup>R</sup>, ZF5.3<sup>R</sup>, Tat<sup>R</sup>, and Arg<sub>8</sub><sup>R</sup>, implying these molecules are taken up by cells in a dynamin-dependent manner.<sup>15</sup> MβCD treatment inhibited aPP5.3<sup>R</sup>, ZF5.3<sup>R</sup>, and Tat<sup>R</sup> uptake, yet enhanced Arg<sub>8</sub><sup>R</sup> uptake, suggesting that the mechanisms of entry are not identical. EIPA also decreased the uptake of the two CPMPs and two CPPs, suggesting that actin metabolism is necessary as part of the uptake mechanism.<sup>15</sup> When evaluated using GIGI, dynasore, MβCD, and EIPA decreased the GR\*-GFP TR of aPP5.3<sup>Dex</sup> and Tat<sup>Dex</sup>; dynasore and EIPA reduced TR of Arg<sub>8</sub><sup>Dex</sup>, but not MβCD. In other words, the CPMPs cannot reach the cytosol when the inhibitors are present and cannot find an alternative pathway to endocytosis (except for perhaps Arg<sub>8</sub><sup>Dex</sup>).<sup>15</sup> Therefore, endocytosis is the primary uptake pathway for aPP5.3 and Tat and not one based on passive diffusion.

#### 1.4.2 Endosomal Escape

Once inside of the cell, miniature proteins escape from the endosome. To evaluate if endosomal acidification was required for endosomal escape, Appelbaum *et al.* tested bafilomycin inhibition of vesicular ATPase (preventing endosomal acidification)<sup>66,67</sup> and indeed did see that acidification was required.<sup>15</sup> Not only do endosomes acidify as they mature, but endosomal protein and lipid markers change during pathway progression.<sup>68</sup> Early endosomes are characterized by Rab5+ vesicles, while late endosomes contain Rab7.<sup>68</sup> In evaluating overlap between rhodamine signal of miniature proteins with GFP-fused endosomal markers (Rab5-GFP or Rab7-GFP), aPP5.3<sup>R</sup> colocalized with both Rab5+ and Rab7+ endosomes.<sup>15</sup>

When Rab5<sup>Q79L</sup> (an inactive GTPase mutant<sup>69</sup>) was used to stop endosomal maturation, Tat<sup>Dex</sup> could not reach cytosol but both Arg<sub>8</sub><sup>Dex</sup> and aPP5.3<sup>Dex</sup> could, implying yet again that miniature proteins and CPPs themselves have differing

mechanisms as they traverse the endosomal pathway.<sup>15</sup> The phosphoinositide 3-kinase (involved in intracellular trafficking) inhibitor wortmannin<sup>70</sup> decreased the ability of Arg<sub>8</sub><sup>Dex</sup> and Tat<sup>Dex</sup> to get to the cytosol, but did not decrease ability of aPP5.3<sup>Dex</sup> to reach the cytosol.<sup>15</sup> ZF5.3 behaved similarly in these assays. Again, while there are differences in the endosomal escape mechanism, some of the cellular pathways are similar. These studies suggested that CPMPs escape from early and late endosomes, but we were interested in providing a more detailed mechanistic pathway.

To this end, Steinauer *et al.* asked whether CPMPs (aPP5.3 and ZF5.3) or other CPPs (D-Arg<sub>8</sub> (a proteolytic resistant version of Arg<sub>8</sub><sup>71</sup>), SAH-p53-8, and CPP12) promoted endosomal rupture to escape from endosomes. Two assays were analyzed to assess both subtle and major forms of endosomal rupture: (1) galectin recruitment and (2) Lys9 leakage.<sup>30</sup> Endosomal rupture allows  $\beta$ -galactosides to move from the lumen of the endosome to the cytosol, resulting in recruitment of galectin proteins (Gal) to repair the endosomal damage. Gal3 and Gal8 are recruited to Rab7+ and Lamp1+, which are present in late endosomes.<sup>72,73</sup> This process can be observed by fusing eGFP to galectin. No CPMP or CPP damaged endosomes at low micromolar concentrations, indicating that major endosomal damage does not contribute to the escape mechanism of CPMPs or CPPs.<sup>30</sup>

In the second assay, Lys9—which is taken up by endosomes but remains trapped without access to the cytosol<sup>74,75</sup>—was used to evaluate transient damage. Lipofectamine RNAiMAX induces endosomal damage<sup>73,76</sup> and was used as a positive control; the molecule showed a dose-dependent increase in the amount of Lys9 that reaches cytosol.<sup>30</sup> No dose-dependency was observed with L-leucyl-L-leucine methyl ester (LLOMe)<sup>77</sup>, which could be due to Lys9 only getting out of endosomes prior to lysosomal stage. Below 2  $\mu$ M there was no significant endosomal leakage of Lys9. At higher concentrations (2.4  $\mu$ M), leakage was observed for aPP5.3 and ZF5.3, but not SAH-p53-8, D-Arg<sub>8</sub>, or CPP12.<sup>30</sup> While aPP5.3 and ZF5.3 can cause minimal endosomal damage but do not cause cellular toxicity (EC<sub>50</sub> values >20  $\mu$ M<sup>30</sup>).

To understand the mechanism by which CPMPs access the cytosol, Steinauer *et al.* designed an siRNA screen to evaluate genes whose knockdown affected either total cellular uptake or cytosolic concentrations. This genome-wide siRNA screen used a high throughput GIGT assay<sup>17</sup> to evaluate whether Dex-tagged CPPs reach the cytosol.<sup>30</sup> Saos-2 (GIGT) cells were transfected with a Dharmacon human genome library, incubated with aPP5.3<sup>Dex</sup>, and their cytosolic localization evaluated using the GIGT protocol in fixed cells.<sup>30</sup> Live cell flow cytometry and FCS were completed on the final 28 hits to evaluate uptake and cytosolic access of ZF5.3<sup>Rho</sup> since it is more stable and reaches cytosol more efficiently.<sup>18,30</sup> In summary, six genes strongly inhibited cytosolic access, 13 moderately inhibited cytosolic access, and one gene promoted cytosolic access. SAH-p53-8<sup>R</sup> was also evaluated in this manner: both ZF5.3 and the stapled peptide had 5 common genes that regulate cytosolic delivery (*VSP39*, *LYPLA1*, *CASC1*, *INA*, and *KLHDC10*).<sup>30</sup>

One of these shared genes, *VPS39* encodes a subunit of a six protein complex known as the homotypic fusion and protein sorting (HOPS) membrane-tethering complex that recruits the remainder of the HOPS complex in Rab7+ endosomes (the HOPS complex is required for fusion of Rab7+ maturing and late endosomes with lysosomes).<sup>78</sup> The class C core vacuole/endosome tethering (CORVET) complex shares four of six subunits with the HOPS complex, but is required for Rab5+ early endosomal fusion with maturing endosomes.<sup>78</sup> Both *VPS39* and *VPS41* (the other unique subunit to HOPS) decreased ZF5.3<sup>R</sup> and SAH-p53-8<sup>R</sup> cytosolic delivery whereas CORVET-specific subunits (*TGFBRAP1* and *VPS8*) did not.<sup>30</sup> *TGFBRAP1* depletion increased both overall uptake and cytosolic localization of ZF5.3<sup>R</sup> and SAH-p53-8<sup>R</sup>. Similar results were observed with D-Arg<sup>8</sup> and CPP12<sup>R</sup>, but ZF5.3<sup>R</sup> and SAH-p53-8<sup>R</sup> may depend on the HOPS pathway more strongly given the larger differences in cytosolic concentrations.<sup>30</sup> These studies imply that HOPS activity is necessary for endosomal escape but CORVET is not.

To evaluate if an active HOPS complex is required for endosomal escape, HOPS-dependent delivery of dextran to lysosomal compartments was quantified using fluorescence colocalization.<sup>30</sup> Dextran will only be delivered to lysosomal compartments if endosomal fusion of Rab7+ endosomes occurs (dependent on an active HOPS complex). Alexa Fluor 488-tagged dextran was added to cells which were stained with Magic Red (becomes fluorescent in presence of active cathepsin B which is an enzyme in mature lysosomes<sup>79</sup>). CPP or CPMP addition to the cells did not affect HOPS activity; these five molecules did not inhibit or enhance HOPS-mediated fusion suggesting active, functional HOPS complex is required.<sup>30</sup> Knockdown of *VPS39* decreased the colocalization of ZF5.3<sup>SiR</sup> with Lamp1-GFP indicating that HOPS activity is required to move ZF5.3<sup>R</sup> to Lamp1+ endosomes prior to escape to the cytosol.<sup>30</sup>

Within the endosomal system, ZF5.3<sup>R</sup> colocalizes minimally with Rab5-GFP (early and maturing endosomes), but strongly with both Rab7-GFP (maturing and late endosomes) and Lamp1-GFP (late endosome/lysosome).<sup>30</sup> When Rab7 is bound to GTP, it interacts with HOPS to mediate fusion with lysosomes, providing a connection between endosomal escape at the late endosome stage.<sup>78</sup> Using YM201636, an inhibitor of the phosphoinositide kinase PIKfyve that enlarges Rab7+ endolysosomes,<sup>80</sup> confocal microscopy and line profiles across the enlarged vesicles showed that the ZF5.3<sup>R</sup> signal was distinct from the GFP signal, indicating that the ZF5.3<sup>R</sup> lies within the endosome and not on the surface.<sup>30</sup> CPMPs localize to intraluminal vesicles (ILVs) as indicated by colocalization of ZF5.3<sup>SiR</sup> with *N*-(lissamine rhodamine B sulfonyl)phosphatidylethanolamine (*N*-Rh-PE, an ILV marker)<sup>81, 30</sup>

Taken together, these results suggest three possible models for endosomal escape: a direct shuttle model where CPMPs directly bind HOPS and as endosomes mature are released to the cytosol, a fusion-mediated escape model where HOPS-mediated fusion results in leakage of CPMPs, and an ILV-mediated escape model where back-fusion releases CPMP into the cytosol. Other CPPs (including CPP12) have shown similar models utilizing compartments inside of endosomes for ultimate release to the cytosol.<sup>82,83</sup>

## 1.5 Applications

### 1.5.1 Stapled Peptides

Hydrocarbon stapled peptides were introduced in 2000<sup>84</sup> and have entered clinical trials,<sup>58</sup> the staple helps to confer both structure and protease resistance in  $\alpha$ -helical peptides.<sup>84</sup> To determine the endosomal escape efficiencies of a series of well-studied stapled peptide inhibitors of the HDM2-p53 interaction,<sup>85</sup> LaRoche *et al.* employed FCS. SAH-p53-4 binds HMD2 with high affinity *in vitro*,<sup>14</sup> but cannot be taken up by Jurkat T-cells. SAH-p53-6 – 8 bind HDM2 with similar affinities ( $K_d \sim 50\text{--}60$  nM), possess an overall +1 charge, and are taken up at similar levels by Jurkat T-cells. Yet even with these similarities, only SAH-p53-8 causes death of HDM2-addicted SJSA-1 cells in culture, indicative of inhibition of the HDM2-p53 interaction.<sup>14</sup> This implies that while these peptides can be taken up by cells, only SAH-p53-8 can reach the cellular environment necessary to exhibit its function. This hypothesis was confirmed by flow cytometry and FCS analysis,<sup>18</sup> which showed that the SAH-p53- series accessed the cytosol at concentrations were  $8 \gg 6 \sim 7 > 4$ . SAH-p53-8 had over 50% delivery efficiency within 30 min in HeLa cells. Interestingly, some unstapled (containing alkene side chain but no cyclization) peptides reached the cytosol at higher levels than SAH-p53-7 but less than SAH-p53-8.<sup>18</sup>

To build upon these observations, Quach *et al.* engineered the penta-Arg motif into SAH-p53-4 (-2 overall charge) to create a cell-permeant variant.<sup>49</sup> The design BP1.1 incorporated the canonical penta-Arg motif with Arg substitutions at  $i$ ,  $i + 4$ ,  $i + 7$ ,  $i + 10$ ,  $i + 11$  (residues 14, 18, 21, 24, 25; +3 charge) mirroring the motif in aPP5.3 and ZF5.3. Results indicated that uptake and endosomal escape are two different biological processes; FCS analysis indicated this construct did not appreciably reach the cytosol.<sup>49</sup> It is possible that the extra constraint of the stapled peptide put the Arg residues in a distinct conformation from aPP5.3 and ZF5.3. Additional penta-Arg placements were evaluated, maintaining an overall charge of +4.<sup>49</sup> BP1.4<sup>R</sup> (5 Arg on one face of the helix but distributed axially throughout peptide) exhibited the highest uptake determined by flow cytometry, possibly resulting from more favorable interactions with surface proteoglycans. However, little material reached the cytosol. BP1.6<sup>R</sup> (Arg at  $i$ ,  $i + 3$ ,  $i + 4$ ,  $i + 7$ , and  $i + 8$ ; one face of helix near C-terminus) reached cytosol at  $284 \pm 23$  nM, comparable to SAH-p53-8<sup>R</sup> ( $256 \pm 33$  nM).<sup>49</sup> It is possible that the N-termini of these constructs were too flexible – again, showing that structure is important (the original hypothesis of developing CPMPs with structure vs unstructured CPPs). In assessing cell viability of disease-relevant cell line (HDM2 expressing SJSA-1 cells); BP1.6 was the most potent in cell viability, even when compared to SAH-p53-8.<sup>14,49</sup> There may be some off-target toxicity at higher  $\mu\text{M}$  concentrations. These studies show that it is necessary to recognize every molecule is unique when designing cell-permeant versions that contain multiple arginine residues. For hydrocarbon stapled peptides, arginine residues should be placed between and/or near the staple for enhanced cell uptake and cytosolic release.

### 1.5.2 Beta Peptides

The concept of strategically placing arginine residues to increase cellular uptake of miniature proteins was also applied to  $\beta$ -peptides, which incorporate  $\beta$  amino acids containing an additional carbon in their backbone.  $\beta$ -peptides retain the ability to form helices and unlike their  $\alpha$ -peptide counterparts, impart additional stability through improved gauche interactions and limited recognition by cellular proteases.<sup>86</sup> Previous studies examined  $\beta^3$ -peptide delivery with no cellular functions,<sup>87–89</sup> but Harker *et al.* was interested in expanding this strategy for  $\beta$ -peptides to exhibit cellular access and biological function. Using similar strategies as Daniels and Schepartz and Smith *et al.*<sup>16,19</sup> by incorporating  $\beta^3$ -homoarginine ( $\beta^3$ hR) residues to distinct locations on a 14-helix (in this case within the salt bridge to retain helical structure),  $\beta^3$ -peptides were able to reach the cell interior.<sup>90</sup> These  $\beta^3$ -peptides containing  $\beta^3$ hR ( $\beta^3$ 53-12SB<sub>2</sub> and  $\beta^3$ 53-12SB<sub>3</sub>) were designed to bind HDM2 and shown to inhibit the interaction of HDM2 with a p53-derived peptide containing fluorescein (p53AB<sup>flu</sup>) *in vitro*.<sup>90</sup> The oncogene HDM2 binds tumor suppressor protein p53 and provides a therapeutically-relevant interaction for inhibition.<sup>85</sup> A subsequent study described  $\beta$ -peptides containing diether and hydrocarbon bridges (similar to stapled peptides) that were taken up by cells and had affinity for hDM2, yet the  $\beta^3$ -peptide  $\beta^3$ 53-12SB<sub>3</sub> containing the cationic patch had the highest cellular uptake and colocalized with endosomes.<sup>91</sup> These studies illustrate that the concepts learned from design of CPMPs including specific positioning of arginine residues can be extended to  $\beta$ -peptides.

### 1.5.3 Delivery of Protein Cargo

We know from previous studies, that miniature proteins can deliver small molecules, including a range of fluorophores (e.g. rhodamine, fluorescein, SiR) and dexamethasone. We began exploring the biological space by evaluating delivery to the cytosol using the model cargo SNAP-tag conjugated to a variety of CPPs and CPMPs (**Figure 1.2**).<sup>25</sup> SNAP-tag (20 kDa) is a self-labeling enzyme derived from human DNA repair protein O<sup>6</sup>-alkylguanine-DNA alkyltransferase (hAGT).<sup>92–94</sup> In addition to analyzing uptake and cytosolic delivery using miniature proteins (aPP5.3 and ZF5.3 as ZiF), we wanted to compare these delivery tools to other molecules, namely unstructured peptides (Arg<sub>8</sub>, penetratin) as well as cyclic peptides (CPP9 and CPP12). Using a pH-sensitive dye to estimate cytosolic access, the trafficking of CPP9 and CPP12 was reported to be similar to aPP5.3 by Qian *et al.*,<sup>12</sup> warranting analysis by FCS to determine exact cytosolic concentrations. The self-labeling enzyme provided a facile handle to append a fluorophore and the majority of constructs were generated as genetic fusions. For those that could not be expressed as a genetic fusion, (e.g. cyclic peptides with nonproteinogenic amino acids), sortase-based conjunction was completed.<sup>25</sup>

Delivery of SNAP-tag tagged with either of two penta-Arg-containing miniature proteins was compared to several canonical CPPs and cyclic peptides. The wild-type SNAP-tag containing a rhodamine fluorophore (SNAP<sup>R</sup>) had minimal levels of total cellular uptake (as determined by flow cytometry) and cytosolic accumulation (<2 nM, quantified by FCS).<sup>25</sup> ZF5.3-SNAP<sup>R</sup> exhibited a 17-fold increase in cellular uptake

compared to SNAP<sup>R</sup>, whereas CPP9-SNAP<sup>R</sup> had comparable levels of total cellular uptake as SNAP<sup>R</sup> alone. This study showed that ZF5.3-SNAP<sup>R</sup> experienced the highest cellular uptake in multiple cell lines (Saos-2, HeLa, and SK-HEP-1) and remained intact even after it reached the cytosol. In analyzing FCS data, ZF5.3-SNAP<sup>R</sup> reached the cytosol at the highest concentrations ( $58 \pm 6.1$  nM with a 1  $\mu$ M delivery concentration). The only other SNAP conjugate to reach appreciable levels (>20 nM), was Penetratin-SNAP<sup>R</sup> ( $23 \pm 2.9$  nM).<sup>25</sup> These studies show that the delivery efficiency of ZF5.3 alone compared to when it is appended to protein cargo decreases from 70% to approximately 6%. This could be due to differences in size between the peptide and protein conjugate, similar to experiments with nanoparticles in which smaller particles deliver more cargo into the interior of the cell than larger ones.<sup>95</sup> Both time- and concentration-dependent changes were present with increasing incubation time and concentration of ZF5.3-SNAP<sup>R</sup>, but no increases were observed for CPP12-SNAP<sup>R</sup> for either time or concentration.<sup>25</sup> It was also of interest to determine whether SNAP would remain active once it reaches the cytosol or whether the acidification of the endosome<sup>62</sup> would render it inactive during its cellular journey. After a 1  $\mu$ M 30 min uptake with CPP-SNAP conjugates, the dye SNAP-Cell<sup>®</sup> 505-Star incubated with cells for 45 min. Diffuse fluorescence was observed in confocal microscopy images and an increase in SNAP-Cell<sup>®</sup> 505-Star signal was exhibited by ZF5.3-SNAP<sup>R</sup> and Pen-SNAP<sup>R</sup> and implying that SNAP-tag is still active when it reaches the cytosol.<sup>25</sup> aPP5.3-SNAP<sup>R</sup> and Arg<sub>8</sub>-SNAP<sup>R</sup> had punctate fluorescence, indicative of being trapped within endosomes. These studies, taken together, support that ZF5.3 is the delivery vehicle that results in the highest cellular uptake and cytosolic concentrations even when compared to canonical CPPs, resonating with peptide data corresponding to ZF5.3.<sup>18,25,30</sup>

To show that additional proteins could be delivered using CPMPs, we evaluated APEX2 delivery using ZF5.3. APEX2 (27 kDa) is an enzyme that biotinylates nearby proteins and is used in determining protein-protein interactions (**Figure 1.2**).<sup>96</sup> After confirming that the addition of ZF5.3 or the rhodamine (R) tag did not impede *in vitro* activity, cells were treated with 1  $\mu$ M APEX2 proteins. There was a 2-fold increase in the total cellular uptake of ZF5.3-APEX2<sup>R</sup> compared to APEX2 alone.<sup>25</sup> ZF5.3-APEX2<sup>R</sup> reached average cytosolic concentrations of  $17 \pm 1.0$  nM and while APEX2 alone reached concentrations of  $4.7 \pm 0.41$  nM. Additionally, ZF5.3-APEX2 was active in cells using an AmplexRed assay (this assay could not state where ZF5.3-APEX2 was present, just that the enzyme could still turn over inside the cell). Ultimately, these studies illustrate that delivery vehicle and cargo identity (size, charge, complexity, etc.) play a role in how much material reaches the cytosol.

#### 1.5.4 Enzyme Replacement Strategy

Previous studies demonstrated that monomeric, non-biologically relevant proteins can be delivered to the cytosol of cells,<sup>25</sup> but the question whether CPMPs could deliver therapeutically-relevant cargo remained unanswered. Citrullinemia type I (CTLN-I) results from the absence or deficiency of argininosuccinate synthetase (AS), an essential component of the urea cycle (**Figure 1.2**), and results in the harmful accumulation of ammonia in blood and cerebrospinal fluid. ZF5.3 can deliver AS, a

cytosolic enzyme made up of four 46 kDa monomers that converts aspartic acid and citrulline into argininosuccinic acid, to the cytosol of cells in culture and the livers of healthy mice.<sup>31</sup> The fusion protein ZF5.3-AS is catalytically active *in vitro* and stabilized in mouse plasma. Additionally, it traffics to the cytosol of cultured Saos-2 and SK-HEP-1 cells, achieving cytosolic concentrations greater than 100 nM (3–10-fold higher than the concentration of endogenous AS). When injected into healthy C57BL/6 mice, ZF5.3-AS reaches the mouse liver to establish concentrations almost 200 nM above baseline. These studies demonstrate that ZF5.3 can deliver a complex protein enzyme to the cytosol at therapeutically relevant concentrations and support its application as an improved delivery vehicle for cytosolic enzyme replacement therapies.

Additional applications that have been studied (unpublished results) include monobodies for inhibitors of protein-protein interactions (e.g. AS27, NS1), transcription regulators (e.g. MeCP2), and gene editors (e.g. Cas9). These results will soon allow us to draw more complete conclusions about the impact of cargo size and charge.

## 1.6 Conclusions

The low efficiency of endosomal release is the most significant problem facing the development of next-generation biologics.<sup>97</sup> Uptake into the endocytic pathway appears to depend predominantly on overall charge.<sup>98,99</sup> Endosomal release is a different beast entirely, and may depend on (a) protein size; (b) folding energy; and (c) the engagement of endosomal remodeling machinery, which may itself be protein dependent. Ongoing and future work will demonstrate the ability of our vehicles to deliver a range of cargo with varying size, oligomerization, charge, etc. The applications described herein explore penta-Arg motifs in stapled peptides, discrete arrays of arginine residues in  $\beta$ -peptides, conjugates of CPMPs with proteins, and enzyme replacement strategies. ZF5.3 itself has the highest endosomal release compared to a number of canonical CPPs and cell penetrating peptides<sup>25</sup> and additional groups have observed high cytosolic delivery of both aPP5.3 and ZF5.3.<sup>12,100</sup> While many of the applications described herein utilize proteinaceous material, we foresee that ZF5.3 could be used as a platform technology to deliver milieu of molecules, such as antibodies (or antibody fragments), RNA, small molecule inhibitors, etc. We also anticipate that as we continue to study the mechanism of CPMPs, we will identify additional determinants of cytosolic access, including endosomal escape pathways.

An additional challenge is the limited number of studies completed in animals of cell-penetrating peptides. Many of the journal articles from the cell-penetrating peptide literature, even in the recent past, only evaluate cell delivery.<sup>57,82,101–111</sup> In order to push the field forward, there is a need to understand the effects of these delivery vehicles in animals, including whether they reach the organs of interest and/or exhibit toxicity. These future *in vitro* and *in vivo* studies may make it possible to correlate cytosolic concentration with uptake/efficacy and predict the best cellular delivery strategies.

The following chapters describe FCS methodology, diffusion parameters of free dye and CPMPs, and delivery of SNAP-tag, argininosuccinate synthetase, and Cas9, detailing our efforts towards cellular and animal studies with ZF5.3-containing proteins.



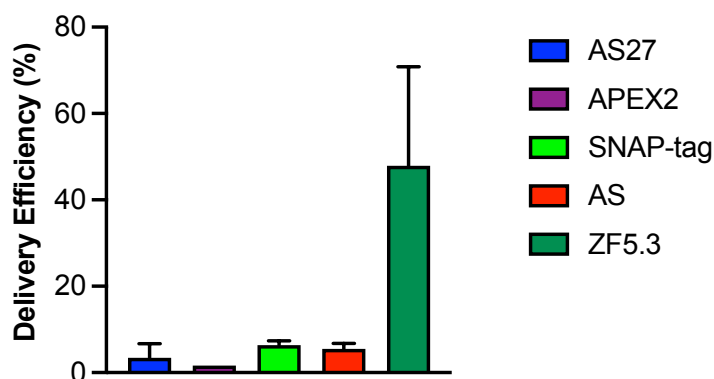
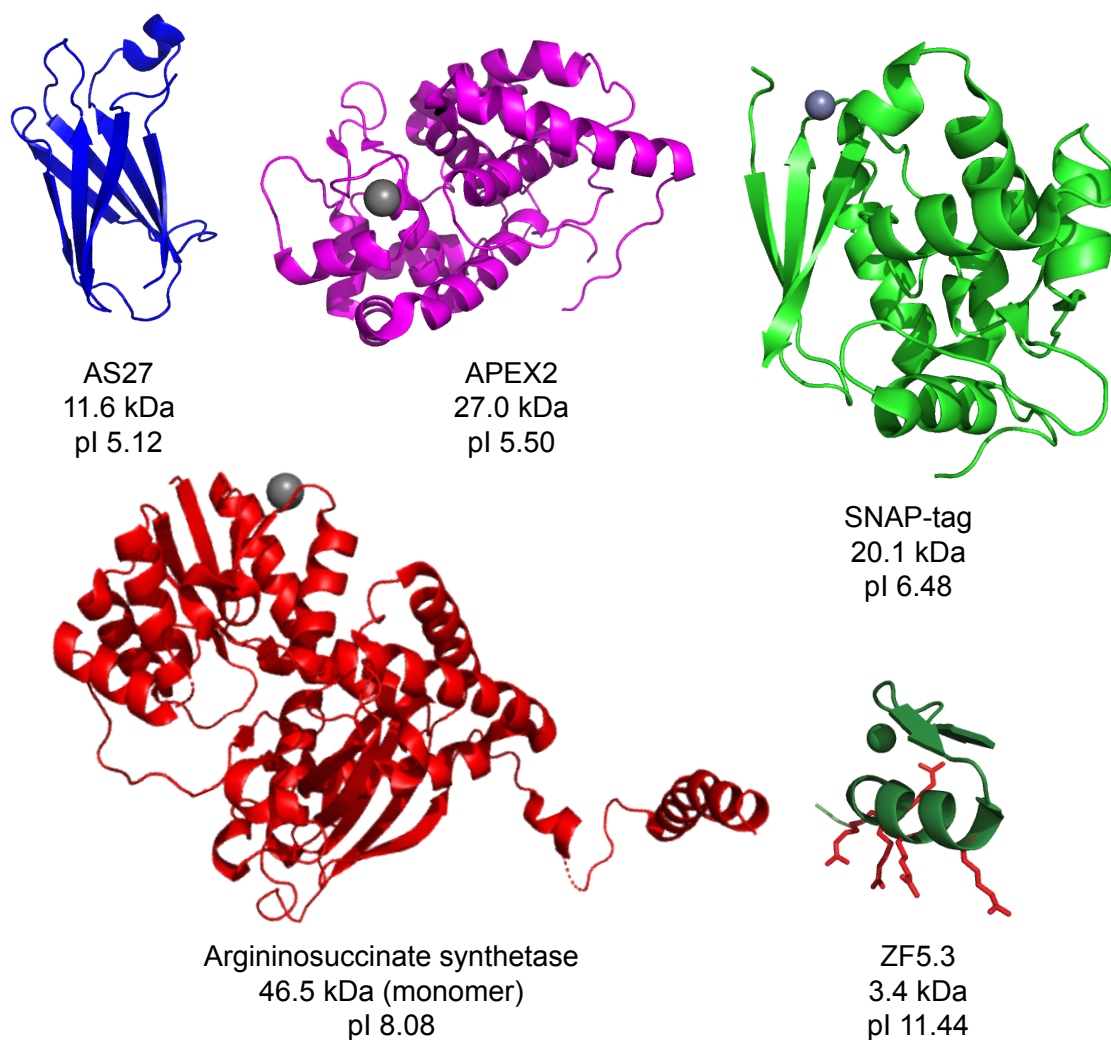


**Figure 1.2.** Proteins delivered to mammalian cells using CPMPs with respective size (kDa) and isoelectric point (pI) information (without CPMP attached). Protein Data Bank files for each protein: AS27 = 5dc4 (structure of AS25, similar to AS27) APEX2 = 1v0h (parent structure of APEX2), SNAP-tag = 3kzz, argininosuccinate synthetase (AS) = 2nz2. Delivery efficiencies (concentration within the cytosol divided by incubation

concentration) of protein cargo when attached to ZF5.3, averaged among cell type, incubation concentration, and incubation time.

## 1.8 References

- (1) Lipinski, C. A. Drug-like Properties and the Causes of Poor Solubility and Poor Permeability. *Curr. Dir. Drug Discov. Rev. Mod. Tech.* **2000**, *44* (1), 235–249. [https://doi.org/10.1016/S1056-8719\(00\)00107-6](https://doi.org/10.1016/S1056-8719(00)00107-6).
- (2) Lipinski, C. A.; Lombardo, F.; Dominy, B. W.; Feeney, P. J. Experimental and Computational Approaches to Estimate Solubility and Permeability in Drug Discovery and Development Settings. *Vitro Models Sel. Dev. Candidates* **1997**, *23* (1), 3–25. [https://doi.org/10.1016/S0169-409X\(96\)00423-1](https://doi.org/10.1016/S0169-409X(96)00423-1).
- (3) Ryser, H. J.-P.; Hancock, R. Histones and Basic Polyamino Acids Stimulate the Uptake of Albumin by Tumor Cells in Culture. *Science* **1965**, *150* (3695), 501. <https://doi.org/10.1126/science.150.3695.501>.
- (4) Green, M.; Loewenstein, P. M. Autonomous Functional Domains of Chemically Synthesized Human Immunodeficiency Virus Tat Trans-Activator Protein. *Cell* **1988**, *55* (6), 1179–1188. [https://doi.org/10.1016/0092-8674\(88\)90262-0](https://doi.org/10.1016/0092-8674(88)90262-0).
- (5) Frankel, A. D.; Pabo, C. O. Cellular Uptake of the Tat Protein from Human Immunodeficiency Virus. *Cell* **1988**, *55* (6), 1189–1193. [https://doi.org/10.1016/0092-8674\(88\)90263-2](https://doi.org/10.1016/0092-8674(88)90263-2).
- (6) Derossi, D.; Joliot, A. H.; Chassaing, G.; Prochiantz, A. The Third Helix of the Antennapedia Homeodomain Translocates through Biological Membranes. *J. Biol. Chem.* **1994**, *269* (14), 10444–10450.
- (7) Fawell, S.; Seery, J.; Daikh, Y.; Moore, C.; Chen, L. L.; Pepinsky, B.; Barsoum, J. Tat-Mediated Delivery of Heterologous Proteins into Cells. *Proc. Natl. Acad. Sci.* **1994**, *91* (2), 664–668. <https://doi.org/10.1073/pnas.91.2.664>.
- (8) Kalafatovic, D.; Giralt, E. Cell-Penetrating Peptides: Design Strategies beyond Primary Structure and Amphipathicity. *Molecules* **2017**, *22* (11). <https://doi.org/10.3390/molecules22111929>.
- (9) McNaughton, B. R.; Cronican, J. J.; Thompson, D. B.; Liu, D. R. Mammalian Cell Penetration, siRNA Transfection, and DNA Transfection by Supercharged Proteins. *Proc. Natl. Acad. Sci.* **2009**, *106* (15), 6111–6116. <https://doi.org/10.1073/pnas.0807883106>.
- (10) Qian, Z.; Liu, T.; Liu, Y.-Y.; Briesewitz, R.; Barrios, A. M.; Jhiang, S. M.; Pei, D. Efficient Delivery of Cyclic Peptides into Mammalian Cells with Short Sequence Motifs. *ACS Chem. Biol.* **2013**, *8* (2), 423–431. <https://doi.org/10.1021/cb3005275>.
- (11) Qian, Z.; Dougherty, P. G.; Pei, D. Monitoring the Cytosolic Entry of Cell-Penetrating Peptides Using a PH-Sensitive Fluorophore. *Chem. Commun.* **2015**, *51* (11), 2162–2165. <https://doi.org/10.1039/C4CC09441G>.
- (12) Qian, Z.; Martyna, A.; Hard, R. L.; Wang, J.; Appiah-Kubi, G.; Coss, C.; Phelps, M. A.; Rossman, J. S.; Pei, D. Discovery and Mechanism of Highly Efficient Cyclic Cell-Penetrating Peptides. *Biochemistry* **2016**, *55* (18), 2601–2612. <https://doi.org/10.1021/acs.biochem.6b00226>.

- (13) Qian, Z.; Dougherty, P. G.; Pei, D. Targeting Intracellular Protein–Protein Interactions with Cell-Permeable Cyclic Peptides. *Curr. Opin. Chem. Biol.* **2017**, *38* (Supplement C), 80–86. <https://doi.org/10.1016/j.cbpa.2017.03.011>.
- (14) Bernal, F.; Tyler, A. F.; Korsmeyer, S. J.; Walensky, L. D.; Verdine, G. L. Reactivation of the P53 Tumor Suppressor Pathway by a Stapled P53 Peptide. *J. Am. Chem. Soc.* **2007**, *129* (9), 2456–2457. <https://doi.org/10.1021/ja0693587>.
- (15) Appelbaum, J. S.; LaRochelle, J. R.; Smith, B. A.; Balkin, D. M.; Holub, J. M.; Schepartz, A. Arginine Topology Controls Escape of Minimally Cationic Proteins from Early Endosomes to the Cytoplasm. *Chem. Biol.* **2012**, *19* (7), 819–830. <https://doi.org/10.1016/j.chembiol.2012.05.022>.
- (16) Daniels, D. S.; Schepartz, A. Intrinsically Cell-Permeable Miniature Proteins Based on a Minimal Cationic PPII Motif. *J. Am. Chem. Soc.* **2007**, *129* (47), 14578–14579. <https://doi.org/10.1021/ja0772445>.
- (17) Holub, J. M.; LaRochelle, J. R.; Appelbaum, J. S.; Schepartz, A. Improved Assays for Determining the Cytosolic Access of Peptides, Proteins, and Their Mimetics. *Biochemistry* **2013**, *52* (50), 9036–9046. <https://doi.org/10.1021/bi401069g>.
- (18) LaRochelle, J. R.; Cobb, G. B.; Steinauer, A.; Rhoades, E.; Schepartz, A. Fluorescence Correlation Spectroscopy Reveals Highly Efficient Cytosolic Delivery of Certain Penta-Arg Proteins and Stapled Peptides. *J. Am. Chem. Soc.* **2015**, *137* (7), 2536–2541. <https://doi.org/10.1021/ja510391n>.
- (19) Smith, B. A.; Daniels, D. S.; Coplin, A. E.; Jordan, G. E.; McGregor, L. M.; Schepartz, A. Minimally Cationic Cell-Permeable Miniature Proteins via  $\alpha$ -Helical Arginine Display. *J. Am. Chem. Soc.* **2008**, *130* (10), 2948–2949. <https://doi.org/10.1021/ja800074v>.
- (20) Via, M. A.; Del Pópolo, M. G.; Wilke, N. Negative Dipole Potentials and Carboxylic Polar Head Groups Foster the Insertion of Cell-Penetrating Peptides into Lipid Monolayers. *Langmuir* **2018**, *34* (9), 3102–3111. <https://doi.org/10.1021/acs.langmuir.7b04038>.
- (21) Takechi-Haraya, Y.; Saito, H. Current Understanding of Physicochemical Mechanisms for Cell Membrane Penetration of Arginine-Rich Cell Penetrating Peptides: Role of Glycosaminoglycan Interactions. *Curr Protein Pept Sci* **2018**. <https://doi.org/10.2174/1389203719666180112100747>.
- (22) Futaki, S.; Suzuki, T.; Ohashi, W.; Yagami, T.; Tanaka, S.; Ueda, K.; Sugiura, Y. Arginine-Rich Peptides: An Abundant Source of Membrane-Permeable Peptides Having Potential as Carriers for Intracellular Protein Delivery. *J. Biol. Chem.* **2001**, *276* (8), 5836–5840. <https://doi.org/10.1074/jbc.M007540200>.
- (23) Park, S. E.; Sajid, M. I.; Parang, K.; Tiwari, R. K. Cyclic Cell-Penetrating Peptides as Efficient Intracellular Drug Delivery Tools. *Mol. Pharm.* **2019**, *16* (9), 3727–3743. <https://doi.org/10.1021/acs.molpharmaceut.9b00633>.
- (24) Qian, Z.; LaRochelle, J. R.; Jiang, B.; Lian, W.; Hard, R. L.; Selner, N. G.; Luechapanichkul, R.; Barrios, A. M.; Pei, D. Early Endosomal Escape of a Cyclic Cell-Penetrating Peptide Allows Effective Cytosolic Cargo Delivery. *Biochemistry* **2014**, *53* (24), 4034–4046. <https://doi.org/10.1021/bi5004102>.
- (25) Wissner, R. F.; Steinauer, A.; Knox, S. L.; Thompson, A. D.; Schepartz, A. Fluorescence Correlation Spectroscopy Reveals Efficient Cytosolic Delivery of

- Protein Cargo by Cell-Permeant Miniature Proteins. *ACS Cent. Sci.* **2018**, *4* (10), 1379–1393. <https://doi.org/10.1021/acscentsci.8b00446>.
- (26) Richard, J. P.; Melikov, K.; Brooks, H.; Prevot, P.; Lebleu, B.; Chernomordik, L. V. Cellular Uptake of Unconjugated TAT Peptide Involves Clathrin-Dependent Endocytosis and Heparan Sulfate Receptors. *J. Biol. Chem.* **2005**, *280* (15), 15300–15306. <https://doi.org/10.1074/jbc.M401604200>.
- (27) Yu, H.; Zou, Y.; Wang, Y.; Huang, X.; Huang, G.; Sumer, B. D.; Boothman, D. A.; Gao, J. Overcoming Endosomal Barrier by Amphotericin B-Loaded Dual PH-Responsive PDMA-b-PDPA Micelleplexes for siRNA Delivery. *ACS Nano* **2011**, *5* (11), 9246–9255. <https://doi.org/10.1021/nn203503h>.
- (28) Maiolo, J. R.; Ottinger, E. A.; Ferrer, M. Specific Redistribution of Cell-Penetrating Peptides from Endosomes to the Cytoplasm and Nucleus upon Laser Illumination. *J. Am. Chem. Soc.* **2004**, *126* (47), 15376–15377. <https://doi.org/10.1021/ja044867z>.
- (29) Deprey, K.; Becker, L.; Kritzer, J.; Plückthun, A. Trapped! A Critical Evaluation of Methods for Measuring Total Cellular Uptake versus Cytosolic Localization. *Bioconjug. Chem.* **2019**, *30* (4), 1006–1027. <https://doi.org/10.1021/acs.bioconjchem.9b00112>.
- (30) Steinauer, A.; LaRoche, J. R.; Knox, S. L.; Wissner, R. F.; Berry, S.; Schepartz, A. HOPS-Dependent Endosomal Fusion Required for Efficient Cytosolic Delivery of Therapeutic Peptides and Small Proteins. *Proc. Natl. Acad. Sci.* **2019**, *116* (2), 512–521. <https://doi.org/10.1073/pnas.1812044116>.
- (31) Knox, S. L.; Wissner, R.; Piszkiwicz, S.; Schepartz, A. Cytosolic Delivery of Argininosuccinate Synthetase Using a Cell-Permeant Miniature Protein. *ACS Cent. Sci.* **2021**, *7* (4), 641–649. <https://doi.org/10.1021/acscentsci.0c01603>.
- (32) Suzuki, T.; Futaki, S.; Niwa, M.; Tanaka, S.; Ueda, K.; Sugiura, Y. Possible Existence of Common Internalization Mechanisms among Arginine-Rich Peptides. *J. Biol. Chem.* **2002**, *277* (4), 2437–2443. <https://doi.org/10.1074/jbc.M110017200>.
- (33) Jones, S. W.; Christison, R.; Bundell, K.; Voyce, C. J.; Brockbank, S. M. V.; Newham, P.; Lindsay, M. A. Characterisation of Cell-Penetrating Peptide-Mediated Peptide Delivery. *Br. J. Pharmacol.* **2005**, *145* (8), 1093–1102. <https://doi.org/10.1038/sj.bjp.0706279>.
- (34) Fuchs, S. M.; Raines, R. T. Polyarginine as a Multifunctional Fusion Tag. *Protein Sci.* **2005**, *14* (6), 1538–1544. <https://doi.org/10.1110/ps.051393805>.
- (35) Sadler, K.; Eom, K. D.; Yang, J.-L.; Dimitrova, Y.; Tam, J. P. Translocating Proline-Rich Peptides from the Antimicrobial Peptide Bactenecin 7. *Biochemistry* **2002**, *41* (48), 14150–14157. <https://doi.org/10.1021/bi026661l>.
- (36) Fernández-Carneado, J.; Kogan, M. J.; Castel, S.; Giralt, E. Potential Peptide Carriers: Amphipathic Proline-Rich Peptides Derived from the N-Terminal Domain of  $\gamma$ -Zein. *Angew. Chem. Int. Ed.* **2004**, *43* (14), 1811–1814. <https://doi.org/10.1002/anie.200352540>.
- (37) Zondlo, N. J.; Schepartz, A. Highly Specific DNA Recognition by a Designed Miniature Protein. *J. Am. Chem. Soc.* **1999**, *121* (29), 6938–6939. <https://doi.org/10.1021/ja990968z>.

- (38) Chin, J. W.; Schepartz, A. Design and Evolution of a Miniature Bcl-2 Binding Protein. *Angew. Chem. Int. Ed.* **2001**, *40* (20), 3806–3809. [https://doi.org/10.1002/1521-3773\(20011015\)40:20<3806::AID-ANIE3806>3.0.CO;2-B](https://doi.org/10.1002/1521-3773(20011015)40:20<3806::AID-ANIE3806>3.0.CO;2-B).
- (39) Gemperli, A. C.; Rutledge, S. E.; Maranda, A.; Schepartz, A. Paralog-Selective Ligands for Bcl-2 Proteins. *J. Am. Chem. Soc.* **2005**, *127* (6), 1596–1597. <https://doi.org/10.1021/ja0441211>.
- (40) Volkman, H. M.; Rutledge, S. E.; Schepartz, A. Binding Mode and Transcriptional Activation Potential of High Affinity Ligands for the CBP KIX Domain. *J. Am. Chem. Soc.* **2005**, *127* (13), 4649–4658. <https://doi.org/10.1021/ja042761y>.
- (41) Kritzer, J. A.; Zutshi, R.; Cheah, M.; Ran, F. A.; Webman, R.; Wongjirad, T. M.; Schepartz, A. Miniature Protein Inhibitors of the P53–HDM2 Interaction. *ChemBioChem* **2006**, *7* (1), 29–31. <https://doi.org/10.1002/cbic.200500324>.
- (42) Blundell, T. L.; Pitts, J. E.; Tickle, I. J.; Wood, S. P.; Wu, C.-W. X-Ray Analysis (1.4-Å Resolution) of Avian Pancreatic Polypeptide: Small Globular Protein Hormone. *Proc. Natl. Acad. Sci.* **1981**, *78* (7), 4175. <https://doi.org/10.1073/pnas.78.7.4175>.
- (43) Glover, I.; Haneef, I.; Pitts, J.; Wood, S.; Moss, D.; Tickle, I.; Blundell, T. Conformational Flexibility in a Small Globular Hormone: X-Ray Analysis of Avian Pancreatic Polypeptide at 0.98-Å Resolution. *Biopolymers* **1983**, *22* (1), 293–304. <https://doi.org/10.1002/bip.360220138>.
- (44) Yu, P.; Liu, B.; Kodadek, T. A High-Throughput Assay for Assessing the Cell Permeability of Combinatorial Libraries. *Nat. Biotechnol.* **2005**, *23* (6), 746–751. <https://doi.org/10.1038/nbt1099>.
- (45) Carey, K. L.; Richards, S. A.; Lounsbury, K. M.; Macara, I. G. Evidence Using a Green Fluorescent Protein-Glucocorticoid Receptor Chimera That the Ran/TC4 GTPase Mediates an Essential Function Independent of Nuclear Protein Import. *J. Cell Biol.* **1996**, *133* (5), 985–996. <https://doi.org/10.1083/jcb.133.5.985>.
- (46) Knox, S. L.; Steinauer, A.; Alpha-Cobb, G.; Trexler, A.; Rhoades, E.; Schepartz, A. Chapter Twenty-One - Quantification of Protein Delivery in Live Cells Using Fluorescence Correlation Spectroscopy. In *Methods in Enzymology*; Chenoweth, D. M., Ed.; Academic Press, 2020; Vol. 641, pp 477–505. <https://doi.org/10.1016/bs.mie.2020.05.007>.
- (47) Waizenegger, T.; Fischer, R.; Brock, R. Intracellular Concentration Measurements in Adherent Cells: A Comparison of Import Efficiencies of Cell-Permeable Peptides. *Biol. Chem.* **2002**, *383* (2), 291–299. <https://doi.org/10.1515/bc.2002.031>.
- (48) Fischer, R.; Waizenegger, T.; Köhler, K.; Brock, R. A Quantitative Validation of Fluorophore-Labelled Cell-Permeable Peptide Conjugates: Fluorophore and Cargo Dependence of Import. *Biochim. Biophys. Acta BBA - Biomembr.* **2002**, *1564* (2), 365–374. [https://doi.org/10.1016/S0005-2736\(02\)00471-6](https://doi.org/10.1016/S0005-2736(02)00471-6).
- (49) Quach, K.; LaRochelle, J.; Li, X.-H.; Rhoades, E.; Schepartz, A. Unique Arginine Array Improves Cytosolic Localization of Hydrocarbon-Stapled Peptides. *Bioorg. Med. Chem.* **2018**, *26* (6), 1197–1202. <https://doi.org/10.1016/j.bmc.2017.11.008>.

- (50) Verdurmen, W. P. R.; Mazlami, M.; Plückthun, A. A Quantitative Comparison of Cytosolic Delivery via Different Protein Uptake Systems. *Sci. Rep.* **2017**, *7* (1), 13194. <https://doi.org/10.1038/s41598-017-13469-y>.
- (51) Peier, A.; Ge, L.; Boyer, N.; Frost, J.; Duggal, R.; Biswas, K.; Edmondson, S.; Hermes, J. D.; Yan, L.; Zimprich, C.; Sadruddin, A.; Kristal Kaan, H. Y.; Chandramohan, A.; Brown, C. J.; Thean, D.; Lee, X. E.; Yuen, T. Y.; Ferrer-Gago, F. J.; Johannes, C. W.; Lane, D. P.; Sherborne, B.; Corona, C.; Robers, M. B.; Sawyer, T. K.; Partridge, A. W. NanoClick: A High Throughput, Target-Agnostic Peptide Cell Permeability Assay. *ACS Chem. Biol.* **2021**, *16* (2), 293–309. <https://doi.org/10.1021/acscchembio.0c00804>.
- (52) Desai, T. J.; Habulihaz, B.; Cannon, J. R.; Chandramohan, A.; Kaan, H. Y. K.; Sadruddin, A.; Yuen, T. Y.; Johannes, C.; Thean, D.; Brown, C. J.; Lane, D. P.; Partridge, A. W.; Evers, R.; Sawyer, T. K.; Hochman, J. Liposome Click Membrane Permeability Assay for Identifying Permeable Peptides. *Pharm. Res.* **2021**. <https://doi.org/10.1007/s11095-021-03005-z>.
- (53) Palm, C.; Jayamanne, M.; Kjellander, M.; Hällbrink, M. Peptide Degradation Is a Critical Determinant for Cell-Penetrating Peptide Uptake. *Biochim. Biophys. Acta BBA - Biomembr.* **2007**, *1768* (7), 1769–1776. <https://doi.org/10.1016/j.bbamem.2007.03.029>.
- (54) Carroll, D. Progress and Prospects: Zinc-Finger Nucleases as Gene Therapy Agents. *Gene Ther.* **2008**, *15* (22), 1463–1468. <https://doi.org/10.1038/gt.2008.145>.
- (55) Krizek, B. A.; Amann, B. T.; Kilfoil, V. J.; Merkle, D. L.; Berg, J. M. A Consensus Zinc Finger Peptide: Design, High-Affinity Metal Binding, a PH-Dependent Structure, and a His to Cys Sequence Variant. *J. Am. Chem. Soc.* **1991**, *113* (12), 4518–4523. <https://doi.org/10.1021/ja00012a021>.
- (56) Madani, F.; Lindberg, S.; Langel, U.; Futaki, S.; Gräslund, A. Mechanisms of Cellular Uptake of Cell-Penetrating Peptides. *J. Biophys. Hindawi Publ. Corp. Online* **2011**, *2011*, 414729–414729. <https://doi.org/10.1155/2011/414729>.
- (57) Patel, S. G.; Sayers, E. J.; He, L.; Narayan, R.; Williams, T. L.; Mills, E. M.; Allemann, R. K.; Luk, L. Y. P.; Jones, A. T.; Tsai, Y.-H. Cell-Penetrating Peptide Sequence and Modification Dependent Uptake and Subcellular Distribution of Green Florescent Protein in Different Cell Lines. *Sci. Rep.* **2019**, *9* (1), 1–9. <https://doi.org/10.1038/s41598-019-42456-8>.
- (58) Walensky, L. D.; Bird, G. H. Hydrocarbon-Stapled Peptides: Principles, Practice, and Progress. *J. Med. Chem.* **2014**, *57* (15), 6275–6288. <https://doi.org/10.1021/jm4011675>.
- (59) Payne, C. K.; Jones, S. A.; Chen, C.; Zhuang, X. Internalization and Trafficking of Cell Surface Proteoglycans and Proteoglycan-Binding Ligands. *Traffic* **2007**, *8* (4), 389–401. <https://doi.org/10.1111/j.1600-0854.2007.00540.x>.
- (60) Hanover, J. A.; Willingham, M. C.; Pastan, I. Kinetics of Transit of Transferrin and Epidermal Growth Factor through Clathrin-Coated Membranes. *Cell* **1984**, *39* (2, Part 1), 283–293. [https://doi.org/10.1016/0092-8674\(84\)90006-0](https://doi.org/10.1016/0092-8674(84)90006-0).
- (61) Lakadamyali, M.; Rust, M. J.; Zhuang, X. Ligands for Clathrin-Mediated Endocytosis Are Differentially Sorted into Distinct Populations of Early

- Endosomes. *Cell* **2006**, *124* (5), 997–1009. <https://doi.org/10.1016/j.cell.2005.12.038>.
- (62) Doherty, G. J.; McMahon, H. T. Mechanisms of Endocytosis. *Annu. Rev. Biochem.* **2009**, *78* (1), 857–902. <https://doi.org/10.1146/annurev.biochem.78.081307.110540>.
- (63) Macia, E.; Ehrlich, M.; Massol, R.; Boucrot, E.; Brunner, C.; Kirchhausen, T. Dynasore, a Cell-Permeable Inhibitor of Dynamin. *Dev. Cell* **2006**, *10* (6), 839–850. <https://doi.org/10.1016/j.devcel.2006.04.002>.
- (64) Rodal, S. K.; Skretting, G.; Garred, Ø.; Vilhardt, F.; van Deurs, B.; Sandvig, K. Extraction of Cholesterol with Methyl- $\beta$ -Cyclodextrin Perturbs Formation of Clathrin-Coated Endocytic Vesicles. *Mol. Biol. Cell* **1999**, *10* (4), 961–974. <https://doi.org/10.1091/mbc.10.4.961>.
- (65) Koivusalo, M.; Welch, C.; Hayashi, H.; Scott, C. C.; Kim, M.; Alexander, T.; Touret, N.; Hahn, K. M.; Grinstein, S. Amiloride Inhibits Macropinocytosis by Lowering Submembranous PH and Preventing Rac1 and Cdc42 Signaling. *J. Cell Biol.* **2010**, *188* (4), 547–563. <https://doi.org/10.1083/jcb.200908086>.
- (66) Yoshimori, T.; Yamamoto, A.; Moriyama, Y.; Futai, M.; Tashiro, Y. Bafilomycin A1, a Specific Inhibitor of Vacuolar-Type H(+)-ATPase, Inhibits Acidification and Protein Degradation in Lysosomes of Cultured Cells. *J. Biol. Chem.* **1991**, *266* (26), 17707–17712. [https://doi.org/10.1016/S0021-9258\(19\)47429-2](https://doi.org/10.1016/S0021-9258(19)47429-2).
- (67) Fischer, R.; Köhler, K.; Fotin-Mleczek, M.; Brock, R. A Stepwise Dissection of the Intracellular Fate of Cationic Cell-Penetrating Peptides. *J. Biol. Chem.* **2004**, *279* (13), 12625–12635. <https://doi.org/10.1074/jbc.M311461200>.
- (68) Huotari, J.; Helenius, A. Endosome Maturation. *EMBO J.* **2011**, *30* (17), 3481–3500. <https://doi.org/10.1038/emboj.2011.286>.
- (69) Barbieri, M. A.; Li, G.; Mayorga, L. S.; Stahl, P. D. Characterization of Rab5:Q79L-Stimulated Endosome Fusion. *Arch. Biochem. Biophys.* **1996**, *326* (1), 64–72. <https://doi.org/10.1006/abbi.1996.0047>.
- (70) Christoforidis, S.; McBride, H. M.; Burgoyne, R. D.; Zerial, M. The Rab5 Effector EEA1 Is a Core Component of Endosome Docking. *Nature* **1999**, *397* (6720), 621–625. <https://doi.org/10.1038/17618>.
- (71) Wender, P. A.; Mitchell, D. J.; Pattabiraman, K.; Pelkey, E. T.; Steinman, L.; Rothbard, J. B. The Design, Synthesis, and Evaluation of Molecules That Enable or Enhance Cellular Uptake: Peptoid Molecular Transporters. *Proc. Natl. Acad. Sci.* **2000**, *97* (24), 13003. <https://doi.org/10.1073/pnas.97.24.13003>.
- (72) Thurston, T. L. M.; Wandel, M. P.; von Muhlinen, N.; Foeglein, Á.; Randow, F. Galectin 8 Targets Damaged Vesicles for Autophagy to Defend Cells against Bacterial Invasion. *Nature* **2012**, *482* (7385), 414–418. <https://doi.org/10.1038/nature10744>.
- (73) Wittrup, A.; Ai, A.; Liu, X.; Hamar, P.; Trifonova, R.; Charisse, K.; Manoharan, M.; Kirchhausen, T.; Lieberman, J. Visualizing Lipid-Formulated siRNA Release from Endosomes and Target Gene Knockdown. *Nat. Biotechnol.* **2015**, *33* (8), 870–876. <https://doi.org/10.1038/nbt.3298>.
- (74) Erazo-Oliveras, A.; Najjar, K.; Dayani, L.; Wang, T.-Y.; Johnson, G. A.; Pellois, J.-P. Protein Delivery into Live Cells by Incubation with an Endosomolytic Agent. *Nat. Methods* **2014**, *11* (8), 861–867. <https://doi.org/10.1038/nmeth.2998>.

- (75) Srinivasan, D.; Muthukrishnan, N.; Johnson, G. A.; Erazo-Oliveras, A.; Lim, J.; Simanek, E. E.; Pellois, J.-P. Conjugation to the Cell-Penetrating Peptide TAT Potentiates the Photodynamic Effect of Carboxytetramethylrhodamine. *PLoS ONE* **2011**, *6* (3), e17732. <https://doi.org/10.1371/journal.pone.0017732>.
- (76) Zhao, M.; Yang, H.; Jiang, X.; Zhou, W.; Zhu, B.; Zeng, Y.; Yao, K.; Ren, C. Lipofectamine RNAiMAX: An Efficient SiRNA Transfection Reagent in Human Embryonic Stem Cells. *Mol. Biotechnol.* **2008**, *40* (1), 19–26. <https://doi.org/10.1007/s12033-008-9043-x>.
- (77) Maejima, I.; Takahashi, A.; Omori, H.; Kimura, T.; Takabatake, Y.; Saitoh, T.; Yamamoto, A.; Hamasaki, M.; Noda, T.; Isaka, Y.; Yoshimori, T. Autophagy Sequesters Damaged Lysosomes to Control Lysosomal Biogenesis and Kidney Injury. *EMBO J.* **2013**, *32* (17), 2336–2347. <https://doi.org/10.1038/emboj.2013.171>.
- (78) Balderhaar, H. J. kleine; Ungermann, C. CORVET and HOPS Tethering Complexes – Coordinators of Endosome and Lysosome Fusion. *J. Cell Sci.* **2013**, *126* (6), 1307. <https://doi.org/10.1242/jcs.107805>.
- (79) Galmes, R.; ten Brink, C.; Oorschot, V.; Veenendaal, T.; Jonker, C.; van der Sluijs, P.; Klumperman, J. Vps33B Is Required for Delivery of Endocytosed Cargo to Lysosomes. *Traffic* **2015**, *16* (12), 1288–1305. <https://doi.org/10.1111/tra.12334>.
- (80) Ikononov, O. C.; Sbrissa, D.; Shisheva, A. YM201636, an Inhibitor of Retroviral Budding and PIKfyve-Catalyzed PtdIns(3,5)P<sub>2</sub> Synthesis, Halts Glucose Entry by Insulin in Adipocytes. *Biochem. Biophys. Res. Commun.* **2009**, *382* (3), 566–570. <https://doi.org/10.1016/j.bbrc.2009.03.063>.
- (81) Willem, J.; ter Beest, M.; Scherphof, G.; Hoekstra, D. A Non-Exchangeable Fluorescent Phospholipid Analog as a Membrane Traffic Marker of the Endocytic Pathway. *Eur. J. Cell Biol.* **1990**, *53* (1), 173–184.
- (82) Sahni, A.; Qian, Z.; Pei, D. Cell-Penetrating Peptides Escape the Endosome by Inducing Vesicle Budding and Collapse. *ACS Chem. Biol.* **2020**, *15* (9), 2485–2492. <https://doi.org/10.1021/acscchembio.0c00478>.
- (83) LeCher, J. C.; Nowak, S. J.; McMurry, J. L. Breaking in and Busting out: Cell-Penetrating Peptides and the Endosomal Escape Problem. *Biomol. Concepts* **2017**, *8* (3–4), 131–141. <https://doi.org/10.1515/bmc-2017-0023>.
- (84) Schafmeister, C. E.; Po, J.; Verdine, G. L. An All-Hydrocarbon Cross-Linking System for Enhancing the Helicity and Metabolic Stability of Peptides. *J. Am. Chem. Soc.* **2000**, *122* (24), 5891–5892. <https://doi.org/10.1021/ja000563a>.
- (85) Böttger, A.; Böttger, V.; Garcia-Echeverria, C.; Chène, P.; Hochkeppel, H.-K.; Sampson, W.; Ang, K.; Howard, S. F.; Picksley, S. M.; Lane, D. P. Molecular Characterization of the Hdm2-P53 Interaction<sup>11</sup>Edited by J. Karn. *J. Mol. Biol.* **1997**, *269* (5), 744–756. <https://doi.org/10.1006/jmbi.1997.1078>.
- (86) Cheng, R. P.; Gellman, S. H.; DeGrado, W. F.  $\beta$ -Peptides: From Structure to Function. *Chem. Rev.* **2001**, *101* (10), 3219–3232. <https://doi.org/10.1021/cr000045i>.
- (87) Rueping, M.; Mahajan, Y.; Sauer, M.; Seebach, D. Cellular Uptake Studies with  $\beta$ -Peptides. *ChemBioChem* **2002**, *3* (2-3), 257–259.

- [https://doi.org/10.1002/1439-7633\(20020301\)3:2/3<257::AID-CBIC257>3.0.CO;2-S](https://doi.org/10.1002/1439-7633(20020301)3:2/3<257::AID-CBIC257>3.0.CO;2-S).
- (88) Potocky, T. B.; Menon, A. K.; Gellman, S. H. Effects of Conformational Stability and Geometry of Guanidinium Display on Cell Entry by  $\beta$ -Peptides. *J. Am. Chem. Soc.* **2005**, *127* (11), 3686–3687. <https://doi.org/10.1021/ja042566j>.
- (89) Umezawa, N.; Gelman, M. A.; Haigis, M. C.; Raines, R. T.; Gellman, S. H. Translocation of a  $\beta$ -Peptide Across Cell Membranes. *J. Am. Chem. Soc.* **2002**, *124* (3), 368–369. <https://doi.org/10.1021/ja017283v>.
- (90) Harker, E. A.; Schepartz, A. Cell-Permeable  $\beta$ -Peptide Inhibitors of P53/HDM2 Complexation. *ChemBioChem* **2009**, *10* (6), 990–993. <https://doi.org/10.1002/cbic.200900049>.
- (91) Bautista, A. D.; Appelbaum, J. S.; Craig, C. J.; Michel, J.; Schepartz, A. Bridged B3-Peptide Inhibitors of P53-HDM2 Complexation: Correlation between Affinity and Cell Permeability. *J. Am. Chem. Soc.* **2010**, *132* (9), 2904–2906. <https://doi.org/10.1021/ja910715u>.
- (92) Juillerat, A.; Gronemeyer, T.; Keppler, A.; Gendreizig, S.; Pick, H.; Vogel, H.; Johnsson, K. Directed Evolution of O6-Alkylguanine-DNA Alkyltransferase for Efficient Labeling of Fusion Proteins with Small Molecules In Vivo. *Chem. Biol.* **2003**, *10* (4), 313–317. [https://doi.org/10.1016/S1074-5521\(03\)00068-1](https://doi.org/10.1016/S1074-5521(03)00068-1).
- (93) Mollwitz, B.; Brunk, E.; Schmitt, S.; Pojer, F.; Bannwarth, M.; Schiltz, M.; Rothlisberger, U.; Johnsson, K. Directed Evolution of the Suicide Protein O6-Alkylguanine-DNA Alkyltransferase for Increased Reactivity Results in an Alkylated Protein with Exceptional Stability. *Biochemistry* **2012**, *51* (5), 986–994. <https://doi.org/10.1021/bi2016537>.
- (94) Keppler, A.; Gendreizig, S.; Gronemeyer, T.; Pick, H.; Vogel, H.; Johnsson, K. A General Method for the Covalent Labeling of Fusion Proteins with Small Molecules in Vivo. *Nat. Biotechnol.* **2003**, *21* (1), 86–89. <https://doi.org/10.1038/nbt765>.
- (95) Prabha, S.; Zhou, W.-Z.; Panyam, J.; Labhasetwar, V. Size-Dependency of Nanoparticle-Mediated Gene Transfection: Studies with Fractionated Nanoparticles. *Int. J. Pharm.* **2002**, *244* (1), 105–115. [https://doi.org/10.1016/S0378-5173\(02\)00315-0](https://doi.org/10.1016/S0378-5173(02)00315-0).
- (96) Lam, S. S.; Martell, J. D.; Kamer, K. J.; Deerinck, T. J.; Ellisman, M. H.; Mootha, V. K.; Ting, A. Y. Directed Evolution of APEX2 for Electron Microscopy and Proximity Labeling. *Nat. Methods* **2015**, *12* (1), 51–54. <https://doi.org/10.1038/nmeth.3179>.
- (97) Fu, A.; Tang, R.; Hardie, J.; Farkas, M. E.; Rotello, V. M. Promises and Pitfalls of Intracellular Delivery of Proteins. *Bioconjug. Chem.* **2014**, *25* (9), 1602–1608. <https://doi.org/10.1021/bc500320j>.
- (98) Thompson, D. B.; Villaseñor, R.; Dorr, B. M.; Zerial, M.; Liu, D. R. Cellular Uptake Mechanisms and Endosomal Trafficking of Supercharged Proteins. *Chem. Biol.* **2012**, *19* (7), 831–843. <https://doi.org/10.1016/j.chembiol.2012.06.014>.
- (99) Cronican, J. J.; Thompson, D. B.; Beier, K. T.; McNaughton, B. R.; Cepko, C. L.; Liu, D. R. Potent Delivery of Functional Proteins into Mammalian Cells in Vitro

- and in Vivo Using a Supercharged Protein. *ACS Chem. Biol.* **2010**, *5* (8), 747–752. <https://doi.org/10.1021/cb1001153>.
- (100) Peraro, L.; Deprey, K. L.; Moser, M. K.; Zou, Z.; Ball, H. L.; Levine, B.; Kritzer, J. A. Cell Penetration Profiling Using the Chloroalkane Penetration Assay. *J. Am. Chem. Soc.* **2018**, *140* (36), 11360–11369. <https://doi.org/10.1021/jacs.8b06144>.
- (101) Lobba, M. J.; Fellmann, C.; Marmelstein, A. M.; Maza, J. C.; Kissman, E. N.; Robinson, S. A.; Staahl, B. T.; Urnes, C.; Lew, R. J.; Mogilevsky, C. S.; Doudna, J. A.; Francis, M. B. Site-Specific Bioconjugation through Enzyme-Catalyzed Tyrosine–Cysteine Bond Formation. *ACS Cent. Sci.* **2020**, *6* (9), 1564–1571. <https://doi.org/10.1021/acscentsci.0c00940>.
- (102) Dougherty, P. G.; Wen, J.; Pan, X.; Koley, A.; Ren, J.-G.; Sahni, A.; Basu, R.; Salim, H.; Appiah Kubi, G.; Qian, Z.; Pei, D. Enhancing the Cell Permeability of Stapled Peptides with a Cyclic Cell-Penetrating Peptide. *J. Med. Chem.* **2019**, *62* (22), 10098–10107. <https://doi.org/10.1021/acs.jmedchem.9b00456>.
- (103) Schneider, A. F. L.; Wallabregue, A. L. D.; Franz, L.; Hackenberger, C. P. R. Targeted Subcellular Protein Delivery Using Cleavable Cyclic Cell-Penetrating Peptides. *Bioconjug. Chem.* **2019**, *30* (2), 400–404. <https://doi.org/10.1021/acs.bioconjchem.8b00855>.
- (104) Lee, H.; Lim, S. I.; Shin, S.-H.; Lim, Y.; Koh, J. W.; Yang, S. Conjugation of Cell-Penetrating Peptides to Antimicrobial Peptides Enhances Antibacterial Activity. *ACS Omega* **2019**, *4* (13), 15694–15701. <https://doi.org/10.1021/acsomega.9b02278>.
- (105) López-Andarias, J.; Saabach, J.; Moreau, D.; Cheng, Y.; Derivery, E.; Laurent, Q.; González-Gaitán, M.; Winssinger, N.; Sakai, N.; Matile, S. Cell-Penetrating Streptavidin: A General Tool for Bifunctional Delivery with Spatiotemporal Control, Mediated by Transport Systems Such as Adaptive Benzopolysulfane Networks. *J. Am. Chem. Soc.* **2020**, *142* (10), 4784–4792. <https://doi.org/10.1021/jacs.9b13621>.
- (106) Allen, J.; Najjar, K.; Erazo-Oliveras, A.; Kondow-McConaghy, H. M.; Brock, D. J.; Graham, K.; Hager, E. C.; Marschall, A. L. J.; Dübel, S.; Juliano, R. L.; Pellois, J.-P. Cytosolic Delivery of Macromolecules in Live Human Cells Using the Combined Endosomal Escape Activities of a Small Molecule and Cell Penetrating Peptides. *ACS Chem. Biol.* **2019**, *14* (12), 2641–2651. <https://doi.org/10.1021/acscchembio.9b00585>.
- (107) Kondow-McConaghy, H. M.; Muthukrishnan, N.; Erazo-Oliveras, A.; Najjar, K.; Juliano, R. L.; Pellois, J.-P. Impact of the Endosomal Escape Activity of Cell-Penetrating Peptides on the Endocytic Pathway. *ACS Chem. Biol.* **2020**, *15* (9), 2355–2363. <https://doi.org/10.1021/acscchembio.0c00319>.
- (108) Lee, H.-J.; Huang, Y.-W.; Chiou, S.-H.; Aronstam, R. S. Polyhistidine Facilitates Direct Membrane Translocation of Cell-Penetrating Peptides into Cells. *Sci. Rep.* **2019**, *9* (1), 9398. <https://doi.org/10.1038/s41598-019-45830-8>.
- (109) Kajiwara, N.; Nomura, N.; Ukaji, M.; Yamamoto, N.; Kohara, M.; Yasui, F.; Sakoda, Y.; Kida, H.; Shibasaki, F. Cell-Penetrating Peptide-Mediated Cell Entry of H5N1 Highly Pathogenic Avian Influenza Virus. *Sci. Rep.* **2020**, *10* (1), 18008. <https://doi.org/10.1038/s41598-020-74604-w>.

- (110) Henning-Knechtel, A.; Kumar, S.; Wallin, C.; Król, S.; Wärmländer, S. K. T. S.; Jarvet, J.; Esposito, G.; Kirmizialtin, S.; Gräslund, A.; Hamilton, A. D.; Magzoub, M. Designed Cell-Penetrating Peptide Inhibitors of Amyloid-Beta Aggregation and Cytotoxicity. *Cell Rep. Phys. Sci.* **2020**, *1* (2), 100014.  
<https://doi.org/10.1016/j.xcrp.2020.100014>.
- (111) Banga, J.; Srinivasan, D.; Sun, C.-C.; Thompson, C. D.; Milletti, F.; Huang, K.-S.; Hamilton, S.; Song, S.; Hoffman, A. F.; Qin, Y. G.; Matta, B.; LaPan, M.; Guo, Q.; Lu, G.; Li, D.; Qian, H.; Bolin, D. R.; Liang, L.; Wartchow, C.; Qiu, J.; Downing, M.; Narula, S.; Fotouhi, N.; DeMartino, J. A.; Tan, S.-L.; Chen, G.; Barnes, B. J. Inhibition of IRF5 Cellular Activity with Cell-Penetrating Peptides That Target Homodimerization. *Sci. Adv.* **2020**, *6* (20), eaay1057.  
<https://doi.org/10.1126/sciadv.aay1057>.

## CHAPTER 2

### Quantification of Protein Delivery Using Fluorescence Correlation Spectroscopy

This chapter was published in *Methods in Enzymology* as

Knox, S. L.; Steinauer, A.; Alpha-Cobb, G.; Trexler, A.; Rhoades, E.; Schepartz, A. **Quantification of protein delivery in live cells using fluorescence correlation spectroscopy.** *Methods in Enzymology.* **2020**, *641*, 477-505.

and has been reproduced with permission from the journal and all co-authors.

## 2.1 Abstract

Fluorescence correlation spectroscopy (FCS) is a quantitative single-molecule method that measures the concentration and rate of diffusion of fluorophore-tagged molecules, both large and small, *in vitro* and within live cells, and even within discrete cellular compartments. FCS is exceptionally well-suited to directly quantify the efficiency of intracellular protein delivery—specifically, how well different “cell-penetrating” proteins and peptides guide proteinaceous materials into the cytosol and nuclei of live mammalian cells. This chapter provides an overview of the procedures necessary to execute robust FCS experiments and evaluate endosomal escape efficiencies: preparation of fluorophore-tagged proteins, incubation with mammalian cells and preparation of FCS samples, setup and execution of an FCS experiment, and a detailed discussion of and custom MATLAB® script for analyzing the resulting autocorrelation curves in the context of appropriate diffusion models.

## 2.2 Introduction

### 2.2.1 Motivations for improving the delivery of intact, active proteins to the cytosol and nucleus

There is enormous current interest in effective strategies for delivering protein, DNA, and RNA therapeutics to the cell interior.<sup>1</sup> With some important exceptions, most proteins and protein-RNA complexes are too large and too polar to diffuse passively across cellular membranes, and instead must enter, circumnavigate, and exit the endocytic pathway to reach the cytosol and internal organelles. The exceptions to this rule — most notably, the Tat transactivator from HIV-1<sup>2,3</sup> and the Antennapedia homeodomain (Antp HD)<sup>4</sup> but others have been identified since<sup>5</sup> — have inspired the synthesis of literally hundreds of potential “cell-penetrating” peptides that have been studied across the globe.<sup>6–18</sup> Much has been learned in the thirty years since the cell-penetrating activities of Tat and Antp HD were discovered.<sup>16</sup> But despite early promise, there is still no general strategy to deliver diverse proteins to the cytosol or nucleus reproducibly and at concentrations that permit their use as therapeutics or research tools. Therapeutic enzymes that operate within the boundaries of the plasma membrane exist — Cerezyme and Fabrazyme are two examples<sup>19</sup> — but these replacement enzymes operate within lysosomes, vesicles within the cell that are topologically separated by a membrane barrier from the cell interior.<sup>20</sup> It is well appreciated that the biochemical problem hindering protein delivery is endosomal release, and that a general and effective strategy for delivering proteins and their complexes to the cell interior would establish a fundamentally new therapeutic modality.<sup>7,20–22</sup>

Although cell-penetrating peptides (CPPs) have been studied for decades, it has been very difficult to optimize their structures and improve activity without a method to directly assess how well they guide a cargo protein out of the endocytic pathway and into the desired cellular compartment, often the cytosol or nucleus. Many indirect methods exist for estimating how much of a protein or protein complex traffics to the cell interior, but only one provides this information directly, quantitatively, and relatively quickly — fluorescence correlation spectroscopy (FCS).<sup>21–23</sup> In recent years, we have

used FCS to study and optimize the delivery efficiency of a family of proteins that carry a defined array of five arginine side chains on a folded  $\alpha$ -helical scaffold; we call these molecules cell-permeant miniature proteins (CPMPs).<sup>6,24–29</sup> This chapter provides a “how-to” guide for executing robust FCS experiments: preparation of fluorophore-tagged CPMP-protein conjugates, a workflow for mammalian cell work, and a detailed discussion of FCS protocols and analysis, including a custom MATLAB® script to analyze FCS traces with appropriate diffusion models.

## 2.2.2 FCS is a unique and useful tool for quantifying protein delivery

Directly measuring the absolute concentration of a protein in the cytosol of a live cell is exceedingly difficult. As a result, multiple assays have been developed to estimate the concentration of a given protein within the cytosol and thereby indirectly inform on the efficiency of intracellular protein delivery. These assays rely on various proxies for absolute protein concentration, including reporter gene expression, luminescence, fluorescence, or enzyme activity, and some adapt nicely to high-throughput analyses.<sup>25,30–39</sup> A recent review by Deprey *et al.* summarizes many of these methods and provides an overview of current macromolecule delivery strategies.<sup>8</sup> Although useful for high-throughput analyses, virtually all of the aforementioned methods estimate cytosolic delivery *via* the amplification of an otherwise low signal (such as a cytosolic fluorescence signal amplified by a multi-turnover enzymatic reaction) and/or provide relative readouts, not absolute measurements. These features complicate the development of the structure-activity relationships needed to optimize the sequence of a putative CPP or CPMP because they fail to separate delivery efficiency from the activity of the protein cargo being delivered. Flow cytometry (FC) provides even less useful information as it fails to distinguish uptake into the endocytic pathway from endosomal release.<sup>26,28,29</sup> Although biochemical fractionation followed by analytical detection can directly measure the concentration of a molecule in the cytosol,<sup>6</sup> this method is exceptionally time-consuming and requires multiple controls to ensure the absence of cross-contamination. Fluorescence correlation spectroscopy, unlike the aforementioned techniques, provides direct, absolute, and quantitative information about cytosolic or nuclear delivery.

## 2.2.3 Introduction to FCS

Fluorescence correlation spectroscopy (FCS) was developed by Magde *et al.* and used initially to detect DNA denaturation by monitoring the time-dependent fluorescence fluctuations of ethidium bromide, a small molecule whose emission intensity increases when it binds DNA.<sup>40,41</sup> The theory that underlies FCS and myriad applications of this technique have been reviewed extensively elsewhere.<sup>21,22,40,42–47</sup> Briefly, FCS collects information on how the fluorescence emission of a population of single molecules fluctuates over time. These time-dependent fluctuations can be fit to an autocorrelation function to provide quantitative information about the concentration and diffusion rate of molecules in the population within a complex biological environment.<sup>21,22</sup> FCS also provides insight into the kinetic and thermodynamic properties of the fluorescent molecule in solution; the temporal relaxation of fluctuations

provides kinetic information such as rate constants and the fluctuations of amplitudes allows for thermodynamic analysis.<sup>21</sup> Advantages of fluorescence as a detection method in live cells include high sensitivity (detection in the low nM range), rapid measurements, and low background.<sup>21</sup>

While the earliest FCS experiments monitored the biophysical properties of fluorescent molecules *in vitro*, recent applications provide workflows that allow FCS to interrogate the properties of molecules *in cellulo*. The earliest FCS experiments related to protein delivery studied the cell-penetrating peptides (CPPs) penetratin (whose sequence is derived from Antp HD) and fibroblast growth factor-derived MTS peptide.<sup>48,49</sup> Subsequent FCS studies have probed CPP behavior in large and giant unilamellar vesicles,<sup>50–52</sup> determined the hydrodynamic particle sizes of peptide-containing nanocarriers,<sup>53</sup> calculated diffusion properties,<sup>54–56</sup> and analyzed CPPs on the plasma membrane.<sup>57</sup> FCS can also be used to analyze cytosolic extracts after cell lysis.<sup>58–60</sup>

We have used FCS in combination with flow cytometry (FC) to differentiate between CPPs that are simply taken up by the endocytic machinery and those that are effectively released into the cytosol and/or nucleus.<sup>26,28,29,61</sup> The data obtained from FC and FCS experiments are used together to calculate an endosomal escape ratio (EER)<sup>29</sup> that provides a measure of endosomal escape and allows straightforward comparisons between different CPPs or CPMPs:

$$\text{EER} = [\text{cytosol}]/\text{TCU} \quad \text{Equation 2.1}$$

where [cytosol] is the cytosolic concentration (in nM) determined by FCS and TCU is the total cellular uptake (in median fluorescence intensity units, MFI) determined by FC. Analysis of the EERs for a variety of CPPs and CPMPs fused to a common protein cargo revealed that CPMPs escape endosomes and traffic into the cytosol and nucleus with very high efficiency,<sup>6,24–29</sup> perhaps because they access a novel portal for endosomal release.<sup>28</sup> This chapter describes a live cell fluorescence correlation spectroscopy method that is used in partnership with flow cytometry to calculate EER values representing cytosolic (or nuclear) delivery of a fluorophore-tagged peptide or protein.

## 2.3 Equipment and Materials

### 2.3.1 Synthesis of fluorophore-tagged CPPs and CPMPs

Methods to generate fluorophore-tagged CPPs or CPMPs that are suitable for FCS measurements have been described.<sup>6,26,28</sup> CPMPs themselves are most easily prepared using solid-phase peptide synthesis; in this case the fluorophore can be appended during synthesis (using custom monomers or orthogonal protecting groups) or post-synthesis. The fluorophore chosen for FCS experiments must be bright and sufficiently photostable to withstand laser powers of several 100 kW/cm<sup>2</sup>.<sup>22,44</sup> FCS-suitable fluorophores span a range of emission wavelengths; the optimal fluorophore will depend on the experimental question and FCS laser setup.<sup>62–67</sup> For example, non-

specific lipid-fluorophore interactions may influence the results of single-molecule spectroscopy experiments.<sup>68</sup> We have had success with Lissamine rhodamine B, which is available in forms suitable for many different bio-orthogonal reactions (e.g. Invitrogen, L20). Once an appropriate fluorophore is selected, multiple methods exist for generating CPMP-protein conjugates; the ones that we find most useful are summarized below.

### 2.3.2 Preparation of fluorophore-tagged CPP- or CPMP-protein fusions

There are several ways to prepare a covalent conjugate between a CPMP, a protein of interest, and a FCS-appropriate fluorophore.<sup>44</sup> We have found two strategies particularly useful. In one, a bacterial expression plasmid encodes a CPMP-protein fusion that includes a C-terminal substrate for a sortase transpeptidase.<sup>29,69,70</sup> Once purified, reaction of this fusion protein with a suitable fluorophore-tagged peptide co-substrate generates a fluorophore-tagged CPMP-protein conjugate, often in high yield. In a second strategy, a bacterial expression plasmid encodes a fusion protein that consists of both a CPMP and a self-labeling enzyme such as a SNAP-, Halo-, or CLIP-tag upon reaction with a fluorophore-containing substrate.<sup>29,71,72</sup> It is important to ensure the method generates a single product—a homogeneous sample in which the fluorophore is linked to a single, pre-determined amino acid side chain—as FCS experiments performed with non-specifically and heterogeneously tagged proteins can be difficult to analyze.<sup>44</sup> Several groups have developed methodology for protein modification, including the incorporation of fluorophores, which is outside the scope of this chapter and is reviewed extensively elsewhere.<sup>73–76</sup>

#### *Calculating the fractional labeling of a fluorophore-tagged CPP- or CPMP-protein fusion*

As described in more detail in **Section 2.6**, FCS provides information on the absolute concentration of a fluorophore-tagged protein within one or more internal cellular compartments. If only a fraction of the protein is labeled with a fluorophore, FCS will *underestimate* the efficiency of cellular delivery. Hence, it is essential to quantify the fractional labeling of a fluorophore-tagged CPP- or CPMP-protein fusion. This value is simply the ratio between the fluorophore concentration in the protein sample ( $[F]$ , established spectrophotometrically) and the protein concentration ( $[P]$ , established using a Bradford (e.g. Bio-Rad, 5000002) or Pierce (e.g. Thermo Scientific, 22660) assay). One must ensure that the fluorophore spectroscopic signal does not interfere with the protein concentration assay. This ratio is then used to calculate the actual concentration of a fluorophore-tagged CPP- or CPMP-protein fusion in the cytosol according to **Equation 2.2**:

$$[\text{cytosol}]_{\text{corr}} = [\text{cytosol}]_{\text{FCS}} * \frac{[P]}{[F]} \quad \text{Equation 2.2}$$

where  $[\text{cytosol}]_{\text{corr}}$  is the corrected cytosolic concentration,  $[\text{cytosol}]_{\text{FCS}}$  is the cytosolic concentration determined by FCS autocorrelation analysis, and  $[P]$  and  $[F]$  are the concentrations of protein or fluorophore in a fluorophore-tagged CPP- or CPMP-protein fusion sample, respectively.

### 2.3.3 Cell Culture Work

#### *Equipment and Instrumentation*

Cell counter for plating (e.g. Cellometer Auto T4, Nexcelom)  
CO<sub>2</sub> incubator at 37 °C with 5% CO<sub>2</sub> (e.g. Autoflow NU-8700, NuAire)

#### *Materials*

6- or 12-well dish (07-200-83, Corning™ 3516; 07-200-82, Corning™ 3513)  
Complete media (see **Table 2.1**)  
Penicillin/streptomycin (p/s) (15140, Gibco)  
Fetal Bovine Serum (FBS), heat inactivated (F4135, Sigma)  
Sodium pyruvate (100 mM, 100X) (11360, Gibco)  
Fluorophore-labeled proteins/peptides  
Dulbecco's phosphate-buffered saline (DPBS) (14190-144, Gibco)  
Treatment media (see **Table 2.1**)  
Hoechst 33342 (H3570, Invitrogen)  
Fibronectin from bovine plasma (F1141, Sigma)  
8-well microscopy slide (Thermo Scientific; Lab-Tek Chambered Coverglass borosilicate, 155411)  
Digital micrometer (e.g. from Mitutoyo, 293-831-30)  
1X TrypLE (no phenol red) (12604, Gibco)  
Trypsin Quenching Media (also the plating media, see **Table 2.1**)  
Dulbecco's modified eagle medium (DMEM) without phenol red, high glucose, with 25 mM HEPES (21063, Gibco)  
Polystyrene round bottom 96-well plate (353077, Falcon)

### 2.3.4 Flow Cytometry

#### *Equipment and Instrumentation*

Flow cytometer with appropriate excitation lasers, e.g. Attune™ NxT Acoustic Focusing Cytometer (Thermo Fisher Scientific)  
Attune™ NxT software (Thermo Fisher Scientific)  
FlowJo software (Version 7.6.1, FlowJo, LLC)  
Attune Focusing Fluid (1X), 10 L (A24904, Thermo Fisher Scientific)  
Attune Wash Solution (A24974, Thermo Fisher Scientific)  
Attune Shutdown Solution (A24975, Thermo Fisher Scientific)

### 2.3.5 FCS

#### *Equipment and Instrumentation*

The methods described here are specific for the LSM 880 Airyscan NLO/FCS Confocal Microscope, which is a ZEISS Axio Observer Z1 inverted microscope equipped with an Airyscan 32-channel GaAsP photon detector that operates at very low laser power, making it suitable for live cell imaging.<sup>78</sup> The instrument we use is equipped with a C-Apochromat 40x/1.2 W Korr FCS M27 objective, but other lenses can

be used. The live-cell incubation chamber is Nunc™ Lab-Tek™ chambered coverglass. Other groups have used older ZEISS models<sup>48,61</sup> and it is also possible to create a non-commercial setup.<sup>79,80</sup> **Figure 2.1** illustrates the essential components of the LSM 880, including the halogen lamp (the light source) and transmission photomultiplier (T-PMT, a transmitted light detector). In the microscope setup, the laser hits a dichroic mirror that reflects the beam through the objective and to the sample. The fluorophore emits photons that pass through the dichroic mirror and travel through the pinhole, finally reaching the detector. These photons originate from the in-focus area of the sample, known as the confocal volume. The dimensions of the confocal volume of the laser must be measured at the beginning of each FCS session (described in **Sections 2.4.3** and **2.6**).

### *Materials*

Alexa Fluor 594 hydrazide (100 nM standard solution in MilliQ water) (A10438, Life Technologies)

## **2.4 Methods**

The following methods (**Figure 2.2**) are generally appropriate for multiple cell lines (e.g., HeLa, Saos-2, SK-HEP-1), concentrations of fluorophore-tagged protein or peptide, and treatment durations. The protocol described here is specific for Lissamine rhodamine B-tagged peptides or proteins. Many of the procedures described herein have been summarized previously.<sup>81</sup>

### **2.4.1 Cellular Treatment**

#### *Day 1*

1. Plate cells in a 6-well dish (a 12-well dish can also be used; the surface area of a 12-well dish is 2.7-fold lower than a 6-well dish) using clear media with FBS but no p/s at a density such that the cells will be 60–80% confluent on the following day. Uptake is highly dependent on cell density, and thus this parameter must be controlled to ensure the most robust comparisons. See **Table 2.1** for media pertaining to specific cell lines and seeding densities. The final volume in a 6-well dish should be 1–2 mL (0.5–1 mL for a 12-well dish).
2. Incubate overnight at 37 °C with 5% CO<sub>2</sub>.

#### *Day 2*

3. Prepare sample treatments (500 µL/well) at various concentrations (typically 0.5–3 µM) with samples diluted into Treatment Media (see **Table 2.1**).
4. Aspirate media, wash wells with 2 mL DPBS twice, aspirating media in between.
5. Add treatment solutions and incubate at 37 °C with 5% CO<sub>2</sub> for desired time (typically 30–120 min). Note: it is difficult to perform a time course study with this workflow in a single day, so we suggest running experiments defined by different incubation times on separate days. A non-treated control is recommended to ensure the sample cells are healthy prior to treatment.

6. During the incubation, measure the thickness of an 8-well microscopy slide (155411, Thermo Scientific) using a digital micrometer to adjust the correction collar of the microscope. Note that adjusting the correction collar based on slide thickness helps focus the microscope for maximum brightness (the brightness is the number of photon counts emitted per second by a molecule, also defined as the count rate).
7. Also during incubation, prepare solutions of fibronectin from bovine plasma (to coat the microscopy dish) and Hoechst 33342 (nuclear stain). Prepare a 1:100 dilution of fibronectin by adding 10  $\mu$ L of 1 mg/mL fibronectin to 990  $\mu$ L DPBS (final concentration 0.1 mg/mL). In addition, make a 1:100 dilution of 10 mg/mL Hoechst 33342 stain by adding 1  $\mu$ L of stain to 99  $\mu$ L of DPBS (the final concentration will be 300 nM in each well after dilution with treatment solution). Fibronectin coating ensures that the cells can efficiently adhere to the glass surface of the microscopy dish and its concentration may need to be adjusted depending on the cell line.
8. Add 200  $\mu$ L of the fibronectin solution from Step 7 to each well of the microscopy dish that will contain live cells and incubate at 37 °C with 5% CO<sub>2</sub> during the uptake and cellular workup. Note that the wells used to evaluate *in vitro* standards need not be coated with fibronectin. It may be necessary to coat the microscopy dish *prior* to addition of the fluorophore-tagged protein to ensure that the fibronectin has sufficient time to adhere during a rapid uptake experiment (less than 30 min).
9. During the last five minutes of the incubation, add 1.85  $\mu$ L Hoechst 33342 solution from Step 7 to each well (again, final concentration of 300 nM/well) and gently rock to ensure complete mixing. Incubate at 37 °C with 5% CO<sub>2</sub> for five minutes.
10. Wash cells three times with 1 mL of DPBS, aspirating between washes.
11. Add 500  $\mu$ L of 1X TrypLE to each well and incubate at 37 °C with 5% CO<sub>2</sub> for the time in **Table 2.1** (cell line dependent) until all cells are lifted from the dish. Extended incubations in TrypLE without FBS quenching may result in cell death. This step is important to both detach the cells and ensure the removal of surface-bound peptides and proteins.<sup>82</sup>
12. Transfer cells from each well into 15 mL Falcon tubes and rinse each well twice with 1 mL of Trypsin Quenching Media (**Table 2.1**), adding each media wash to the corresponding Falcon tube.
13. Centrifuge the cell suspensions at 200 *g* for 3 min at room temperature.
14. Aspirate the supernatant and resuspend the cells in 1 mL clear DMEM (no phenol red, 25 mM HEPES, no FBS, no sodium pyruvate, no p/s).
15. Centrifuge the cell suspensions at 200 *g* for 3 min at room temperature.
16. During the above pelleting, remove the fibronectin solution from the microscopy dish and wash three times with 200  $\mu$ L of DPBS. Allow the third wash of DPBS to sit in the dish until ready to plate cells. Note: do not let the dish dry during this step.
17. After pelleting, aspirate the supernatant and resuspend the cells in 600  $\mu$ L clear DMEM (no phenol red, 25 mM HEPES, no FBS, no sodium pyruvate, no p/s). The HEPES is necessary to prolong cellular lifetime.

18. After aspirating the last DPBS wash from a well, add 300  $\mu\text{L}$  of the cell suspension to the well on the microscopy dish. Note: the amount of cell suspension to be plated is dependent on the viability of the cells after the treatment. Ideally, cells are fully viable (>90%) after the treatment and the majority will re-adhere to the microscopy dish. If treatment with the protein of interest decreases cell viability, optimal treatment concentration ranges should be determined from independent, quantitative cell viability studies.
19. Incubate the microscopy dish at 37 °C and 5%  $\text{CO}_2$  for ~15–20 min or until the flow cytometry portion of the experiment is completed.
20. Centrifuge the Falcon tubes with the remaining 300  $\mu\text{L}$  of cells at 200 x  $g$  for 3 min at room temperature.
21. Aspirate the supernatant and resuspend the cells in 200  $\mu\text{L}$  of DPBS.
22. Transfer the cell suspension into an Eppendorf tube (1.5 mL) or a polystyrene round bottom 96-well plate (#353077, Falcon) for flow cytometry analysis.

#### **2.4.2 Flow cytometry of cells treated with a fluorophore-tagged CPP- or CPMP-protein fusion**

Perform flow cytometry at room temperature on at least 10,000 cells, using a flow rate of 500  $\mu\text{L}/\text{min}$  to collect the cell suspension. The procedure below makes use of an Attune NxT Acoustic Focusing Flow Cytometer and 1.5-mL Eppendorf tubes or 96-well plates. Flow cytometry provides information about total cellular uptake of a fluorophore-tagged CPP- or CPMP-protein fusion relative to a non-treated control.

1. First gate non-treated live cells on the basis of forward scatter (FSC) and side scatter (SSC) to identify the healthy cell population and eliminate dead cells. Note that different cell types can display different FCS and SSC characteristics due to differences in granularity and size. A detailed explanation of how to define a gating strategy is found in the Attune NxT Flow Cytometer user manual.<sup>83</sup> Once a gate for the healthy cell population is defined, the gating parameters can be reused for each experiment with that cell type.
2. Monitor the Hoechst 33342 and Lissamine rhodamine B channels (if both laser lines are available). Obtain the fluorescence intensities of at least 10,000 cells in the population (a healthy, non-treated cell population should be used as a control). The violet laser (Thermo Fisher, Upgrade Kit 100022777) excites at 405 nm and the instrument can detect emission of  $440 \pm 50$  nm to monitor the nuclear stain. For Lissamine rhodamine B, we prefer the yellow laser (Thermo Fisher, Upgrade Kit 100022779) which excites at 561 nm to allow detection of  $585 \pm 16$  nm emission.
3. Export the data for use with FlowJo (see **Section 2.5**). Note that the instrument user manual illustrates how to obtain descriptive statistics from the Attune NxT software.<sup>83</sup>

#### **2.4.3 FCS of cells treated with fluorophore-tagged CPP- or CPMP-protein fusions**

1. Once at the microscope, set the temperature of the incubator (XL unit) to 37 °C if available. Note: it may be possible to extend cell lifetimes if the instrument is also

equipped with a CO<sub>2</sub> chamber (such as Heating Insert P S1 and CO<sub>2</sub>-Cover PM S1, ZEISS). The experiments described herein do not make use of an instrument equipped in this way; however, we have found that including HEPES in the DMEM buffer can extend cellular lifetime when using an instrument that lacks a CO<sub>2</sub> chamber.

2. Select the 40X water immersion lens (C-Apochromat 40x/1.2 W Korr FCS M27 objective) and carefully unscrew the objective to adjust the correction collar to the measured dish thickness (see **Section 2.4.1** Step 6 for measurement procedure). Screw the lens back into the turret and add a drop of MilliQ water to the objective.
3. Add 200–400 µL of 100 nM Alexa Fluor 594 hydrazide in MilliQ water standard solution to the well that was measured with the digital micrometer and then mount the microscopy dish. Ensure that the lens is positioned below the standard well. The Alexa Fluor 594 standard solution should be used at the start of each session to optimize microscope parameters (see Step 6) and calculate the confocal volume of the laser (see **Section 2.6**).
4. In the FCS workspace, the following parameters should be applied (note that these parameters are specific for Lissamine rhodamine B-tagged materials but can be adjusted depending on the fluorophore used):
  - a. Summary of Acquisition Parameters: The laser used for FCS will depend on the fluorophore being analyzed. For rhodamine-tagged materials, a DPSS 561-10 nm laser can be used. Follow the instructions published by the manufacturer to determine measure time, bleach time, laser strength, and pinhole settings. ZEISS recommends starting with a bleach time of 0 s<sup>78</sup> and we follow this suggestion. Higher laser strengths may increase apparent diffusion times due to saturation of the fluorescence intensity, which is discussed further in a chapter by Petrov and Schwille.<sup>23</sup> The pinhole diameter varies depending on the excitation wavelength.<sup>78</sup>
  - b. Summary of Correlation Parameters: Correlation parameters - including binning times, the maximum correlation time, and the number of tau channels - must be defined as they are used to obtain autocorrelation functions. We set binning to 0.20 µs, the maximum correlation time to 1000 s, and the tau channels to 8. The ZEISS manual describes how to display the autocorrelation function (the temporal autocorrelation function defined in **Equation 2.5**).<sup>78</sup>
5. Change the measure time to 60 s (or a timeframe long enough to complete the following operation) and click 'Start Experiment'. Increase the Z-position until a rapid spike in signal intensity occurs (typically between 4–5 mm if the lens was zeroed at the minimum Z-position). The signal intensity should be between 800–1100 kHz. Note: do not begin measurements until the microscope reaches 37 °C, as diffusion is highly temperature-dependent.<sup>84</sup>
6. Set the pinhole to 1 Airy unit (AU) and adjust it in both the X- and Y-directions with the coarse and fine programs. This process ensures the pinhole of the 561 nm laser is positioned for maximum intensity.
7. Change the measure time to 5 s and record ten 5-s traces of the 100 nM Alexa Fluor 594 standard. Note that, with this protocol, no fitting (based on a specific

diffusion model) of the autocorrelation curves is completed at the microscope, although the ZEISS software has the capabilities to perform fitting operations as well.

8. To image live cells, position the stage such that the objective lens is below a well that contains cells. Use the live brightfield (PMT channel) and the Hoechst 33342 channels to focus the cells in the Z-direction. The nuclei should be in focus prior to initiating FCS measurements. It is important that cells are flat and adhered properly to ensure that cytosolic or nuclear selection is accurate and that the movement of the stage will not detach cells from the dish. SK-HEP-1 cells need to incubate longer than Saos-2 and HeLa cells at 37 °C before they are flat.
9. Obtain an image of the cells using the brightfield, Hoechst 33342, and rhodamine channels.
10. Click the FCS tab and select “positions” so that the crosshair of the laser can be positioned in specific cellular locations. Select several cytosolic (or nuclear) locations with the crosshair for sequential measurements. Avoid bright punctae as these typically represent endosomes. Sudden spikes in fluorescence intensity during an FCS measurement typically originate from endosomes traversing through the focal volume or by moving cells if they have not adhered properly. If the detector receives too many photons, it will shut down automatically.
11. Begin the experiment, collecting ten 5-s traces at each chosen position within the cell. The count rate (the number of photons hitting the detector) and an autocorrelation curve of the count rate will be generated.
12. Complete Steps 8–11 for all samples, collecting data for as many cells as possible.
13. Save all images as .ism files and export FCS curves as .fcs files.
14. Turn off lasers and clean optics once completed.

## 2.5 Analysis

Flow cytometry data can be analyzed using FlowJo software (Version 7.6.1, FlowJo, LLC). Confocal images can be opened using FIJI (<https://imagej.net/Fiji>), which allows one to examine individual channels or create a composite image. FCS data can be analyzed using various diffusion models (described in **Section 2.6**).

## 2.6 Theory/Calculation

### 2.6.1 Introduction

Fluorescence correlation spectroscopy (FCS) is a biophysical tool that measures the concentrations of fluorescently labeled molecules in the pico- to nanomolar range, as well as their diffusion coefficients. Traditionally, diffusion coefficients are measured by monitoring the rate of a system’s relaxation back to equilibrium from an initial state displaced from equilibrium.<sup>21</sup> FCS can determine these quantities from a system at steady state, whether that system is at equilibrium or not, by taking advantage of the spontaneous local fluctuations from Brownian motion and the Poisson process for chemical reactions.<sup>21,22</sup> The local fluctuations are observed using a fluorescence-based readout by fluorescently tagging the molecule of interest. Since the average

concentrations in the system, (e.g. within the cytosol of a living cell) remain constant in space and time at long-time periods, the system can be understood as an average of randomly selected  $\tau$  (time) intervals.<sup>21</sup> During these intervals, molecules constantly diffuse in and out of the local subvolume, resulting in local changes in concentration and therefore, fluctuations in fluorescence. The optical properties of the laser used to excite the fluorophore create a detection volume—known as the confocal volume—which is equivalent to the local subvolume described above. One criterion that must be met for FCS is that diffusing fluorescent molecules must be able to freely traverse areas of high (inside the confocal volume) and low (outside the confocal volume) excitation intensities; to meet this criterion, the confocal volume must be less than the volume in which the particles are confined (within the cell).<sup>21</sup> Since the volume of a mammalian cell (typically 100-10000 fL<sup>85,86</sup>) is greater than the confocal volume (typically 0.57-0.75 fL<sup>28</sup>), this condition is met.

To extract meaningful information (such as the diffusion coefficient,  $D$ ), a statistical analysis of the fluctuation data needs to be completed. Experimental measurements count photons during specific time intervals,  $\tau$ .<sup>21</sup> The autocorrelation function  $G(\tau)$  (**Equation 2.3**) is an ensemble average and is independent of  $\tau$  because the system is in steady state. The average product of fluctuation amplitude at successive time points is a decreasing function of  $\tau$  as fluctuations regress to the steady state—that is to say there will be a decrease in fluctuations over time (**Figure 2.2**).<sup>21</sup>

## 2.6.2 Theory

Multiple models exist for characterizing molecular diffusion; we have found FCS experiments involving fluorophore-tagged CPP- or CPMP-protein fusions can be analyzed effectively using 3D diffusion and anomalous 3D diffusion models for *in vitro* and *in cellulo* measurements, respectively. Descriptions of other diffusion types have been extensively reviewed by Schwille and Haustein, Regner *et al.*, and Metzler *et al.*, among others.<sup>22,87–90</sup> In buffer, fluorescently labeled molecules do not encounter many obstacles in their diffusion paths and so a simple 3D diffusion model can be used to fit the autocorrelation curves and calculate diffusion times and concentrations, described by:

$$G(\tau) = \left(\frac{1}{N}\right) \frac{1}{\left(1 + \frac{\tau}{\tau_{diff}}\right) \sqrt{\left(1 + s^2 \frac{\tau}{\tau_{diff}}\right)}} \quad \text{Equation 2.3}$$

where  $G(\tau)$  is the autocorrelation function,  $N$  is the average number of molecules in the confocal volume,  $\tau$  is time,  $\tau_{diff}$  is the diffusion time, and  $s$  is the shape factor. In contrast, diffusion within a cell cannot be described by Brownian motion because the crowded cell interior hinders the movement of molecules. Instead, fluorescent molecules *in cellulo* are described by anomalous diffusion. This equation is similar to 3D diffusion but includes an anomalous diffusion coefficient:

$$G(\tau) = \left(\frac{1}{N}\right) \frac{1}{\left(1 + \frac{\tau}{\tau_{diff}}\right)^\alpha \sqrt{\left(1 + s^2 \frac{\tau}{\tau_{diff}}\right)}} + G(\infty) \quad \text{Equation 2.4}$$

where  $\alpha$  is the anomalous diffusion coefficient and  $G(\infty)$  is background autocorrelation.

$G(0)$  is a thermodynamic property that provides information regarding concentration and brightness of fluorescent molecules in a system. Fluorescent molecules interact negligibly with each other, so the motion of each molecule is only correlated with itself. This situation describes the ideal system in which the number of molecules in the observation volume can be described by a Poisson distribution, thereby allowing  $G(0)$  to represent the absolute number of molecules of a fluorophore in the observation region (or confocal volume).<sup>23</sup> If the confocal volume is known (see **Section 2.6.3** for determination), the concentration of the fluorophore can be calculated. The amplitude of  $G(0)$  varies inversely with the number of fluorescent molecules in the observation volume. If the confocal volume decreases, a given fluorophore can be more concentrated for the FCS experiment (i.e. measurements would still be sensitive in higher nM ranges).<sup>21</sup>

Before beginning FCS measurements in cells, it is advisable to conduct *in vitro* characterization of fluorescently labeled proteins and peptides dissolved in buffer. A theoretical diffusion coefficient of a spherical, globular macromolecule can be calculated from its respective molecular weight using the Stokes-Einstein equation, as described before.<sup>28,88</sup> Diffusion coefficients can be measured by FCS and compared to the calculated values. Measured values should match the theoretical ones, especially for proteins that are assumed to be spherical. If they do not, the protein might not behave as expected in solution, *i.e.*, it could be multimeric. Free, small molecule fluorophores typically exhibit  $\tau_{\text{diff}}$  values that are smaller than those for fluorophore-labeled proteins. *In cellulo*, the  $\tau_{\text{diff}}$  of any given protein may be larger than that of the pure protein dissolved in buffer.

### 2.6.3 Calculations

A temporal autocorrelation is applied to the fluorescence intensities obtained over the course of the 5-s experiment, which normalizes how the fluorescence changes over short periods of time:

$$G(t) = \frac{\langle F(t)F(t+\tau) \rangle}{\langle F(t) \rangle^2} \quad \text{Equation 2.5}$$

where  $F(t)$  is the fluorescence at time  $t$  and  $\langle F(t)F(t + \tau) \rangle$  is an average of how the fluorescence changes from its mean intensity.<sup>22,90</sup> The measured temporal correlation function can then be fit to the appropriate diffusion model (such as **Equation 2.3** or **2.4**).

The intensity and temporal autocorrelation curves generated by the ZEISS software at the microscope<sup>78</sup> are exported for use with a custom MATLAB® script. Based on the diffusion model selected (the equation mode), the script averages the autocorrelation data of the ten 5-s traces, calculates the least squares residuals, and generates a best fit line of  $G(\tau)$ . Using  $G(\tau)$ ,  $\tau_{\text{diff}}$  is determined from the inflection point. The count rate data is used to generate intensity plots. This MATLAB® script produces

files containing the following: fit parameters, average correlation curve and standard deviation, intensity, percent bleaching, and correlation times. In addition, the agreement (standard deviation between curves that is normalized after averaging over small window from 0.03–0.06 ms) and noise (function of  $\tau$ ; represents the standard deviation of correlation in the intercept region at 0.3–0.75 ms and is normalized by magnitude) are generated. The MATLAB® script is available from GitHub (<https://github.com/schepartzlab/FCS>).

For quantitative FCS, the confocal volume of the laser must be known. It can be measured in multiple ways, including using a dilutional series of a sample with a known concentration or calculating the volume from the FCS fit of a sample with a known diffusion coefficient.<sup>26,28,87</sup> We use the latter method; the advantage of using a well-characterized fluorophore is that the sample concentration does not have to be known, as long as it falls within the dynamic range of FCS. For the 561-nm laser, Alexa Fluor™ 594 hydrazide serves this purpose well.

Briefly, to calculate the confocal volume, the autocorrelation data obtained from a 100 nM sample of Alexa Fluor™ 594 hydrazide are fit to a 3D diffusion model (**Equation 2.3**, MATLAB® script equation mode = 2). Because the diffusion coefficient  $D$  of the reference fluorophore is known ( $5.20 \times 10^{-6} \text{ cm}^2 \text{ s}^{-1}$ ),<sup>28</sup> fitting these data to **Equation 2.3** allows one to extract the shape factor  $s$  and the effective confocal volume  $V_{eff}$ , according to **Equations 2.6 and 2.7**:

$$\omega_1 = \sqrt{(4D\tau_{diff})} \quad \text{Equation 2.6}$$

$$V_{eff} = \pi^{3/2}\omega_1^3 * (1/s) \quad \text{Equation 2.7}$$

where  $\omega_1$  is the lateral extension (or radius) of the effective confocal volume.<sup>89</sup> The final concentration  $C$  in the effective confocal volume  $V_{eff}$  can be calculated as follows:

$$C = N/(NA * V_{eff}) \quad \text{Equation 2.8}$$

where  $NA$  is Avogadro's number ( $6.022 \times 10^{23} \text{ mol}^{-1}$ ).

In our experimental setup using the LSM 880 in combination with the DPSS 561-nm laser,  $V_{eff}$  ranges from 0.57–0.75 femtoliters. Slight day-to-day variations in the volume are expected as the volume depends on the coverglass thickness and the adjustment with the correction collar. Because of this inherent variability, it is crucial to determine  $V_{eff}$  at the beginning of each experiment and for each new microscopy dish using the same experimental settings, such as temperature and laser power, as for any subsequent *in cellulo* experiments.

To analyze *in cellulo* FCS experiments, set the MATLAB® script equation mode to 9. The script will use **Equation 2.4** to generate  $G(\tau)$  and determine the number of molecules in the confocal volume and  $\tau_{diff}$ . The fit autocorrelation curves are evaluated to retain only high-quality data points, as described previously.<sup>28</sup> We exclude

autocorrelation curves that exhibit diffusion times ( $\tau_{diff}$ ) that are more than 10-fold higher than the value calculated for the same protein in buffer. The observed *in cellulo* diffusion time of a protein is expected to be longer than its *in vitro* diffusion time because of the crowded cellular environment. If the diffusion time in cellulo is smaller than the value *in vitro*, protein degradation should be suspected and evaluated if possible. Finally, traces with poor signal—counts per molecule (cpm) below 1 kHz and/or low anomalous diffusion coefficients ( $\alpha < 0.3$ )—are also discarded. We typically retain at least 75% of the collected data with these cutoff parameters. Use **Equation 2.8** to calculate the cytosolic or nuclear concentration of the fluorophore-tagged protein or peptide.

With the median fluorescence intensity obtained from flow cytometry and the cytosolic concentrations calculated from FCS, applying **Equation 2.1** allows comparison of different fluorophore-tagged CPMP- or CPP-protein conjugates to understand endosomal escape.

## 2.7 Conclusions

FCS has real advantages for quantifying protein delivery, as it is both quantitative and sensitive, but the technique is unquestionably challenging for novices. First, the setup needed to modify a confocal microscope for FCS is costly and requires genuine expertise, especially for custom-built models. Second, the experiment itself demands a pure, unique, and site-specifically labeled protein, whose synthesis and purification can be challenging, especially for large or fragile proteins and enzymes (although novel methods to achieve this goal continue to appear).<sup>44,91</sup> Third, the interpretation of FCS data can be complicated by artifacts related to intracellular protein aggregation or degradation, which may artificially decrease or increase both the calculated values for the diffusion coefficient  $D$  and intracellular concentrations. Additional techniques may be used to identify degradation events.<sup>26</sup> Despite these challenges, when applied properly and with suitable controls, FCS provides information that is difficult to achieve in any other way, and can improve understanding of how (and how well) delivered proteins traffic within and between cellular compartments. FCS can also be used in combination with genetic knockdown strategies to identify genes whose expression modulates the efficiency of endosomal release.<sup>28</sup> In conclusion, FCS is a robust technique that provides quantitative information about the concentration of a fluorescent species in a sample with numerous biological and biophysical applications.

## 2.8 Figures

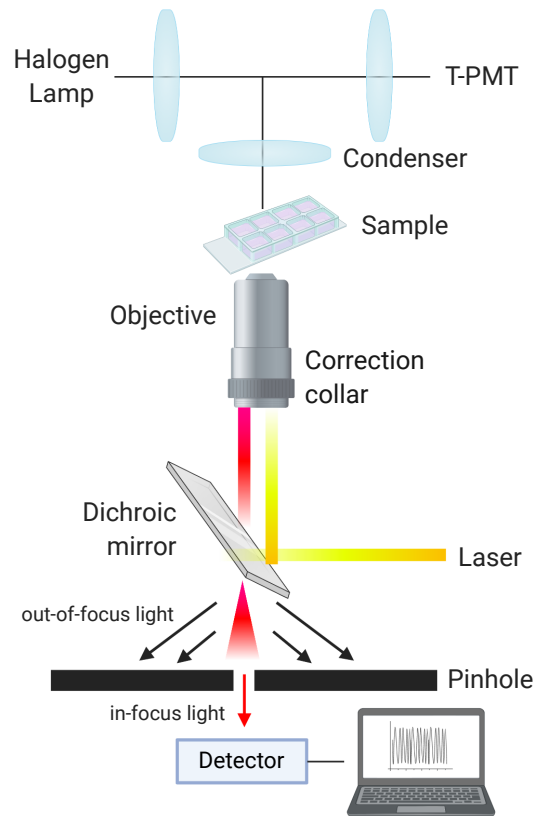


**Figure 2.1. Microscope set up for FCS.** In brief, an inverted microscope allows FCS analysis of a live cell sample and the setup uses a pinhole to differentiate out-of-focus and in-focus light. T-PMT is the transmission photomultiplier. Figure was created with BioRender.com.

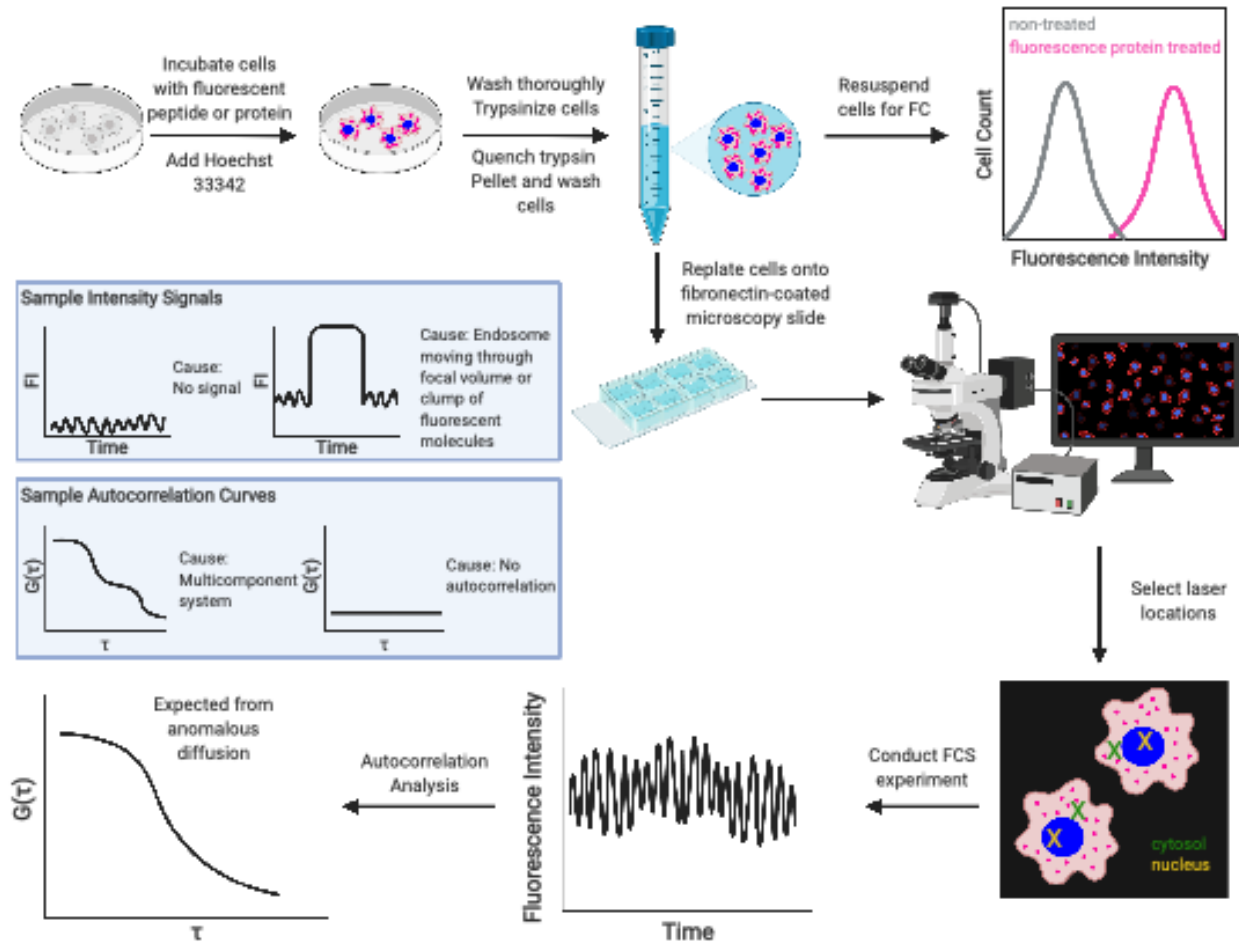


**Figure 2.2. Workflow for flow cytometry (FC) and FCS experiments.** In brief, adherent mammalian cells are treated with fluorophore-labeled protein and labeled with Hoescht 33342 to stain the nuclei. After stringent washing steps, cells are lifted from the culture dish using TrypLE and then quenched with FBS-containing media. Cells are centrifuged, washed several times prior to a final sedimentation, and split into samples for resuspension for flow cytometry and replating onto a microscopy slide for FCS studies. At the microscope and using the stained nuclei to find the focal plane, the user selects locations in either the cytosol or nucleus for the laser. In addition to expected signal and autocorrelation, several sample fluorescence intensity (FI) and autocorrelation curves are shown that could indicate a different mode of diffusion. Figure was created with BioRender.com.

## 2.9 Tables

**Table 2.1. Information needed to prepare various mammalian cell lines for FCS experiments.<sup>a</sup>**

Cell Line	Seeding Density (cells/well)	Complete Media (refer to the ATCC website)	Treatment Media	Plating & Trypsin Quenching Media	Approximate Trypsin Incubation Time (min)
HeLa (CCL-2, ATCC)	120,000	Eagle's Minimum Essential Medium (30-2003, ATCC) with 10% FBS, 1X p/s	Clear DMEM (11965, Gibco), no FBS, no p/s	Clear DMEM (10% FBS, no phenol red, no p/s)	10
Saos-2 (HTB-85, ATCC)	120,000	McCoy's 5A (M8403, Sigma) with 15% FBS, 1X p/s, 1X GlutaMAX, 1X sodium pyruvate (35050, Gibco)	McCoy's 5A (SH30270, HyClone), no phenol red, no FBS, no p/s, and no sodium pyruvate	Clear McCoy's (15% FBS, no phenol red, no p/s, and no sodium pyruvate)	10
SK-HEP-1 (HTB-52, ATCC)	150,000	Minimum Essential Medium Eagle (51411C, Sigma) with 10% FBS, 1X p/s	Clear MEM, no phenol red, no FBS, and no p/s	Clear MEM (10% FBS, no phenol red, and no p/s)	3

<sup>a</sup>The precise media chosen will depend on the experiment and cell type. FBS aids in cell health, but may interfere by non-specifically binding fluorophore-labeled proteins and modulating their uptake. It may make sense in some contexts to include FBS and/or p/s. HEPES is necessary for CO<sub>2</sub>-buffering in the plating media to extend cellular lifetimes. To avoid spectral interference with FCS, ensure that the treatment, plating, and trypsin media do not contain phenol red.<sup>77</sup> The addition of GlutaMAX and sodium pyruvate aid in the growth of Saos-2 cells.

## 2.10 References

- (1) Safary, A.; Akbarzadeh Khiavi, M.; Mousavi, R.; Barar, J.; Rafi, M. A. Enzyme Replacement Therapies: What Is the Best Option? *BioImpacts BI* **2018**, *8* (3), 153–157. <https://doi.org/10.15171/bi.2018.17>.
- (2) Frankel, A. D.; Pabo, C. O. Cellular Uptake of the Tat Protein from Human Immunodeficiency Virus. *Cell* **1988**, *55* (6), 1189–1193. [https://doi.org/10.1016/0092-8674\(88\)90263-2](https://doi.org/10.1016/0092-8674(88)90263-2).
- (3) Green, M.; Loewenstein, P. M. Autonomous Functional Domains of Chemically Synthesized Human Immunodeficiency Virus Tat Trans-Activator Protein. *Cell* **1988**, *55* (6), 1179–1188. [https://doi.org/10.1016/0092-8674\(88\)90262-0](https://doi.org/10.1016/0092-8674(88)90262-0).

- (4) Derossi, D.; Joliot, A. H.; Chassaing, G.; Prochiantz, A. The Third Helix of the Antennapedia Homeodomain Translocates through Biological Membranes. *J. Biol. Chem.* **1994**, *269* (14), 10444–10450.
- (5) Cronican, J. J.; Beier, K. T.; Davis, T. N.; Tseng, J.-C.; Li, W.; Thompson, D. B.; Shih, A. F.; May, E. M.; Cepko, C. L.; Kung, A. L.; Zhou, Q.; Liu, D. R. A Class of Human Proteins That Deliver Functional Proteins into Mammalian Cells In Vitro and In Vivo. *Chem. Biol.* **2011**, *18* (7), 833–838.  
<https://doi.org/10.1016/j.chembiol.2011.07.003>.
- (6) Appelbaum, J. S.; LaRochelle, J. R.; Smith, B. A.; Balkin, D. M.; Holub, J. M.; Schepartz, A. Arginine Topology Controls Escape of Minimally Cationic Proteins from Early Endosomes to the Cytoplasm. *Chem. Biol.* **2012**, *19* (7), 819–830.  
<https://doi.org/10.1016/j.chembiol.2012.05.022>.
- (7) Beilhartz, G. L.; Sugiman-Marangos, S. N.; Melnyk, R. A. Repurposing Bacterial Toxins for Intracellular Delivery of Therapeutic Proteins. *Biochem. Pharmacol.* **2017**, *142*, 13–20. <https://doi.org/10.1016/j.bcp.2017.04.009>.
- (8) Deprey, K.; Becker, L.; Kritzer, J.; Plückthun, A. Trapped! A Critical Evaluation of Methods for Measuring Total Cellular Uptake versus Cytosolic Localization. *Bioconjug. Chem.* **2019**, *30* (4), 1006–1027.  
<https://doi.org/10.1021/acs.bioconjchem.9b00112>.
- (9) Futaki, S.; Suzuki, T.; Ohashi, W.; Yagami, T.; Tanaka, S.; Ueda, K.; Sugiura, Y. Arginine-Rich Peptides: An Abundant Source of Membrane-Permeable Peptides Having Potential as Carriers for Intracellular Protein Delivery. *J. Biol. Chem.* **2001**, *276* (8), 5836–5840. <https://doi.org/10.1074/jbc.M007540200>.
- (10) Gaj, T.; Liu, J.; Anderson, K. E.; Sirk, S. J.; Barbas, C. F. Protein Delivery Using Cys2-His2 Zinc-Finger Domains. *ACS Chem. Biol.* **2014**, *9* (8), 1662–1667.  
<https://doi.org/10.1021/cb500282g>.
- (11) Guidotti, G.; Brambilla, L.; Rossi, D. Cell-Penetrating Peptides: From Basic Research to Clinics. *Trends Pharmacol. Sci.* **2017**, *38* (4), 406–424.  
<https://doi.org/10.1016/j.tips.2017.01.003>.
- (12) Habault, J.; Poyet, J.-L. Recent Advances in Cell Penetrating Peptide-Based Anticancer Therapies. *Mol. Basel Switz.* **2019**, *24* (5), 927.  
<https://doi.org/10.3390/molecules24050927>.
- (13) McNaughton, B. R.; Cronican, J. J.; Thompson, D. B.; Liu, D. R. Mammalian Cell Penetration, siRNA Transfection, and DNA Transfection by Supercharged Proteins. *Proc. Natl. Acad. Sci.* **2009**, *106* (15), 6111–6116.  
<https://doi.org/10.1073/pnas.0807883106>.
- (14) Patel, A.; Patel, M.; Yang, X.; Mitra, A. K. Recent Advances in Protein and Peptide Drug Delivery: A Special Emphasis on Polymeric Nanoparticles. *Protein Pept. Lett.* **2014**, *21* (11), 1102–1120.  
<https://doi.org/10.2174/0929866521666140807114240>.
- (15) Qian, Z.; Martyna, A.; Hard, R. L.; Wang, J.; Appiah-Kubi, G.; Coss, C.; Phelps, M. A.; Rossman, J. S.; Pei, D. Discovery and Mechanism of Highly Efficient Cyclic Cell-Penetrating Peptides. *Biochemistry* **2016**, *55* (18), 2601–2612.  
<https://doi.org/10.1021/acs.biochem.6b00226>.
- (16) Stanzl, E. G.; Trantow, B. M.; Vargas, J. R.; Wender, P. A. Fifteen Years of Cell-Penetrating, Guanidinium-Rich Molecular Transporters: Basic Science, Research

- Tools, and Clinical Applications. *Acc. Chem. Res.* **2013**, *46* (12), 2944–2954. <https://doi.org/10.1021/ar4000554>.
- (17) Thompson, D. B.; Cronican, J. J.; Liu, D. R. Engineering and Identifying Supercharged Proteins for Macromolecule Delivery into Mammalian Cells. *Methods Enzymol.* **2012**, *503*, 293–319. <https://doi.org/10.1016/B978-0-12-396962-0.00012-4>.
- (18) Walensky, L. D.; Bird, G. H. Hydrocarbon-Stapled Peptides: Principles, Practice, and Progress. *J. Med. Chem.* **2014**, *57* (15), 6275–6288. <https://doi.org/10.1021/jm4011675>.
- (19) Solomon, M.; Muro, S. Lysosomal Enzyme Replacement Therapies: Historical Development, Clinical Outcomes, and Future Perspectives. *Adv. Drug Deliv. Rev.* **2017**, *118*, 109–134. <https://doi.org/10.1016/j.addr.2017.05.004>.
- (20) Beck, M. Treatment Strategies for Lysosomal Storage Disorders. *Dev. Med. Child Neurol.* **2018**, *60* (1), 13–18. <https://doi.org/10.1111/dmcn.13600>.
- (21) Elson, E. L. Fluorescence Correlation Spectroscopy: Past, Present, Future. *Biophys. J.* **2011**, *101* (12), 2855–2870. <https://doi.org/10.1016/j.bpj.2011.11.012>.
- (22) Schwille, P.; Hausteil, E. Fluorescence Correlation Spectroscopy - An Introduction to Its Concepts and Applications. *Spectroscopy* **2001**, *94*(22).
- (23) Petrov, E.; Schwille, P. State of the Art and Novel Trends in Fluorescence Correlation Spectroscopy; 2007; Vol. 6, pp 145–197.
- (24) Daniels, D. S.; Schepartz, A. Intrinsically Cell-Permeable Miniature Proteins Based on a Minimal Cationic PPII Motif. *J. Am. Chem. Soc.* **2007**, *129* (47), 14578–14579. <https://doi.org/10.1021/ja0772445>.
- (25) Holub, J. M.; LaRochelle, J. R.; Appelbaum, J. S.; Schepartz, A. Improved Assays for Determining the Cytosolic Access of Peptides, Proteins, and Their Mimetics. *Biochemistry* **2013**, *52* (50), 9036–9046. <https://doi.org/10.1021/bi401069g>.
- (26) LaRochelle, J. R.; Cobb, G. B.; Steinauer, A.; Rhoades, E.; Schepartz, A. Fluorescence Correlation Spectroscopy Reveals Highly Efficient Cytosolic Delivery of Certain Penta-Arg Proteins and Stapled Peptides. *J. Am. Chem. Soc.* **2015**, *137* (7), 2536–2541. <https://doi.org/10.1021/ja510391n>.
- (27) Smith, B. A.; Daniels, D. S.; Coplin, A. E.; Jordan, G. E.; McGregor, L. M.; Schepartz, A. Minimally Cationic Cell-Permeable Miniature Proteins via  $\alpha$ -Helical Arginine Display. *J. Am. Chem. Soc.* **2008**, *130* (10), 2948–2949. <https://doi.org/10.1021/ja800074v>.
- (28) Steinauer, A.; LaRochelle, J. R.; Knox, S. L.; Wissner, R. F.; Berry, S.; Schepartz, A. HOPS-Dependent Endosomal Fusion Required for Efficient Cytosolic Delivery of Therapeutic Peptides and Small Proteins. *Proc. Natl. Acad. Sci.* **2019**, *116* (2), 512–521. <https://doi.org/10.1073/pnas.1812044116>.
- (29) Wissner, R. F.; Steinauer, A.; Knox, S. L.; Thompson, A. D.; Schepartz, A. Fluorescence Correlation Spectroscopy Reveals Efficient Cytosolic Delivery of Protein Cargo by Cell-Permeant Miniature Proteins. *ACS Cent. Sci.* **2018**, *4* (10), 1379–1393. <https://doi.org/10.1021/acscentsci.8b00446>.

- (30) Chao, T.-Y.; Raines, R. T. Fluorogenic Label to Quantify the Cytosolic Delivery of Macromolecules. *Mol. Biosyst.* **2013**, *9* (3), 339–342. <https://doi.org/10.1039/C3MB25552B>.
- (31) Kwon, Y. D.; Oh, S. K.; Kim, H. S.; Ku, S.-Y.; Kim, S. H.; Choi, Y. M.; Moon, S. Y. Cellular Manipulation of Human Embryonic Stem Cells by TAT-PDX1 Protein Transduction. *Mol. Ther.* **12** (1), 28–32. <https://doi.org/10.1016/j.ymthe.2005.03.010>.
- (32) Li, M.; Tao, Y.; Shu, Y.; LaRoche, J. R.; Steinauer, A.; Thompson, D.; Schepartz, A.; Chen, Z.-Y.; Liu, D. R. Discovery and Characterization of a Peptide That Enhances Endosomal Escape of Delivered Proteins in Vitro and in Vivo. *J. Am. Chem. Soc.* **2015**, *137* (44), 14084–14093. <https://doi.org/10.1021/jacs.5b05694>.
- (33) Loison, F.; Nizard, P.; Sourisseau, T.; Le Goff, P.; Debure, L.; Le Drean, Y.; Michel, D. A Ubiquitin-Based Assay for the Cytosolic Uptake of Protein Transduction Domains. *Mol. Ther.* **2005**, *11* (2), 205–214. <https://doi.org/10.1016/j.ymthe.2004.10.010>.
- (34) Peitz, M.; Pfannkuche, K.; Rajewsky, K.; Edenhofer, F. Ability of the Hydrophobic FGF and Basic TAT Peptides to Promote Cellular Uptake of Recombinant Cre Recombinase: A Tool for Efficient Genetic Engineering of Mammalian Genomes. *Proc. Natl. Acad. Sci.* **2002**, *99* (7), 4489–4494. <https://doi.org/10.1073/pnas.032068699>.
- (35) Qian, Z.; Liu, T.; Liu, Y.-Y.; Briesewitz, R.; Barrios, A. M.; Jhiang, S. M.; Pei, D. Efficient Delivery of Cyclic Peptides into Mammalian Cells with Short Sequence Motifs. *ACS Chem. Biol.* **2013**, *8* (2), 423–431. <https://doi.org/10.1021/cb3005275>.
- (36) Qian, Z.; Dougherty, P. G.; Pei, D. Monitoring the Cytosolic Entry of Cell-Penetrating Peptides Using a PH-Sensitive Fluorophore. *Chem. Commun.* **2015**, *51* (11), 2162–2165. <https://doi.org/10.1039/C4CC09441G>.
- (37) Verdurmen, W. P. R.; Mazlami, M.; Plückthun, A. A Quantitative Comparison of Cytosolic Delivery via Different Protein Uptake Systems. *Sci. Rep.* **2017**, *7* (1), 13194. <https://doi.org/10.1038/s41598-017-13469-y>.
- (38) Wender, P. A.; Goun, E. A.; Jones, L. R.; Pillow, T. H.; Rothbard, J. B.; Shinde, R.; Contag, C. H. Real-Time Analysis of Uptake and Bioactivatable Cleavage of Luciferin-Transporter Conjugates in Transgenic Reporter Mice. *Proc. Natl. Acad. Sci.* **2007**, *104* (25), 10340–10345. <https://doi.org/10.1073/pnas.0703919104>.
- (39) Zuris, J. A.; Thompson, D. B.; Shu, Y.; Guiling, J. P.; Bessen, J. L.; Hu, J. H.; Maeder, M. L.; Joung, J. K.; Chen, Z.-Y.; Liu, D. R. Cationic Lipid-Mediated Delivery of Proteins Enables Efficient Protein-Based Genome Editing in Vitro and in Vivo. *Nat. Biotechnol.* **2015**, *33* (1), 73–80. <https://doi.org/10.1038/nbt.3081>.
- (40) Elliot L. Elson. Quick Tour of Fluorescence Correlation Spectroscopy from Its Inception. *J. Biomed. Opt.* **2004**, *9* (5), 855–856. <https://doi.org/10.1117/1.1779234>.
- (41) Magde, D.; Elson, E.; Webb, W. W. Thermodynamic Fluctuations in a Reacting System-Measurement by Fluorescence Correlation Spectroscopy. *Phys. Rev. Lett.* **1972**, *29* (11), 705–708. <https://doi.org/10.1103/PhysRevLett.29.705>.

- (42) Elson, E. L.; Magde, D. Fluorescence Correlation Spectroscopy. I. Conceptual Basis and Theory. *Biopolymers* **1974**, *13* (1), 1–27. <https://doi.org/10.1002/bip.1974.360130102>.
- (43) Hess, S. T.; Huang, S.; Heikal, A. A.; Webb, W. W. Biological and Chemical Applications of Fluorescence Correlation Spectroscopy: A Review. *Biochemistry* **2002**, *41* (3), 697–705. <https://doi.org/10.1021/bi0118512>.
- (44) Kim, S. A.; Heinze, K. G.; Schwille, P. Fluorescence Correlation Spectroscopy in Living Cells. *Nat. Methods* **2007**, *4* (11), 963–973. <https://doi.org/10.1038/nmeth1104>.
- (45) Ries, J.; Schwille, P. Fluorescence Correlation Spectroscopy. *BioEssays* **2012**, *34* (5), 361–368. <https://doi.org/10.1002/bies.201100111>.
- (46) *Fluorescence Correlation Spectroscopy: Theory and Applications*; Rigler, R., Elson, E. S., Eds.; Springer Series in Chemical Physics; Springer-Verlag: Berlin Heidelberg, 2001. <https://doi.org/10.1007/978-3-642-59542-4>.
- (47) Tian, Y.; Martinez, M. M.; Pappas, D. Fluorescence Correlation Spectroscopy: A Review of Biochemical and Microfluidic Applications. *Appl. Spectrosc.* **2011**, *65* (4), 115A-124A. <https://doi.org/10.1366/10-06224>.
- (48) Fischer, R.; Waizenegger, T.; Köhler, K.; Brock, R. A Quantitative Validation of Fluorophore-Labelled Cell-Permeable Peptide Conjugates: Fluorophore and Cargo Dependence of Import. *Biochim. Biophys. Acta BBA - Biomembr.* **2002**, *1564* (2), 365–374. [https://doi.org/10.1016/S0005-2736\(02\)00471-6](https://doi.org/10.1016/S0005-2736(02)00471-6).
- (49) Waizenegger, T.; Fischer, R.; Brock, R. Intracellular Concentration Measurements in Adherent Cells: A Comparison of Import Efficiencies of Cell-Permeable Peptides. *Biol. Chem.* **2002**, *383* (2), 291–299. <https://doi.org/10.1515/bc.2002.031>.
- (50) Ciobanasu, C.; Harms, E.; Tünnemann, G.; Cardoso, M. C.; Kubitscheck, U. Cell-Penetrating HIV1 TAT Peptides Float on Model Lipid Bilayers. *Biochemistry* **2009**, *48* (22), 4728–4737. <https://doi.org/10.1021/bi900365s>.
- (51) Kolesinska, B.; Eyer, K.; Robinson, T.; Dittrich, P. S.; Beck, A. K.; Seebach, D.; Walde, P. Interaction of B3/B2-Peptides, Consisting of Val-Ala-Leu Segments, with POPC Giant Unilamellar Vesicles (GUVs) and White Blood Cancer Cells (U937) – A New Type of Cell-Penetrating Peptides, and a Surprising Chain-Length Dependence of Their Vesicle- and Cell-Lysing Activity. *Chem. Biodivers.* **2015**, *12* (5), 697–732. <https://doi.org/10.1002/cbdv.201500085>.
- (52) Magzoub, M.; Pramanik, A.; Gräslund, A. Modeling the Endosomal Escape of Cell-Penetrating Peptides: Transmembrane PH Gradient Driven Translocation across Phospholipid Bilayers. *Biochemistry* **2005**, *44* (45), 14890–14897. <https://doi.org/10.1021/bi051356w>.
- (53) Draffehn, S.; Eichhorst, J.; Wiesner, B.; Kumke, M. U. Insight into the Modification of Polymeric Micellar and Liposomal Nanocarriers by Fluorescein-Labeled Lipids and Uptake-Mediating Lipopeptides. *Langmuir* **2016**, *32* (27), 6928–6939. <https://doi.org/10.1021/acs.langmuir.6b01487>.
- (54) Braun, K.; Beining, M.; Wiessler, M.; Lammers, T.; Pipkorn, R.; Hennrich, U.; Nokihara, K.; Semmler, W.; Debus, J.; Waldeck, W. BioShuttle Mobility in Living Cells Studied with High-Resolution FCS & CLSM Methodologies. *Int. J. Med. Sci.* **2012**, *9* (5), 339–352. <https://doi.org/10.7150/ijms.4414>.

- (55) Gehne, S.; Sydow, K.; Dathe, M.; Kumke, M. U. Characterization of Cell-Penetrating Lipopeptide Micelles by Spectroscopic Methods. *J. Phys. Chem. B* **2013**, *117* (46), 14215–14225. <https://doi.org/10.1021/jp406053g>.
- (56) Vukojević, V.; Gräslund, A.; Bakalkin, G. Fluorescence Imaging with Single-Molecule Sensitivity and Fluorescence Correlation Spectroscopy of Cell-Penetrating Neuropeptides. In *Neuropeptides: Methods and Protocols*; Merighi, A., Ed.; Methods in Molecular Biology; Humana Press: Totowa, NJ, 2011; pp 147–170. [https://doi.org/10.1007/978-1-61779-310-3\\_9](https://doi.org/10.1007/978-1-61779-310-3_9).
- (57) Vasconcelos, L.; Lehto, T.; Madani, F.; Radoi, V.; Hällbrink, M.; Vukojević, V.; Langel, Ü. Simultaneous Membrane Interaction of Amphipathic Peptide Monomers, Self-Aggregates and Cargo Complexes Detected by Fluorescence Correlation Spectroscopy. *Biochim. Biophys. Acta BBA - Biomembr.* **2018**, *1860* (2), 491–504. <https://doi.org/10.1016/j.bbamem.2017.09.024>.
- (58) Rezgui, R.; Blumer, K.; Yeoh-Tan, G.; Trexler, A. J.; Magzoub, M. Precise Quantification of Cellular Uptake of Cell-Penetrating Peptides Using Fluorescence-Activated Cell Sorting and Fluorescence Correlation Spectroscopy. *Biochim. Biophys. Acta BBA - Biomembr.* **2016**, *1858* (7, Part A), 1499–1506. <https://doi.org/10.1016/j.bbamem.2016.03.023>.
- (59) Ruttekolk, I. R.; Verdurmen, W. P. R.; Chung, Y.-D.; Brock, R. Measurements of the Intracellular Stability of CPPs. In *Cell-Penetrating Peptides: Methods and Protocols*; Langel, Ü., Ed.; Methods in Molecular Biology; Humana Press: Totowa, NJ, 2011; pp 69–80. [https://doi.org/10.1007/978-1-60761-919-2\\_6](https://doi.org/10.1007/978-1-60761-919-2_6).
- (60) Zaro, J. L.; Shen, W.-C. Quantitative Comparison of Membrane Transduction and Endocytosis of Oligopeptides. *Biochem. Biophys. Res. Commun.* **2003**, *307* (2), 241–247. [https://doi.org/10.1016/S0006-291X\(03\)01167-7](https://doi.org/10.1016/S0006-291X(03)01167-7).
- (61) Quach, K.; LaRoche, J.; Li, X.-H.; Rhoades, E.; Schepartz, A. Unique Arginine Array Improves Cytosolic Localization of Hydrocarbon-Stapled Peptides. *Bioorg. Med. Chem.* **2018**, *26* (6), 1197–1202. <https://doi.org/10.1016/j.bmc.2017.11.008>.
- (62) Kapusta, P. Absolute Diffusion Coefficients: Compilation of Reference Data for FCS Calibration. *PicoQuant GmbH* **2010**, *1*, 1–2.
- (63) Müller, C. B.; Loman, A.; Pacheco, V.; Koberling, F.; Willbold, D.; Richtering, W.; Enderlein, J. Precise Measurement of Diffusion by Multi-Color Dual-Focus Fluorescence Correlation Spectroscopy. *EPL Europhys. Lett.* **2008**, *83* (4), 46001. <https://doi.org/10.1209/0295-5075/83/46001>.
- (64) Petrášek, Z.; Schwille, P. Precise Measurement of Diffusion Coefficients Using Scanning Fluorescence Correlation Spectroscopy. *Biophys. J.* **2008**, *94* (4), 1437–1448. <https://doi.org/10.1529/biophysj.107.108811>.
- (65) Pristinski, D.; Kozlovskaya, V.; Sukhishvili, S. A. Fluorescence Correlation Spectroscopy Studies of Diffusion of a Weak Polyelectrolyte in Aqueous Solutions. *J. Chem. Phys.* **2004**, *122* (1), 014907. <https://doi.org/10.1063/1.1829255>.
- (66) Sezgin, E.; Schneider, F.; Galiani, S.; Urbančič, I.; Waithe, D.; Lagerholm, B. C.; Eggeling, C. Measuring Nanoscale Diffusion Dynamics in Cellular Membranes with Super-Resolution STED-FCS. *Nat. Protoc.* **2019**, *14* (4), 1054–1083. <https://doi.org/10.1038/s41596-019-0127-9>.

- (67) Widengren, J.; Schwille, P. Characterization of Photoinduced Isomerization and Back-Isomerization of the Cyanine Dye Cy5 by Fluorescence Correlation Spectroscopy. *J. Phys. Chem. A* **2000**, *104* (27), 6416–6428. <https://doi.org/10.1021/jp000059s>.
- (68) Zhang, Z.; Yomo, D.; Gradinaru, C. Choosing the Right Fluorophore for Single-Molecule Fluorescence Studies in a Lipid Environment. *Biochim. Biophys. Acta BBA - Biomembr.* **2017**, *1859* (7), 1242–1253. <https://doi.org/10.1016/j.bbamem.2017.04.001>.
- (69) Popp, M. W.-L.; Antos, J. M.; Ploegh, H. L. Site-Specific Protein Labeling via Sortase-Mediated Transpeptidation. *Curr. Protoc. Protein Sci.* **2009**, *Chapter 15*, Unit-15.3. <https://doi.org/10.1002/0471140864.ps1503s56>.
- (70) Theile, C. S.; Witte, M. D.; Blom, A. E. M.; Kundrat, L.; Ploegh, H. L.; Guimaraes, C. P. Site-Specific N-Terminal Labeling of Proteins Using Sortase-Mediated Reactions. *Nat. Protoc.* **2013**, *8* (9), 1800–1807. <https://doi.org/10.1038/nprot.2013.102>.
- (71) England, C. G.; Luo, H.; Cai, W. HaloTag Technology: A Versatile Platform for Biomedical Applications. *Bioconjug. Chem.* **2015**, *26* (6), 975–986. <https://doi.org/10.1021/acs.bioconjchem.5b00191>.
- (72) Gautier, A.; Juillerat, A.; Heinis, C.; Corrêa, I. R., Jr.; Kindermann, M.; Beaufile, F.; Johnsson, K. An Engineered Protein Tag for Multiprotein Labeling in Living Cells. *Chem. Biol.* **2008**, *15* (2), 128–136. <https://doi.org/10.1016/j.chembiol.2008.01.007>.
- (73) Hermanson, G. T. Chapter 10 - Fluorescent Probes. In *Bioconjugate Techniques (Third edition)*; Academic Press: Boston, 2013; pp 395–463.
- (74) Hoyt, E. A.; Cal, P. M. S. D.; Oliveira, B. L.; Bernardes, G. J. L. Contemporary Approaches to Site-Selective Protein Modification. *Nat. Rev. Chem.* **2019**, *3* (3), 147–171. <https://doi.org/10.1038/s41570-019-0079-1>.
- (75) Rosen, C. B.; Francis, M. B. Targeting the N Terminus for Site-Selective Protein Modification. *Nat. Chem. Biol.* **2017**, *13* (7), 697–705. <https://doi.org/10.1038/nchembio.2416>.
- (76) Toseland, C. P. Fluorescent Labeling and Modification of Proteins. *J. Chem. Biol.* **2013**, *6* (3), 85–95. <https://doi.org/10.1007/s12154-013-0094-5>.
- (77) Stadtfeld, M.; Varas, F.; Graf, T. Fluorescent Protein-Cell Labeling and Its Application in Time-Lapse Analysis of Hematopoietic Differentiation. *Methods Mol. Med.* **2005**, *105*, 395–412.
- (78) Carl Zeiss Microscopy GmbH. *LSM 880 NLO Operating Manual*; 2014.
- (79) Politi, A. Z.; Cai, Y.; Walther, N.; Hossain, M. J.; Koch, B.; Wachsmuth, M.; Ellenberg, J. Quantitative Mapping of Fluorescently Tagged Cellular Proteins Using FCS-Calibrated Four-Dimensional Imaging. *Nat. Protoc.* **2018**, *13* (6), 1445–1464. <https://doi.org/10.1038/nprot.2018.040>.
- (80) Wachsmuth, M.; Weidemann, T.; Müller, G.; Hoffmann-Rohrer, U. W.; Knoch, T. A.; Waldeck, W.; Langowski, J. Analyzing Intracellular Binding and Diffusion with Continuous Fluorescence Photobleaching. *Biophys. J.* **2003**, *84* (5), 3353–3363.
- (81) Steinauer, A. *Chemical Synthesis and Biological Mechanism of Intracellular Delivery of Engineered Biomolecules*, Yale University, New Haven, CT, 2018.

- (82) Burlina, F.; Sagan, S.; Bolbach, G.; Chassaing, G. Quantification of the Cellular Uptake of Cell-Penetrating Peptides by MALDI-TOF Mass Spectrometry. *Angew. Chem. Int. Ed.* **2005**, *44* (27), 4244–4247. <https://doi.org/10.1002/anie.200500477>.
- (83) Attune™ NxT Software User Guide. Thermo Fisher Scientific Inc. 2016.
- (84) Guo, M.; Gelman, H.; Gruebele, M. Coupled Protein Diffusion and Folding in the Cell. *PLOS ONE* **2014**, *9* (12), e113040–e113040. <https://doi.org/10.1371/journal.pone.0113040>.
- (85) Andersen, B. B.; Gundersen, H. J. G.; Pakkenberg, B. Aging of the Human Cerebellum: A Stereological Study. *J. Comp. Neurol.* **2003**, *466* (3), 356–365. <https://doi.org/10.1002/cne.10884>.
- (86) Frank, A. O.; Chuong, C. J. C.; Johnson, R. L. A Finite-Element Model of Oxygen Diffusion in the Pulmonary Capillaries. *J. Appl. Physiol.* **1997**, *82* (6), 2036–2044. <https://doi.org/10.1152/jappl.1997.82.6.2036>.
- (87) Buschmann, V.; Krämer, B.; Koberling, F. Quantitative FCS: Determination of the Confocal Volume by FCS and Bead Scanning with the Microtime 200. **2009**.
- (88) Einstein, A. On the Motion of Small Particles Suspended in Liquids at Rest Required by the Molecular-Kinetic Theory of Heat. *Ann. Phys.* **1905**, *17* (549–560), 208.
- (89) Rüttinger, S.; Buschmann, V.; Krämer, B.; Erdmann, R.; Macdonald, R.; KOBERLING, F. Comparison and Accuracy of Methods to Determine the Confocal Volume for Quantitative Fluorescence Correlation Spectroscopy. *J. Microsc.* **2008**, *232* (2), 343–352. <https://doi.org/10.1111/j.1365-2818.2008.02105.x>.
- (90) Saffarian, S.; Elson, E. L. Statistical Analysis of Fluorescence Correlation Spectroscopy: The Standard Deviation and Bias. *Biophys. J.* **2003**, *84* (3), 2030–2042. [https://doi.org/10.1016/S0006-3495\(03\)75011-5](https://doi.org/10.1016/S0006-3495(03)75011-5).
- (91) Marmelstein, A. M.; Lobba, M. J.; Mogilevsky, C. S.; Maza, J. C.; Brauer, D. D.; Francis, M. B. Tyrosinase-Mediated Oxidative Coupling of Tyrosine Tags on Peptides and Proteins. *J. Am. Chem. Soc.* **2020**, *142* (11), 5078–5086. <https://doi.org/10.1021/jacs.9b12002>.

## CHAPTER 3

### Diffusion of Free Dyes and Cell-Permeant Miniature Proteins Using Fluorescence Correlation Spectroscopy

Parts of this chapter are included in

Steinauer, A.; LaRochelle, J. R.; Knox, S. L.; Wissner, R. F.; Barry, S.; Schepartz, A. **HOPS-dependent endosomal fusion required for efficient cytosolic delivery of therapeutic peptides and small proteins.** *PNAS.* **2019**, *116* (2), 512-521.

and have been adapted with permission from all co-authors.

### 3.1 Abstract

Fluorescence correlation spectroscopy (FCS) can be used to directly and absolutely quantify the concentration of fluorophore that reaches the cytosol of cells. To understand diffusion-related properties of cell-permeant miniature proteins (CPMPs) and cell penetrating peptides (CPPs) tagged with a dye, it is necessary to study these molecules at consistent temperatures and compare them to corresponding parameters of free dye. This chapter supports experiments conducted in Steinauer *et al.*, illustrating that CPMPs and CPPs exhibit longer diffusion times in cells as compared to themselves and free dye in solution. We evaluated a panel of five dyes, similar in size and charge to the dye used to label CPMPs and CPPs. Studied by confocal microscopy, flow cytometry, and FCS, only two out of these five dyes passed final FCS analysis for calculations to determine diffusion coefficients in cells. The *in vitro*  $D$  calculated for SNAP-Cell TMR Star and Atto590 chloroalkane correspond well to another standard, small molecule dye. Within the cell,  $D$  of SNAP-Cell TMR Star was approximately 2-fold larger compared to CPMPs and suggesting CPMPs reach the cytosol intact. Studies using CPMPs and CPPs at 37 °C confirmed that diffusion is temperature-dependent, as  $D$  became larger as the temperature increased. The experiments described herein support delivery of intact CPMPs and CPPs.

### 3.2 Introduction

Fluorescence correlation spectroscopy (FCS) is a biophysical technique that can quantify the amount of material that reaches the cytosol of a cell and provide information on the mobility and size of the molecule under study.<sup>1</sup> Fluctuations in fluorescence intensity can be analyzed by generating an autocorrelation curve, a measure of self-similarity over time. The inflection point of the autocorrelation curve is proportional to the size of the molecule to which a fluorophore is attached—which can be used as a check to ensure that the fluorophore is still attached—and provides the diffusion time ( $\tau_{\text{diff}}$ ).<sup>2</sup>  $\tau_{\text{diff}}$  can be converted to a diffusion coefficient ( $D$ ), which is inversely proportional to the size of the molecule.<sup>3</sup> Molecules that are smaller would be expected to have a larger diffusion coefficient as the molecule traverses through more space in a shorter period of time. Typical small molecules (such as calcein) at similar molecular weights to fluorophores (~500–900 g/mol) exhibit diffusion coefficients between  $3.0$  and  $3.8 \times 10^{-6} \text{ cm}^2 \text{ s}^{-1}$  in buffer.<sup>4</sup> In the cell, anomalous diffusion is a result of the crowded cellular environment—a molecule moving through the cell may encounter organelles, proteins, or other molecules.<sup>5</sup> These interactions with cell components generally result in the decrease of the molecule of interest's  $D$ , evidenced by calcein ( $D$  decreases to  $1.5 \times 10^{-6} \text{ cm}^2 \text{ s}^{-1}$  in endosomes of cells).<sup>6</sup>

Cell-permeant miniature proteins (CPMPs) and cell penetrating peptides (CPPs) have been studied in live cells using FCS to determine the amount of material that reaches the cytosol.<sup>1</sup> To validate previous analyses using HPLC- and UPLC-based methods which concluded CPMPs do not degrade within the cell,<sup>1,7</sup> our goal was to determine diffusion coefficients of free dye and compare them to  $D$  of CPMPs. We analyzed five dyes similar in size and charge to the fluorophore used to tag CPMPs

**(Figure 3.1).** We hypothesized that FCS autocorrelation traces of free dye in cells would exhibit shorter diffusion times than those obtained for CPMPs.

Additionally, it was important to measure molecules at 37 °C and not at 25 °C as previously completed since diffusion is a temperature-dependent process.<sup>1</sup> Alexa Fluor™ 594 hydrazide exhibits a diffusion coefficient of  $3.88 \times 10^{-6} \text{ cm}^2 \text{ s}^{-1}$  at 25 °C in water<sup>8</sup> but this value rises to  $5.20 \times 10^{-6} \text{ cm}^2 \text{ s}^{-1}$  at 37 °C since increased temperature is directly proportional to kinetic energy. We wanted to evaluate the CPMPs aPP5.3<sup>R</sup> and ZF5.3<sup>R</sup>, as well as the CPPs CPP12<sup>R</sup>, SAH-p53-8<sup>R</sup>, and D-Arg<sub>8</sub><sup>R</sup> to confirm that diffusion is dependent on temperature and provide evidence of intact peptides within the cell.

### **3.3 Methods**

#### **3.3.1 Cell Preparation for Flow Cytometry and Fluorescence Correlation Spectroscopy**

Saos-2 cells (120,000) were plated in McCoy's 5A without phenol red, supplemented with 15% fetal bovine serum (FBS), and without penicillin/streptomycin (p/s) 24–48 h prior to the experiment. On the day of the experiment, the cells were washed twice with 1 mL DPBS and incubated with 1 mL of 50–100 nM dye solution (100 nM of Lissamine Rhodamine B sulfonyl chloride and 5 µL Lipofectamine RNAiMAX incubated for 5 min prior to addition to cells) in clear McCoy's 5A (without phenol red, FBS, or p/s) for 30 min at 37 °C with 5% CO<sub>2</sub>. Cells were washed three times with 1 mL DPBS and 500 µL/well of TrypLE Express (without phenol red) were added and the cells incubated at 37 °C, 5% CO<sub>2</sub> until cells were lifted, up to 10 min total. Cells were added to 15 mL Falcon tubes and centrifuged in 3 mL McCoy's 5A (supplemented with 15% FBS) at 200 g for 3 min. Cells were resuspended in 600 µL McCoy's 5A (containing HEPES) and 300 µL of this suspension were added to a fibronectin-coated borosilicate 8-well dish for FCS analysis. Cells adhered at 37 °C and 5% CO<sub>2</sub> for approximately 15 min prior to confocal microscopy and FCS. The second half of the suspension was centrifuged at 200 g for 2 min, resuspended in 200 µL DPBS, and analyzed by flow cytometry.

#### **3.3.2 Flow Cytometry**

Flow cytometry was performed on an Attune NxT flow cytometer (excitation laser: 561 nm, emission filter:  $585 \pm 16 \text{ nm}$ ) at room temperature. At least 10,000 cells were analyzed for each sample. Flow cytometry data was analyzed using the Attune NxT software.

#### **3.3.3 Fluorescence Correlation Spectroscopy (FCS)**

FCS was conducted on an LSM 880 (Carl Zeiss). FCS measurements for 100 nM Alexa Fluor™ 594 hydrazide (in water) were obtained at 37 °C. Fluorescent fluctuations over time were recorded on a GaAsP detector and traces were converted to autocorrelation curves using a custom MATLAB script. The FCS traces for each dye

50–100 nM (**1–5**) analyzed were obtained (in DMEM containing 25 mM HEPES). The fit autocorrelation traces from live-cell measurements were then evaluated and filtered as described before.<sup>1</sup> Briefly, we discarded traces that displayed poor signal with counts per molecule (cpm) below 1 kHz and/or low anomalous diffusion coefficients ( $\alpha < 0.3$ ).<sup>9</sup> With these parameters, we typically retained at least 75% of the collected data points. Traces were collected for both nucleus and cytosol for each condition but only those which passed analysis are reflected here (those which did not pass were discarded). *In vitro* data was fit to 3D diffusion while *in cellulo* data were fit to an anomalous model of 3D diffusion.<sup>1,2</sup>

### 3.3.4 Peptide Diffusion Times using FCS

To measure diffusion times using FCS, peptides (CPP12<sup>R</sup>, SAH-p53-8<sup>R</sup>, ZF5.3<sup>R</sup>, aPP5.3<sup>R</sup>, and D-Arg<sub>8</sub><sup>R</sup>) were prepared at 100 nM in DMEM. Diffusion times were measured in serum-free DMEM without phenol red (containing 25 mM HEPES, pH 7.2) at 37 °C in triplicate. Alexa Fluor™ 594 hydrazide was analyzed in Milli-Q water. The diffusion times were then converted to diffusion coefficients.

### 3.3.5 Calculation of Diffusion Coefficients of Dyes and Peptides

The diffusion coefficient ( $D$ ) of Alexa Fluor™ 594 at 37 °C was calculated using **Equation 3.1**:

$$D(T) = D(25\text{ °C}) \cdot \frac{t+273.15}{\eta(t)} \cdot 2.985 \cdot 10^{-6} \text{ Pa} \cdot \text{s} \cdot \text{K}^{-1} \quad \text{Equation 3.1}$$

where  $t = 37\text{ °C}$ ,  $D$  of Alexa Fluor™ 594 at 25 °C is  $3.88 \times 10^{-6} \text{ cm}^2 \text{ s}^{-1}$ ,<sup>8</sup> and the viscosity ( $\eta$ ) of water is 0.6913 mPa s at 37 °C.

Diffusion times ( $\tau_{\text{diff}}$ ) can be converted to  $D$  using **Equation 3.2**:

$$\omega = \sqrt{4D\tau_{\text{diff}}} \quad \text{Equation 3.2}$$

where  $\omega$  is the radius of the confocal detection volume ( $2.97 \times 10^{-7} \text{ cm}$ , determined from  $D$  and  $\tau_{\text{diff}}$  of Alexa Fluor™ 594 hydrazide).

$\tau_{\text{diff}}$  of dyes **1–5** and peptides (both *in vitro* and *in cellulo*) obtained by FCS analysis were converted to  $D$  by rearranging the previous equation into **Equation 3.3**:

$$D = \frac{\omega^2}{4\tau_{\text{diff}}} \quad \text{Equation 3.3}$$

## 3.4 Results and Discussion

### 3.4.1 Diffusion of Free Dyes *In Vitro* and *In Cellulo*

To provide evidence whether peptide degradation occurs in the cell, we chose to evaluate the diffusion coefficients of small molecule fluorophores and compare them to

the diffusion coefficients we observe for CPMPs. CPMPs are typically labeled with Lissamine rhodamine B sulfonyl chloride (**1**) to track the location of CPMP within the cell using confocal microscopy, flow cytometry, and FCS. This version of rhodamine is impermeant to cells on its own, which we confirmed by the absence of signal in the rhodamine channel using confocal microscopy (**Figure 3.2**). Interestingly, even in the presence of Lipofectamine RNAiMAX, a reagent that is used to permeabilize membranes for transfections,<sup>10</sup> **1** did not reach the cell interior. The trypsinization step in our protocol may provide means for the dye to diffuse back out of the cell resulting in the lack of rhodamine fluorescence.

To determine the diffusion coefficient of a red, cell-permeant dye similar in size and charge to **1** in the cytosol and nucleus of Saos-2 cells, we assessed four potential dyes (**Figure 3.1**). SNAP-Cell TMR-Star (**2**) exhibits the same charge as **1**, carrying one positive and one negative charge to form an overall neutral molecule. Atto590 chloroalkane (**3**) has been used as a fluorescent substrate for HaloTag in cells<sup>11</sup> and carries a +1 charge. Instead of the chloroalkane, another form of Atto590 with a +1 charge contains a N-hydroxysuccinimide (NHS) ester (**4**) that can react with primary amines.<sup>12</sup> Finally, Rhodamine B (**5**) is the parent scaffold for **1**, but includes a carboxylic acid that can cyclize to turn the fluorophore on or off depending on the local environment.

Saos-2 cells were treated with 50–100 nM of free dye for 30 min at 37 °C with 5% CO<sub>2</sub>, washed with DPBS, lifted using TrypLE, and replated for confocal microscopy. Both **2** and **4** contain signal in the rhodamine channel: **4** is more diffuse (representative of cytosolic presence) while **2** is more punctate (representative of being trapped within endosomes). **4** shows dose-dependency as the treatment concentration increases from 50 nM to 100 nM. Dyes **1**, **3**, and **5** are not cell permeable as there is no difference in the images compared to nontreated cells. No signal was observed for **3** even though the NHS ester version was permeable (**Figures 3.2** and **3.3A**) and others have reported the use of the chloroalkane as cell-permeant.<sup>11</sup>

We next turned to flow cytometry to provide a more quantitative picture of the total cellular uptake of this panel of dyes (**Figure 3.3A**). Saos-2 cells were treated with 50–100 nM of free dye for 30 min at 37 °C with 5% CO<sub>2</sub>, washed with DPBS, lifted using TrypLE, and resuspended in DPBS for flow cytometry analysis. As observed with confocal microscopy, treatment of Saos-2 cells with **1** did not result in material that accessed the cell interior, even in the presence of Lipofectamine RNAiMAX. 50 nM of **2** increased the median fluorescence intensity (MFI) 81-fold above nontreated cells. **3** exhibited MFI of 990 ± 24 AU, more uptake than expected from the absence of signal in the rhodamine channel using confocal microscopy. Dye **4** shows a dose-dependency in cellular uptake—when the treatment concentration increased from a 50 to 100 nM, the MFI increased by 3.3-fold. Finally, as expected, **5** was unable to traverse the cell membrane and failed to reach the interior of cells.

Flow cytometry cannot distinguish between material trapped within endosomes and that which reaches the cytosol, but FCS can be used to probe whether a

fluorescent molecule reaches intracellular locations such as the cytosol or nucleus. Saos-2 cells were treated with 50–100 nM of free dye for 30 min at 37 °C with 5% CO<sub>2</sub>, washed with DPBS, lifted using TrypLE, and replated for FCS. We were unable to obtain FCS traces for **1**, **1** in the presence of Lipofectamine RNAiMAX, and **5**. Cells treated with 100 nM of **4** were too bright to complete FCS measurements as the GaAsP detector shut down even at lower laser intensities. Dyes **2** and **3** reached the cytosol and nucleus (**Figure 3.3B**). It was expected that **3** would reach the interior of the cell based on previous reports,<sup>11</sup> but the confocal and flow cytometry data indicated minimal material was present inside the cell. The FCS data confirms that **3** can in fact traverse cell membranes. There were no significant differences between the concentrations obtained in the cytosol or nucleus for either **2** or **3**, and these dyes reached similar cytosolic concentrations.

The *in vitro* diffusion coefficients for **1**, **2**, and **4** were all on the same order of magnitude as each other and the Alexa Fluor™ 594 hydrazide standard (**Table 3.1**). Since these dyes are all approximately the same size, these results were expected. Only two dyes out of the entire panel provided autocorrelation curves that could be fit to an equation of anomalous diffusion,<sup>2</sup> so these were the only dyes in which we could derive diffusion coefficients (**Table 3.1**). We were unable to fit nuclear autocorrelation traces of 50 nM **4** since some traces had high  $\tau_{\text{diff}}$  (indicating sticking to organelles) and therefore failed to pass analysis. There were no significant differences between cytosol and nuclear  $\tau_{\text{diff}}$  for dyes **2** and **3**. We note that the  $\tau_{\text{diff}}$  for **2** are shorter than those obtained with **3** and could vary due to interactions of the dyes within the cell since **3** carries an alkyl chain that could participate in additional hydrophobic interactions. As expected,  $\tau_{\text{diff}}$  of **2** increased in the cytosol and nucleus compared to *in vitro* due to the crowded cellular environment resulting in anomalous diffusion. The increase in  $\tau_{\text{diff}}$  corresponds to a smaller  $D$  and indicates that **2** cannot move around the cellular environment as freely. When compared to CPMPs aPP5.3<sup>R</sup> and ZF5.3<sup>R</sup> (where R is the Lissamine rhodamine B tag), the  $D$  of **2** is approximately 2-fold higher ( $D = 71 \pm 13$  and  $88 \pm 10 \mu\text{m}^2 \text{s}^{-1}$  in cytosol for aPP5.3<sup>R</sup> and ZF5.3<sup>R</sup>, respectively). To observe significant changes in diffusion times, others have reported that the mass ratios should be at least eight.<sup>2</sup> The CPMPs are only 5–6-fold more massive than dyes **2** and **3**, making changes in diffusion based on molecular weight more difficult to observe. The data, taken together, support the hypothesis that the fluorescent signal from CPMPs evaluated by FCS in Saos-2 cells is not simply free dye but intact CPMP.

### 3.4.2 Diffusion Times of CPMPs and CPPs at 37 °C

Diffusion depends on the size of the molecule and its local environment (concentration gradient, temperature, etc.).  $D$  of aPP5.3<sup>R</sup>, ZF5.3<sup>R</sup>, and SAH-p53-8<sup>R</sup> in Dulbecco's modified eagle's medium (DMEM) (203.1, 190.5, and 233.9  $\mu\text{m}^2 \text{s}^{-1}$ , respectively) and in HeLa cells (44.1, 74.0, and 47.1  $\mu\text{m}^2 \text{s}^{-1}$ , respectively) were previously reported at room temperature.<sup>1</sup> These data indicate that CPMPs and CPPs exhibit  $D$  approximately 2.6–5 times as long *in vitro* compared to *in cellulo*. Since the FCS measurements described in Steinauer *et al.* were conducted at 37 °C, it was important to evaluate whether temperature affected the diffusion times of CPMPs and

CPPs as expected. *In vitro*  $\tau_{\text{diff}}$  and their corresponding  $D$  values (calculated using **Equation 3.2**) for aPP5.3<sup>R</sup>, ZF5.3<sup>R</sup>, D-Arg<sub>8</sub><sup>R</sup>, SAH-p53-8<sup>R</sup>, and CPP12<sup>R</sup> are listed in **Table 3.2**.

Compared to **1** and Alexa Fluor™ 594 hydrazide, the CPMPs and CPPs exhibit longer (approximately 2-fold) diffusion times (and therefore smaller  $D$  values) *in vitro*. The  $D$  of CPMPs ( $231 \pm 2$  to  $262 \pm 3 \mu\text{m}^2 \text{s}^{-1}$ ) are slightly slower than smaller peptides ( $306 \pm 1$  to  $323 \pm 2 \mu\text{m}^2 \text{s}^{-1}$ ), which is expected given the size difference between the constructs (28–36 amino acids for CPMPs versus 8–14 amino acids for CPPs). Increasing the temperature from 25 °C to 37 °C should increase  $D$ , which is observed with the increase of  $D$  for aPP5.3<sup>R</sup>, ZF5.3<sup>R</sup>, and SAH-p53-8<sup>R</sup> compared to LaRoche *et al.*<sup>1</sup> Inside the cytosol, the observed  $D$  of each CPMP and CPP decreases by 3- to 82-fold. Specifically, we observe cytosolic  $D$  that were more than 50 times smaller for D-Arg<sub>8</sub><sup>R</sup> and CPP12<sup>R</sup>, compared to  $D$  commonly observed for aPP5.3<sup>R</sup>, ZF5.3<sup>R</sup>, and SAH-p53-8<sup>R</sup>.<sup>1</sup> Such a large decrease in  $D$  may be a sign of supramolecular aggregation or binding to intracellular factors.

### 3.5 Conclusions

To provide evidence whether peptide degradation occurs in the cell, we chose to determine *in cellulo* diffusion coefficients of dyes **1–5** and compare them to the diffusion coefficients observed for CPMPs. Dyes **1** and **5** were not cell permeable as determined by confocal microscopy and flow cytometry. **3** did not exhibit signal via confocal microscopy but flow cytometry revealed that minimal levels reach the cell interior. Additional studies using FCS supported that **3** accesses the cytosol and nucleus of Saos-2 cells. The *in vitro*  $D$  calculated for **2** and **3** correspond well to another small molecule dye used as a standard (Alexa Fluor™ 594). Within the cell, **2**'s  $D$  was approximately 2-fold higher compared to aPP5.3<sup>R</sup> and ZF5.3<sup>R</sup> and supports the hypothesis that the fluorescent signal from CPMPs evaluated by FCS in Saos-2 cells is not simply free dye. Studies using CPMPs and CPPs at 37 °C confirmed that diffusion is temperature-dependent, as  $D$  became larger as the temperature increased. The experiments described herein establish FCS-derived parameters for dyes and CPMPs both in DMEM as well as within the cell.

### 3.6 Figures

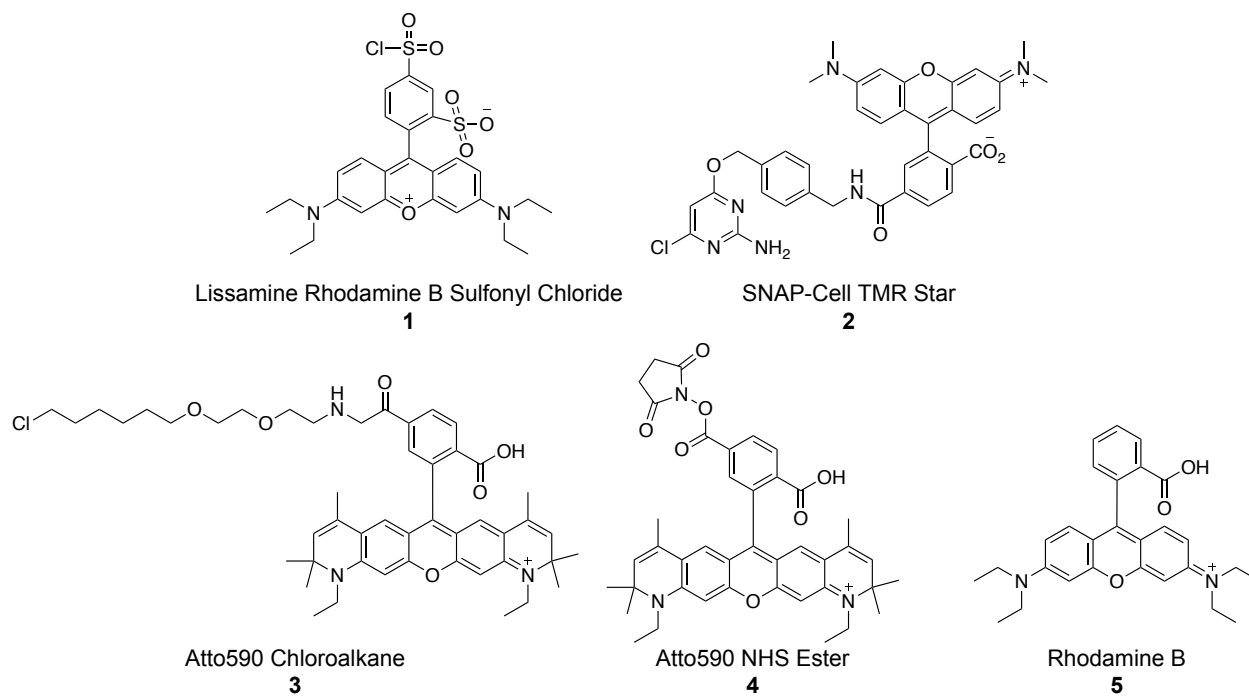


**Figure 3.1.** Structures of dyes studied (counter ions not shown).

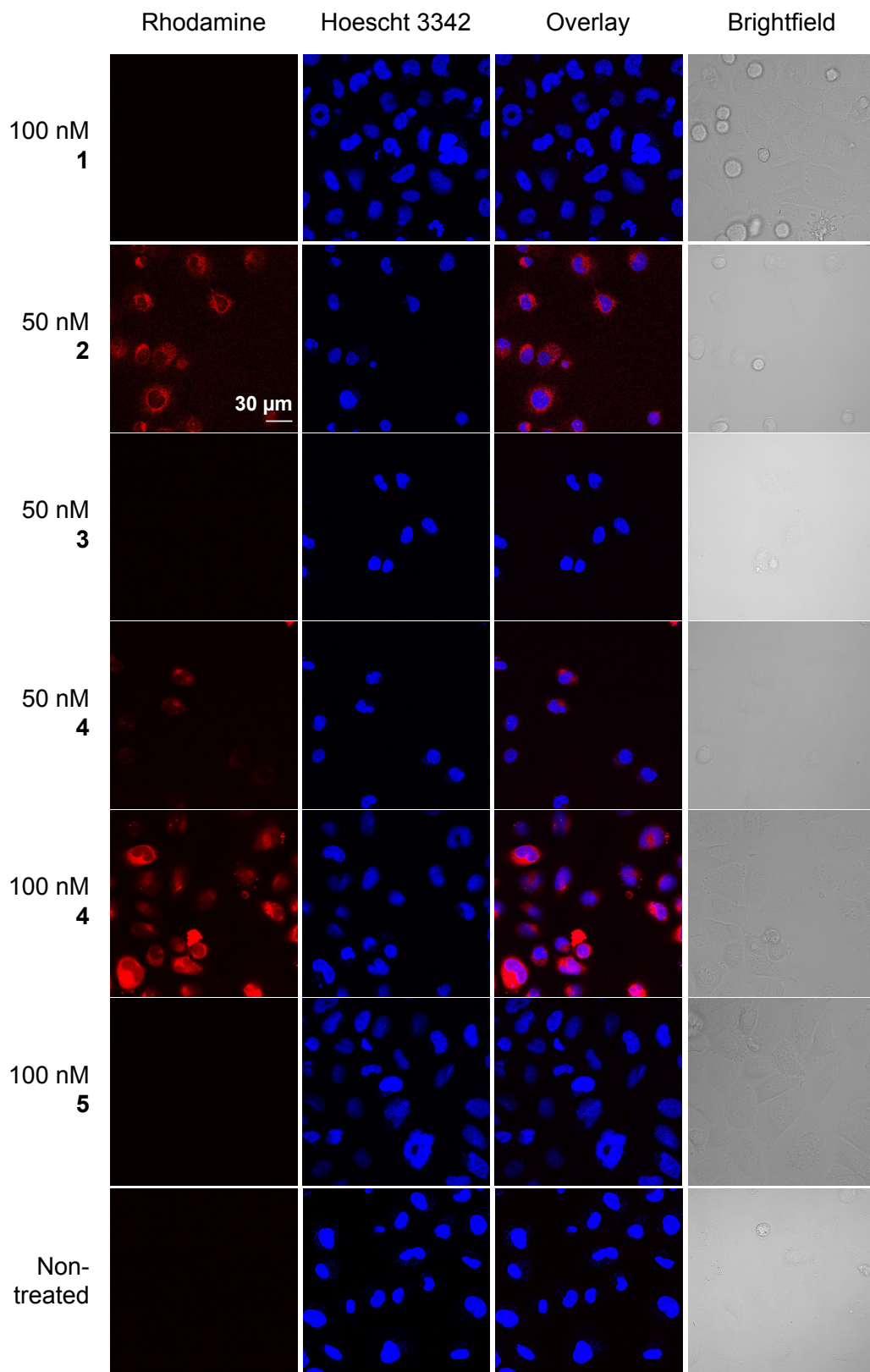


**Figure 3.2.** Total cellular uptake of dyes 1–5 assessed using confocal microscopy in Saos-2 cells after a 30 min incubation. Scale bar = 30  $\mu$ m.

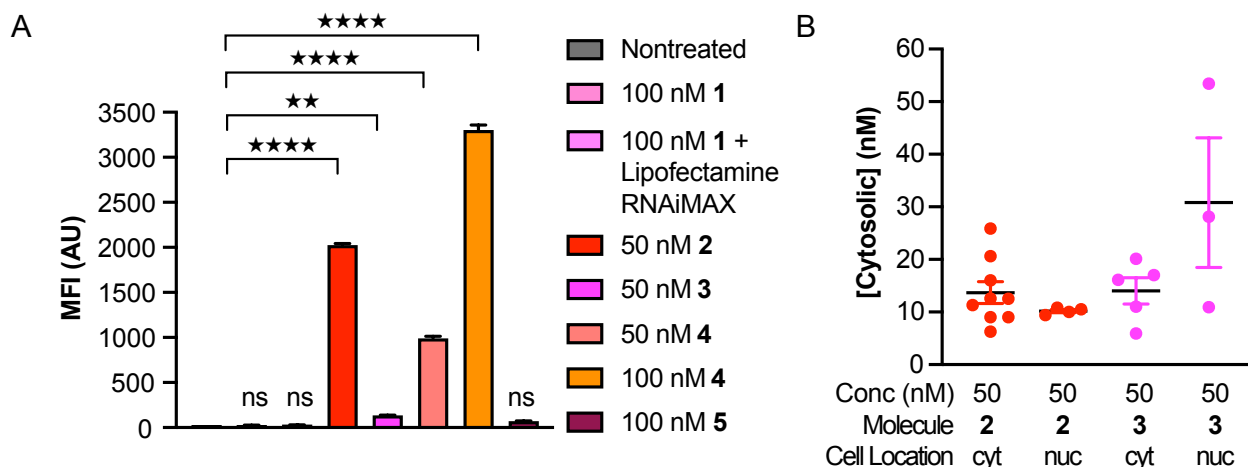


**Figure 3.3.** (A) Bar plot illustrating total cellular uptake of dyes 1–5 during a 30 min incubation at 37 °C. MFI values represent the median fluorescence intensity of cells (10,000 cells each). Error bars represent the standard error of the mean. The MFI of each treatment condition was compared to nontreated cells using a one-way analysis of variance (ANOVA) followed by Dunnett’s multiple comparisons test. \*\*\*\* $p \leq 0.0001$ , \*\*\* $p \leq 0.001$ , \*\* $p \leq 0.01$ , \* $p \leq 0.05$ , ns = nonsignificant. (B) Cytosolic access of dyes 2 and 3 assessed using fluorescence correlation spectroscopy after a 30 min incubation. The average cytosolic and nuclear concentrations of 2 or 3 were compared using an unpaired t test. cyt = cytosol, nuc = nucleus.

### 3.7 Tables

**Table 3.1.** Diffusion times ( $\tau_{diff}$ ) and diffusion coefficients ( $D$ ) of dyes measured *in vitro* and *in cellulo* using FCS. *In vitro* diffusion parameters were calculated from 1–3 autocorrelation curves. Cytosol diffusion parameters were calculated from 5–9 autocorrelation curves. Diffusion parameters in the nucleus were calculated from 3–4 autocorrelation curves. N.D. = not determined (as a result of the dye not reaching the cell interior, the dye unable to be evaluated by FCS, or not obtained).

Molecule	<i>In Vitro</i> $\tau_{diff}$ (ms)	<i>In Vitro</i> $D$ ( $\mu\text{m}^2 \text{s}^{-1}$ )	Cytosol $\tau_{diff}$ (ms)	Cytosol $D$ ( $\mu\text{m}^2 \text{s}^{-1}$ )	Nucleus $\tau_{diff}$ (ms)	Nucleus $D$ ( $\mu\text{m}^2 \text{s}^{-1}$ )
1	0.0428 ± 0.0004	515 ± 5	N.D.	N.D.	N.D.	N.D.
2	0.0450	490	0.9 ± 0.2	33 ± 7	0.9 ± 0.4	42 ± 11
3	N.D.	N.D.	4 ± 1	8 ± 2	2.7 ± 0.7	10 ± 2
4	0.0523 ± 0.0003	422 ± 2	N.D.	N.D.	N.D.	N.D.
5	N.D.	N.D.	N.D.	N.D.	N.D.	N.D.
Alexa Fluor 594 hydrazide	0.0424	520 <sup>a</sup>	N.D.	N.D.	N.D.	N.D.

<sup>a</sup>Calculated using **Equation 3.1**.

**Table 3.2.** *In vitro* diffusion times ( $\tau_{\text{diff}}$ ) and diffusion coefficients ( $D$ ) of 100 nM CPMPs and CPPs at 37 °C compared to free fluorophores (at 100 nM). *In cellulo*  $D$  of CPMPs and CPPs measured in the cytosol of Saos-2 cells. Error is standard error of the mean. N.D. = not determined.

Molecule	<i>In vitro</i> $\tau_{\text{diff}}$ (ms)	<i>In vitro</i> $D$ ( $\mu\text{m}^2 \text{s}^{-1}$ )	Cytosol $D$ ( $\mu\text{m}^2 \text{s}^{-1}$ )
aPP5.3 <sup>R</sup>	0.0953 ± 0.0009	231 ± 2	86 ± 7.1
ZF5.3 <sup>R</sup>	0.0843 ± 0.0009	262 ± 3	82 ± 10
D-Arg <sub>8</sub> <sup>R</sup>	0.0722 ± 0.0001	306 ± 1	4.4 ± 0.37
SAH-p53-8 <sup>R</sup>	0.0682 ± 0.0004	323 ± 2	57 ± 21
CPP12 <sup>R</sup>	0.0692 ± 0.0004	318 ± 2	3.9 ± 0.29
Lissamine Rhodamine B Sulfonyl Chloride (1)	0.0428 ± 0.0004	515 ± 5	N.D.
Alexa Fluor™ 594 hydrazide	0.0424	520 <sup>a</sup>	N.D.

<sup>a</sup>Calculated using **Equation 3.1**.

### 3.8 References

- (1) LaRochelle, J. R.; Cobb, G. B.; Steinauer, A.; Rhoades, E.; Schepartz, A. Fluorescence Correlation Spectroscopy Reveals Highly Efficient Cytosolic Delivery of Certain Penta-Arg Proteins and Stapled Peptides. *J. Am. Chem. Soc.* **2015**, *137* (7), 2536–2541. <https://doi.org/10.1021/ja510391n>.
- (2) Schwille, P.; Hausteil, E. Fluorescence Correlation Spectroscopy - An Introduction to Its Concepts and Applications. *Spectroscopy* **2001**, *94*(22).
- (3) *Fluorescence Correlation Spectroscopy: Theory and Applications*; Rigler, R., Elson, E. S., Eds.; Springer Series in Chemical Physics; Springer-Verlag: Berlin Heidelberg, 2001. <https://doi.org/10.1007/978-3-642-59542-4>.
- (4) di Cagno, M. P.; Clarelli, F.; Våbenø, J.; Lesley, C.; Rahman, S. D.; Cauzzo, J.; Franceschini, E.; Realdon, N.; Stein, P. C. Experimental Determination of Drug Diffusion Coefficients in Unstirred Aqueous Environments by Temporally Resolved Concentration Measurements. *Mol. Pharm.* **2018**, *15* (4), 1488–1494. <https://doi.org/10.1021/acs.molpharmaceut.7b01053>.
- (5) Oliveira, F. A.; Ferreira, R. M. S.; Lapas, L. C.; Vainstein, M. H. Anomalous Diffusion: A Basic Mechanism for the Evolution of Inhomogeneous Systems. *Front. Phys.* **2019**, *7* (18). <https://doi.org/10.3389/fphy.2019.00018>.
- (6) Yoshida, N.; Tamura, M.; Kinjo, M. Fluorescence Correlation Spectroscopy: A New Tool for Probing the Microenvironment of the Internal Space of Organelles. *Single Mol.* **2000**, *1* (4), 279–283. [https://doi.org/10.1002/1438-5171\(200012\)1:4<279::AID-SIMO279>3.0.CO;2-S](https://doi.org/10.1002/1438-5171(200012)1:4<279::AID-SIMO279>3.0.CO;2-S).

- (7) Appelbaum, J. S.; LaRoche, J. R.; Smith, B. A.; Balkin, D. M.; Holub, J. M.; Schepartz, A. Arginine Topology Controls Escape of Minimally Cationic Proteins from Early Endosomes to the Cytoplasm. *Chem. Biol.* **2012**, *19* (7), 819–830. <https://doi.org/10.1016/j.chembiol.2012.05.022>.
- (8) Nitsche, J. M.; Chang, H.-C.; Weber, P. A.; Nicholson, B. J. A Transient Diffusion Model Yields Unitary Gap Junctional Permeabilities from Images of Cell-to-Cell Fluorescent Dye Transfer Between *Xenopus* Oocytes. *Biophys. J.* **2004**, *86* (4), 2058–2077. [https://doi.org/10.1016/S0006-3495\(04\)74267-8](https://doi.org/10.1016/S0006-3495(04)74267-8).
- (9) Bronstein, I.; Israel, Y.; Kepten, E.; Mai, S.; Shav-Tal, Y.; Barkai, E.; Garini, Y. Transient Anomalous Diffusion of Telomeres in the Nucleus of Mammalian Cells. *Phys. Rev. Lett.* **2009**, *103* (1), 018102. <https://doi.org/10.1103/PhysRevLett.103.018102>.
- (10) Zhao, M.; Yang, H.; Jiang, X.; Zhou, W.; Zhu, B.; Zeng, Y.; Yao, K.; Ren, C. Lipofectamine RNAiMAX: An Efficient SiRNA Transfection Reagent in Human Embryonic Stem Cells. *Mol. Biotechnol.* **2008**, *40* (1), 19–26. <https://doi.org/10.1007/s12033-008-9043-x>.
- (11) Bottanelli, F.; Kromann, E. B.; Allgeyer, E. S.; Erdmann, R. S.; Wood Baguley, S.; Sirinakis, G.; Schepartz, A.; Baddeley, D.; Toomre, D. K.; Rothman, J. E.; Bewersdorf, J. Two-Colour Live-Cell Nanoscale Imaging of Intracellular Targets. *Nat. Commun.* **2016**, *7* (1), 10778. <https://doi.org/10.1038/ncomms10778>.
- (12) Nanda, J. S.; Lorsch, J. R. Chapter Eight - Labeling a Protein with Fluorophores Using NHS Ester Derivatization. In *Methods in Enzymology*; Lorsch, J., Ed.; Academic Press, 2014; Vol. 536, pp 87–94. <https://doi.org/10.1016/B978-0-12-420070-8.00008-8>.

## CHAPTER 4

### Comparison of Cellular Uptake Using Various Cell-Permeant Miniature Proteins and Cell-Penetrating Peptides

Parts of this chapter are included in

Wissner, R. F.; Steinauer, A.; Knox, S. L.; Thompson, A. D.; Schepartz, A.  
**Fluorescence Correlation Spectroscopy Reveals Efficient Cytosolic Delivery of Protein Cargo by Cell-Permeant Miniature Proteins.** *ACS Cent. Sci.* **2018**, *4* (10), 1379-1393. <https://pubs.acs.org/doi/10.1021/acscentsci.8b00446>.

and are adapted with permission from all co-authors. Further permissions related to the material excerpted should be directed to the ACS.

## 4.1 Abstract

New methods for delivering proteins into the cytosol of mammalian cells are being reported at a rapid pace. Differentiating between these methods in a quantitative manner is difficult, however, as most assays for evaluating cytosolic protein delivery are qualitative and indirect and thus often misleading. Here we make use of flow cytometry to determine the relative total cellular uptake that seven different previously reported “cell-penetrating peptides” (CPPs) transport a model protein cargo—the self-labeling enzyme SNAP-tag—as a first step in understanding how much material gets into the cell. Our results suggest that the cell-permeant miniature protein ZF5.3 can deliver SNAP-tag in the highest quantities to three different cell lines. While ZF5.3-SNAP-Rho consistently reaches the interior of cells, we do see subtle cell line dependent differences in uptake among the remaining CPPs.

## 4.2 Introduction

There have been hundreds of reports of cell-penetrating peptides (CPPs) that encompass a wide variety of structures and methods of uptake. While some peptides stimulate endocytosis to reach the interior of the cell, others access the cytosol through direct penetration of the cell membrane. To render CPPs that utilize endocytosis tools for therapeutic prospects, the molecules must not only be taken up by the cell, but also escape from the endosomes that encapsulate them at the beginning of their journey. It is important to conduct a head-to-head comparison of the abilities of CPPs to deliver cargo into cells to understand whether these vehicles can move the field of protein delivery forward. Flow cytometry and fluorescence correlation spectroscopy (FCS) are used to study delivery, measuring total cellular uptake and cytosolic concentrations, respectively. Both methods are compatible with live cells and provide direct, quantitative information.

Here, we utilize the cargo SNAP-tag, which is a self-labeling enzyme derived from human DNA repair protein *O*<sup>6</sup>-alkylguanine-DNA alkyltransferase (hAGT).<sup>1–3</sup> SNAP-tag has been engineered to be stable inside cells and avoid proteolysis.<sup>2</sup> This enzyme provides a proof-of-concept to evaluate differences in uptake between previously described CPPs and cell-permeant miniature proteins (CPMPs). Specifically, unstructured CPPs R<sub>8</sub> and penetratin,<sup>4,5</sup> cyclic CPPs CPP9 and CPP12,<sup>6,7</sup> and CPMPs ZF5.3, aPP5.3, and ZiF<sup>8–10</sup> were analyzed (**Figure 4.1**). In addition to direct comparisons between delivery vehicles, we wanted to show that delivery of cargo is not cell line specific through the evaluation of Saos-2, HeLa, and SK-HEP-1 cells. R<sub>8</sub>, penetratin, ZF5.3, aPP5.3, and ZiF were expressed at the N-terminus of SNAP-tag with a C-terminal His<sub>6</sub> tag for immobilized metal affinity chromatography. CPP9 and CPP12 were appended to SNAP-tag by sortase labeling. SNAP-tag conjugates reacted with benzylguanine rhodamine (Rho) to generate fluorescently labeled proteins for flow cytometry analysis. As a whole, our results demonstrate that the CPMP ZF5.3 promotes the efficient uptake of appended protein cargo across multiple cell lines, while other CPMPs, unstructured CPPs, and cyclic CPPs do so to a lesser extent.

## 4.3 Methods

### 4.3.1 Cell Culture

Saos-2, HeLa, and SK-HEP-1 cell stocks were purchased from the American Type Culture Collection (ATCC). Saos-2 cells were cultured in McCoy's 5A medium supplemented with 15% fetal bovine serum (FBS), sodium pyruvate (1 mM), penicillin (100 units/mL), and streptomycin (100 µg/mL). HeLa cells were cultured in DMEM supplemented with 10% FBS, penicillin (100 units/mL), and streptomycin (100 µg/mL). SK-HEP-1 cells were cultured in EMEM supplemented with 10% FBS, penicillin (100 units/mL), and streptomycin (100 µg/mL). All cell cultures were maintained at 37 °C in a humidified atmosphere at 5% CO<sub>2</sub>.

### 4.3.2 Flow Cytometry

One day prior to performing uptake experiments, ~40,000 Saos-2, HeLa, or SK-HEP-1 cells in 1 mL of their respective media (McCoy's 5A medium supplemented with 15% FBS for Saos-2, DMEM supplemented with 10% FBS for HeLa, or EMEM supplemented with 10% FBS for SK-HEP-1) were plated into 12-well tissue culture treated plates and allowed to adhere overnight. The following morning, the cells were washed three times with DPBS, and the media was replaced with 500 µL of respective medium (without FBS supplementation) containing 1 µM solutions of each rhodamine-labeled SNAP-tag conjugate. The cells were incubated for 30 min at 37 °C and 5% CO<sub>2</sub>. The cells were washed three times with DPBS prior to lifting with 500 µL of trypsin for 5 min at 37 °C. The cells were then transferred to a 15 mL Falcon tube containing 1 mL of respective medium supplemented with FBS (15% for Saos-2 and 10% for HeLa and SK-HEP-1) and centrifuged at 500 *g* for 2 min. The cells were then washed by resuspension in DPBS and again sedimented at 500 *g* for 2 min. The cells were finally suspended in 100 µL of DPBS and transferred to microcentrifuge tubes prior to obtaining flow cytometry measurements. Flow cytometry measurements were performed using an Attune NxT flow cytometer equipped with a 561 nm laser for excitation of rhodamine.

## 4.4 Results and Discussion

The differences in the overall uptake of each SNAP-tag conjugate were studied using flow cytometry. Saos-2 cells were treated with 1 µM of each Rho-labeled SNAP-tag conjugate for 30 min at 37 °C, washed with DPBS, lifted with TrpLE to remove surface-bound protein, washed again, and resuspended in DPBS for flow cytometry analysis. The treatments led to evenly distributed populations of fluorescent cells with the median fluorescence intensity of this distribution over 3–5 independent replicates shown (**Figure 4.2**). Overall, the CPPs and CPMPs studied fall into four categories: cells treated with CPP9-SNAP-Rho were not measurably more fluorescent than cells treated with SNAP-Rho. Cells treated with CPP12-SNAP-Rho and aPP5.3-SNAP-Rho showed comparable levels of fluorescence throughout the cell interior, reaching values approximately 2-fold higher than that observed when cells were treated with SNAP-Rho. Cells treated with R<sub>8</sub>-SNAP-Rho and ZiF-SNAP-Rho exhibited higher levels of total

cellular fluorescence that were nearly 5-fold higher than that of cells treated with SNAP-Rho. The highest levels of total intracellular fluorescence were observed when cells were treated with Pen-SNAP-Rho (an 11-fold increase relative to cells treated with SNAP-Rho) and ZF5.3-SNAP-Rho (a 17-fold increase relative to cells treated with SNAP-Rho).

To broaden these findings, we repeated the flow cytometry experiments in two other common cell lines (HeLa and SK-HEP-1) and obtained similar results, implying that the level to which each SNAP-tag conjugate is taken up by endocytosis is comparable within this set of cell lines (**Figure 4.2**). Subtle cell line differences exist in that ZF5.3-SNAP-Rho reached a MFI of  $2942 \pm 210$  AU in SK-HEP-1 cells, higher than Saos-2 cells ( $2141 \pm 86$  AU) and HeLa cells ( $1251 \pm 9$  AU). In Saos-2 and HeLa cells, Pen-SNAP-Rho exhibited the second highest cellular uptake, but R<sub>8</sub>-SNAP-Rho experienced the second highest MFI in SK-HEP-1 cells. The differences between SNAP-tag conjugates in HeLa cells were more subtle than in the SK-HEP-1 and Saos-2 cell lines.

Overall, these results are consistent with previous flow cytometry studies demonstrating that the overall cellular uptake of ZF5.3 is significantly higher than that of unstructured CPPs and other CPMPs.<sup>9,11</sup> Our results are also consistent with flow cytometry studies demonstrating that the total levels of ZiF-mediated protein delivery are similar to those achieved by unstructured CPPs.<sup>10</sup> In addition, we found the overall uptake of Pen-SNAP-Rho to be significantly higher than that of R<sub>8</sub>-SNAP-Rho, which contradicts several uptake studies performed with molecules lacking an appended cargo.<sup>12–14</sup> Finally, in light of a previously published report,<sup>7</sup> we were surprised to find that the overall uptake of cyclic CPP-SNAP-tag conjugates (CPP9-SNAP-Rho and CPP12-SNAP-Rho) were significantly lower than those measured for any other tested unstructured CPP or CPMP conjugate. The SK-HEP-1 cell line resulted in the highest cellular uptake by flow cytometry out of all cell lines studied. As a whole, our results demonstrate that the CPMP ZF5.3 promotes the efficient uptake of a large appended protein cargo across multiple cell lines, while other CPMPs, unstructured CPPs, and cyclic CPPs do so to a lesser extent.

## 4.5 Conclusions

Despite the increasing number of reported methods for protein delivery,<sup>15</sup> most assays used to assess trafficking into the cytosol are qualitative and indirect and can therefore be misleading. These limitations make evaluating progress in the field of protein delivery extremely challenging. In this chapter, we analyze the relative efficiencies with which unstructured CPPs, CPMPs, and synthetic cyclic CPPs transport a model, self-labeled enzyme into the cell using flow cytometry. It is important to note that flow cytometry cannot provide information on individual cellular compartments and includes the fraction of material present in endosomes. Additional studies building upon these flow cytometry experiments (not described here) found that the extent of cytosolic trafficking of protein cargo cannot be ascertained accurately using confocal microscopy, flow cytometry, or enzymatic activity assays—the compartmental resolution and

precision afforded by FCS were required to distinguish conjugates that accumulate in the cytosol in appreciable levels from those that do not.<sup>16</sup>

## 4.6 Figures

Vehicle Library	
<b>cell-permeant miniature proteins (CPMPs)</b>	
ZF5.3: MYSCNVC GKAFVLSRHLNRHLRVHRRAT	
aPP5.3: MGPSQPTYPGDDAPV RDLIRFYDLRRYLNVVTRHRY	
ZiF: MLEPGEKPYKCPECGKSFSAALVAHQRTHTGKKS	
<b>cyclic peptides (cCPPs)</b>	<b>unstructured CPPs (uCPPs)</b>
CPP9: cyclo(fΦRrRrQ)-PEG <sub>2</sub>	R8: MRRRRRRRRR
CPP12: cyclo(FfΦRrRrQ)-PEG <sub>2</sub>	Pen: MRQIKIWFQNRMMKWKK

**Figure 4.1.** Vehicle library for evaluating cellular uptake. Each vehicle is conjugated to SNAP-tag. For ZF5.3 and aPP5.3, the residues comprising the 5.3 motif are shown in red. For CPP9 and CPP12, lowercase letters represent d-amino acids, Φ represents L-naphthylalanine, and PEG2 represents a 2-unit ethylene glycol spacer.

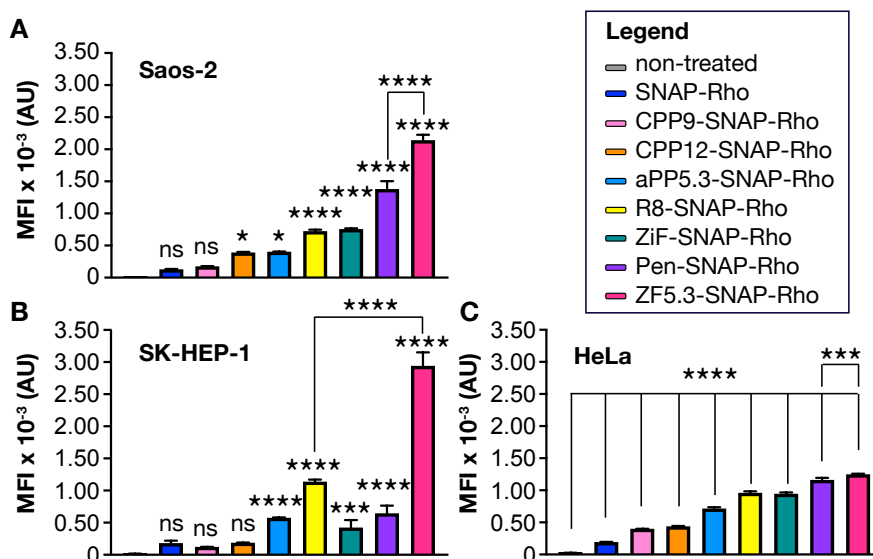


**Figure 4.2.** Total cell uptake of Rho-tagged SNAP-tag conjugates in HeLa and SK-HEP-1 cells assessed by flow cytometry. (A) Bar plots illustrating the relative uptake of each Rho-tagged SNAP-tag conjugate after 30 min incubation and treatment with trypsin to remove surface bound protein in Saos-2 cells, (B) bar plots illustrating the relative uptake of each Rho-tagged SNAP-tag conjugate in SK-HEP-1 cells and (C) bar plots illustrating the relative uptake of each Rho-tagged SNAP-tag conjugate in HeLa cells. MFI values represent the average median fluorescence intensity of cells determined from 3–12 individual replicates (10,000 cells each). Error bars represent the standard error of the mean. MFI values corresponding to each SNAP-tag conjugate were statistically compared to non-treated cells. \*\*\*\* $p \leq 0.0001$ , \*\*\* $p \leq 0.001$ , \*\* $p < 0.01$ , \* $p \leq 0.05$ ; one-way ANOVA followed by post hoc Dunnett's test.

## 4.7 References

- (1) Juillerat, A.; Gronemeyer, T.; Keppler, A.; Gendreizig, S.; Pick, H.; Vogel, H.; Johnsson, K. Directed Evolution of O6-Alkylguanine-DNA Alkyltransferase for Efficient Labeling of Fusion Proteins with Small Molecules In Vivo. *Chem. Biol.* **2003**, *10* (4), 313–317. [https://doi.org/10.1016/S1074-5521\(03\)00068-1](https://doi.org/10.1016/S1074-5521(03)00068-1).
- (2) Mollwitz, B.; Brunk, E.; Schmitt, S.; Pojer, F.; Bannwarth, M.; Schiltz, M.; Rothlisberger, U.; Johnsson, K. Directed Evolution of the Suicide Protein O6-Alkylguanine-DNA Alkyltransferase for Increased Reactivity Results in an Alkylated Protein with Exceptional Stability. *Biochemistry* **2012**, *51* (5), 986–994. <https://doi.org/10.1021/bi2016537>.
- (3) Keppler, A.; Gendreizig, S.; Gronemeyer, T.; Pick, H.; Vogel, H.; Johnsson, K. A General Method for the Covalent Labeling of Fusion Proteins with Small Molecules in Vivo. *Nat. Biotechnol.* **2003**, *21* (1), 86–89. <https://doi.org/10.1038/nbt765>.
- (4) Mitchell, D. J.; Steinman, L.; Kim, D. T.; Fathman, C. G.; Rothbard, J. B. Polyarginine Enters Cells More Efficiently than Other Polycationic Homopolymers. *J. Pept. Res.* **2000**, *56* (5), 318–325. <https://doi.org/10.1034/j.1399-3011.2000.00723.x>.
- (5) Derossi, D.; Joliot, A. H.; Chassaing, G.; Prochiantz, A. The Third Helix of the Antennapedia Homeodomain Translocates through Biological Membranes. *J. Biol. Chem.* **1994**, *269* (14), 10444–10450.
- (6) Qian, Z.; LaRochelle, J. R.; Jiang, B.; Lian, W.; Hard, R. L.; Selner, N. G.; Luechapanichkul, R.; Barrios, A. M.; Pei, D. Early Endosomal Escape of a Cyclic Cell-Penetrating Peptide Allows Effective Cytosolic Cargo Delivery. *Biochemistry* **2014**, *53* (24), 4034–4046. <https://doi.org/10.1021/bi5004102>.
- (7) Qian, Z.; Martyna, A.; Hard, R. L.; Wang, J.; Appiah-Kubi, G.; Coss, C.; Phelps, M. A.; Rossman, J. S.; Pei, D. Discovery and Mechanism of Highly Efficient Cyclic Cell-Penetrating Peptides. *Biochemistry* **2016**, *55* (18), 2601–2612. <https://doi.org/10.1021/acs.biochem.6b00226>.
- (8) Appelbaum, J. S.; LaRochelle, J. R.; Smith, B. A.; Balkin, D. M.; Holub, J. M.; Schepartz, A. Arginine Topology Controls Escape of Minimally Cationic Proteins from Early Endosomes to the Cytoplasm. *Chem. Biol.* **2012**, *19* (7), 819–830. <https://doi.org/10.1016/j.chembiol.2012.05.022>.
- (9) LaRochelle, J. R.; Cobb, G. B.; Steinauer, A.; Rhoades, E.; Schepartz, A. Fluorescence Correlation Spectroscopy Reveals Highly Efficient Cytosolic Delivery of Certain Penta-Arg Proteins and Stapled Peptides. *J. Am. Chem. Soc.* **2015**, *137* (7), 2536–2541. <https://doi.org/10.1021/ja510391n>.
- (10) Gaj, T.; Liu, J.; Anderson, K. E.; Sirk, S. J.; Barbas, C. F. Protein Delivery Using Cys2-His2 Zinc-Finger Domains. *ACS Chem. Biol.* **2014**, *9* (8), 1662–1667. <https://doi.org/10.1021/cb500282g>.
- (11) Holub, J. M.; LaRochelle, J. R.; Appelbaum, J. S.; Schepartz, A. Improved Assays for Determining the Cytosolic Access of Peptides, Proteins, and Their Mimetics. *Biochemistry* **2013**, *52* (50), 9036–9046. <https://doi.org/10.1021/bi401069g>.

- (12) Duchardt, F.; Fotin-Mleczek, M.; Schwarz, H.; Fischer, R.; Brock, R. A Comprehensive Model for the Cellular Uptake of Cationic Cell-Penetrating Peptides. *Traffic* **2007**, *8* (7), 848–866. <https://doi.org/10.1111/j.1600-0854.2007.00572.x>.
- (13) Nakase, I.; Niwa, M.; Takeuchi, T.; Sonomura, K.; Kawabata, N.; Koike, Y.; Takehashi, M.; Tanaka, S.; Ueda, K.; Simpson, J. C.; Jones, A. T.; Sugiura, Y.; Futaki, S. Cellular Uptake of Arginine-Rich Peptides: Roles for Macropinocytosis and Actin Rearrangement. *Mol. Ther.* **2004**, *10* (6), 1011–1022. <https://doi.org/10.1016/j.ymthe.2004.08.010>.
- (14) Jones, S. W.; Christison, R.; Bundell, K.; Voyce, C. J.; Brockbank, S. M. V.; Newham, P.; Lindsay, M. A. Characterisation of Cell-Penetrating Peptide-Mediated Peptide Delivery. *Br. J. Pharmacol.* **2005**, *145* (8), 1093–1102. <https://doi.org/10.1038/sj.bjp.0706279>.
- (15) Lee, Y.-W.; Luther, D. C.; Kretzmann, J. A.; Burden, A.; Jeon, T.; Zhai, S.; Rotello, V. M. Protein Delivery into the Cell Cytosol Using Non-Viral Nanocarriers. *Theranostics* **2019**, *9* (11), 3280–3292. <https://doi.org/10.7150/thno.34412>.
- (16) Wissner, R. F.; Steinauer, A.; Knox, S. L.; Thompson, A. D.; Schepartz, A. Fluorescence Correlation Spectroscopy Reveals Efficient Cytosolic Delivery of Protein Cargo by Cell-Permeant Miniature Proteins. *ACS Cent. Sci.* **2018**, *4* (10), 1379–1393. <https://doi.org/10.1021/acscentsci.8b00446>.

## CHAPTER 5

### Cytosolic Delivery of Argininosuccinate Synthetase Using a Cell-Permeant Miniature Protein

Parts of this chapter are included in

Knox, S. L.; Wissner, R.; Piszkiwicz, S.; Schepartz, A. **Cytosolic Delivery of Argininosuccinate Synthetase Using a Cell-Permeant Miniature Protein.** *ACS Cent. Sci.* **2021**, 7 (4), 641-649. <https://pubs.acs.org/doi/10.1021/acscentsci.0c01603>.

and are adapted with permission from all co-authors. Further permissions related to the material excerpted should be directed to the ACS.

## 5.1 Abstract

Citrullinemia type I (CTLN-I) results from the absence or deficiency of argininosuccinate synthetase (AS), a 46 kD enzyme that acts in the cytosol of hepatocytes to convert aspartic acid and citrulline into argininosuccinic acid. AS is an essential component of the urea cycle, and its absence or deficiency results in the harmful accumulation of ammonia in blood and cerebrospinal fluid. No disease-modifying treatment of CTLN-I exists. Here we report that the cell-permeant miniature protein (CPMP) ZF5.3 (ZF) can deliver AS to the cytosol of cells in culture and the livers of healthy mice. The fusion protein ZF-AS is catalytically active *in vitro*, stabilized in plasma, and traffics successfully to the cytosol of cultured Saos-2 and SK-HEP-1 cells, achieving cytosolic concentrations greater than 100 nM. This value is between 3–10-fold higher than the concentration of endogenous AS ( $11 \pm 1$  to  $44 \pm 5$  nM). When injected into healthy C57BL/6 mice, ZF-AS reaches the mouse liver to establish concentrations almost 200 nM above baseline. These studies demonstrate that ZF5.3 can deliver a complex protein enzyme to the cytosol at therapeutically relevant concentrations and support its application as an improved delivery vehicle for therapeutic proteins that function in the cytosol, including enzyme replacement therapies.

## 5.2 Introduction

Protein-based drugs represent the fastest growing segment of the modern-day pharmacopeia. More than one quarter of all new drugs approved over the past three years are biologics.<sup>1</sup> These new molecular entities—which include antibodies, antibody-drug conjugates, cytokines, fusion proteins, growth factors, and enzymes—treat diseases ranging from lymphomas to macular degeneration to asthma, and are projected to account for 35% of the global pharmaceutical revenue by 2025.<sup>2,3</sup> Yet despite this enormous impact on human health, the full potential of protein therapeutics cannot yet be realized for one simple reason: most proteins cannot readily reach the cell interior – the cytosol. This singular limitation hinders the development of protein therapeutics that replace, inhibit, or activate therapeutic targets within the cytosol, nucleus, or interior organelles. Although it has been thirty years since the first reports of cell penetration by the HIV protein known as Tat,<sup>4,5</sup> the reality is that most proteinaceous materials are taken up by cells into the endocytic pathway, and within the endocytic pathway they remain.<sup>6,7</sup> There is little question that a more complete understanding of the mechanisms by which proteinaceous materials escape endosomes would accelerate the design of next-generation protein therapeutics that effectively target the large fraction of the proteome that remains undruggable.<sup>8</sup>

The enormous interest in promoting protein delivery has led to multiple reports of peptide-based materials capable of “endosomal release”.<sup>6,7</sup> Unfortunately, few of these reports compare different delivery vehicles under identical conditions and in a manner that allows a direct and quantitative assessment of how much material reaches the cytosol.<sup>9</sup> Fewer still evaluate whether the material that reaches the cytosol remains intact. Recently it was reported that the cell-permeant miniature protein (CPMP) ZF5.3

(ZF) traffics with unprecedented efficiency to the cytosol and nucleus without cytotoxic effects,<sup>8,10,11</sup> even when fused to protein cargo.<sup>9</sup> A head-to-head comparison of seven putative cell-penetrating peptides (CPPs), macrocycles<sup>12</sup>, and CPMPs as delivery vehicles for the model cargo SNAP-tag (188 aa, 20 kD) established that the CPMP ZF5.3<sup>8,10,11</sup> could deliver SNAP-tag to the cytosol at concentrations 2- to 9-fold higher than any other vehicle tested.<sup>9</sup> Subsequent work showed that the efficacy of ZF5.3 as a delivery vehicle may be related to a previously unrecognized portal for endosomal escape that demands the homotypic fusion and vacuole protein sorting (HOPS) complex, an essential component of the endocytic machinery.<sup>8</sup> These studies provide evidence that ZF5.3-enzyme fusions can escape endosomes with unprecedented efficiency, and suggest that they do so *via* a defined and underexploited mechanism. Here we ask whether ZF5.3 can deliver a therapeutically relevant cargo, a complex, multimeric enzyme that is lost or mutated in patients with citrullinemia type 1 (CTLN-1).

The metabolic disorder CTLN-I results from loss or depletion of argininosuccinate synthetase (AS), a tetrameric enzyme that converts citrulline and aspartic acid to argininosuccinic acid within the cytosol of hepatocytes (**Figure 5.1A**).<sup>13</sup> AS is an essential component of the urea cycle, and its absence or deficiency blocks the conversion of ammonia, a byproduct of amino acid catabolism, into urea.<sup>14</sup> Without AS, ammonia accumulates in blood and cerebrospinal fluid, resulting in multiple neurological effects that include permanent brain damage.<sup>15</sup> Current treatments for CTLN-I include diet control, nitrogen scavenger therapy, hemodialysis, and liver transplantation, but all are symptomatic—none of these treatments target the underlying cause of disease.<sup>15</sup> Enzyme replacement therapy would provide a disease-modifying alternative to current symptomatic treatments with the potential to significantly improve patient quality of life. Previous studies have described the delivery of adeno-associated virus (AAV) vectors encoding AS to mice and extracellular vesicles (EVs) containing AS to hepatocytes.<sup>16,17</sup> Although these approaches highlight the feasibility of AS enzyme replacement therapy, obstacles remain that hamper their implementation as therapeutics.<sup>18–24</sup> We hypothesized that fusion of the CPMP ZF5.3 to AS would generate a fusion protein with improved ability to traffic directly into the cell cytosol, an essential first step in circumnavigating concerns with delivery via AAV vectors and EVs.

Here we show that ZF-AS, a fusion protein containing both ZF5.3 and AS, retains the ability to oligomerize, is catalytically active *in vitro*, and resists rapid proteolysis in plasma. Quantitative analysis of intracellular trafficking using fluorescence correlation spectroscopy<sup>11,25</sup> reveals that ZF-AS traffics to the cytosol of Saos-2 and SK-HEP-1 cells to achieve cytosolic concentrations as high as  $111 \pm 19$  nM; this concentration is 3–10-fold higher than the endogenous concentration of AS in mouse liver homogenate ( $11 \pm 1$  to  $44 \pm 5$  nM). When injected into healthy C57BL/6 mice, ZF-AS reaches the mouse liver to achieve concentrations almost 200 nM above baseline. These studies provide proof-of-concept that the CPMP ZF5.3<sup>8–11</sup> can deliver a complex, multimeric enzyme to the cytosol of cultured cells and internal mouse organs.

## 5.3 Results and Discussion

### 5.3.1 Expression, purification, and characterization of AS and ZF-AS

Our first task was to prepare samples of AS and ZF-AS that were suitable for both *in vitro* analysis of enzyme activity and plasma stability as well as the optimization of enzyme-linked immunosorbent (ELISA) assays to detect these materials within serum and liver. The sequence encoding human AS (411 aa, 46.5 kD) and its N-terminal fusion with ZF (27 aa, 3.2 kD) were cloned into a pET-32a expression vector downstream of a His<sub>6</sub>-SUMO tag, overexpressed in BL21-Gold (DE3) competent *E. coli*, and purified by immobilized metal affinity chromatography (IMAC). The SUMO-tag was subsequently removed using SUMO protease<sup>26</sup> and the final materials were purified to ≥ 90% homogeneity using size exclusion chromatography (SEC) (**Figure 5.2A**). Protein identities were confirmed by LC/MS (**Figure 5.2C**). When analyzed by high-resolution preparative gel filtration, AS co-eluted with phosphorylase B (97.2 kD) and aldolase (158 kD) standards (**Figure 5.2D**). ZF-AS eluted slightly earlier than AS and aldolase, suggesting that both AS and ZF-AS assemble predominantly into tetramers in the micromolar concentration range and that the fusion of ZF to the AS N-terminus did not measurably alter the tetramer equilibrium dissociation constant (**Figure 5.2D**).<sup>27</sup>

We next assessed whether ZF-AS could recapitulate the essential biochemical and biophysical metrics associated with AS. Although point mutations near the AS active site (such as A118T and T119I) lead to modest (< 5 °C) decreases in thermal stability ( $T_M$ ) as assessed by differential scanning fluorimetry (wild-type  $T_M$  = 49 °C),<sup>28</sup> no reports describe the effects of N- or C-terminal fusions on thermal stability. The apparent  $T_M$  of purified AS determined by circular dichroism (CD) spectroscopy (48.1 °C) was in line with previous reports (49 °C)<sup>28</sup> and only modestly higher than the value determined for ZF-AS (46.6 °C) under identical conditions (**Figure 5.1B**). Although the melting transitions of both AS and ZF-AS were irreversible, their pre-melt wavelength-dependent CD spectra were virtually identical and consistent with significant  $\alpha$ -helical secondary structure, as expected (**Figure 5.2E**). The time-dependent proteolytic stabilities of AS and ZF-AS in mouse plasma were also virtually identical, with close to 70% fully intact protein remaining after 6 hours (**Figure 5.3**).

Samples of AS<sup>Rho</sup> and ZF-AS<sup>Rho</sup> used for confocal microscopy, flow cytometry, and FCS were prepared in a three-step process. AS and ZF-AS were first expressed as fusion proteins containing both a N-terminal His<sub>6</sub>-SUMO tag and a C-terminal LPETGG tag; these materials were then subjected to a sortase-catalyzed transpeptidation reaction<sup>29–31</sup> with GGGK<sup>Rho</sup>, a tetrapeptide containing Lissamine rhodamine B (Rho) at the C-terminus. To streamline the synthesis, we designed a one-pot reaction to simultaneously remove the His<sub>6</sub>-SUMO tag and append GGGK<sup>Rho</sup> (**Figure 5.4A**) to produce AS<sup>Rho</sup> and ZF-AS<sup>Rho</sup>. Reaction duration, temperature, and buffer composition were varied to optimize yield and purity (**Figure 5.5**); we found that dialyzing SUMO protease, sortase, and AS or ZF-AS into the same HEPES-containing buffer at pH 7 prior to the one-pot reaction resulted in the highest yield of labeled and purified product. Final materials were purified by SEC and analyzed by electrospray mass spectrometry (**Figure 5.4B** and **C**).

### 5.3.2 ZF-AS fusion proteins are catalytically active

Argininosuccinate synthetase (AS) plays a critical role in the segment of primary metabolism known as the urea cycle, which eliminates excess nitrogen through the combined action of six enzymes and two mitochondrial transporters.<sup>32</sup> As the third enzyme in this pathway, AS converts aspartic acid, citrulline, and ATP into argininosuccinic acid.<sup>32</sup> The two-step enzymatic reaction leads ultimately to the release of argininosuccinic acid, PP<sub>i</sub>, and AMP (**Figure 5.1A**), and can be followed spectrophotometrically by monitoring the release of either pyrophosphate or AMP.<sup>33</sup> Historically, AS activity has been quantified using a discontinuous assay that monitors urea production<sup>34</sup> or citrulline utilization,<sup>35</sup> or continuously by monitoring the pyrophosphate-dependent oxidation of nicotinamide adenine dinucleotide (NADH).<sup>36</sup> While PP<sub>i</sub> is a byproduct of the initial AS-catalyzed activation of aspartic acid, AMP release occurs only upon formation of the final product argininosuccinic acid. Thus, we chose to monitor release of AMP by coupling its production to NADH oxidation in a well-validated enzyme-linked assay that uses myokinase to convert AMP to ADP (**Figure 5.6**).<sup>37</sup> The catalytic constants determined in this way are summarized in **Table 5.2**.

First we sought to compare the catalytic constants of recombinant AS and ZF-AS to previously determined values for AS isolated from *E. coli* and human or bovine liver.<sup>15,33,38–42</sup> Reported values of  $k_{\text{cat}}$  for AS vary from <0.1 to 1 s<sup>-1</sup>,<sup>33,38,39,41,42</sup> while  $K_{\text{M}}$  values range from 0.01 to 112 μM.<sup>33,39–43</sup> The catalytic constants determined for human AS purified from BL21-Gold (DE3) cells fell cleanly within this range, with  $k_{\text{cat}}$  and  $K_{\text{M}}$  values of 0.39 ± 0.01 s<sup>-1</sup> and 52 ± 5 μM, respectively (**Figure 5.1C–E**, **Figure 5.6E**). The catalytic constants determined for ZF-AS also fell in this range, with respect to both  $k_{\text{cat}}$  (0.16 ± 0.01 s<sup>-1</sup>) and  $K_{\text{M}}$  (33 ± 10 μM), although we note that the  $k_{\text{cat}}$  measured for ZF-AS is 2.4-fold lower than that of AS. Heat-denaturation of AS and ZF-AS at 95 °C led to completely inactive enzymes, with no significant time-dependent change in absorbance at 340 nm for either sample (**Figure 5.6F**). The kinetic constants of AS<sup>Rho</sup> and ZF-AS<sup>Rho</sup> also fell within the expected ranges, with  $k_{\text{cat}}$  values of 0.44 ± 0.02 s<sup>-1</sup> and 0.32 ± 0.05 s<sup>-1</sup> and  $K_{\text{M}}$  values of 34 ± 8 μM and 6 ± 8 μM, respectively, for AS<sup>Rho</sup> and ZF-AS<sup>Rho</sup>. Although the AS C-terminus participates in hydrophobic interactions and a single salt bridge within the tetrameric complex visualized by crystallography,<sup>27</sup> the uniformity of the kinetic constants determined for ZF-AS, AS<sup>Rho</sup>, and ZF-AS<sup>Rho</sup> indicate that the enzyme tolerates the addition of ZF to the N-terminus and the addition of a LPETGGGK<sup>Rho</sup> tag to the C-terminus. Overall, these kinetic studies provide confidence that both ZF-AS and ZF-AS<sup>Rho</sup> can process aspartic acid and citrulline into argininosuccinic acid *in vitro*. In addition to the activity studies described here, we confirmed that ZF-AS and AS displayed comparable catalytic activities when spiked into a liver homogenate (**Figure 5.7**).

### 5.3.3 Evaluation of uptake by Saos-2 cells using flow cytometry and confocal microscopy

With purified, catalytically active, Rho-labeled materials in hand, we turned to confocal microscopy and flow cytometry to assess the relative uptake of ZF-AS<sup>Rho</sup> and AS<sup>Rho</sup> by Saos-2 cells, which are well-suited for subsequent analysis by fluorescence correlation spectroscopy (FCS).<sup>25</sup> Briefly, cells were treated for 1 h with 1–3 μM purified

ZF-AS<sup>Rho</sup> or AS<sup>Rho</sup>, washed, treated with trypsin to eliminate cell surface-bound material, imaged using confocal microscopy (**Figure 5.8A and B**), and assayed *en masse* via flow cytometry (**Figure 5.8C and D**). When visualized using confocal microscopy, Saos-2 cells show clear evidence of punctate rhodamine fluorescence when treated with increasing concentrations of ZF-AS<sup>Rho</sup> (**Figure 5.9**), whereas little punctate fluorescence is observed in cells treated with AS<sup>Rho</sup> (**Figure 5.8B and Figure 5.9**). The difference in overall uptake is more evident when ZF-AS<sup>Rho</sup>- and AS<sup>Rho</sup>-treated Saos-2 cells are evaluated *en masse* using flow cytometry (**Figure 5.8C and D**). The median fluorescence intensity (MFI) of Saos-2 cells treated with AS<sup>Rho</sup> increases modestly if at all (1.6-fold) as the incubation concentration increases from 1 to 3  $\mu$ M, while the MFI of Saos-2 cells treated with ZF-AS<sup>Rho</sup> increases 7.4-fold over the same concentration range. Overall, treatment of Saos-2 cells for 1 h with ZF-AS<sup>Rho</sup> resulted in higher MFI values than observed when cells were treated with ZF-SNAP<sup>Rho</sup> at all concentrations (1–3  $\mu$ M) and time points (0.5 and 2 h).<sup>9</sup> Although work is still necessary to fully assess the cargo requirements of cytosolic delivery using ZF5.3, it is possible that the higher overall uptake of ZF-AS<sup>Rho</sup> relative to ZF-SNAP<sup>Rho</sup> is related to differences in overall charge that may affect association with the plasma membrane.<sup>44–46</sup>

### 5.3.4 Evaluation of cytosolic trafficking of AS<sup>Rho</sup> and ZF-AS<sup>Rho</sup> using fluorescence correlation spectroscopy (FCS)

After assessing cellular uptake by confocal microscopy and flow cytometry, we used FCS<sup>8,9,25</sup> to track the concentration-dependent endosomal release of ZF-AS<sup>Rho</sup> and AS<sup>Rho</sup> into the cytosol of Saos-2 cells (**Figure 5.8E and Figure 5.10**). These experiments revealed that treatment of Saos-2 cells with 1 to 3  $\mu$ M ZF-AS<sup>Rho</sup> leads to cytosolic ZF-AS<sup>Rho</sup> concentrations between  $35 \pm 4$  nM and  $111 \pm 19$  nM after 1 h. ZF-AS<sup>Rho</sup> achieves the highest cytosolic concentration at 2  $\mu$ M; the minimal differences between 2  $\mu$ M and 3  $\mu$ M may illustrate saturation of the cellular mechanism required for endosomal release.<sup>8</sup> By contrast, the cytosolic concentrations achieved by AS<sup>Rho</sup> fell between  $26 \pm 6$  nM and  $77 \pm 30$  nM and were not dose-dependent. The largest difference in cytosolic concentrations achieved by AS<sup>Rho</sup> and ZF-AS<sup>Rho</sup> (4-fold) was observed at an incubation concentration of 3  $\mu$ M. It is notable that the cytosolic concentrations achieved by ZF-AS<sup>Rho</sup> are lower than previously observed for ZF-SNAP<sup>Rho</sup>, even at shorter incubation times.<sup>9</sup> This difference may reflect the fact that ZF-AS<sup>Rho</sup> is a tetramer of 49.9 kD monomers and ZF-SNAP<sup>Rho</sup> is a monomer (23.3 kD). Cytosolic fractionation experiments confirmed that ZF-AS<sup>Rho</sup> remains intact when delivered to the cytosol of Saos-2 cells (**Figure 5.11**).

We also assessed whether cytosolic delivery of ZF-AS<sup>Rho</sup> demanded a covalent linkage between AS and ZF5.3. Specifically, we evaluated whether ZF5.3 (unadorned by a fluorescent tag) would increase the ability of AS<sup>Rho</sup> to (1) localize within the endosomal pathway (“uptake”); and (2) reach the cytosol (“endosomal release”). Saos-2 cells were incubated for 1 h with 1  $\mu$ M AS<sup>Rho</sup> plus 0–1  $\mu$ M ZF5.3; the total cellular uptake of AS<sup>Rho</sup> was determined by flow cytometry and the concentration of AS<sup>Rho</sup> in the cytosol was determined using FCS (**Figure 5.12A**). Increasing amounts of ZF5.3 led to a dose-dependent increase in the total cellular uptake of AS<sup>Rho</sup> (**Figure 5.12B**) but no

change in the amount of AS<sup>Rho</sup> that reaches the cytosol (**Figure 5.12C**). These results confirm that efficient cytosolic delivery of ZF5.3-AS demands a covalent linkage between AS and ZF5.3, and are fully consistent with the previous observation that ZF5.3 does not increase the amount of Lys9<sup>Rho</sup> that reaches the cytosol when the two are co-delivered.<sup>8</sup>

### 5.3.5 Evaluation of uptake by SK-HEP-1 cells using flow cytometry and confocal microscopy

Next we turned to SK-HEP-1 cells, human hepatic adenocarcinoma cells that naturally express low levels of AS, providing a disease-relevant system.<sup>47</sup> SK-HEP-1 cells were treated with between 0.5 and 3  $\mu$ M ZF-AS<sup>Rho</sup> or AS<sup>Rho</sup> for 1 or 2 h, washed, treated with trypsin, and evaluated using confocal microscopy, flow cytometry, and FCS (**Figure 5.13**, **Figure 5.14**, **Figure 5.15A** and **B**). Cells treated with AS<sup>Rho</sup> show no increase in punctate fluorescence with incubation time but a minimal increase with respect to concentration (**Figure 5.14**). By contrast, ZF-AS<sup>Rho</sup> showed both time- and dose-dependent increases in punctate fluorescence (**Figure 5.14**). The median fluorescence intensity (MFI) of cells treated with 0.5 to 3  $\mu$ M AS<sup>Rho</sup> increased modestly from  $4540 \pm 50$  to  $6860 \pm 110$  AU over this concentration range, whereas the MFI of cells treated with analogous concentrations of ZF-AS<sup>Rho</sup> exhibited dose dependency and increased from  $11000 \pm 1000$  AU to a maximum of  $38000 \pm 2000$  AU (**Figure 5.13C** and **E**). The decrease in overall uptake at 3  $\mu$ M could be the result of cell death (**Figure 5.15C**). The overall uptake of both AS<sup>Rho</sup> and ZF-AS<sup>Rho</sup> was also time-dependent, as observed previously,<sup>9</sup> with higher uptake observed at longer incubation times (**Figure 5.13E**).

### 5.3.6 Evaluation of cytosolic trafficking of AS<sup>Rho</sup> and ZF-AS<sup>Rho</sup> in SK-HEP-1 cells using FCS

After assessing cellular uptake by confocal microscopy and flow cytometry, we used FCS<sup>8,9,25</sup> to track the endosomal release of ZF-AS<sup>Rho</sup> and AS<sup>Rho</sup> by monitoring the concentration of each protein within the SK-HEP-1 cytosol as a function of dose (1–3  $\mu$ M) and time (1–2 h) (**Figure 5.13A** and **Figure 5.15D**). These experiments revealed several important observations. First, the FCS data revealed that AS<sup>Rho</sup> itself reaches the SK-HEP-1 cytosol more efficiently than previously studied proteins lacking ZF.<sup>9</sup> The concentration of AS<sup>Rho</sup> in the cytosol averages  $47 \pm 6$  nM, which is 24-fold larger than that achieved by SNAP-tag<sup>Rho</sup> under comparable conditions ( $2 \pm 1$  nM in Saos-2 cells) despite the difference in molecular mass.<sup>9</sup> Importantly, the amount of AS<sup>Rho</sup> that traffics into the cytosol is independent of both dose (0.5–3  $\mu$ M) and incubation time (1–2 h). Second, the improvements in cytosolic trafficking of AS due to ZF (no significant differences at 2 and 3  $\mu$ M) are smaller than previously observed for the model protein SNAP-tag (approximately 2.3-fold at 2 and 3  $\mu$ M).<sup>9</sup> At lower concentrations the dose-response was non-linear, with maximal cytosolic concentrations of ZF-AS<sup>Rho</sup> observed at 1  $\mu$ M with a 1 h incubation (**Figure 5.13F**). ZF-AS<sup>Rho</sup> reaches the SK-HEP-1 cytosol at concentrations greater than 50  $\mu$ M under all experimental conditions, whereas a 3  $\mu$ M dose is required for AS<sup>Rho</sup> to reach this threshold. A final observation is that there are

subtle cell line-dependent differences; in Saos-2 cells, an incubation concentration of 2  $\mu\text{M}$  led to the highest cytosolic concentration of ZF-AS<sup>Rho</sup>, whereas only 1  $\mu\text{M}$  dose was required to reach this concentration in SK-HEP-1 cells. Taken together, these data indicate that ZF can transport AS into the cytosol of multiple cell lines to achieve concentrations that approximate that of endogenous AS in a healthy C57BL/6 mouse liver (**Figure 5.16**). We note that the presence of Zn<sup>2+</sup> is essential for delivery of ZF-AS: when prepared in the absence of Zn<sup>2+</sup>, the concentration of ZF-AS<sup>Rho</sup> that reaches the cytosol falls to the level achieved by AS<sup>Rho</sup> alone (**Figure 5.15E and F**). This finding is consistent with previous reports that disruption of the  $\alpha$ -helix in aPP5.3 also lowers delivery efficiency.<sup>48</sup>

### 5.3.7 Endotoxin Analysis and Removal

The outer membrane of Gram-negative bacteria such as *E. coli* is replete with lipopolysaccharides (LPS) known as endotoxins.<sup>49</sup> LPS is released from lysed bacteria<sup>50</sup> and can co-purify with proteins isolated from *E. coli*.<sup>51,52</sup> Interaction of the hexa-acyl chain of LPS with Toll-like receptor 4 (TLR4) in complex with myeloid differentiation factor 2 (MD-2) activates the innate immune response in mammalian cells and can cause myriad detrimental effects, including cytokine storm.<sup>53–56</sup> Indeed, AS has been reported to itself bind LPS.<sup>13,57</sup> Our experiments necessitated that endotoxin levels be reduced to less than five endotoxin units (EU) per kilogram of mouse (1 EU/mL protein) prior to animal studies.<sup>58–60</sup> We initially quantified endotoxin levels using a *Limulus* amoebocyte lysate (LAL), which exploits the endotoxin binding activity of Factor C in the innate immune response of horseshoe crabs.<sup>61</sup> Using the LAL assay, we quantified the level of endotoxin contamination in samples of AS and ZF-AS isolated from BL21-Gold (DE3) cells (**Figure 5.17A–C**). This assay revealed endotoxin levels of  $9.3 \pm 1.1$  EU/mL (AS) and  $9.6 \pm 0.3$  EU/mL (ZF-AS), significantly higher than those in MilliQ water and buffer ( $0.068 \pm 0.001$  and  $0.067 \pm 0.000$  EU/mL, respectively), limiting the potential dose in a mouse study to  $<1$   $\mu\text{M}$  (0.25 mg/kg).

We made use of the engineered BL21(DE3) *E. coli* strain ClearColi® and extensive wash steps to reduce the endotoxin contamination of AS and ZF-AS in preparation for animal studies (**Figure 5.18A**). ClearColi® lacks multiple genes required for lipid A biosynthesis ( $\Delta\text{gutQ}$ ,  $\Delta\text{kdsD}$ ,  $\Delta\text{lpxL}$ ,  $\Delta\text{lpxM}$ ,  $\Delta\text{pagP}$ ,  $\Delta\text{lpxP}$ , and  $\Delta\text{etpA}$ ).<sup>53,62</sup> To evaluate the level of endotoxin contamination in materials generated in ClearColi®, we used an engineered HEK293 cell line (HEK-Blue™ hTLR4, InvivoGen) that reports on the direct interaction of endotoxin with TLR4 and MD-2 of the innate immune system with a chromophore that is monitored at 640 nm (**Figure 5.18B**).<sup>55,56,63,64</sup> We first assessed the endotoxin levels of the SUMO protease used during the purification workflow of AS and ZF-AS (**Figure 5.18C**). The endotoxin levels in the SUMO protease samples decreased from  $59 \pm 6$  EU/mL for material expressed in BL21-Gold (DE3) cells to  $0.03 \pm 0.02$  EU/mL for material produced in ClearColi®, a 2,000-fold reduction. In T7 Express cells, just an additional wash step decreased endotoxin levels almost 60-fold.

We next assessed the levels of endotoxin contamination in samples of AS and ZF-AS expressed in different *E. coli* strains (**Figure 5.18C**). Expression of AS and ZF-

AS in ClearColi® led to endotoxin levels that were reduced by 16,500-fold (AS) or 2,000-fold (ZF-AS) from levels observed for samples expressed in BL21-Gold (DE3) cells. The level of endotoxin contamination in the final ZF-AS sample ( $0.091 \pm 0.006$  EU/mL) was suitable to allow mouse dosing at 3 mg/kg. The ClearColi®-derived proteins AS and ZF-AS exhibited  $k_{\text{cat}}$  values ( $0.40 \pm 0.02 \text{ s}^{-1}$  and  $0.19 \pm 0.01 \text{ s}^{-1}$ , respectively) similar to the enzymes purified from BL21-Gold (DE3) cells (**Figure 5.1D**). The  $K_M$  values of ClearColi® purified proteins did slightly decrease by 1.6- and 3-fold compared to AS and ZF-AS purified from BL21-Gold (DE3) cells, respectively (**Figure 5.1E**).

### 5.3.8 Delivery to Healthy Mice

With endotoxin-free material in hand, we next asked whether ZF-AS purified from ClearColi® would reach the liver of C57BL/6 mice when administered *in vivo*. A set of thirty C57BL/6 mice were injected intravenously via the tail vein with 3 mg/kg ZF-AS (15 mice) or vehicle (phosphate buffered saline (pH 7.4)) (15 mice), and the time-dependent concentrations of AS-containing proteins in serum and liver were evaluated using organ-specific ELISAs detecting an internal AS epitope (**Figure 5.19**). These assays were optimized to quantify dilutions of ZF-AS at concentrations between 1.6 and 200 nM (in serum) and 0.1 and 6.0 nM (in liver) (**Figure 5.20**). Mice injected with 3 mg/kg ZF-AS showed a total ZF-AS concentration in serum of  $390 \pm 1706$  nM ( $19400 \pm 8300$  ng/mL) above baseline (vehicle signal) within the first five minutes of dosing. The rapid loss of ZF-AS from serum observed here is consistent with the previous observation that intravenous injection of 0.11–0.43 mg/kg rat-liver purified AS remains in serum for less than 15 min post-dose.<sup>65</sup> Mice injected with vehicle alone showed an initial liver concentration of AS-containing protein of roughly  $410 \pm 40$  nM ( $19300 \pm 1700$  ng/mL), which was defined as baseline. We note that this value does not rigorously reflect the concentration of endogenous AS in the liver as the ELISA was optimized to quantify ZF-AS, not AS. Mice injected with 3 mg/kg ZF-AS showed a total ZF-AS concentration in the liver of  $190 \pm 60$  nM above baseline at short times; this value decreased to baseline values over the course of 1 h. Although the rapid clearance of ZF-AS from the liver is not ideal, this initial study shows definitively that ZF-AS is non-toxic to mice at 3 mg/kg, stable in plasma, and reaches the liver at concentrations close to 200 nM within 1 h of dosing. Experiments to assess the efficacy of ZF-AS versus AS in an established mouse model for CTLN-I (*Ass1<sup>fold</sup>*.mice)<sup>66</sup> will be described in due course.

### 5.4 Conclusions

Previous work has provided evidence that a fusion of the cell-permeant miniature protein (CPMP) ZF5.3 (ZF) with the small model protein SNAP-tag can enter cells and escape from endosomes with greater efficiency than fusions to either canonical (penetratin) or macrocyclic (CPP9 and CPP12)<sup>12</sup> delivery vehicles.<sup>9</sup> Here we report that ZF is also capable of delivering a large and complex urea cycle enzyme, argininosuccinate synthetase, to the cytosol of cells in culture and the livers of healthy mice. The fusion protein ZF-AS is catalytically active *in vitro*, stabilized in plasma, and traffics successfully and in fully intact form to the cytosol of cultured cells, achieving

cytosolic concentrations greater than 100 nM. This value is between 3–10-fold higher than the concentration of endogenous AS ( $11 \pm 1$  to  $44 \pm 5$  nM). When injected into healthy C57BL/6 mice, ZF-AS reaches the mouse liver at concentrations almost 200 nM above baseline. These studies demonstrate that ZF5.3 can deliver a complex protein enzyme to the cytosol at therapeutically relevant concentrations and support its further development as an improved vehicle for cytosolic enzyme replacement therapies. These studies should also motivate efforts to establish more detailed design rules for protein endosomal escape<sup>11</sup> that are guided by directly quantifying delivery efficiency, not activity.

## 5.5 Methods

### 5.5.1 Materials

#### *Plasmid Design, Protein Expression, and Protein Purification*

DNA primers and gBlocks® for Gibson Assembly® were purchased from Integrated DNA Technologies, Inc (Coralville, IA). A Gibson Assembly® Cloning Kit, Phusion® High-Fidelity DNA Polymerase, deoxynucleotide (dNTP) solution mix, DpnI, T4 polynucleotide kinase, and T4 DNA ligase were purchased from New England BioLabs (Ipswich, MA). DNA sequencing was performed by Quintara Biosciences. *E. coli* BL21-Gold (DE3) cells were purchased from Agilent (Santa Clara, CA). ClearColi® cells were from Lucigen (Middleton, WI). TALON resin was from Takara Bio USA, Inc. (Shiga, Japan). LB Broth Powder (Lennox and Miller), 2M N,N-diisopropylethylamine (DIEA) in N-methylpyrrolidone (NMP), and Lissamine Rhodamine B sulfonyl chloride (mixed isomers) were purchased from Thermo Fisher Scientific (Waltham, MA). Standard Fmoc-protected amino acids (all possessing the L-configuration) were purchased from Novabiochem. Fmoc-Lys(Mtt)-OH, H-Rink Amide-ChemMatrix® resin, Phosphorylase B, aldolase, and ovalbumin were purchased from MilliporeSigma (Burlington, MA). Trifluoroacetic acid (TFA), O-(benzotriazol-1-yl)-N,N,N',N'-tetramethyluronium hexafluorophosphate (HBTU), 1-hydroxybenzotriazole hydrate (HOBt), piperidine, carbenicillin disodium salt, kanamycin sulfate, ampicillin sodium salt, Super Glycerol, HEPES, 1M Tris HCl solution (pH 7.4), and dithiothreitol (DTT) were purchased from AmericanBio (Canton, MA). SOC outgrowth media was purchased from New England BioLabs (Ipswich, MA). Any kD™ Mini-PROTEAN® TGX™ Precast Protein Gels (10- or 15-well) were purchased from Bio-Rad Laboratories (Hercules, CA). All other reagents were obtained from commercial sources and used without further purification, unless otherwise stated.

#### *Plasma Stability Assay*

Plasma was collected from C57BL/6 male mice (containing lithium heparin as the anticoagulant) and supplied by Charles River Laboratories (Wilmington, MA). 10% Mini-PROTEAN® TGX™ Precast Protein Gels (15-well) were purchased from Bio-Rad Laboratories (Hercules, CA). iBlot™ transfer stack (PVDF) were obtained from ThermoFisher Scientific (Waltham, MA). ASS1 (D4O4B) XP® Rabbit mAb #70720 and

HRP-linked anti-Rabbit IgG antibody (7074S) were from Cell Signaling Technology (Danvers, MA). Anti-ASS1 antibody (EPR12399(B)) and Recombinant Anti-ASS1 antibody (EPR12398) were from Abcam (Cambridge, UK). ASS1 antibody (HPA020934) was from MilliporeSigma (Burlington, MA). Anti-SNAP-tag antibody (polyclonal, P9310S) was purchased from New England BioLabs (Ipswich, MA). Milk, non-fat, dry, Omniblock™ was from AmericanBio (Canton, MA). Amersham ECL Prime Western Blotting Detection Reagent was from Cytiva (Marlborough, MA). All other reagents were obtained from commercial sources and used without further purification, unless otherwise stated.

### *Activity Assay*

Beta-nicotinamide adenine dinucleotide reduced disodium salt (NADH) and adenosine-5'-triphosphate (ATP) were purchased from MP Biomedicals (Burlingame, CA). Pyruvate kinase/lactate dehydrogenase enzymes from rabbit muscle and myokinase from rabbit muscle were obtained from Sigma-Aldrich (St. Louis, MO). Adenosine 5'-monophosphate was purchased from Acros Organics (Fair Lawn, NJ). Phosphoenolpyruvic acid monopotassium salt was obtained from Alfa Aesar (Ward Hill, MA). All other reagents were obtained from commercial sources and used without further purification, unless otherwise stated.

### *Liver Homogenate Activity Assay*

C57BL/6 mouse liver was obtained from Charles River Laboratories. L-[U-<sup>14</sup>C] aspartic acid (NEC268E050UC), Optiplate-96 HB (6005290), and Microscint 40 scintillation fluid (6013641) were obtained from Perkin Elmer (Waltham, MA). Tris HCl (T718), adenosine triphosphate (ATP, A2383), KCl (P9333), arginase (A3133), and argininosuccinic acid (A5707) were purchased from Sigma-Aldrich (St. Louis, MO). L-citrulline (110470250) was from Acros (Belgium). Roche (Basel, Switzerland) supplied phosphoenolpyruvate (PEP, P10108294001) and pyruvate kinase (10109045001). 96-well Millipore Multiscreen 0.45 µm Hydrophilic Low Protein Duapore Membrane plates (MAHVN4550) were from Millipore (Burlington, MA). BT AG 50W-X8 Cation Exchange Resin (1435441) was obtained from Bio-Rad (Hercules, CA). All other reagents were obtained from commercial sources and used without further purification, unless otherwise stated.

### *Cell Culture and Assays*

Saos-2 and SK-HEP-1 cells were purchased from American Type Culture Collection (ATCC, Manassas, VA). McCoy's 5A medium (with and without phenol red), Minimum Essential Medium Eagle (EMEM, with and without phenol red), and fibronectin were purchased from MilliporeSigma (Burlington, MA). Nunc™ Lab-Tek™ I Chambered Coverglass slides (8 Well, 0.8 cm<sup>2</sup>), TrypLE, fetal bovine serum (FBS), Dulbecco's modified eagle medium (DMEM, with and without phenol red), minimum essential media (MEM, with and without phenol red), Hoescht 33342 stain, GlutaMAX, sodium pyruvate, and TrypLE were purchased from Thermo Fisher Scientific (Waltham, MA).

Penicillin/streptomycin and Dulbecco's phosphate-buffered saline (DPBS) were from Life Technologies (Carlsbad, CA). All other reagents were obtained from commercial sources and used without further purification, unless otherwise stated.

### *Endotoxin Testing*

ToxinSensor™ Chromogenic Limulus Amebocyte Lysate (LAL) Endotoxin Assay Kit was obtained from GenScript Biotech (Piscataway, NJ). HEK-Blue™ hTLR4 cells that contained 250X HEK-Blue™ Selection, Normocin™ (50 mg/mL), and HEK-Blue™ Detection were purchased from InvivoGen (San Diego, CA). All other reagents were obtained from commercial sources and used without further purification, unless otherwise stated.

### *Mouse Enzyme-Linked Immunosorbent Assays*

Read Buffer T, Donkey anti-Goat-SulfoTag, and MSD Standard Bind Plate were obtained from MSD (Mumbai, India). Superblock was from ScyTek Laboratories (West Logan, UT). ASS1 (D4O4B) XP® Rabbit mAb #70720 was from Cell Signaling Technology (Danvers, MA). ASS1 Polyclonal Primary Antibody was from Thermo Fisher Scientific (Waltham, MA). All other reagents were obtained from commercial sources and used without further purification, unless otherwise stated.

## **5.5.2 Equipment**

For plasmid and fluorophore quantification, a ND-1000 spectrophotometer (NanoDrop) was used. An Allegra X-14R Centrifuge (VWR) was used for protein purification. ChemiDoc MP and ChemiDoc XRS (Bio-Rad) instruments were used for imaging SDS-PAGE gels and Western blots. AKTA Pure FPLC (Cytiva, with a HiLoad™ Superdex 200 16/600 pg column) was utilized for protein purification. A Biotage Initiator+ Alstra (Biotage) and HPLC (Agilent, using a semiprep Grace Vydac C18 (218TP) column) were used for peptide synthesis and purification. A LC-MS Waters Xevo QTOF high-resolution MS was used for identification of argininosuccinate synthetase (AS) and ZF5.3-AS (ZF-AS) and a Waters Synapt G2-Si mass spectrometer equipped with an electrospray ionization source was used for identification of AS<sup>Rho</sup> and ZF-AS<sup>Rho</sup>. Circular dichroism studies were completed with a Circular Dichroism Spectrometer (Aviv). The iBlot™ Transfer System (Thermo Fisher Scientific) was used for Western blots. A Synergy 2 Plate Reader (BioTek) was utilized for enzyme activity studies. A Packard Topcount NxT (PerkinElmer) was used for scintillation counting. For cellular uptake, confocal microscopy, and fluorescence correlation spectroscopy, an Attune NxT Flow Cytometer (Thermo Fisher Scientific) and LSM 880 (Zeiss) were used. Finally, the enzyme-linked immunosorbent assays were analyzed on a MSD Sector Imager (MSD).

## **5.5.3 Sequences of Expressed Proteins**

Note that ZF5.3 is abbreviated as ZF.

### **His<sub>6</sub>-SUMO-AS Protein Sequence**

MHHHHHHSDSEVNQEAKPEVKPEVKPETHINLKVSDGSSEIFFKIKKTTPLRRLMEAF  
KRQGKEMDSLRFYLDGIRIQADQTPEDLDMEDNDIIEAHREQIGGMSSKGSVVLAYSG  
GLDTSCILVWLKEQGYDVIAYLANIGQKEDFEEARKKALKLGAKKVFIEDVSREFVEEFI  
WPAIQSSALYEDRYLLGTSLARPCIARKQVEIAQREGAKYVSHGATGKGNDQVRFELS  
CYSLAPQIKVIAPWRMPEFYNRFKGRNDLMEYAKQHGIPIVTPKPNPWSMDENLMHIS  
YEAGILENPKNQAPPGLYTKTQDPAKAPNTPDILEIEFKKGVPVKVTNVKDGTTHTQSL  
ELFMYLNEVAGKHGVGRIDIVENRFIGMKSRIYETPAGTILYHAHLDIEAFTMDREVRK  
IKQGLGLKFAELVYTGFWHSPECECFVRHCIAKSQERVEGKVQVSVLKGQVYILGRES  
LSLYNEELVSMNVQGDYEPTDATGFININSLRLKEYHRLQSKVTAK

### **His<sub>6</sub>-SUMO-ZF5.3-AS (His<sub>6</sub>-SUMO-ZF-AS) Protein Sequence**

MHHHHHHSDSEVNQEAKPEVKPEVKPETHINLKVSDGSSEIFFKIKKTTPLRRLMEAF  
KRQGKEMDSLRFYLDGIRIQADQTPEDLDMEDNDIIEAHREQIGGYSCNVCGKAFVLS  
RHLNRHLRVHRRATGSGMSSKGSVVLAYSGGLDTSCILVWLKEQGYDVIAYLANIGQK  
EDFEEARKKALKLGAKKVFIEDVSREFVEEFIWPAIQSSALYEDRYLLGTSLARPCIARK  
QVEIAQREGAKYVSHGATGKGNDQVRFELSCYSLAPQIKVIAPWRMPEFYNRFKGRN  
DLMEYAKQHGIPIVTPKPNPWSMDENLMHISYEAGILENPKNQAPPGLYTKTQDPAK  
PNTPDILEIEFKKGVPVKVTNVKDGTTHTQSLLELFMYLNEVAGKHGVGRIDIVENRFIGM  
KSRIYETPAGTILYHAHLDIEAFTMDREVRKIKQGLGLKFAELVYTGFWHSPECECFVR  
HCIAKSQERVEGKVQVSVLKGQVYILGRESPLSLYNEELVSMNVQGDYEPTDATGFINI  
NSLRLKEYHRLQSKVTAK

### **His<sub>6</sub>-SUMO-AS-LPETGG Protein Sequence**

MHHHHHHSDSEVNQEAKPEVKPEVKPETHINLKVSDGSSEIFFKIKKTTPLRRLMEAF  
KRQGKEMDSLRFYLDGIRIQADQTPEDLDMEDNDIIEAHREQIGGMSSKGSVVLAYSG  
GLDTSCILVWLKEQGYDVIAYLANIGQKEDFEEARKKALKLGAKKVFIEDVSREFVEEFI  
WPAIQSSALYEDRYLLGTSLARPCIARKQVEIAQREGAKYVSHGATGKGNDQVRFELS  
CYSLAPQIKVIAPWRMPEFYNRFKGRNDLMEYAKQHGIPIVTPKPNPWSMDENLMHIS  
YEAGILENPKNQAPPGLYTKTQDPAKAPNTPDILEIEFKKGVPVKVTNVKDGTTHTQSL  
ELFMYLNEVAGKHGVGRIDIVENRFIGMKSRIYETPAGTILYHAHLDIEAFTMDREVRK  
IKQGLGLKFAELVYTGFWHSPECECFVRHCIAKSQERVEGKVQVSVLKGQVYILGRES  
LSLYNEELVSMNVQGDYEPTDATGFININSLRLKEYHRLQSKVTAKLPETGG

### **His<sub>6</sub>-SUMO-ZF5.3-AS-LPETGG Protein Sequence**

MHHHHHHSDSEVNQEAKPEVKPEVKPETHINLKVSDGSSEIFFKIKKTTPLRRLMEAF  
KRQGKEMDSLRFYLDGIRIQADQTPEDLDMEDNDIIEAHREQIGGYSCNVCGKAFVLS  
RHLNRHLRVHRRATGSGMSSKGSVVLAYSGGLDTSCILVWLKEQGYDVIAYLANIGQK  
EDFEEARKKALKLGAKKVFIEDVSREFVEEFIWPAIQSSALYEDRYLLGTSLARPCIARK  
QVEIAQREGAKYVSHGATGKGNDQVRFELSCYSLAPQIKVIAPWRMPEFYNRFKGRN  
DLMEYAKQHGIPIVTPKPNPWSMDENLMHISYEAGILENPKNQAPPGLYTKTQDPAK  
PNTPDILEIEFKKGVPVKVTNVKDGTTHTQSLLELFMYLNEVAGKHGVGRIDIVENRFIGM  
KSRIYETPAGTILYHAHLDIEAFTMDREVRKIKQGLGLKFAELVYTGFWHSPECECFVR  
HCIAKSQERVEGKVQVSVLKGQVYILGRESPLSLYNEELVSMNVQGDYEPTDATGFINI  
NSLRLKEYHRLQSKVTAKLPETGG

### **His<sub>6</sub>-SUMO Protease Protein Sequence**

MHHHHHHLVPELNEKDDDDQVQKALASRENTQLMNRDNIETVRDFKTLAPRRWLNDTI  
IEFFMKYIEKSTPNTVAFNSFFYTNLSERGYQGVRWRMKRKKTQIDKLDKIFTPINLNQS  
HWALGIIDLKKTIGYVDSLNGPNAMSFALDLDLQKYVMEESKHTIGEDFDLIHLDCPQ  
QPNGYDCGIYVCMNTLYGSADAPLDFDYKDAIRMRRFIAHLILTALK

### **Sortase-His<sub>6</sub> Protein Sequence**

MQAKPQIPKDKSKVAGYIEIPDADIKEPVYPGPATREQLNRGVSFAKENQSLDDQNISIA  
GHTFIDRPNYQFTNLKAAKKGSMVYFKVGNETRKYKMTSIRNVKPTAVEVLDEQKGKD  
KQLTLITCDDYNEETGVWETRKIFVATEVKLEHHHHHH

## **5.5.4 Expression and Purification of Proteins**

### *pET-32a Plasmid Construction*

The sequence of argininosuccinate synthetase (AS) from human or ZF-AS with a N-terminal His<sub>6</sub>-SUMO tag were codon optimized for *E. coli* expression, cloned into a linearized pET-32a vector, and expressed in the BL21-Gold (DE3) *E. coli* strain or ClearColi®.

Primers for linearization of commercial pET-32a for Gibson Assembly reactions:<sup>9</sup>

5'-ATGTATATCTCCTTCTTAAAGTTAAACAAAATTATT-3'

5'-TAACAAAGCCCGAAAGGAAG-3'

Primers for insertion of C-terminal LPETGG tag using pET32a\_His<sub>6</sub>-SUMO-AS or pET32a\_His<sub>6</sub>-SUMO-ZF-AS:

Forward: TTGCCTGAGACAGGTGGATAACAAAGCCCGAAAGGAAG

Reverse: CTTTGCTGTCACTTTGGATTG

### *Transformation of Proteins in BL21-Gold (DE3) Cells*

1 µL of plasmid (concentrations ≥100 ng/µL) containing either His<sub>6</sub>-SUMO-AS, His<sub>6</sub>-SUMO-ZF-AS, His<sub>6</sub>-SUMO-AS-LPETGG, His<sub>6</sub>-SUMO-ZF-AS-LPETGG, His<sub>6</sub>-SUMO protease, or Sortase-His<sub>6</sub> were added to a thawed tube of BL21-Gold (DE3) cells and incubated on ice for 15 min. The cells were heat shocked at 42 °C for 30 s and put back onto ice for 2 min. 450 µL of SOC outgrowth media were added and the cells recovered for 1 h at 37 °C and 200 RPM. 150 µL of the recovered cells were added to carbenicillin or kanamycin containing agar plates and incubated at 37 °C overnight.

### *Expression of AS Containing Proteins in BL21-Gold (DE3) Cells*

His<sub>6</sub>-SUMO-AS, His<sub>6</sub>-SUMO-ZF-AS, His<sub>6</sub>-SUMO-AS-LPETGG, and His<sub>6</sub>-SUMO-ZF-AS-LPETGG were expressed in BL21-Gold (DE3) *E. coli*. For each L expressed, one starter culture containing 5 mL LB Lennox, 5 µL 1000X carbenicillin, and 1 colony of the respective bacteria containing the appropriate plasmid was prepared. These cultures incubated at 37 °C and 200 RPM for 3.5 h. After the initial incubation, the starter culture was added to 1 L of LB Lennox and 100 mg of ampicillin; the bacteria incubated at 37 °C and 200 RPM until the OD<sub>600</sub> reached 0.6–0.8. At this time, the cultures were

inoculated with 1 mM IPTG and the temperature was reduced to 18 °C. Expression occurred overnight.

#### *Purification of AS Containing Proteins in BL21-Gold (DE3) Cells*

The following buffers were used for purification: stock buffer (50 mM sodium phosphate monobasic monohydrate, 300 mM NaCl, 10% glycerol, pH 7.5), wash buffer (stock buffer + 1 mM DTT), elution buffer (stock buffer + 1 mM DTT and 250 mM imidazole), and dialysis buffer (30 mM HEPES, 500 mM NaCl, 1 mM DTT, 10% glycerol, pH 7.5, and 100  $\mu$ M ZnCl<sub>2</sub> for ZF-containing constructs). The overnight cell culture was spun down for 30 min at 4000 RPM and 4 °C; the supernatant was removed. Cell pellets were resuspended in 15 mL of wash buffer (1 tablet cOmplete, mini EDTA-free protease inhibitor cocktail (Sigma-Aldrich, St. Louis, MO) was added per L of culture). The lysate was sonicated for 8 min total (30 s on, 30 s off) at 30% duty cycle. The lysate was cleared by centrifugation for 45 min at 4 °C and 10,000 RPM. 1 mL fractions of Talon resin were added to Eppendorf tubes (3 mL of Talon resin/L of culture). These were centrifuged at max speed for 3 min and the supernatant was removed. The lysate was combined with the Talon resin and added to a 50 mL Falcon tube. The tube rotated on a rotisserie at 4 °C for 1 h. The slurry was added to a column and the flowthrough was drained (flowthrough was collected in a 50 mL Falcon tube for SDS-PAGE). The resin was washed 3X with 30 mL wash buffer. Each wash step was collected for SDS-PAGE analysis. The protein was eluted with 3 X 5 mL fractions of elution buffer. SDS-PAGE samples were prepared of the elution fractions as well as for other steps of the purification (20  $\mu$ L sample + 5  $\mu$ L 5X SDS-page loading dye). SDS-PAGE was completed (200 V for 25–30 min). Fractions containing protein were combined and dialyzed overnight at 4 °C. The following day, the protein was concentrated using Amicon spin filters (10 or 30 kDa MWCO) and subsequently quantified using Pierce™ 660 nm reagent. Protein was stored at -80 °C until further use. His<sub>6</sub>-SUMO-AS yielded 7.3 mg/L culture, His<sub>6</sub>-SUMO-ZF-AS yielded 2.7 mg/L culture, His<sub>6</sub>-SUMO-AS-LPETGG yielded 5.4 mg/L culture, and His<sub>6</sub>-SUMO-ZF-AS-LPETGG yielded 6.3 mg/L culture.

#### *Expression of His<sub>6</sub>-SUMO protease in BL21-Gold (DE3) Cells*

His<sub>6</sub>-SUMO protease was expressed in BL21-Gold (DE3) *E. coli*. For each L expressed, one starter culture containing 5 mL LB Lennox, 5  $\mu$ L 1000X carbenicillin, and 1 colony of the respective bacteria containing the appropriate plasmid was prepared. These cultures incubated at 37 °C and 200 RPM for 3.5 h. After the initial incubation, the starter culture was added to 1 L of LB Miller and 100 mg of ampicillin; the bacteria incubated at 37 °C and 200 RPM until the OD<sub>600</sub> reached 0.6–0.8. At this time, the cultures were inoculated with 1 mM IPTG and the temperature was reduced to 18 °C. Expression occurred overnight.

#### *Purification of His<sub>6</sub>-SUMO protease in BL21-Gold (DE3) Cells*

The following buffers were used for purification: resuspension buffer (50 mM HEPES (pH 8), 150 mM NaCl, 10% glycerol), wash buffer (50 mM HEPES (pH 8), 500 mM NaCl, 10% glycerol), elution buffer (50 mM HEPES (pH 8), 150 mM NaCl, 250 mM imidazole, 10% glycerol), and dialysis buffer (50 mM HEPES (pH 7), 500 mM NaCl, 10% glycerol, 1 mM DTT). Since this enzyme is a protease, no protease inhibitors were incorporated into the purification. The protein was kept on ice to prevent degradation. Overnight cultures were spun down at 4300 RPM for 30 min at 4 °C. The supernatant was removed and the cell pellet was resuspended in resuspension buffer. The cell slurry was sonicated for 8 min (cycles of 30 s on/30 s off) at 30% duty cycle. The cell lysate was added to a 50 mL Falcon tube and centrifuged for 45 min at 10,000 RPM and 4 °C. 1 mL fractions of Talon resin were added to Eppendorf tubes (3 mL of Talon resin/L of culture). These were centrifuged at max speed for 3 min and the supernatant was removed. The lysate was combined with the Talon resin and put into a 50 mL Falcon tube. The tube rotated on a rotisserie at 4 °C for 1 h. The slurry was added to a column and the flowthrough was drained (flowthrough was collected in a 50 mL Falcon tube for SDS-PAGE analysis). The resin was washed 4X with 20 mL of wash buffer. Each wash step was collected for SDS-PAGE and future analysis. The protein was eluted with 3 X 5 mL fractions of elution buffer. SDS-PAGE samples were prepared of the elution fractions as well as for other steps of the purification (20 µL sample + 5 µL 5X SDS-page loading dye). SDS-PAGE was completed (200 V for 25 min). Fractions containing protein were combined and dialyzed overnight at 4 °C. The following day, the protein was concentrated using Amicon spin filters (10 kDa MWCO) and subsequently quantified using Pierce™ 660 nm reagent. Protein was stored at -80 °C until further use.

### *SUMO Cleavage*

SUMO protease was added in 1.14 molar excess to a His<sub>6</sub>-SUMO-containing protein (His<sub>6</sub>-SUMO-AS or His<sub>6</sub>-SUMO-ZF-AS) in a 3–5 mL reaction volume (30 mM HEPES pH 7.5, 500 mM NaCl, and 10% glycerol). The reaction occurred for 4 h at room temperature. Any precipitation that occurred was spun down and only supernatant was concentrated for size exclusion chromatography (SEC).

### *Expression and Purification of SNAP-tag-His<sub>6</sub> in BL21-Gold (DE3) Cells*

SNAP-tag-His<sub>6</sub> was expressed and purified as detailed in Wissner *et al.*<sup>9</sup>

### *Expression of Sortase-His<sub>6</sub> in BL21-Gold (DE3) Cells*

Sortase was cloned into a pET30b vector as a C-terminal His<sub>6</sub> fusion protein. Sortase was expressed in BL21-Gold (DE3) *E. coli*. For each L expressed, one starter culture containing 5 mL LB Lennox, 5 µL 1000X kanamycin, and 1 colony of the respective bacteria containing the appropriate plasmid was prepared. These cultures incubated at 37 °C and 200 RPM for 3.5 h. After the initial incubation, the starter culture was added to 1 L of LB Miller and 100 mg of kanamycin; the bacteria incubated at 37 °C and 200 RPM until the OD<sub>600</sub> reached 0.5–0.6. At this time, the cultures were inoculated

with 0.5 mM IPTG and the temperature was reduced to 30 °C. Expression occurred overnight.

#### *Purification of Sortase-His<sub>6</sub>*

The following buffers were used for purification: resuspension buffer (20 mM Tris pH 7.4, 150 mM NaCl, 10% glycerol), wash buffer (20 mM Tris pH 7.4, 500 mM NaCl, 10 mM imidazole, 10% glycerol), elution buffer (20 mM Tris pH 7.4, 150 mM NaCl, 200 mM imidazole, 10% glycerol), and dialysis buffer (50 mM HEPES (pH 7), 500 mM NaCl, 10% glycerol, 1 mM DTT). Overnight cultures were spun down at 4300 RPM for 30 min at 4 °C. The supernatant was removed and the cell pellet was resuspended in 20 mL resuspension buffer (also containing 1 protease inhibitor tablet per L LB media). The cell slurry was sonicated for 8 min (cycles of 30 s on/ 30 s off). The cell lysate was added to a 50 mL Falcon tube and centrifuged for 45 min at 10,000 RPM and 4 °C. 1 mL fractions of Talon resin were added to Eppendorf tubes (3 mL of Talon resin/L of culture). These were centrifuged at max speed for 3 min and the supernatant was removed. The lysate was combined with the Talon resin and put into a 50 mL Falcon tube. The tube rotated on a rotisserie at 4 °C for 1 h. The slurry was added to a column and the flowthrough was drained (flowthrough was collected in a 50 mL Falcon tube for SDS-PAGE). The resin was washed 3X (25 mL each) with wash buffer. Each wash step was collected for SDS-PAGE and future analysis. The protein was eluted with 3 X 5 mL fractions of elution buffer. SDS-PAGE samples were prepared of the elution fractions as well as for other steps of the purification (20 µL sample + 5 µL 5X SDS-page loading dye). SDS-PAGE was completed (200 V for 25 min). Fractions containing protein were combined and dialyzed overnight at 4 °C. The following day, the protein was concentrated using Amicon spin filters (10 kDa MWCO) and subsequently quantified using Pierce™ 660 nm reagent. Protein was stored at -80 °C until further use.

#### *Synthesis of GGGK<sup>Rho</sup>*

GGGK<sup>Rho</sup> was synthesized as previously described.<sup>9</sup> Briefly, using a Biotage Altra, Fmoc-Lys(Mtt)-OH was coupled to Rink amide ChemMatrix resin using HBTU, HOBt, and 2M DIEA in NMP, followed by Fmoc deprotection and subsequent coupling of three Fmoc-Gly-OH residues to generate Fmoc-GGGK(Mtt). After the final coupling step, the resin was washed 3X with DMF and then 3X with DCM to shrink the resin. The resin dried overnight at room temperature. To deprotect the Mtt group on the Lys residue, 3% TFA in DCM was added to the vessel (3X, 15 min). The resin was washed 3X alternating between DCM and DMF with a final 3 rinses using DMF. The resin was transferred to a 50 mL round bottom flask. The vessel was flushed with nitrogen and 3 equivalents of Lissamine rhodamine B sulfonyl chloride, DIPEA (6 equiv), anhydrous DMF were added to the vessel to label the peptide overnight at room temperature. The next day, the resin was washed thoroughly with DMF. The Fmoc group of the N-terminal glycine residue was deprotected in 20% piperidine in DMF (2X, 15 min) and subsequently cleaved from the resin using 95% TFA, 2.5% TIPS, and 2.5% water for 3 h. The peptide was ether precipitated, brought up in ACN:H<sub>2</sub>O, and lyophilized.

GGGK<sup>Rho</sup> was purified by HPLC over a Grace Vydac C18 (218TP) column and identified by mass spectrometry.

### *One-Pot Cleavage and Labeling Reaction*

To optimize the concurrent SUMO cleavage and sortase labeling reaction, various concentrations of GGGK<sup>Rho</sup> (200 and 500  $\mu$ M), temperature (4  $^{\circ}$ C, 25  $^{\circ}$ C, 37  $^{\circ}$ C), and time (2–17 h) were assessed (**Figure 5.5**). In addition, buffer composition and pH were analyzed. When all proteins were dialyzed into the same buffer overnight at 4  $^{\circ}$ C (50 mM HEPES, pH 7.0, 10% glycerol, 500 mM NaCl, 1 mM DTT), the labeling reaction was optimal with limited precipitation during the course of the reaction. Final reaction conditions included 35  $\mu$ M desired protein, 40  $\mu$ M SUMO protease, 75  $\mu$ M sortase, and 500  $\mu$ M GGGK<sup>Rho</sup>. To generate AS<sup>Rho</sup>, the reaction took place for 2 h at room temperature. For ZF-AS<sup>Rho</sup>, the reaction took place for 4 h at room temperature. On average, the labeling efficiency for AS<sup>Rho</sup> was 29% and ZF-AS<sup>Rho</sup> was 28%.

### *Size Exclusion Chromatography (SEC)*

A HiLoad<sup>®</sup> 16/600 Superdex<sup>®</sup> 200 pg column (stored and operated at 4  $^{\circ}$ C) was washed with 2 column volumes (CV) of degassed and sterile filtered MilliQ water. The column equilibrated in 30 mM HEPES pH 7.5, 500 mM NaCl, and 10% glycerol (Buffer A) for 1.5 CV. The product of the SUMO cleavage or concurrent cleavage and labeling reaction was concentrated to 500  $\mu$ L and applied to a 5 mL sample loop. The sample loop was washed with 25 mL of Buffer A as the sample was injected onto the column. The system flow rate was 0.2 mL/min and fractions were collected in 0.5 mL aliquots for a total of 1.5 CV. Fractions were analyzed using SDS-PAGE analysis and those containing protein were pooled, concentrated, quantified by Pierce<sup>™</sup> 660 nm reagent, and stored at -80  $^{\circ}$ C. Final protein samples were assessed by SDS-PAGE and purity was determined by densitometry analysis in FIJI (Version 2.0.0).

### *Determination of Labeling Efficiencies for FC and FCS Correction Factors*

The purification scheme described above was unable to separate rhodamine-labeled proteins (denoted as AS<sup>Rho</sup> and ZF-AS<sup>Rho</sup>) from unlabeled, so the calculated labeling efficiencies were used as a correction factor for flow cytometry and FCS studies. AS<sup>Rho</sup> and ZF-AS<sup>Rho</sup> were quantified using Pierce<sup>™</sup> 660 nm reagent. The concentration of appended fluorophore (Lissamine rhodamine B) was calculated by measuring the absorbance of the sample at 670 nm and applying Beer's law (molar absorptivity of Lissamine rhodamine B = 112,000 M<sup>-1</sup> cm<sup>-1</sup>). The ratio of protein:fluorophore was calculated and used as a correction factor in the determination of total cellular uptake and cytosolic concentrations.<sup>25</sup>

### **5.5.5 Determination of Oligomerization State**

The C-terminus of AS is involved in the tetramer formation of the protein.<sup>27</sup> To assess whether appending ZF to the N-terminus affected oligomerization, we compared

the SEC chromatograms using a HiLoad® 16/600 Superdex® 200 pg (**Figure 5.2D**) to standards of ovalbumin (45 kD), phosphorylase B (97.2 kD), and aldolase (158 kD). These standards are close to the sizes of the monomer, dimer, and tetramer forms of AS, respectively. A HiLoad® 16/600 Superdex® 200 pg was washed with filter-sterilized and degassed water for 1.5 CV (180 mL) followed by a 1.5 CV equilibration in 30 mM HEPES (pH 7.5), 500 mM NaCl, 1 mM DTT, 10% glycerol. Prior to addition on the column, each protein solution was centrifuged for 3 min at 21,000 RCF. The supernatant was removed, any pellet discarded, and 200–500 µL of 4 mg/mL standards (ovalbumin, phosphorylase B, and aldolase) were injected onto the AKTA Pure FPLC at 4 °C. 200 µL of ZF-AS (49.9 kD, 3.2 mg/mL) and 300 µL of AS (46.5 kD, 1.9 mg/mL) were injected onto the column. The system flow was set at 0.4 mL/min. The absorbance at 280 nm was monitored as a function of column volume.

### 5.5.6 Circular Dichroism (CD) Analysis

4 mL AS and ZF-AS (at 40 µg/mL) were dialyzed into buffer (50 mM sodium phosphate monohydrate monobasic (pH 7.51), 300 mM NaCl, <10% glycerol, and 1 mM DTT) at 4 °C overnight. Buffer, AS (47.2 µg/mL), or ZF-AS (29.9 µg/mL) were added a 1 cm cuvette containing a stir bar. To obtain initial spectra, wavelength scans were performed from 215–300 nm on buffer, AS, and ZF-AS at 25 °C using an Aviv CD spectrometer. **Figure 5.2E** shows the signal in molar ellipticity for AS and ZF-AS with buffer signal subtracted. For the temperature melt, the signal was monitored at 225 nm from 25 to 65 °C in 5 °C increments. At each temperature, the sample equilibrated for 5 min and the signal was averaged over 1 min prior to collection. Raw data (in  $m^\circ$ ) were converted to molar ellipticity ( $[\Theta]$ , in  $\text{deg}\cdot\text{cm}^2\cdot\text{dmol}^{-1}$ ) by

$$[\Theta] = m^\circ * M / (10 * L * C) \quad \text{Equation 5.1}$$

where M is the mean residual weight (for AS it is 113.49 g/mol, for ZF-AS is it 113.17 g/mol), L is the pathlength of the cuvette (in cm), and C is the concentration of the sample (in g/L).<sup>67</sup> The  $T_M$  was determined by fitting the molar ellipticity as a function of temperature to a Boltzmann sigmoidal curve in Prism (Version 8.4.3)

### 5.5.7 Plasma Stability

#### *Anti-AS Antibody Sensitivity Analysis*

Four commercial anti-AS antibodies were selected (from Sigma, Cell Signaling Technology, and Abcam) that targeted different portions of the AS protein (either the N-terminus, middle of the AS, or C-terminus). Specifically, antibody HPA020934 (Sigma) recognizes a central AS epitope (between residues 164 and 241), antibody ASS1 (D4O4B) XP® Rabbit mAb (Cell Signaling Technology, CST) recognizes an epitope near the C-terminus containing Glu401, antibody Abcam1 (EPR12399(B), Abcam) recognizes an epitope between residues 350 and 411, and antibody Abcam2 (EPR12398, Abcam) recognizes an epitope near the N-terminus of AS. A 2-fold serial dilution of either AS or ZF-AS was prepared (0–100 nM). A gel was run for 1 hr at 150 V with 15 µL of each sample added to the lane (samples prepared with 20 µL of protein

and 5  $\mu\text{L}$  of 5X Laemmli buffer). Western blot analysis was completed for each commercial antibody as described below.

#### *Stability of AS and ZF-AS in Mouse Plasma*

To determine the stability of AS and ZF-AS in mouse plasma, 100 nM of AS, ZF-AS, and SNAP-tag were added to 100% plasma from C57BL/6 mice. The plasma was pre-warmed to 37 °C. The plasma incubated for six hours at 37 °C (samples were parafilmmed to prevent evaporation) and 20  $\mu\text{L}$  samples were prepared for timepoints at 0, 5, 30, 60, 160, 260, and 360 minutes. During each time point, samples were flash frozen in a mixture of acetone/dry ice and stored at -80 °C. All samples were thawed on ice and spun down at max RPM for 3 min and 4 °C. The supernatant was removed and of this, 3  $\mu\text{L}$  of 5X Laemmli buffer were added to 3  $\mu\text{L}$  of supernatant and 9  $\mu\text{L}$  of MilliQ water (final plasma concentration of 25%). To the original sample tube (containing any pellet or insoluble material), 12  $\mu\text{L}$  of denaturing solution (8 M urea and 1% (w/v) sodium dodecyl sulfate) were added; 3  $\mu\text{L}$  of 5X Laemmli buffer were also added. A 10% SDS-PAGE gel was run for 1 h at 150 V with 12  $\mu\text{L}$  of each sample added to the lane. Western blot analysis was completed as described below using the CST C-terminal anti-AS antibody or NEB polyclonal anti-SNAP-tag antibody. Data was analyzed by evaluating densitometry in FIJI (Version 2.0.0). The 0 min time point was used to normalize all other subsequent time points. The samples from the soluble fraction (supernatant) and those from the pellet were normalized separately, and then the normalized values were added together to incorporate total intact AS, ZF-AS, or SNAP-tag protein from both the supernatant and pellet. This sum was normalized to the 0 min time point (defined as 1).

#### *Western Blot Analyses*

SDS-PAGE was completed for the sample. A 5% milk in 1X TBST buffer solution was prepared for use as blocking buffer. The gel was transferred to the iBlot® setup and the blot occurred for 5 min. After 5 min, the blot paper was transferred to a container with the milk solution. The blot was blocked for 1 h at room temperature with shaking. 15 mL of a 1:1000 dilution of anti-AS (or anti-SNAP-tag) antibody were added to the container. The primary antibody solution incubated overnight at 4 °C with shaking. The next day, the primary antibody solution was removed and the blot paper was washed 3X with 1X TBST for 5 min. A 1:1000 dilution of secondary antibody (anti-rabbit IgG-HRP) was prepared in 15 mL of 5% milk. The secondary antibody incubated at room temperature with shaking for 1 h. The primary antibody solution was removed and the blot paper was washed 3X with 1X TBST for 5 min. A 1:1 ratio of HRP substrate and peroxide solution (Amersham ECL Prime Western Blotting Detection Reagent) was prepared, added to the container with the blot paper, and incubated for 5 min with shaking at room temperature. Blots were imaged on a ChemiDoc MP using a chemiluminescent filter and the ladder was imaged using Epi-White illumination.

#### **5.5.8 Activity Assay**

### *Determination of Michaelis-Menten parameters $K_M$ and $k_{cat}$ for AS and ZF-AS catalytic activity*

The catalytic activities of AS and ZF-AS were determined using a continuous spectrophotometric assay described by McMurry *et al.*<sup>37</sup> This coupled assay links the time-dependent production of AMP to the oxidation of NADH and the associated decrease in absorbance at 340 nm (**Figure 5.6A**). Here, the production of AMP by AS or ZF-AS drives the subsequent coupled enzymatic reactions forward: myokinase converts one molecule of AMP to two molecules of ADP; pyruvate kinase uses one molecule of ADP to dephosphorylate phosphoenolpyruvic acid (PEP) to generate pyruvate and ATP; NADH reduces pyruvate to lactate and generates  $\text{NAD}^+$ , which is detected at 340 nm.

#### *Assay validation*

To validate the assay, we (1) determined the minimum [AS] necessary to observe a time-dependent decrease in absorbance at 340 nm; (2) confirmed that the conversion of citrulline and aspartate into argininosuccinic acid limited the rate of the time-dependent decrease in absorbance at 340 nm; and (3) ensured that at the assay concentrations the time-dependent decrease in absorbance at 340 nm was linear.

To determine the minimum [AS] necessary to observe a time-dependent decrease in the absorbance at 340 nm, we set-up test reactions containing 100 mM HEPES pH 7.5, 1 mM DTT, 10 mM MgCl, 2.5 mM ATP, 1 mM phosphoenolpyruvic acid (PEP), 0.2 mM NADH, 0.5 U myokinase, 3.6 U pyruvate kinase/lactate dehydrogenase, 1 mM aspartate, and 1 mM citrulline in a 96-well plate format. Reaction mixtures that lacked AS or ZF-AS were first monitored for two min at 37 °C to ensure that the absorbance at 340 nm was stable. Reactions were then initiated by the addition of 50 nM AS or ZF-AS and the absorbance at 340 nm was monitored every 16 s over the course of 10 min on a BioTek Synergy 2 plate reader. All reactions were performed in triplicate. Error was plotted as standard error (SE). Subsequent experiments were performed at 100 nM AS or ZF-AS, and this concentration produced a larger change in absorbance as a function of time (**Figure 5.6B**). In addition to identifying reaction conditions, these controls established that both AS or ZF-AS and the substrates citrulline and aspartate must be present to observe a decrease in absorbance at 340 nm (**Figure 5.6B**).

We next sought to validate that the observed decrease in absorbance at 340 nm reflected only the AS or ZF-AS catalyzed conversion of aspartate and citrulline into argininosuccinate and not any subsequent steps. Reactions were set up as described above alongside those containing 2-fold higher concentrations of the downstream enzymes myokinase, pyruvate kinase, and lactate dehydrogenase. For the 1X samples, 0.5 U myokinase and 3.6 U pyruvate kinase/lactate dehydrogenase were used, while for 2X reactions, 1 U myokinase and 7.2 U pyruvate kinase/lactate dehydrogenase were used. All reagents except for AS or ZF-AS were added to a 96-well plate. Reaction mixtures that lacked AS or ZF-AS were first monitored for two min at 37 °C to ensure

that the absorbance at 340 nm was stable. Reactions were then initiated by the addition of 100 nM AS or ZF-AS and the absorbance at 340 nm was monitored every 16 s over the course of 6 min (**Figure 5.6C**). The assay was performed in triplicate on a 96-well plate at 37 °C. Error was plotted as standard error of the mean (SEM). The slopes (rate of change in absorbance as a function of time) of the 1X and 2X reactions were not significantly different according to an unpaired t-test ( $P < 0.05$ ) conducted using Prism Version 8.4.3, confirming that the change in absorbance at 340 nm reflects the rate at which AMP is generated upon the conversion of citrulline and aspartate to argininosuccinic acid.

To validate an enzyme activity assay, there are two additional criteria that must be met. First, the initial reaction slopes must be linear to allow for quantification of product.<sup>68</sup> We established previously that the reaction of 100 nM AS or ZF-AS resulted in a linear slope (**Figure 5.6B**). Second, the amount of AMP produced from the AS or ZF-AS reaction must be within a linear range. This means that the production of AMP must be linear with respect to the absorbance at 340 nm ( $Abs_{340}$ ). This control also further validates that the rate limiting step is due to the production of AMP and not from any other product of a coupling enzyme in the assay.

To determine the absorbance response for increasing amounts of AMP, 100 mM HEPES pH 7.5, 1 mM DTT, 10 mM MgCl, 1 mM phosphoenolpyruvic acid (PEP), 0.2 mM NADH, 0.5 U myokinase, 3.6 U pyruvate kinase/lactate dehydrogenase, 1 mM aspartate, and 1 mM citrulline were used. All reagents except for AMP were added to a 96-well plate. Reactions were initiated with the addition of either 0–1 mM AMP and absorbance was monitored every 16 s at 340 nm (for NADH) over 10 min. The assay was completed in triplicate on a 96-well plate at 37 °C. Error was plotted as standard error (SE).

An AMP standard curve was created by adding AMP directly to the coupling enzymes to determine at what concentrations of AMP produced a linear response within the range of the output assay. Within AMP concentrations of 0–0.06 mM, the response was linear (**Figure 5.6D**). The  $Abs_{340}$  values obtained from the concentrations of AMP within the linear range (0–0.06 mM) correspond to the  $Abs_{340}$  values produced by the addition of 100 nM AS or ZF-AS in the assay. This set of experiments established the linearity of the activity assay and completed validation.

#### *Calculating $K_M$ and $k_{cat}$ for AS and ZF-AS*

With a validated assay in hand, we moved on to calculating Michaelis-Menten parameters  $K_M$  and  $k_{cat}$ .<sup>69</sup> We set up a series of reactions containing 100 mM HEPES pH 7.5, 1 mM DTT, 10 mM MgCl, 2.5 mM ATP, 1 mM phosphoenolpyruvic acid (PEP), 0.2 mM NADH, 0.5 U myokinase, 3.6 U pyruvate kinase/lactate dehydrogenase, 1 mM aspartate, and 0–0.5  $\mu$ M citrulline, and verified that the absorbance at 340 nm was stable over the course of two min. Reactions were then initiated by the addition of 100 nM AS or ZF-AS and absorbance was monitored at 340 nm every 16 s for 10 min. The

assay was completed in triplicate on a 96-well plate at 37 °C. Error was plotted as standard error (SE).

The absorbance of NADH at 340 nm was converted into the amount of NADH (in  $\mu\text{mol}$ ) using Beer's law:

$$A = \epsilon bc \quad \text{Equation 5.2}$$

where A is the absorbance,  $\epsilon$  is the molar absorptivity (6220 L/mol\*cm for NADH), b is the path length (0.314 cm for the 96-well plate (Corning™ 3631)), and c is the concentration in M.

Since one mole of AMP is produced per two moles of NADH, c must be divided by 2 to obtain the [AMP]. Initial velocities ( $V_o$ ) of the reaction at different concentrations of citrulline (**Figure 5.6E**) were calculated using the slopes of the [AMP] as a function of time graphs at each concentration of citrulline,

$$V_o = \Delta[\text{AMP}]/t \quad \text{Equation 5.3}$$

where t is time in s.

We obtained Michaelis-Menten kinetics at steady-state by applying the following equation,<sup>69</sup>

$$V_o = V_{max} ([S]/([S] + K_M)) \quad \text{Equation 5.4}$$

where  $V_o$  is the initial velocity of the reaction,  $V_{max}$  is the maximum velocity of the reaction, [S] is substrate concentration, and  $K_M$  is the substrate concentration at which the reaction rate is half its maximal value. Error was represented as standard error. Michaelis-Menten curves were constructed using non-linear regression analysis of the initial velocity plots in Prism (Version 8.4.3) and subsequently used to define  $V_{max}$  and  $K_M$ .

We calculated  $k_{cat}$  using the following equation,

$$k_{cat} = (V_{max}/[E]_T) \quad \text{Equation 5.5}$$

where  $[E]_T$  is the total enzyme concentration in the assay (100 nM).

The error associated with the  $k_{cat}$  and  $K_M$  values in the Prism (Version 8.4.3) analysis was converted from standard error (SE) to standard error of the mean by dividing the SE by the square root of the number of samples (n=3).

#### *Additional Validation of Heat-Denatured Enzymes*

1  $\mu\text{M}$  AS and 1  $\mu\text{M}$  ZF-AS were heat inactivated by incubating at 95 °C for 10 min. These enzymes were used as described in the section "Calculating  $K_M$  and  $k_{cat}$  for AS and ZF-AS." The graphs in **Figure 5.6F** illustrate the absorbance at 340 nm as a

function of time. Linear regression was used to fit the absorbance data at each citrulline concentration in Prism (Version 8.4.3). The slopes were not significantly different from the blank (containing no enzyme), indicating that the heat-denatured enzymes were inactive.

### 5.5.9 Activity of AS and ZF-AS in Mouse Liver Homogenate

We assessed whether ZF-AS was active in liver homogenate, utilizing an established radioactive method to detect enzymatic activity.<sup>70</sup> In this assay, liver from C57BL/6 mice is homogenized and AS or ZF-AS is added to the homogenate. AS (or ZF-AS) reacts with [<sup>14</sup>C]-aspartic acid and citrulline, allowing downstream enzymes in the urea cycle (present in the homogenate) to produce labeled fumarate and malate (**Figure 5.7A** and **B**). [<sup>14</sup>C]-aspartate is retained in a cation exchange column, while only the [<sup>14</sup>C]-labeled fumarate and malate are eluted and subsequently analyzed using a scintillation counter to quantify radioactivity.

C57BL/6 mouse liver was homogenized in 10 mM Tris HCl (pH 7.5) and 3 mM argininosuccinic acid at 4°C using a Bead Ruptor 24 Elite Homogenizer (4 m/s, 2 cycles, 15 s, 10 s dwell at 4°C). Each liver was prepared and stored separately at ≤ -70 °C. Livers were weighed for total protein quantification using Coomassie reagent. To a 96-well U-bottom assay plate, the following were added (90 µL total reaction volume/well): 10 µL liver homogenate (final concentration 1.5 mg/mL), 10 µL AS or ZF-AS (9X final assay concentration, in 10 mM Tris HCl (pH 7.5)), 50 µL incubation buffer (final assay concentration 55 mM Tris HCl (pH 8.5), 5.5 mM L-citrulline, 4.4 mM ATP, 6.6 mM MgCl<sub>2</sub>, 20.2 mM KCl, and 20.2 mM phosphoenolpyruvate), and 20 µL 225 µM L-[U-<sup>14</sup>C] aspartate (final concentration 50 µM). 32 units of arginase and 20 units of pyruvate kinase were added immediately prior to incubation. The plate incubated with shaking at 37 °C for 30 min. The reaction was quenched by adding 20 µL of 18% sulfosalicylic acid to each well. Column elution was performed at room temperature using a 96-well Millipore Multiscreen 0.45 µm Hydrophilic Low Protein Duapore Membrane plate, manually preloaded with Bio-Rad AG 50W-X8 Dowex Resin. 50 µL of deionized water passed over the resin and were added to the plate using vacuum filtration; this wash was discarded. 60 µL of the reaction mixture was added to the membrane/resin plate and vacuum filtered onto an Optiplate-96 HB. The filter plate was washed with 100 µL of deionized water and captured onto the Optiplate. 200 µL of Microsint 40 (Perkin Elmer) was added to the Optiplate (total volume of 350 µL, 10 µL unrecovered). The Optiplate was placed on a plate shaker and mixed for 1 min (at room temperature). The radioactivity was quantified on a Packard Topcount NxT using a <sup>14</sup>C radiolabel protocol to read counts per minute (cpm); each well was read for 1 min. The radioactive signal (cpm) obtained from all wells containing 1.5 mg/mL liver homogenate with no enzyme added were averaged and defined as baseline. The baseline represents the amount of endogenous AS activity present in the mouse liver homogenate. The baseline was subtracted from the radioactive signal from samples where either 0.3–4.4 µM AS or ZF-AS (or 1.1–4.4 µM SUMO protease) were added. To obtain the percent increase above baseline, the baseline-corrected signal was divided by the baseline signal and multiplied by 100%.

## 5.5.10 Cell Culture and Assays

### *General Information*

Saos-2 cells were cultured in McCoy's 5A medium supplemented with 15% fetal bovine serum (FBS), sodium pyruvate (1 mM), penicillin (100 units/mL), and streptomycin (100 µg/mL). SK-HEP-1 cells were cultured in Eagle's modified essential media (EMEM) supplemented with 10% FBS, penicillin (100 units/mL), and streptomycin (100 µg/mL). All cell cultures were maintained at 37 °C in a humidified atmosphere at 5% CO<sub>2</sub>. Procedures for flow cytometry and fluorescence correlation spectroscopy (FCS) were performed using the method described by Knox *et al.*<sup>25</sup>

### *Flow Cytometry*

100,000–120,000 Saos-2 cells were plated on a 6-well dish (or 80,000 SK-HEP-1 cells). After 48 h, cells were washed twice with clear McCoy's 5A (Saos-2) or clear MEM (SK-HEP-1) (2 mL each time). Cells incubated with 0.5–3 µM ZF-AS<sup>Rho</sup> or AS<sup>Rho</sup> for 1 or 2 h. With 5 min left of the incubation (at either 55 min or 115 min), 300 nM Hoechst 3342 was added to the wells for 5 min (and incubated at 37 °C with 5% CO<sub>2</sub>). During incubation, a fibronectin-coated microscopy slide was prepared using a 1:100 dilution of fibronectin by adding 10 µL of 1mg/mL fibronectin to 990 µL DPBS (final concentration 0.1mg/mL). This microscopy slide incubated at 37 °C until use. After incubation, cells were washed three times with DPBS and lifted with 1 mL clear trypsin (TrypLE) to remove surface-bound protein. Cells were transferred into a 15-mL Falcon tube and the cells were washed with 2 mL FBS-containing clear McCoy's 5A (Saos-2) or clear MEM (SK-HEP-1). Cells were centrifuged at 200 *g* for 3 min. Media was removed and cells were washed once with 1 mL clear DMEM (no FBS), and then sedimented at 200 *g* for 3 min. Cells were resuspended in 600 µL clear DMEM and 300 µL of this suspension were plated onto the microscopy dish (for FCS, see "Confocal Microscopy and Fluorescence Correlation Spectroscopy (FCS)"). The other 300 µL were centrifuged at 200 *g* for 3 min and resuspended in 200 µL DPBS. The resuspension was transferred to an Eppendorf tube and flow cytometry was completed using the Attune NxT flow cytometer. 10,000 cells were analyzed for each sample. Data was analyzed using FlowJo 10.6.2 and the median fluorescence values with standard error of the mean were reported. The median calculated from the raw data was multiplied by a correction factor to account for differences in rhodamine labeling efficiencies between AS<sup>Rho</sup> and ZF-AS<sup>Rho</sup>.

### *Confocal Microscopy and Fluorescence Correlation Spectroscopy (FCS)*

FCS was completed as previously described.<sup>8,9,25</sup> 100,000–120,000 Saos-2 cells (or 80,000 SK-HEP-1 cells) were plated in clear McCoy's 5A (clear MEM for SK-HEP-1) on a 6-well dish. After 48 h, cells were washed twice with 2 mL clear McCoy's 5A (clear MEM for SK-HEP-1). Cells incubated with 0.5–3 µM ZF-AS<sup>Rho</sup> or AS<sup>Rho</sup> for 1–2 h. During the last 5 min of the incubation, Hoechst 3342 was added to the wells for a final concentration of 300 nM. During incubation, a fibronectin-coated slide was prepared by

adding 10  $\mu\text{L}$  of 1 mg/mL fibronectin to 990  $\mu\text{L}$  DPBS (final concentration 0.1 mg/mL). This microscopy slide incubated at 37  $^{\circ}\text{C}$  until use. Cells were washed three times with DPBS and lifted with clear trypsin (TrypLE) to remove surface-bound peptide. Cells were transferred into a 15-mL Falcon tube and the well was washed with 2 mL FBS-containing clear McCoy's 5A (FBS-containing clear MEM for SK-HEP-1). Cells were centrifuged at 200  $g$  for 3 min. Media was removed, cells were washed once with 1 mL clear DMEM, and cells were sedimented at 200  $g$  for 3 min. Cells were resuspended in 600  $\mu\text{L}$  clear DMEM and 300  $\mu\text{L}$  were plated onto the microscopy dish. Cells adhered at 37  $^{\circ}\text{C}$  with 5%  $\text{CO}_2$  for 40 min. Confocal microscopy was completed to analyze cell morphology and localization of dye. FCS measurements were obtained on an LSM 880 using ZEN software and traces were analyzed using MATLAB as previously described.<sup>8,11,25</sup> The cytosolic concentration calculated from the raw data was multiplied by a correction factor to account for differences in rhodamine labeling efficiencies between  $\text{AS}^{\text{Rho}}$  and  $\text{ZF-AS}^{\text{Rho}}$ . Autocorrelation curves (**Figure 5.10 and 5.15D**) were displayed starting at  $\tau = 10^{-2}$  ms as that is the timescale for anomalous diffusion and the point in which the y-intercept is equal to 1/number particles in the confocal volume.

### *Cytosolic Fractionation*

On day 1, Saos-2 cells ( $5 \times 10^6$  cells) were plated in clear McCoy's media supplemented with 15% FBS in a T175 flask. On day 2, the cells were washed with 25 mL DPBS three times and treated with 1  $\mu\text{M}$   $\text{AS}^{\text{Rho}}$  or  $\text{ZF-AS}^{\text{Rho}}$  (diluted in clear McCoy's media, no FBS) or clear McCoy's media (as a non-treated control). The cells incubated at 37  $^{\circ}\text{C}$  with 5%  $\text{CO}_2$  for 1 h. After incubation, cells were washed with 25 mL DPBS three times and lifted off of the dish with 4 mL clear TrypLE Express for 10 min. The cell slurry was then added to a Falcon tube containing 8 mL clear McCoy's media supplemented with 15% FBS and centrifuged at 200  $g$  for 3 min. The supernatant was removed, cells were washed with 3 mL of DPBS, and sedimented again at 200  $g$  for 3 min. A second wash was performed under the same conditions. Next, cells were resuspended in 1 mL cold isotonic sucrose buffer (290 mM sucrose, 10 mM imidazole pH 7.0, 1 mM DTT, and 1 cOmplete protease inhibitor cocktail per 10 mL buffer) and centrifuged at 200  $g$  for 3 min. The cells were then suspended in 150  $\mu\text{L}$  of isotonic sucrose buffer, transferred to 0.5 mL microtubes containing 1.4 mm ceramic beads (Omni International) and homogenized using a Bead Ruptor 4 (Omni International) for 8 s at speed 1. Homogenized cells were transferred to polycarbonate ultracentrifuge tubes and centrifuged at 350  $kg$  for 30 min at 4  $^{\circ}\text{C}$  to isolate the cytosolic fraction. 20  $\mu\text{L}$  of each cytosolic fraction was mixed with 5  $\mu\text{L}$  of 5X SDS loading dye, boiled for seven min, and 20  $\mu\text{L}$  was loaded onto a 10% SDS-PAGE gel. In addition to the non-treated,  $\text{AS}^{\text{Rho}}$ -treated, and  $\text{ZF-AS}^{\text{Rho}}$ -treated samples, 100 nM of either  $\text{AS}^{\text{Rho}}$  or  $\text{ZF-AS}^{\text{Rho}}$  were added to non-treated cytosol. The gel ran at 200 V for 30 min. Western blot analysis was performed using an anti-AS antibody (Cell Signaling Technology) as described above.

### *Evaluation of ZF $\text{Zn}^{2+}$ Dependence in SK-HEP-1 Cells*

The sequence of ZF is derived from an optimized zinc finger module.<sup>10,71,72</sup> Isolated zinc finger modules coordinate a single Zn<sup>2+</sup> ion *via* a conserved Cys<sub>2</sub>His<sub>2</sub> motif that contributes significantly to the stability of the canonical ββ<sub>2</sub>α fold.<sup>73</sup> Equilibrium dissociation constants for Zn<sup>2+</sup> binding can range from 2 to 5.7 pM.<sup>72,74,75</sup> Indeed, the extent of α-helical secondary structure of ZF increases in the presence of Zn<sup>2+</sup>, as judged by CD.<sup>10</sup> To evaluate whether total uptake and cytosolic delivery of ZF-AS<sup>Rho</sup> was also Zn<sup>2+</sup>-dependent, we prepared samples of ZF-AS<sup>Rho</sup> in the absence of Zn<sup>2+</sup>, treated SK-HEP-1 cells with 1 μM of both materials for 1 h, and evaluated the cells using the methods described above for both flow cytometry and FCS (**Figure 5.15E and F**).

### 5.5.11 Endotoxin Analysis

#### *Limulus Amebocyte Lysate Assay*

To test for the presence of endotoxin in AS and ZF-AS samples derived from BL21-Gold (DE3) cells, ToxinSensor™ Chromogenic Limulus Amebocyte Lysate (LAL) Endotoxin Assay Kit was used according to GenScript Biotech's instructions. Briefly, this method utilizes a chromogenic endpoint determination and can detect up to 0.01 EU/mL. A standard curve was generated using the Abs<sub>545nm</sub> signal from serial dilutions of *E. coli* endotoxin standard prepared in endotoxin-free water (0.1, 0.25, 0.5, 1 EU/mL). Abs<sub>545nm</sub> of 500 nM samples of AS and ZF-AS purified from BL21-Gold (DE3) cells were obtained. The amount of endotoxin present in the samples was calculated using the standard curve obtained from the experiment ( $y=0.6726x-0.08382$ ). We note that the absorbances for 500 nM AS and ZF-AS were higher than the value of 1 EU/mL, so the values reported are the minimum endotoxin present in the samples. Values of endotoxin contamination (in EU/mL) reported in **Figure 5.17C** correspond to the levels in 3 μM of protein sample after size exclusion chromatography.

#### *AS and ZF-AS Expression and Purification in ClearColi®*

pET32a\_His<sub>6</sub>-SUMO-AS and pET32a\_His<sub>6</sub>-SUMO-ZF-AS were transformed and expressed according to the manufacturer's (Lucigen) instructions. Glycerol stocks of ClearColi® with the pET32a\_His<sub>6</sub>-SUMO-AS and pET32a\_His<sub>6</sub>-SUMO-ZF-AS plasmids were used to grow a 27 g pellet of His<sub>6</sub>-SUMO-AS (10 L culture) and a 19 g pellet of His<sub>6</sub>-SUMO-ZF-AS (15 L culture) according to the manufacturer's protocol for expression. The pellet was resuspended in 150 mL of Buffer A (50 mM sodium phosphate monohydrate pH 7.5, 300 mM NaCl, 1 mM TCEP, 10% glycerol, 30 mM imidazole) that also contained protease inhibitor mix (Proteoloc Protease Inhibitor Cocktail, 44204, Expedeon) and base muncher (ab270049, Abcam). The pellet was disrupted with a single passage using a Constant Systems Cell Disruptor at 27k psi and the cleared lysate was centrifuged at 14,000 RPM for 30 min at 4 °C. 5 mL of Talon resin was washed with endotoxin-free water and added to the cleared lysate. This slurry incubated for 1 h at 4 °C with rotation. During the 1 h incubation, half of Buffer A was mixed with 0.1% Triton X-114 and stored on ice at 4 °C. The Talon resin was centrifuged and washed with 50 mL Buffer A (no Triton X-114). The sample was then loaded on to

an OmniFit (15815344, Fisher Scientific) column attached to an AKTA FPLC previously treated with NaOH and equilibrated with endotoxin free water, followed by Buffer A (pump A), and Buffer B (pump B, 50 mM sodium phosphate monohydrate pH 7.5, 300 mM NaCl, 1 mM TCEP, 10% glycerol, 250 mM imidazole). The sample on the column was washed with 40 column volumes (CVs) of Buffer A with 0.1% Triton X-114 followed by 60 CVs of Buffer A (no Triton X-114). The protein was eluted with 100% Buffer B. Fractions containing protein (as determined by SDS-PAGE) were dialyzed overnight at 4 °C in Snakeskin 3 kDa MWCO membrane (11552541, Fisher Scientific) in 1 L of dialysis buffer (30 mM HEPES pH 7.5, 500 mM NaCl, 10% glycerol).

### *SUMO Protease Expression and Purification in ClearColi® Cells*

SUMO protease was transformed and expressed according to Lucigen instructions. Briefly, pET32a\_His<sub>6</sub>-SUMO protease was electroporated into ClearColi® cells. 40 mL Miller Broth starter cultures containing 1X carbenicillin shook overnight at 37 °C. 4 L of media containing ampicillin (100 mg/L media) were inoculated with starter cultures and grown until an OD<sub>600</sub> ~0.6–0.8. The cultures were then induced with 1 mM IPTG, and incubated at 200 RPM and 30 °C for 4 h. After 4 h, the media was spun down and supernatant media was removed. Purification took place as described above (SUMO Protease Expression and Purification in BL21-Gold (DE3) Cells) with the following amendments: all instruments, plastic and glass, magnetic stirrers, spatulas soaked in 0.1 M NaOH overnight and were thoroughly washed with endotoxin-free water prior to use. All buffers were prepared in sterile/pyrogenic Corning bottles and filter sterilized prior to use. Talon resin was washed with 40 CVs of lysis/binding buffer and 0.2% Triton X-114 followed by 40 CVs of lysis/binding buffer prior to elution.

### *SUMO Cleavage of ClearColi® His<sub>6</sub>-SUMO-AS and His<sub>6</sub>-SUMO-ZF-AS*

SUMO protease was added in 1:1 molar ratio with either His<sub>6</sub>-SUMO-AS or His<sub>6</sub>-SUMO-ZF-AS for 3 h at room temperature. Cleavage was assessed via SDS-PAGE. The protein was concentrated to 3–5 mL for SEC on a Sephadex 75 16/60 column. The AKTA FPLC and SEC column were treated with 0.1 M NaOH overnight and washed thoroughly with endotoxin-free water. The cleavage mixture was injected onto the SEC column and run at 0.5 mL/min (in 50 mM sodium phosphate monohydrate pH 7.5, 300 mM NaCl, 1 mM TCEP, 10% glycerol). Fractions eluted into endotoxin-free 96-deep well plates. Fractions with protein (determined via SDS-PAGE) were pooled and concentrated (using 10 kDa MWCO Vivaspin filters) at 4 °C. Final protein samples were quantified and stored at -80 °C. 28.5 mg of AS (2.85 mg/L culture) and 14.4 mg of ZF-AS (0.96 mg/L culture) were obtained and used for mouse studies after endotoxin analysis using the HEK-Blue endotoxin assay.

### *HEK-Blue Endotoxin Assay*

The Lucigen user manual for ClearColi® indicates that the modified LPS molecule of ClearColi® can be detected by LAL, requiring use of an alternative assay to quantify endotoxin.<sup>76</sup> The HEK-Blue™ hTLR4 cell line (InvivoGen) produces results only

if the endotoxin triggers an immune response and elicits a response from TLR-4 receptors.<sup>55,56,63,64</sup> This assay can distinguish between standard endotoxin in BL21-Gold (DE3) cells and ClearColi® modified endotoxin. The endotoxin contamination of AS, ZF-AS, and SUMO protease derived from BL21-Gold (DE3), T7 Express, and ClearColi® cells was determined in HEK-Blue™ hTLR4 cells following protocols supplied from InvivoGen. Briefly, HEK-Blue™ hTLR4 cells were cultured in high glucose (4.5 g/L) DMEM containing 2 mM L-glutamine, 10% (v/v) FBS, 100 U/mL penicillin, 100 µg/mL streptomycin, 1X HEK-Blue™ Selection, and 100 µg/mL Normocin™. Serial dilutions of proteins (0–3 µM) and endotoxin standards (0–1 EU/mL) were prepared and added to a 96-well plate. 11,000 HEK-Blue™ hTLR4 cells were added and incubated at 37 °C and 5% CO<sub>2</sub> for 23 h. HEK-Blue™ Detection was added to the plate and incubated for 3 h at 37 °C and 5% CO<sub>2</sub>. Absorbance at 640 nm was measured using a BioTek Synergy 2 plate reader. A standard curve of absorbance at 640 nm as a function of concentration of endotoxin standard (0.01–0.1 EU/mL to support assay linearity) was generated. Absorbance values for the protein samples (AS, ZF-AS, SUMO protease) that fell within the range of the standard curve were used to calculate the amount of endotoxin contamination (EU/mL) using the linear regression obtained from the endotoxin standard curve using Prism (Version 8.4.3). Values of endotoxin contamination (in EU/mL) reported in **Figure 5.18C** correspond to the levels in 3 µM of protein sample.

### 5.5.12 Quantification of Endogenous [AS] in C57BL/6 Mouse Liver

Endogenous AS in C57BL/6 mouse liver was quantified using an enzyme-linked immunosorbent assay (ELISA). 6.10–10,000 ng/mL standards were made with purified AS. 4 unique mouse liver homogenates were analyzed by preparing homogenates in 1:10–1:10,000,000 dilutions. All sample dilutions (homogenates, AS standards, antibody dilutions) were prepared in Assay Buffer (Superblock). All steps were performed at ambient temperature. Except for blocking (150 µL/well) and washes (3 x 300 µL/well), 50 µL/well reagent volume was used for all steps. Similarly, except for blocking (2–2.5 h), secondary antibody (40 min), and washes, all reagent/sample incubations were 1 h with gentle shaking. In between each ELISA step, unbound reagents were removed by washing the plate with Wash Buffer (1X PBST). First, MSD Standard Bind 96-well plates were coated with 1 µg/mL ASS1 (D404B) XP Rabbit mAb in 1X PBS. Following binding of samples (either AS standards in buffer or liver homogenate), the presence of AS was detected using 1,000 ng/mL ASS1 Polyclonal Primary Antibody (Thermo Fisher Scientific, PA5-18679). Signal was developed by incubating plates with a secondary antibody (0.5 µg/mL Donkey anti-Goat-SulfoTag (R32AG-1, MSD)). Following the addition of 2X MSD Read Buffer, plates were read within 5 min on the MSD Sector Platform. Data was analyzed in SoftMax Pro GxP 5.4 and graphs were fit to a 5-PL regression function with fixed weighting,

$$y = ((min - max)/(1 + (x/ED_{50})^{Hill's\ slope})^{asymmetry\ factor}) + max \quad \text{Equation 5.6}$$

where min is the minimum asymptote, max is the maximum asymptote, ED<sub>50</sub> is the inflection point (or effective dose), Hill's slope represents information about the AS and anti-AS antibody interaction, and the asymmetry factor is due to the asymmetry of the

shape of the graph.<sup>77</sup> In **Figure 5.16**, A = min, B = Hill's slope, C = inflection point, D = max, and G = asymmetry factor. The Hook effect<sup>78</sup> was observed for purified AS (at high concentrations of 12500–100000 ng/mL), so these data points were excluded from analysis.

The linear range for the AS standards was determined to be  $19000 \pm 1000$  to  $219000 \pm 5000$  au, corresponding to 12.2 ng/mL to 1562 ng/mL AS (0.26–33.57 nM). The ECL signal for the individual mouse livers assessed was within the standard linear range at dilution factors of 1:10 and 1:100. To calculate the concentration of AS within the liver, the ECL signals of dilutions 1:10 and 1:100 were used as the y value in the 5-PL regression fit from known concentrations of AS in buffer:

$$y = ((1080 - 255000)/(1 + \left(\frac{x}{44.5}\right)^{1.31})^{0.438}) + 255000 \quad \text{Equation 5.7}$$

Solving for x produces a result in ng/mL. For example, for Liver 1, the average y-value at a 1:10 dilution was  $68300 \pm 2500$  au. When solving for x using *Equation 5.7*, 45.1 ng/mL AS was present in liver homogenate. Since this liver homogenate sample was a 1:10 dilution, the x value must be multiplied by 10 to obtain the concentration of endogenous AS in neat liver homogenate (451 ng/mL). This value was converted to nM using the molecular weight of AS (46,530 g/mol).

### 5.5.13 Dosing of ZF-AS into C57BL/6 Mice

Mouse studies were completed by Charles River Laboratories and complied with all applicable sections of the Final Rules of the Animal Welfare Act Regulations (Code of Federal Regulations, Title 9), the *Public Health Service Policy on Humane Care and Use of Laboratory Animals* from the Office of Laboratory Animal Welfare, and the *Guide for the Care and Use of Laboratory Animals* from the National Research Council. 15 male, naïve C57BL/6 mice (Charles River Laboratories, Raleigh, North Carolina) were dosed with 3 mg/kg ZF-AS (stock solutions were diluted to the appropriate concentration with phosphate buffered saline (pH 7.4)) while an additional 15 mice (same breed and sex as above) were treated with phosphate buffered saline (pH 7.4, vehicle). Animals received a single bolus, intravenous injection via the tail vein of either vehicle or ZF-AS (3 mg/kg) on Day 1. Mice were euthanized at time points 0.083, 0.5, 1, 4, and 24 h. Approximately 0.4 mL of whole blood was collected from each animal after euthanasia via the vena cava with no anticoagulant. After clotting at room temperature, blood samples were processed to serum through centrifugation at room temperature. The blood samples processed for plasma were maintained on ice until processed and the samples were centrifuged under refrigerated (2–8 °C) conditions. The resulting plasma was separated into two aliquots containing plasma in the first aliquot and the remaining cell pellet in the second aliquot. Serum was stored at -60 to -90 °C prior to analysis. Next, liver tissue was rinsed with saline, blotted dry, and weighed before processing it into the left lobe, median lobe, and right and caudate lobes (combined). After weighing each lobe, the samples were frozen in liquid nitrogen and stored at -60 to -90 °C until analysis.

### 5.5.14 Enzyme-Linked Immunosorbent Assays for Determination of [ZF-AS] in Mouse Serum and Liver

#### *Determination of ZF-AS Standard Curve for Mouse Serum*

The ELISA described above was used to determine a standard curve of ZF-AS for mouse serum. Briefly, MSD Standard Bind 96-well plates were coated with 1 µg/mL ASS1 (D404B) XP Rabbit mAb for 1 h. Unbound reagents were washed away three times with 300 µL of 1X PBST. 150 µL Superblock was added to each well and incubated for 1 h at room temperature. Unbound reagents were washed away three times with 300 µL of 1X PBST. 160 µL of 0–10,000 ng/mL ZF-AS in mouse serum were added to the plate and incubated for 1 h. The plate was washed three times with 300 µL of 1X PBST. 50 µL of 1,000 ng/mL ASS1 Polyclonal Primary Antibody (Thermo Fisher Scientific, PA5-18679) were added and the plate incubated for 1 h. The plate was washed three times with 300 µL of 1X PBST. 50 µL of 0.5 µg/mL Donkey anti-Goat-SulfoTag (R32AG-1, MSD) were added to the plate. Following a 1 h incubation, the plate was washed three times with 300 µL 1X PBST and subsequently 150 µL of 2X Read Buffer T (MSD) were added to the plate. The plate was read within 5 min on the MSD Sector Platform. The ELC signal obtained from 78.1–10000 ng/mL (1.6–200 nM) ZF-AS in mouse serum was within the linear range and used as a standard curve, fit using a 4-PL regression in SoftMax Pro GxP 5.4

$$y = ((min - max)/(1 + (x/ED_{50})^{Hill's\ slope})) + max \quad \text{Equation 5.8}$$

where min is the minimum asymptote, max is the maximum asymptote, ED<sub>50</sub> is the inflection point (or effective dose), and Hill's slope represents information about the ZF-AS and anti-AS antibody interaction.<sup>77</sup> **Figure 5.20** shows a representative curve for serum obtained from analysis, in which A = min, B = Hill's slope, C = inflection point, and D = max.

#### *Determination of ZF-AS Standard Curve for Liver Homogenate*

The ELISA described above was used to determine a standard curve of ZF-AS for mouse liver homogenate (represented by results obtained in Superblock). Briefly, MSD Standard Bind 96-well plates were coated with 1 µg/mL ASS1 (D404B) XP Rabbit mAb for 1 h. Unbound reagents were washed away three times with 300 µL of 1X PBST. 150 µL Superblock was added to each well and incubated for 1 h at room temperature. Unbound reagents were washed away three times with 300 µL of 1X PBST. 100 µL of 0–300 ng/mL ZF-AS in Superblock were added to the plate and incubated for 1 h. The plate was washed three times with 300 µL of 1X PBST. 50 µL of 1,000 ng/mL ASS1 Polyclonal Primary Antibody (Thermo Fisher Scientific, PA5-18679) were added and the plate incubated for 1 h. The plate was washed three times with 300 µL of 1X PBST. 50 µL of 0.5 µg/mL Donkey anti-Goat-SulfoTag (R32AG-1, MSD) were added to the plate. Following a 1 h incubation, the plate was washed three times with 300 µL 1X PBST and subsequently 150 µL of 2X Read Buffer T (MSD) were added to the plate. The plate was read within 5 min on the MSD Sector Platform. The ELC signal obtained from 4.69–300 ng/mL (0.1–6.0 nM) ZF-AS in Superblock was within the linear

range and used as a standard curve for ZF-AS material present in mouse liver homogenate, fit using a 4-PL regression in SoftMax Pro GxP 5.4. **Figure 5.20** shows a representative curve for liver homogenate obtained from analysis, in which A = min, B = Hill's slope, C = inflection point, and D = max.

#### *Determination of [ZF-AS] in Mouse Serum and Liver*

Serum samples from individual mice (either vehicle or 3 mg/kg ZF-AS-treated) were assessed to detect the amount of ZF-AS present in the samples. Appropriately sized liver sections were added to homogenization tubes containing homogenization beads. Homogenization buffer was added in a 1:3 ratio (tissue:buffer). Tissues were homogenized using the Precellys Evolution at 5,000 RPM for 30 s; 2 cycles with a 60 s rest between each cycle. This was performed 3 times. Then the tubes were centrifuged under refrigeration for 10 min at 16,000 RCF. The supernatant was removed, split into 3 equally sized aliquots, and stored at -70°C.

Reagents were thawed at room temperature. For serum quality controls (QCs), stock concentrations of 200, 1200, and 8000 ng/mL ZF-AS in assay buffer were used; for liver homogenate QCs, stock concentrations of 10, 50, and 240 ng/mL ZF-AS in assay buffer (PBS) were used. 50 µL of Coating Solution (1 µg/mL ASS1 XP Rabbit mAb in 1X PBS) were added to each well of a MSD Standard Bind Plate (MSD, L15XA-3). The plate incubated at room temperature on an orbital shaker for 1 h. The plate was washed 3X with 300 µL/well of wash buffer (1X PBST). 150 µL of Superblock (Scytek, AAA999) was added to each well. The plate incubated for 1.25 h on an orbital shaker at room temperature. The plate was washed 3X with 300 µL/well of wash buffer. 50 µL of 1:20 standards (for serum: 78.1–320,000 ng/mL ZF-AS in assay buffer; for liver homogenate: 2.34–160,000 ng/mL ZF-AS in assay buffer), 1:20 QCs (example preparation: 10 µL of the neat QC diluted with 190 µL of Superblock), blanks, and diluted samples (either serum or liver homogenate diluted to be within the linear range of the respective ELISA) were added in duplicate to the plate. The plate incubated at room temperature on an orbital shaker for 1 h. The plate was washed 3X with 300 µL/well of wash buffer. 50 µL of the primary detection antibody (1 µg/mL ASS1 Polyclonal Antibody in Superblock) were added to each well and the plate incubated at room temperature on an orbital shaker for 1 h. Next, the plate was washed 3X with 300 µL/well of wash buffer. 50 µL of the secondary detection antibody (1:1001 Donkey anti-Goat-SulfoTag in Superblock) were added to each well and the plate incubated at room temperature on an orbital shaker for 1 h. The plate was washed 3X with 300 µL/well of wash buffer. 150 µL of 2X Read Buffer T (R92TC-1; per vendor recommendations, this reagent (stock 4X) was diluted with an equal volume of DI water prior to use) were added to each well and the plate was analyzed using an MSD Sector Imager. Data was fit to the standard curve for either serum or liver homogenate to determine the concentration of ZF-AS present in vehicle- or ZF-AS-treated mice. For kinetic analysis, Phoenix pharmacokinetic software using a non-compartmental approach was applied, consistent with intravenous bolus route of administration for parameter estimation.

## 5.6 Figures

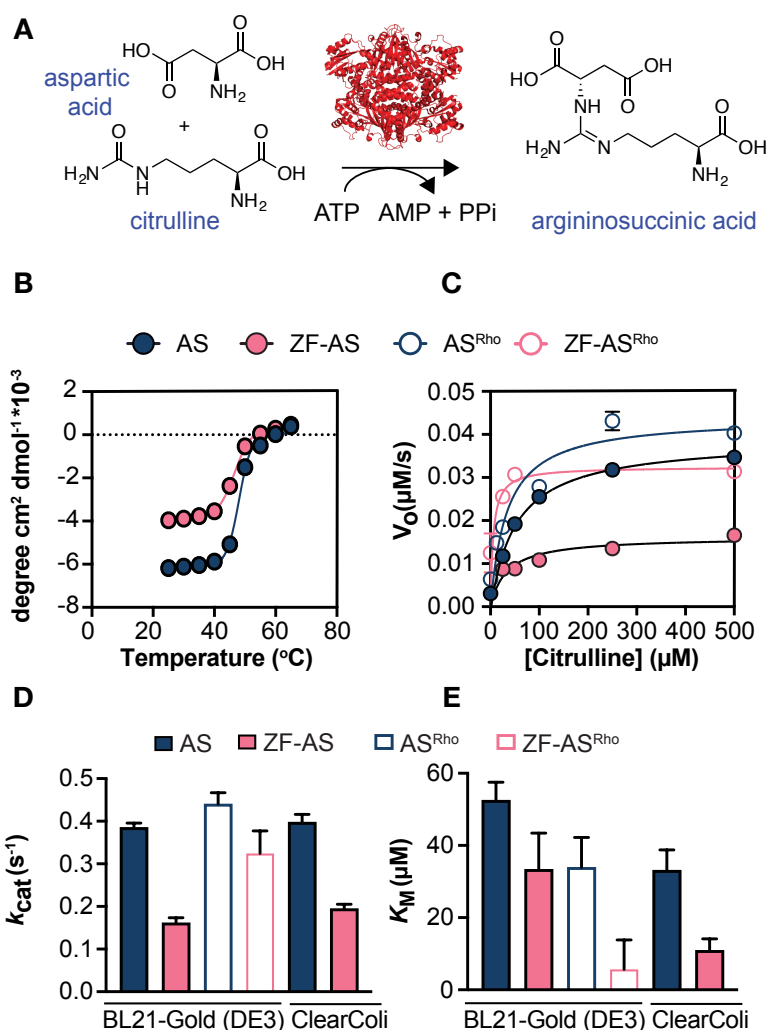


**Figure 5.1.** (A) Argininosuccinate synthetase (AS) catalyzes the conversion of aspartic acid and citrulline into argininosuccinic acid during the first cytosolic step of the urea cycle. (B) Graphs illustrating the change in molar ellipticity at 222 nm of AS and ZF-AS as a function of temperature. The apparent  $T_M$  of each protein (48.1  $^{\circ}\text{C}$  for AS and 46.6  $^{\circ}\text{C}$  for ZF-AS) was determined by fitting the melting curve to a Boltzmann sigmoidal curve in Prism (Version 8.4.3); the melts were not reversible. (C) Plot illustrating the initial velocity ( $V_o$ ) of NADH production (as determined by the absorbance at 340 nm) as a function of citrulline concentration (0–500  $\mu\text{M}$ ) in reactions containing 100 nM AS, ZF-AS, AS<sup>Rho</sup>, or ZF-AS<sup>Rho</sup> (all expressed in BL21-Gold (DE3)). (D) Bar graph showing  $k_{\text{cat}}$  values for AS, ZF-AS, AS<sup>Rho</sup>, and ZF-AS<sup>Rho</sup>, as determined from the best fit of the initial velocity data to the Michaelis-Menten equation (expressed in either BL21-Gold (DE3) for biochemical analyses or ClearColi® for mouse studies). (E) A bar graph representing  $K_M$  values of AS, ZF-AS, AS<sup>Rho</sup>, and ZF-AS<sup>Rho</sup> with respect to citrulline (expressed in either BL21-Gold (DE3) for biochemical analyses or ClearColi® for mouse studies).  $V_o$  plots were fit to a standard Michaelis-Menten equation using Prism (Version 8.4.3). For the  $V_o$  plots, error bars represent the standard error. Error bars in the  $k_{\text{cat}}$  and  $K_M$  bar graphs represent the standard error of the mean.

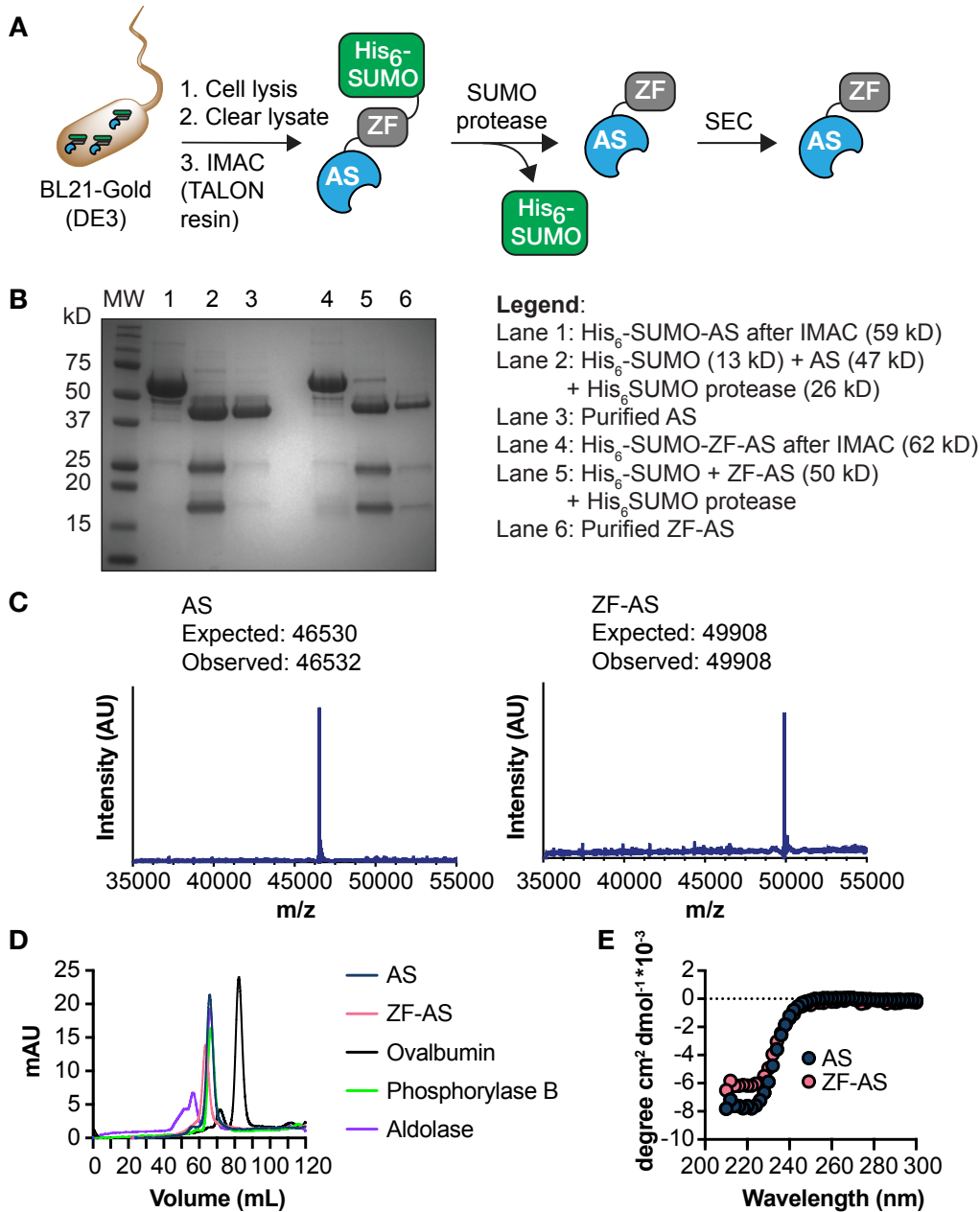


**Figure 5.2.** (A) Workflow used to generate and purify AS and ZF-AS. IMAC = immobilized metal affinity chromatography, SEC = size exclusion chromatography (B) SDS-PAGE analysis illustrating the purity of AS and ZF-AS after each step of the workflow. Final samples of AS and ZF-AS were 93 and 90% pure, respectively. (C) LC/MS analysis of purified AS and ZF-AS. (D) Analytical fast protein liquid chromatography (FPLC) elution profiles of AS, ZF-AS, ovalbumin (45 kD), phosphorylase B (97.5 kD), and aldolase (158 kD) from a HiLoad® 16/600 Superdex® 200 pg column in 30 mM HEPES (pH 7.5), 500 mM NaCl, 10% glycerol, and 1 mM DTT at 4 °C. Aldolase elutes as a mixture of a monomer and a dimer. (E) Wavelength-dependent circular dichroism (CD) spectra of purified AS (1.01  $\mu\text{M}$ ) and ZF-AS (0.60

$\mu\text{M}$ ) in 50 mM sodium phosphate (pH 7.5), 300 mM NaCl, 10% glycerol, and 1 mM DTT. Measurements < 210 nm could not be obtained due to the presence of glycerol and high salt.

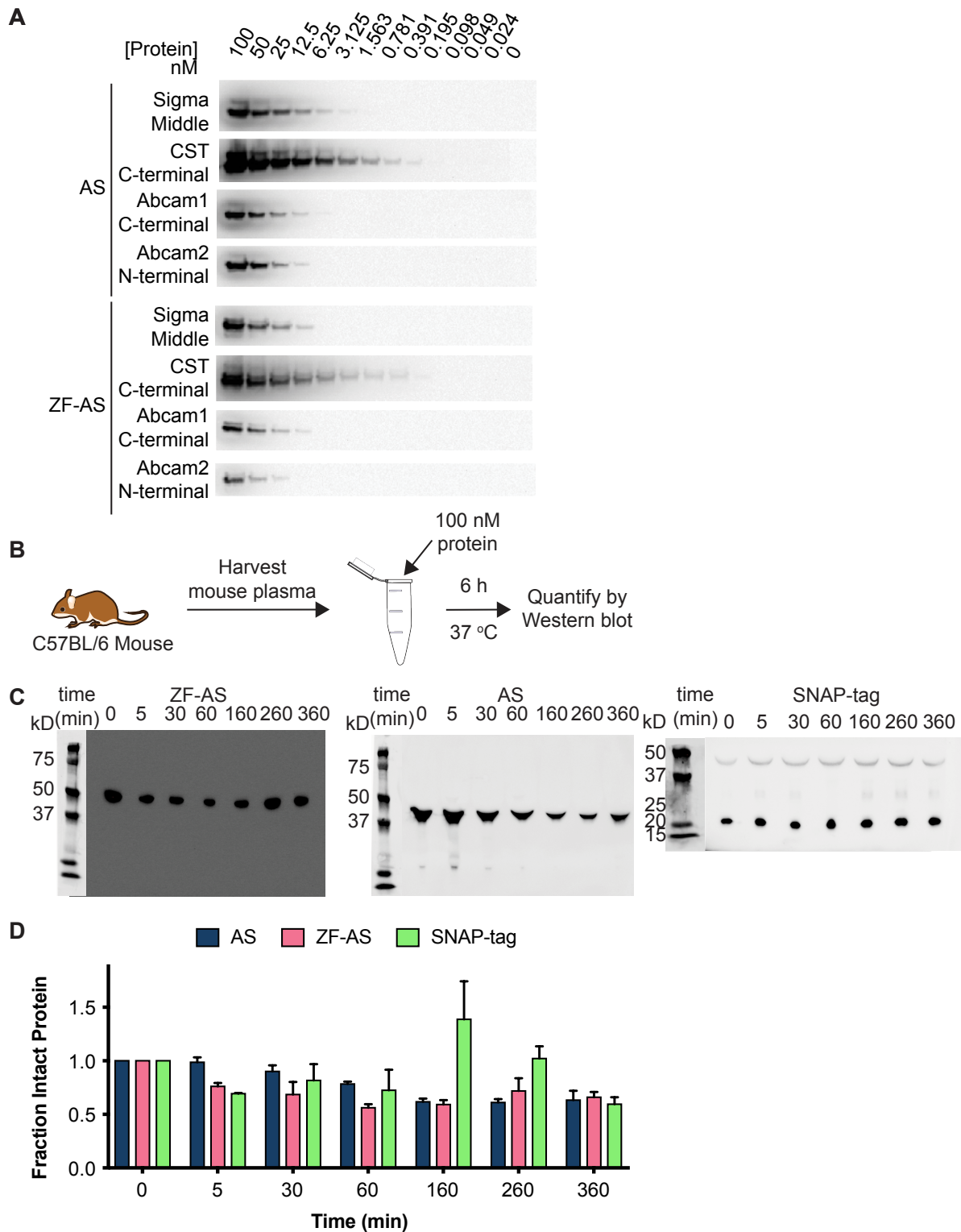


**Figure 5.3.** (A) Detection of 0–100 nM AS and ZF-AS in buffer (30 mM HEPES (pH 7.5), 500 mM NaCl, and 10% glycerol) by commercially available anti-AS antibodies (1:1000 dilution in 5% milk). Antibody HPA020934 (Sigma) recognizes a central AS

epitope (between residues 164 and 241); antibody ASS1 (D4O4B) XP® Rabbit mAb (Cell Signaling Technology, CST) recognizes a C-terminal epitope containing Glu401; antibody Abcam1 (EPR12399(B), Abcam) recognizes an epitope between residues 350 and 411, near the C-terminus of AS; antibody Abcam2 (EPR12398, Abcam) recognizes an epitope near the N-terminus of AS. (B) Workflow used to determine the time-dependent stability of 100 nM AS, ZF-AS, or SNAP-tag in C57BL/6 mouse plasma at 37 °C. (C) Representative Western blots illustrating time-dependent loss of AS and ZF (detected using the D4O4B CST anti-AS antibody), as well as SNAP-tag (detected using antibody P9310S, New England BioLabs) in mouse plasma over 6 h at 37 °C. Bands were visualized with Amersham ECL Prime Western Blotting Detection Reagent (RPN2232, GE Healthcare) which reacts with horseradish peroxidase conjugated to a secondary rabbit IgG antibody (CST). Blots were imaged on a ChemiDoc MP using a chemiluminescent filter and the ladder was imaged using ambient light. (D) Bar plot quantifying Western blot detection of AS, ZF-AS, or SNAP-tag after incubation in mouse plasma. Aliquots removed at the indicated times were diluted 4-fold prior to SDS-PAGE analysis (10% gel). Using FIJI (Version 2.0.0), the density of the band at  $t = 0$  min was normalized to 1 and all subsequent band densities were compared to  $t = 0$  min.

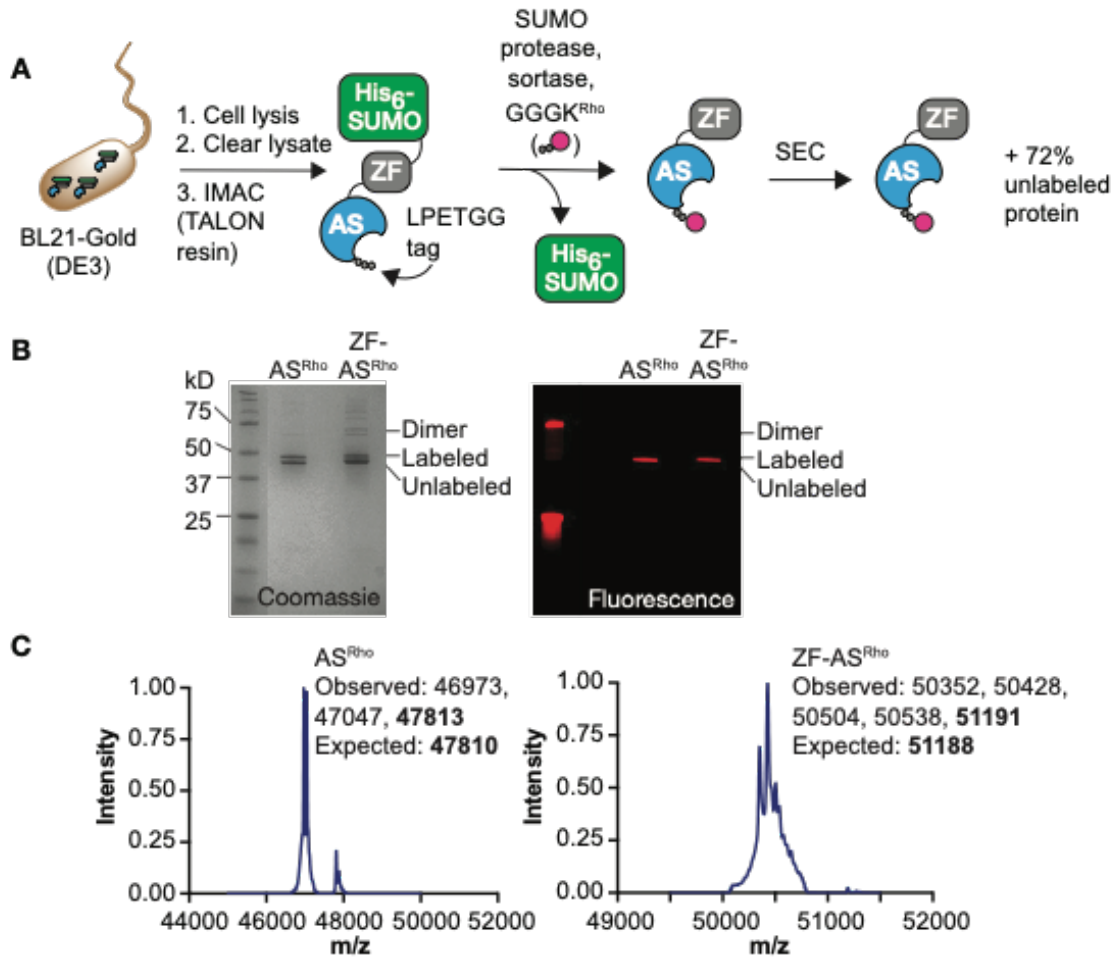


**Figure 5.4.** (A) Workflow used to purify AS<sup>Rho</sup> (47.8 kD) and ZF-AS<sup>Rho</sup> (51.2 kD) from His<sub>6</sub>-SUMO-AS-LPETGG and His<sub>6</sub>-SUMO-ZF-AS-LPETGG expressed in BL21-Gold (DE3) *E. coli* after SUMO cleavage and sortase-catalyzed transpeptidation. (B) SDS-PAGE analysis of AS<sup>Rho</sup> and ZF-AS<sup>Rho</sup> purified by size-exclusion chromatography. SEC is unable to separate the rhodamine-tagged proteins AS<sup>Rho</sup> and ZF-AS<sup>Rho</sup> from the SUMO-cleaved sortase substrates AS-LPETGG and ZF-AS-LPETGG. The material referred to as AS<sup>Rho</sup> is 95% pure (determined using FIJI V2.0.0) and is composed of a mixture of AS<sup>Rho</sup> (labeled) and AS-LPETGG (unlabeled), with a Rho labeling efficiency of approximately 29%. The material referred to as ZF-AS<sup>Rho</sup> is 87% pure and is composed of a mixture of both ZF-AS<sup>Rho</sup> (labeled) and ZF-AS-LPETGG (unlabeled), with a Rho labeling efficiency of approximately 28%. (C) LC/MS analysis of purified AS<sup>Rho</sup> (expected m/z 47810, observed 47813) and ZF-AS<sup>Rho</sup> (expected m/z 51188, observed 51191). **Table 5.1** denotes additional masses observed in the spectra.



°C, (B) room temperature (RT), and (C) 4 °C. Each temperature evaluated resulted in varying degrees of precipitation of the protein. (D) When SUMO protease, sortase, and His<sub>6</sub>-SUMO-ZF-AS-LPETGG were prepared in the same buffer (50 mM HEPES, pH 7.0, 10% glycerol, 500 mM NaCl, 1 mM DTT), minimal precipitation occurred and the two reactions proceeded smoothly at RT to generate ZF-AS<sup>Rho</sup>. Analogous reactions were also performed with AS<sup>Rho</sup>. Preparative-scale one-pot cleavage/labeling reactions were performed at RT for 4 h. Uncleaved protein represents His<sub>6</sub>-SUMO-ZF-AS-LPETGG and His<sub>6</sub>-SUMO-ZF-AS<sup>Rho</sup>, while cleaved protein indicates ZF-AS and ZF-AS<sup>Rho</sup>. HSZAS = His<sub>6</sub>-SUMO-ZF-AS-LPETGG, S = sortase, SP = SUMO protease, ON = overnight.

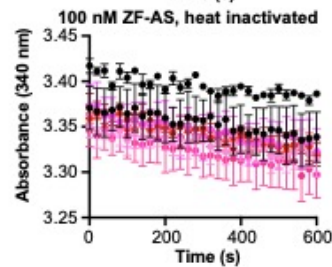
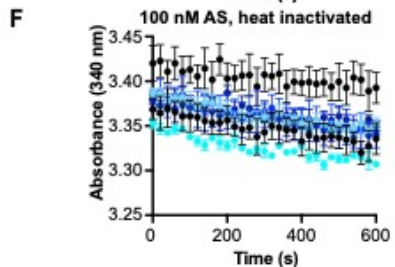
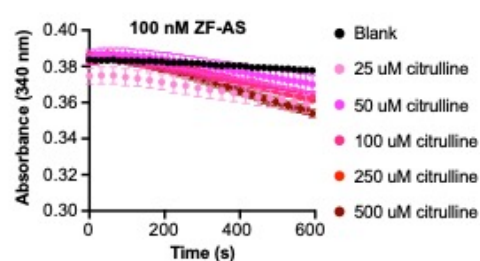
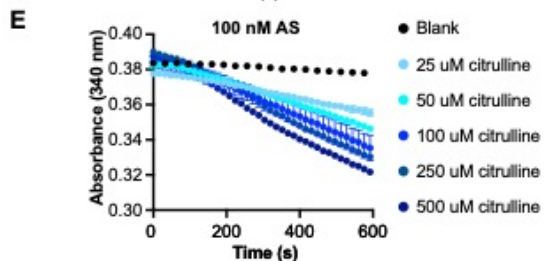
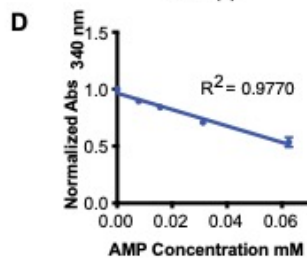
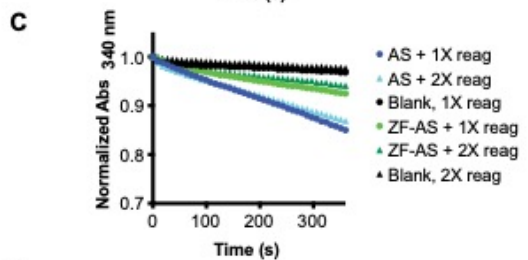
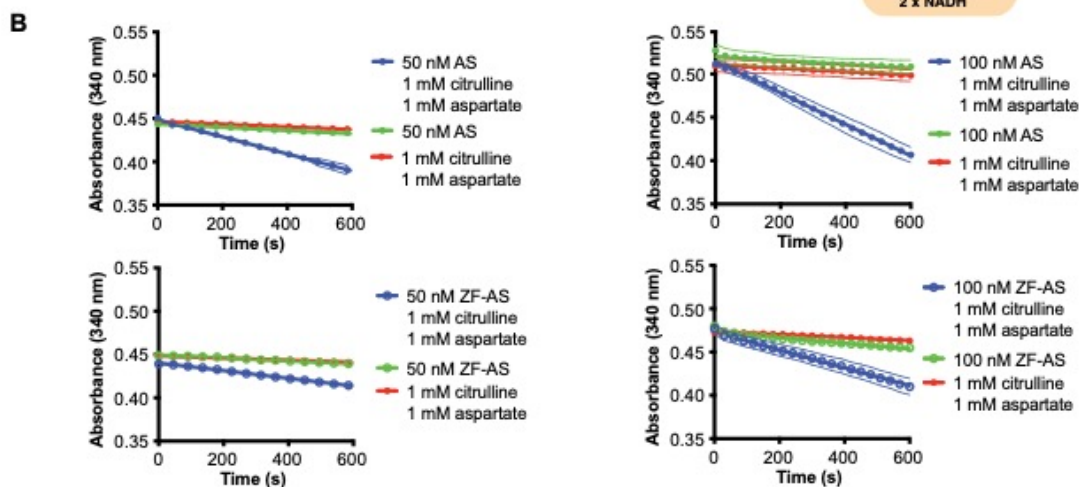
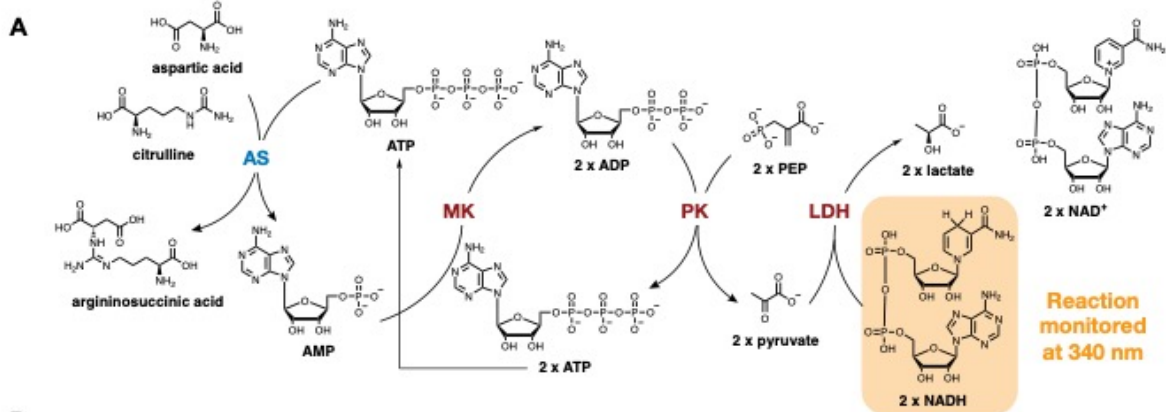


**Figure 5.6.** (A) Reaction scheme illustrating the series of coupled enzymatic reactions used to monitor the catalytic activity of AS and ZF-AS. This continuous spectrophotometric assay quantifies the production of AMP by AS and ZF-AS by monitoring the time-dependent loss in absorbance of NADH. AS = argininosuccinate synthetase, MK = myokinase, PK = pyruvate kinase, LDH = lactate dehydrogenase (B) Plots illustrating the time-dependent loss in NADH absorbance in the presence of either 50 or 100 nM AS or ZF-AS. Reaction occurs only when both substrates (citrulline and aspartic acid) and enzyme (AS or ZF-AS) are present. (C) Plots illustrating the lack of dependence of the reaction rate (time-dependent loss in NADH absorbance) on the concentration of the enzymes that comprise the coupled assay. Reactions contain 100 nM of AS or ZF-AS and either 1X or 2X MK, PK, and LDH. Blank reactions include 1X or 2X enzyme mix (MK, PK, and LDH) but not AS or ZF-AS. (D) Plot illustrating that the absorbance of NADH at 340 nm is linearly related to [AMP] between 0 and 0.06 mM. (E) Plots illustrating the time-dependent loss in NADH absorbance in presence of 0–500  $\mu$ M citrulline and 100 nM AS or ZF-AS. (F) Plots illustrating the lack of time-dependent loss in NADH absorbance in the presence of 0–500  $\mu$ M citrulline and 100 nM heat denatured (incubated at 95 °C for 10 min) AS or ZF-AS.

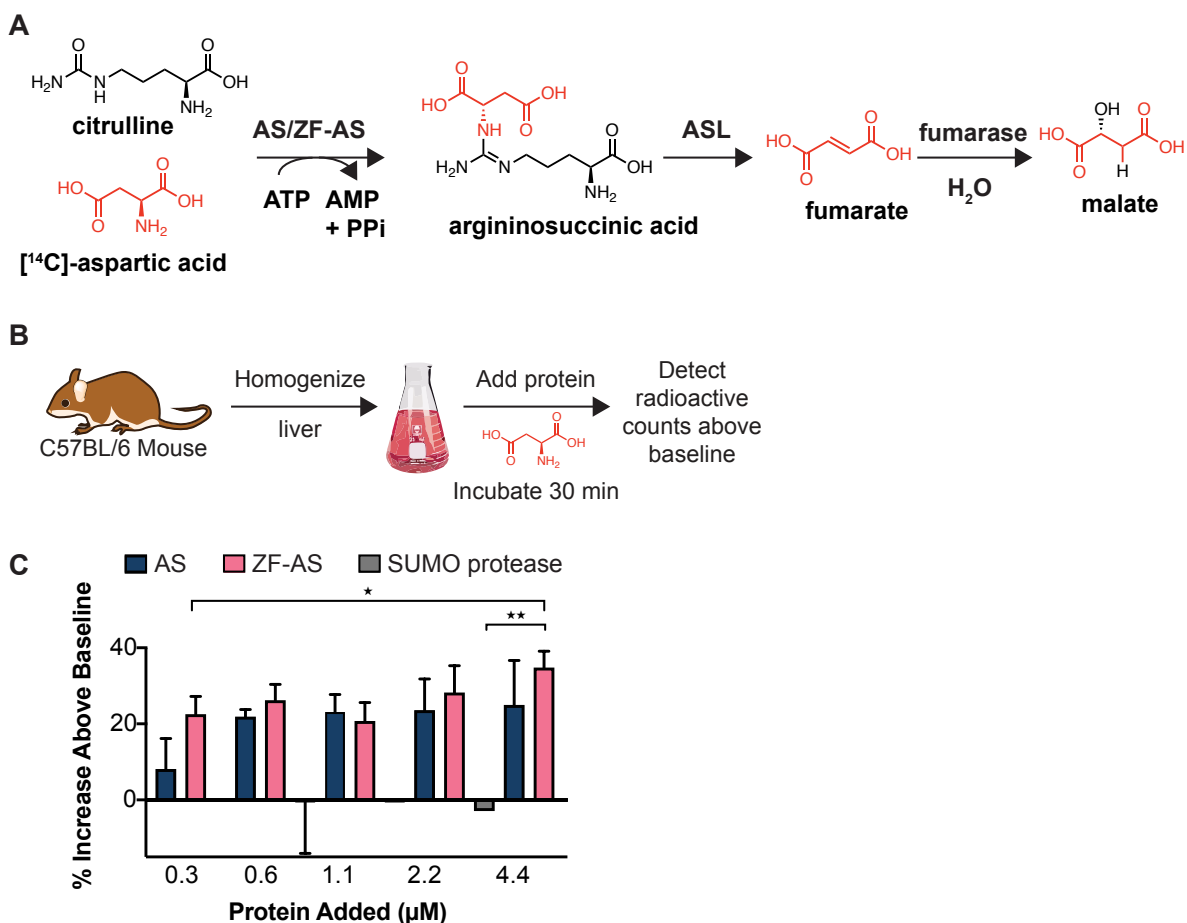


**Figure 5.7.** AS and ZF-AS are active when added to mouse liver homogenate. (A) The activity of AS and ZF-AS was assayed by monitoring the conversion of [<sup>14</sup>C]-aspartic acid, citrulline, and ATP to [<sup>14</sup>C]-argininosuccinic acid, AMP, and PP<sub>i</sub>. [<sup>14</sup>C]-Argininosuccinic acid is subsequently converted to [<sup>14</sup>C]-fumarate by argininosuccinate lyase (ASL) and into [<sup>14</sup>C]-malate by fumarase. (B) Livers (containing endogenous AS, ASL, and fumarase) of C57BL/6 mice were homogenized. [<sup>14</sup>C]-aspartic acid and either 0.3–4.4 μM AS or ZF-AS were added to the homogenate and the mixture incubated for 30 min. After incubation, the homogenate was applied to a cation exchange column (Bio-Rad BT AG 50W-X8 Resin) which retains only [<sup>14</sup>C]-aspartic acid; the eluted [<sup>14</sup>C] labeled fumarate and malate were then quantified with a scintillation counter (Packard Topcount NxT). (C) Bar graph showing the percent increase over baseline signal of the combined [<sup>14</sup>C]-fumarate and [<sup>14</sup>C]-malate signal observed after incubation with increasing AS, ZF-AS, or SUMO protease after 30 min incubation with mouse liver homogenate. Since mouse liver homogenate contains endogenous AS, we analyzed the percent increase of radioactivity above the endogenous activity of AS (defined as baseline). The average percent increase above baseline of each AS condition (0.3–4.4 μM) was statistically compared to the average percent increase above baseline of each ZF-AS condition (0.3–4.4 μM) using an unpaired t-test, two-tailed using Prism (Version 8.4.3). The average percent increase above baseline of each SUMO protease condition

(1.1–4.4  $\mu\text{M}$ ) was statistically compared to the average percent increase above baseline of either AS or ZF-AS conditions (1.1–4.4  $\mu\text{M}$ ) using an unpaired t-test, two-tailed. \*\*\*\* $p \leq 0.001$ , \*\*\* $p \leq 0.01$ , \*\* $p \leq 0.05$ , \* $p < 0.1$ .

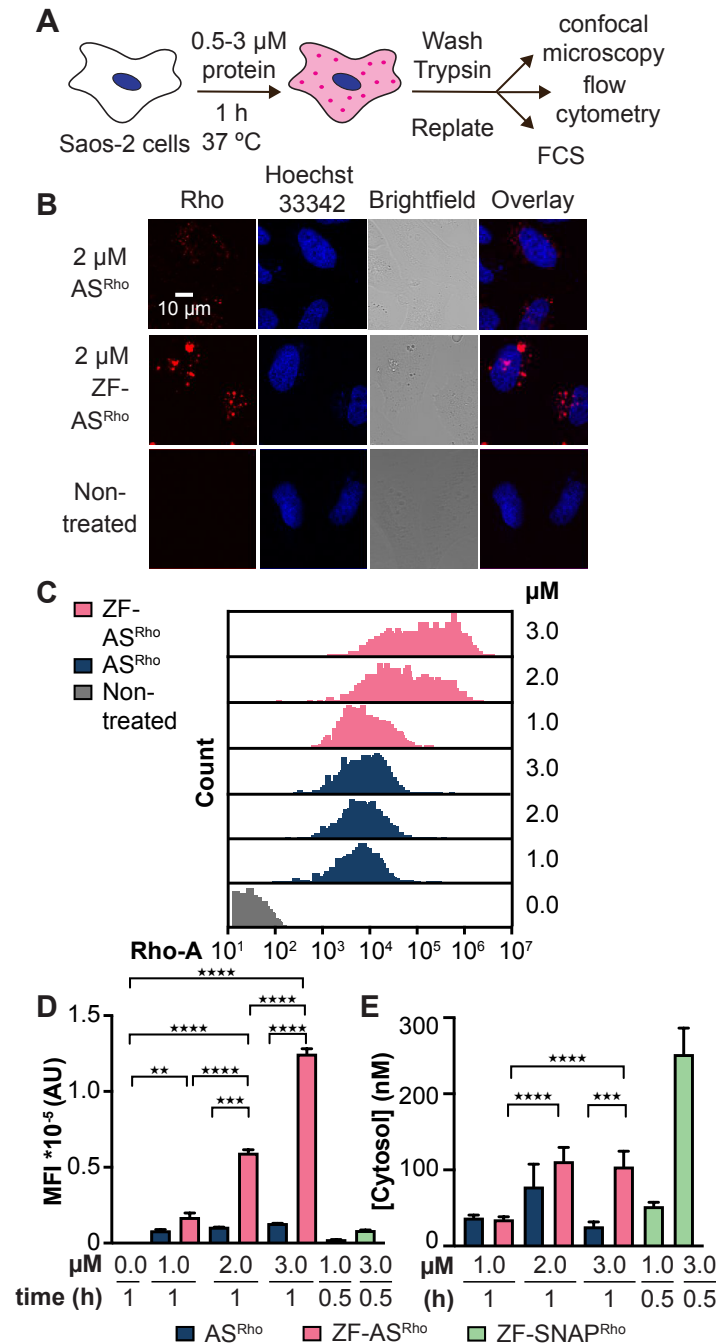


**Figure 5.8.** (A) Scheme illustrating confocal microscopy, flow cytometry, and fluorescence correlation spectroscopy (FCS) workflow. Saos-2 cells were treated with 1–3  $\mu\text{M}$  of AS<sup>Rho</sup> or ZF-AS<sup>Rho</sup> for 1 h. Cells were washed, treated with trypsin, and either screened using flow cytometry or re-plated and imaged using confocal microscopy and FCS. (B) Total cellular uptake of AS<sup>Rho</sup> and ZF-AS<sup>Rho</sup> assessed using confocal microscopy. Live cell images of Saos-2 cells treated with 2  $\mu\text{M}$  of the indicated protein for 1 h. Scale bar = 10  $\mu\text{m}$ . (C) Histograms and (D) bar plots illustrating total cellular uptake of 1–3  $\mu\text{M}$  AS<sup>Rho</sup> or ZF-AS<sup>Rho</sup> during a 1 h incubation at 37  $^{\circ}\text{C}$ . Data for ZF-

SNAP<sup>Rho</sup> were previously published.<sup>9</sup> MFI values represent the median fluorescence intensity of cells (10,000 cells each). Error bars represent the standard error of the mean. The MFI values of AS<sup>Rho</sup> at each concentration (1–3  $\mu$ M) were statistically compared to the MFI values of ZF-AS<sup>Rho</sup> at each concentration (1–3  $\mu$ M). \*\*\*\* $p \leq 0.0001$ , \*\*\* $p \leq 0.001$ , \*\* $p \leq 0.01$ , \* $p \leq 0.05$ ; one-way analysis of variance (ANOVA) followed by Tukey's multiple comparisons test. (E) Cytosolic access of AS<sup>Rho</sup> and ZF-AS<sup>Rho</sup> assessed using fluorescence correlation spectroscopy. Bar plot illustrating the cytosolic concentrations achieved in Saos-2 cells after a 1 h incubation with 1–3  $\mu$ M of AS<sup>Rho</sup> and ZF-AS<sup>Rho</sup>. The average intracellular concentrations of each AS<sup>Rho</sup> treatment condition (1–3  $\mu$ M) were statistically compared to the average intracellular concentration of each ZF-AS<sup>Rho</sup> treatment condition (1–3  $\mu$ M) using an one-way ANOVA followed by Sidak's multiple comparisons test. \*\*\*\* $p \leq 0.0001$ , \*\*\* $p \leq 0.001$ , \*\* $p \leq 0.01$ , \* $p \leq 0.05$ .

### Saos-2 Cells

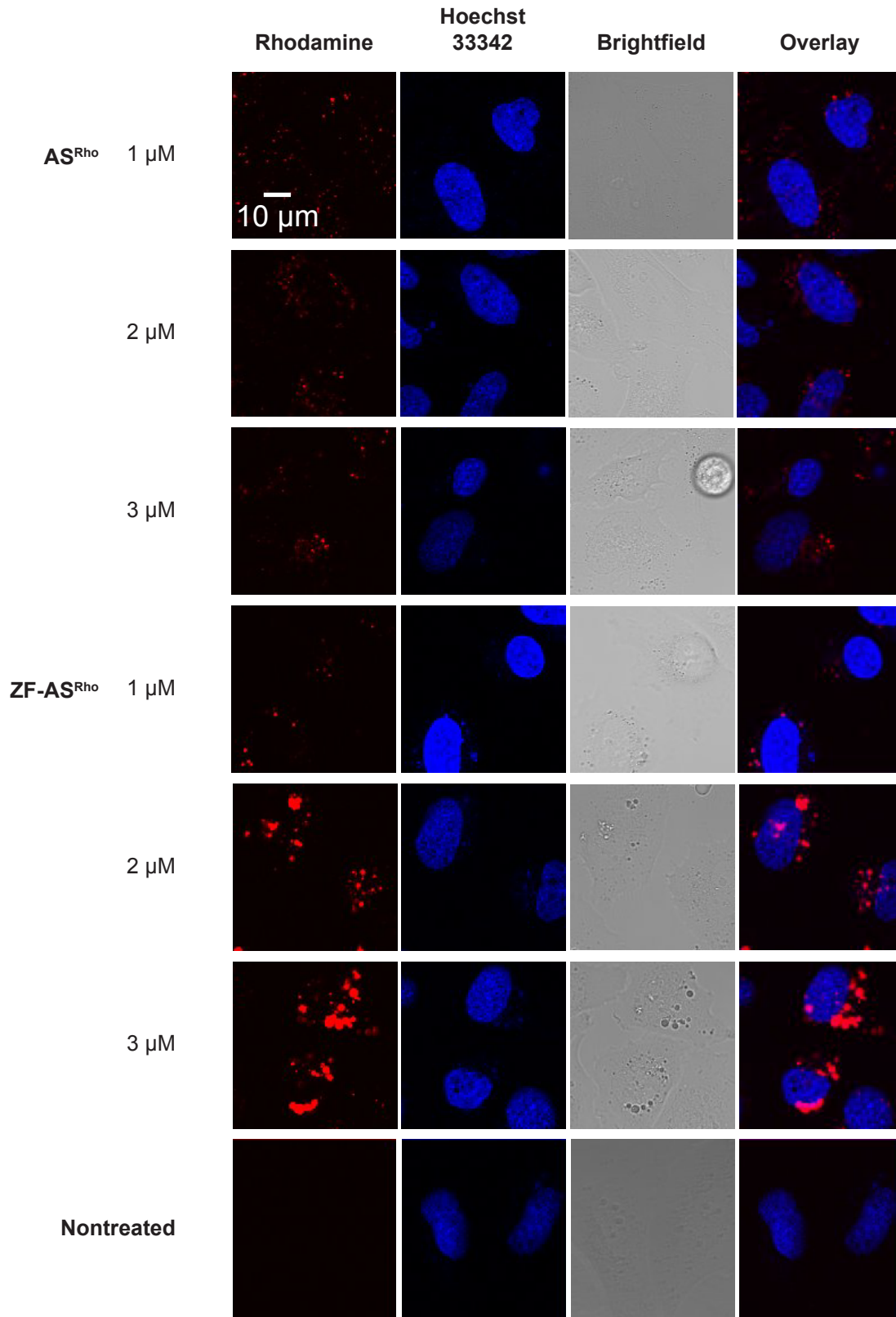


**Figure 5.9.** Saos-2 cells were treated with 1–3  $\mu\text{M}$   $\text{AS}^{\text{Rho}}$  or  $\text{ZF-AS}^{\text{Rho}}$  for 1 h. After treatment, cells were washed, treated with trypsin to remove any surface-bound protein, and re-plated on a fibronectin-coated microscopy slide. The lissamine rhodamine B moiety of  $\text{AS}^{\text{Rho}}$  and  $\text{ZF-AS}^{\text{Rho}}$  was excited with a diode-pumped solid-state (DPSS) 561-10 nm laser; a 405 nm laser was used to excite Hoescht 33342 (representing the nucleus); a halogen lamp was used to obtain brightfield images. The overlay panel shows both the rhodamine (Rho) and Hoescht 33342 signals.

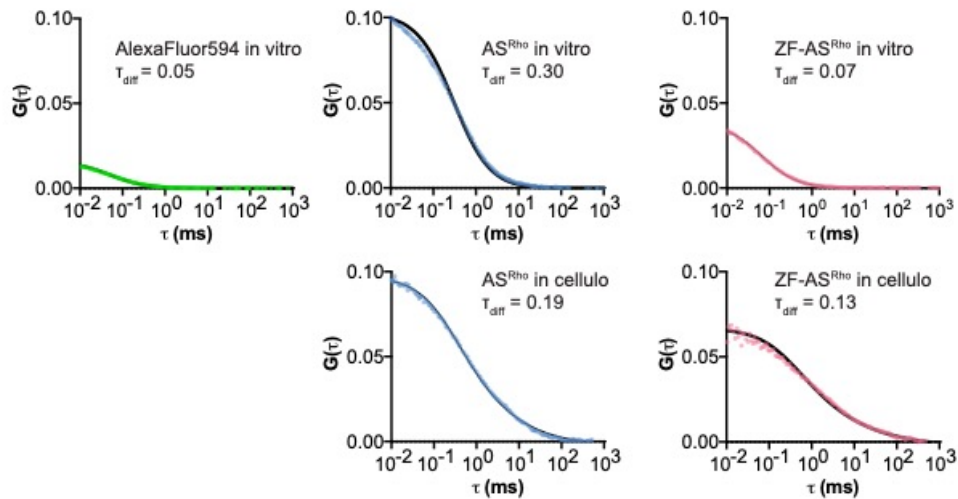


**Figure 5.10.** Autocorrelation traces ( $G(\tau)$ ) of 100 nM AlexaFluor594 (in MilliQ water),  $AS^{Rho}$  (in DMEM), and ZF- $AS^{Rho}$  (in DMEM) *in vitro*. *In cellulo* traces for  $AS^{Rho}$  and ZF- $AS^{Rho}$  in Saos-2 cells. *In vitro* traces (green, blue, pink) were fit to a 3D diffusion model (black curve). *In cellulo* traces (blue, pink) were fit to a 3D anomalous diffusion model (black curve).  $\tau_{diff}$  is the diffusion time in ms. All autocorrelation curves were obtained using the methods described in Knox *et al.*<sup>2</sup>

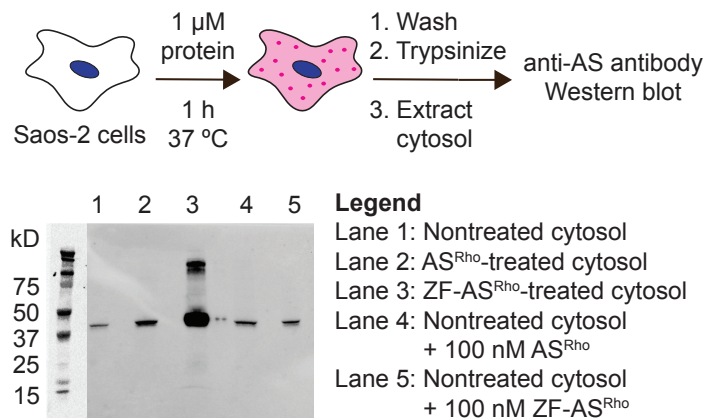


**Figure 5.11.** Cytosolic fractionation of Saos-2 cells after treatment with 1  $\mu$ M ZF- $AS^{Rho}$  and  $AS^{Rho}$  visualized by Western blot using an anti-AS antibody (Cell Signaling Technology). In addition to the non-treated,  $AS^{Rho}$ -treated, and ZF- $AS^{Rho}$ -treated samples (lanes 1–3), 100 nM of either  $AS^{Rho}$  (lane 4) or ZF- $AS^{Rho}$  (lane 5) were added to non-treated cytosol.

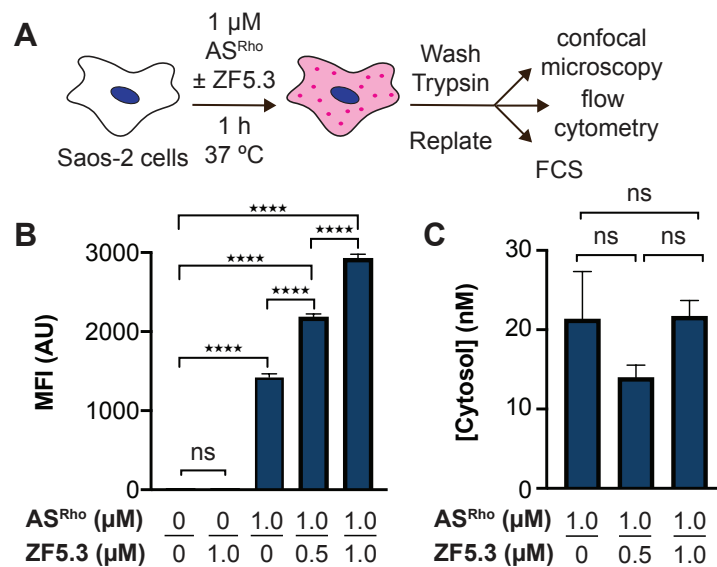


**Figure 5.12.** Assessment of co-administration of AS<sup>Rho</sup> and ZF5.3. (A) Workflow of experiment. Briefly, Saos-2 cells were treated with 1  $\mu\text{M AS}^{\text{Rho}}$  with 0–1  $\mu\text{M ZF5.3}$  for 1 h and worked up as described in the Supplementary Information. (B) Bar plot illustrating total cellular uptake of 1  $\mu\text{M AS}^{\text{Rho}}$  with 0–1  $\mu\text{M ZF5.3}$  during a 1 h incubation at 37  $^{\circ}\text{C}$ . Unlabeled ZF5.3 was prepared as previously described.<sup>9</sup> MFI values represent the median fluorescence intensity of cells (10,000 cells each). Error bars represent the standard error of the mean. The MFI values of nontreated cells were statistically compared to the MFI values of AS<sup>Rho</sup> of each treatment concentration. Additionally, the MFI values of each AS<sup>Rho</sup> treatment condition were statistically compared to the MFI values to each other using an one-way analysis of variance (ANOVA) followed by Tukey’s multiple comparisons test. (C) Cytosolic access of AS<sup>Rho</sup> assessed using fluorescence correlation spectroscopy. Bar plot illustrating the cytosolic concentrations achieved in Saos-2 cells after a 1 h incubation with 1  $\mu\text{M AS}^{\text{Rho}}$  with 0–1  $\mu\text{M ZF5.3}$ . The average intracellular concentrations of each AS<sup>Rho</sup> treatment condition were statistically compared to the average intracellular concentration of each treatment condition using an one-way ANOVA followed by Tukey’s multiple comparisons test. \*\*\*\* $p \leq 0.0001$ , \*\*\* $p \leq 0.001$ , \*\* $p \leq 0.01$ , \* $p \leq 0.05$ , ns = nonsignificant.

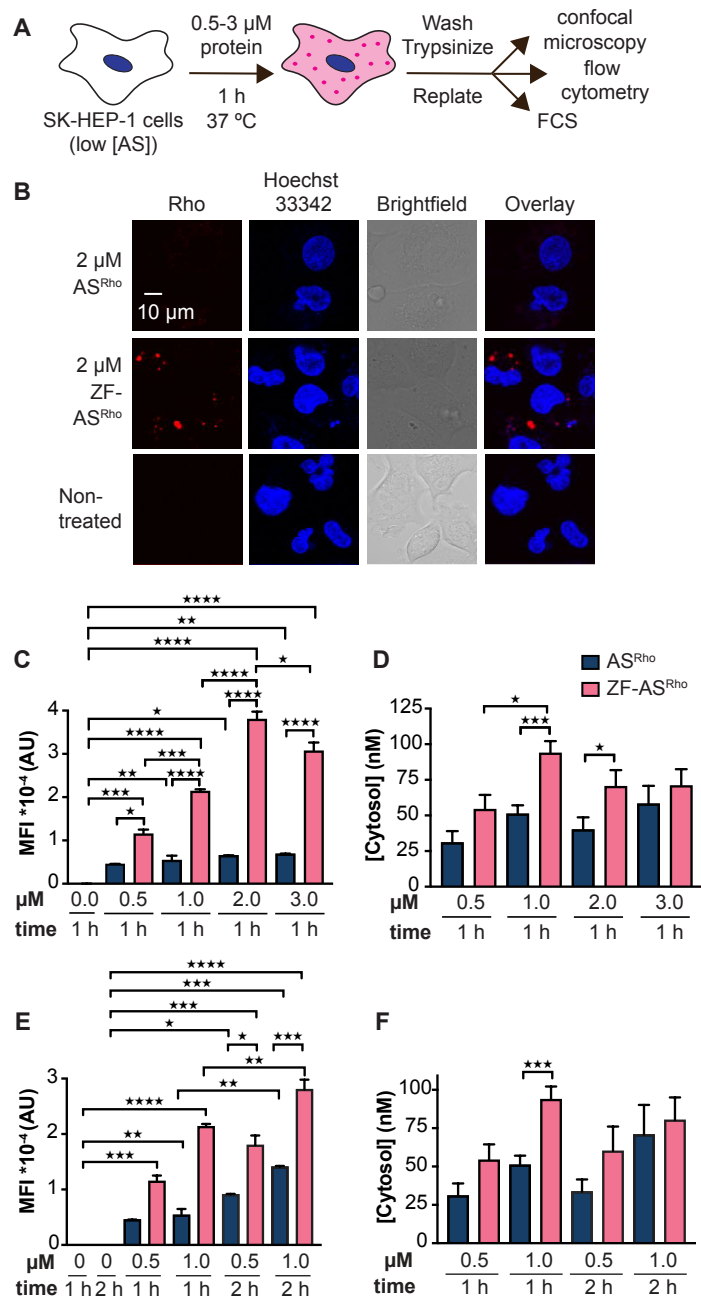


**Figure 5.13.** (A) Scheme of confocal microscopy, flow cytometry, and fluorescence correlation spectroscopy (FCS) experiments. SK-HEP-1 cells were treated with 0.5–3  $\mu\text{M}$  of AS<sup>Rho</sup> or ZF-AS<sup>Rho</sup> for 1 or 2 h. Cells were washed, trypsinized, and either used for flow cytometry or re-plated and evaluated by confocal microscopy and FCS. (B) Total cell uptake of AS<sup>Rho</sup> and ZF-AS<sup>Rho</sup> assessed by confocal microscopy. Live cell images of SK-HEP-1 cells treated with 2  $\mu\text{M}$  of protein for 1 h. Scale bar = 10  $\mu\text{m}$ . (C) Bar plots illustrating total cellular uptake of AS<sup>Rho</sup> and ZF-AS<sup>Rho</sup> at 0.5–3  $\mu\text{M}$  during a 1 h incubation. MFI values represent the median fluorescence intensity of cells (10,000 cells each). Error bars represent the standard error of the mean. The MFI values of AS<sup>Rho</sup> at each concentration (0.5–3  $\mu\text{M}$ ) were statistically compared to the MFI values of

ZF-AS<sup>Rho</sup> at each concentration (0.5–3  $\mu$ M). \*\*\*\* $p \leq 0.0001$ , \*\*\* $p \leq 0.001$ , \*\* $p \leq 0.01$ , \* $p \leq 0.05$ ; one-way analysis of variance (ANOVA) followed by Tukey's multiple comparisons test. (D) Bar plot of cytosolic concentrations in SK-HEP-1 cells with a 1 h treatment of 0.5–3  $\mu$ M of AS<sup>Rho</sup> or ZF-AS<sup>Rho</sup>. The average intracellular concentrations of each AS<sup>Rho</sup> treatment condition (0.5–3  $\mu$ M) were statistically compared to the average intracellular concentration of each ZF-AS<sup>Rho</sup> treatment condition (0.5–3  $\mu$ M) using an unpaired t-test, two-tailed. \*\*\*\* $p \leq 0.0001$ , \*\*\* $p \leq 0.001$ , \*\* $p \leq 0.01$ , \* $p \leq 0.05$ . (E) Bar plots illustrating total cellular uptake of AS<sup>Rho</sup> and ZF-AS<sup>Rho</sup> at 0.5–1  $\mu$ M during a 1 or 2 h incubation. MFI values represent the median fluorescence intensity of cells (10,000 cells each). Error bars represent the standard error of the mean. MFI values corresponding to each AS conjugate were statistically compared to all other protein samples. \*\*\*\* $p \leq 0.0001$ , \*\*\* $p \leq 0.001$ , \*\* $p \leq 0.01$ , \* $p \leq 0.05$ ; one-way analysis of variance (ANOVA) followed by Tukey's multiple comparisons test. (F) Bar plot of cytosolic concentrations in SK-HEP-1 cells with a 1 or 2 h treatment of 0.5–1  $\mu$ M of AS<sup>Rho</sup> or ZF-AS<sup>Rho</sup>. The average intracellular concentrations of each AS<sup>Rho</sup> treatment condition (0.5–1  $\mu$ M, 1 or 2 h) were statistically compared to the average intracellular concentration of each ZF-AS<sup>Rho</sup> treatment condition (0.5–3  $\mu$ M) using an unpaired t-test, two-tailed. \*\*\*\* $p \leq 0.0001$ , \*\*\* $p \leq 0.001$ , \*\* $p \leq 0.01$ , \* $p \leq 0.05$ .

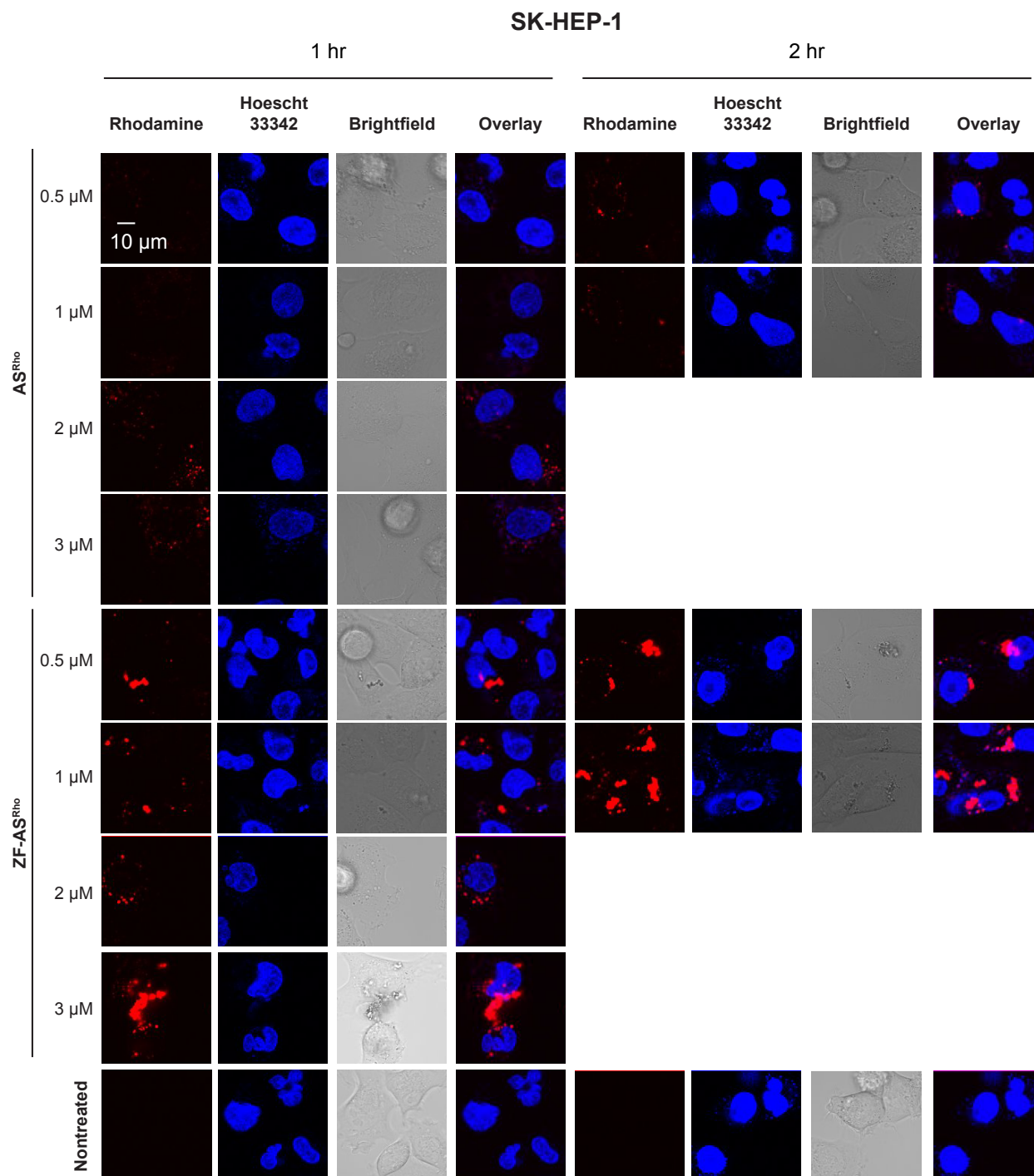


**Figure 5.14.** SK-HEP-1 cells were treated with 0.5–3  $\mu$ M AS<sup>Rho</sup> or ZF-AS<sup>Rho</sup> for 1 or 2 h. After treatment, cells were washed, treated with trypsin to remove any surface bound protein, and re-plated on a fibronectin-coated microscopy slide for confocal microscopy. Lissamine rhodamine B (representing AS<sup>Rho</sup> or ZF-AS<sup>Rho</sup>) was excited with a diode-pumped solid-state (DPSS) 561-10 nm laser; a 405 nm laser was used to excite Hoescht 33342 (representing the nucleus); a halogen lamp was used to obtain brightfield images. The overlay panel shows both the rhodamine (Rho) and Hoescht 33342 signals.

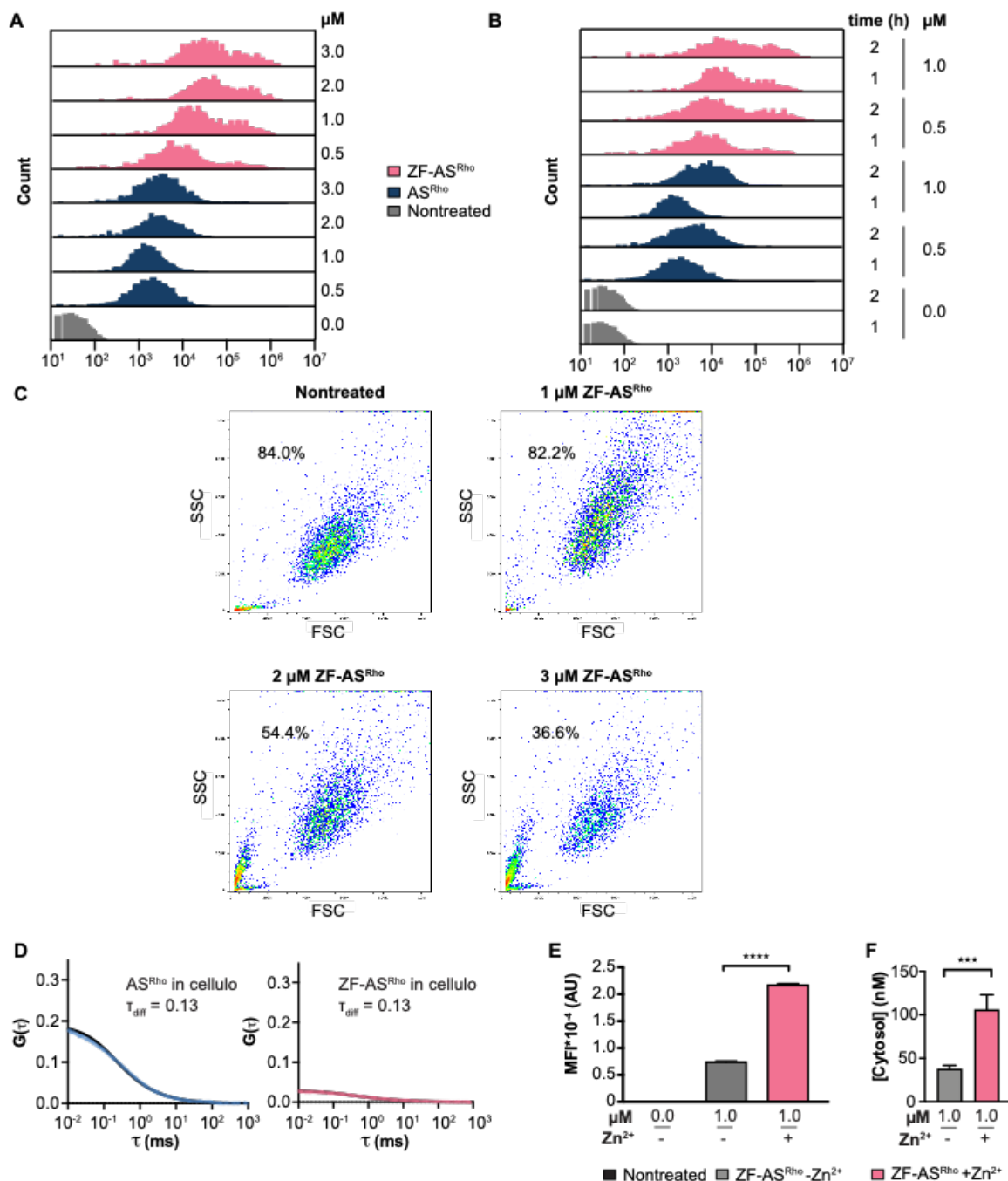


**Figure 5.15.** (A) Histograms from flow cytometry of AS<sup>Rho</sup> and ZF-AS<sup>Rho</sup> in SK-HEP-1 cells after a 1 h uptake. (B) Histograms from flow cytometry of AS<sup>Rho</sup> and ZF-AS<sup>Rho</sup> in SK-HEP-1 cells after a 2 h uptake. (C) Flow cytometry scatter plots showing cell health of the SK-HEP-1 populations for non-treated cells and cells treated with 1–3 μM ZF-AS<sup>Rho</sup>. The percentages on the graphs represent the fraction of total cells (10,000) that were gated in the healthy cell population. (D) *In cellulo* autocorrelation traces ( $G(\tau)$ ) of AS<sup>Rho</sup> and ZF-AS<sup>Rho</sup> for SK-HEP-1 cells. Traces (blue, pink) were fit to a 3D anomalous diffusion model (black curve).  $\tau_{diff}$  is the diffusion time in ms. (E) Bar plot illustrating total

cellular uptake of SK-HEP-1 cells incubated for 1 h with 1  $\mu\text{M}$  ZF-AS<sup>Rho</sup> with or without the presence of  $\text{Zn}^{2+}$ . MFI values represent the median fluorescence intensity of cells (10,000 cells each). Error bars represent the standard error of the mean. MFI values of the two samples were statistically compared to each other using an unpaired t-test, two-tailed. (F) Bar plot of cytosolic concentrations of SK-HEP-1 cells incubated for 1 h with 1  $\mu\text{M}$  ZF-AS<sup>Rho</sup> with or without the presence of  $\text{Zn}^{2+}$ . The average intracellular concentrations of the two samples were statistically compared to each other using an unpaired t-test, two-tailed. \*\*\*\* $p \leq 0.0001$ , \*\*\* $p \leq 0.001$ , \*\* $p \leq 0.01$ , \* $p \leq 0.05$ .

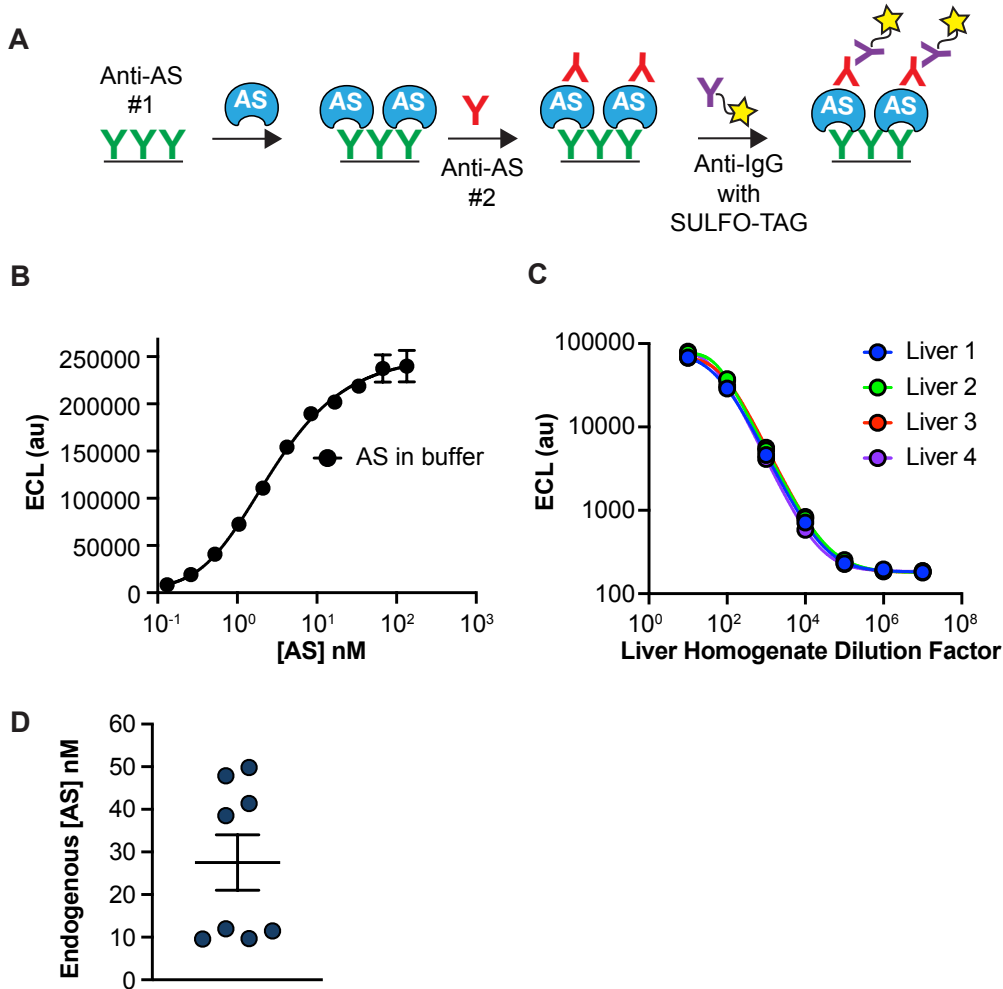


**Figure 5.16.** (A) Scheme for detection of AS in mice using a modified sandwich enzyme-linked immunosorbent assay (ELISA) performed using 96-well plates coated with ASS1 (D404B) XP Rabbit mAB (Cell Signaling Technology). After addition of AS (or liver samples), a second anti-AS antibody was added (ASS1 Polyclonal, Thermo Fisher Scientific). Donkey anti-Goat-SULFO-TAG™ (MSD), an anti-IgG antibody, allowed for the detection of AS proteins via electrochemiluminescence (ECL). The ECL signal was analyzed with a MSD Sector Imager. (B) AS detection in Superblock to provide a standard curve to calculate concentrations of AS in mice. Data were fit to a 5-PL curve<sup>79</sup> ( $y = ((A-D)/((1+(x/C)^B)^G))+D$ ), where  $A = 4.613e+03$ ,  $B = 0.729$ ,  $C = 2.668$ ,  $D = 2.50e+05$ , and  $G = 4.244$ .  $R^2=0.999$ . (C) AS detection of AS in liver homogenate (four C57BL/6 mice analyzed). Data were fit to a 5-PL curve where for liver 1:  $A=7.82e+04$ ,  $B=1.12$ ,  $C=47$ ,  $D=180$ , and  $G=0.831$ ;  $R^2=1$ . Liver 2:  $A=7.91e+04$ ,  $B=1.96$ ,  $C=49.4$ ,  $D=179$ , and  $G=0.465$ ;  $R^2=1$ . Liver 3:  $A=6.98e+04$ ,  $B=1.52$ ,  $C=63.9$ ,  $D=174$ , and  $G=0.606$ ;  $R^2=1$ . Liver 4:  $A=9.13e+04$ ,  $B=1.19$ ,  $C=45$ ,  $D=185$ , and  $G=0.845$ ;  $R^2=1$ . (D) Endogenous AS concentrations in liver homogenate at various dilution factors within the linear response of the assay (dilution factors 1:10 and 1:100). The range of endogenous AS in C57BL/6 mouse liver is  $11 \pm 1$  to  $44 \pm 5$  nM.

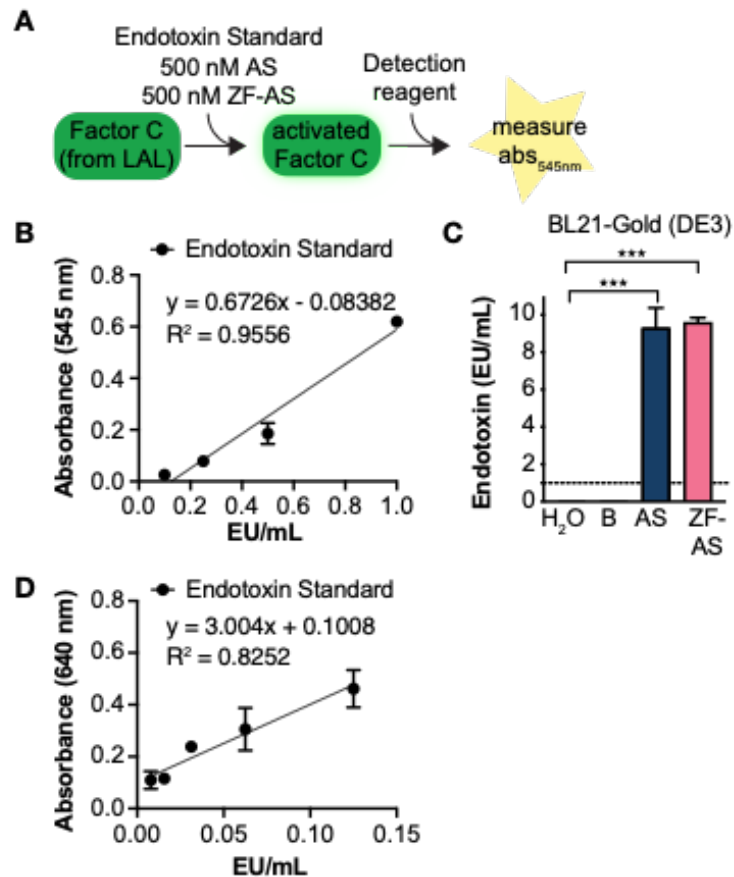


**Figure 5.17.** (A) Experimental scheme for the *Limulus* amebocyte lysate (LAL) assay. The lipid tail of endotoxin binds to and activates Factor C (a protease present in LAL), which allows for cleavage of a proprietary chromophore from a peptide. The production of the chromophore is monitored by absorbance at 545 nm. (B) Graph showing the absorbance at 545 nm as a function of endotoxin concentration (0.1–1 EU/mL). Linear regression was performed using Prism (Version 8.4.3). Error is standard error. (C) Determination via LAL assay of endotoxin contamination (EU/mL) of MilliQ water, buffer (30 mM HEPES (pH 7.5), 500 mM NaCl, 10% glycerol), 3  $\mu$ M AS, and 3  $\mu$ M ZF-AS. Values were obtained using the linear regression in (B). Error is standard error of the mean. The average endotoxin level of MilliQ water was statistically compared to the average endotoxin level of each protein sample using an one-way ANOVA followed by Dunnett's multiple comparisons test. \*\*\*\* $p \leq 0.0001$ , \*\*\* $p \leq 0.001$ , \*\* $p \leq 0.01$ , \* $p \leq 0.05$ . (D) Example graph showing the absorbance at 640 nm as a function of endotoxin concentration (0.0078–0.125 EU/mL). Linear regression was performed using Prism (Version 8.4.3). Endotoxin standards were prepared and analyzed each time the assay was conducted. Error is standard error.

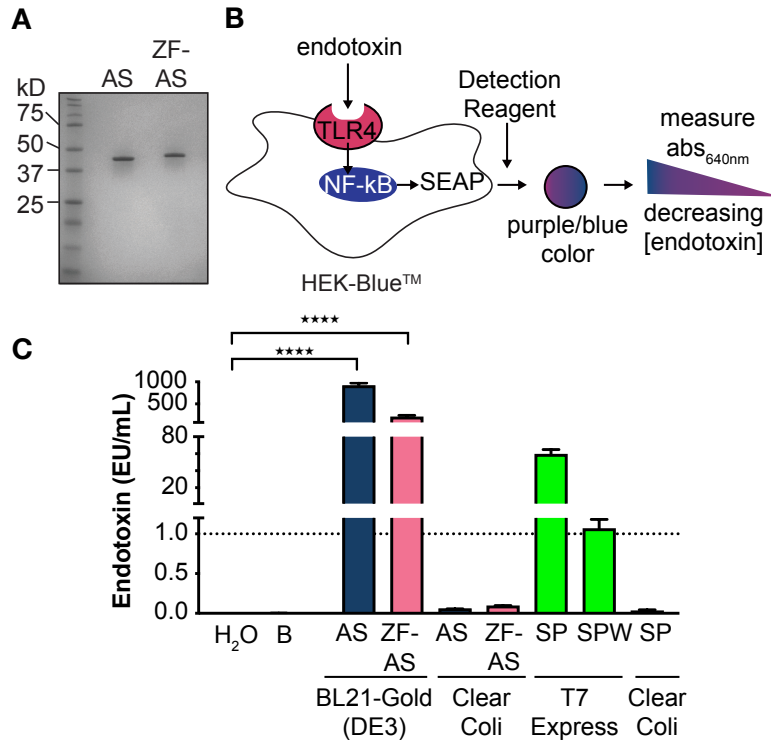


**Figure 5.18.** (A) SDS-PAGE analysis illustrating final purity of AS and ZF-AS from ClearColi® for *in vivo* mouse study use. Final purity of both AS and ZF-AS was >99%. (B) Experimental scheme for the HEK-Blue™ cell-based assay, which monitors the binding of endotoxin to the TLR4 receptor and activates downstream cellular signals (NF-κB production). When NF-κB is activated, a secreted embryonic alkaline phosphatase (SEAP) is produced and secreted into the media. The absorbance of a proprietary SEAP detection reagent is monitored at 640 nm. (C) Endotoxin levels (EU/mL) as determined from the HEK-Blue hTLR4 response with HEK-Blue™ Detection. The HEK-Blue hTLR4 assay measures the interaction of the hexa-acyl chain of endotoxin (and can distinguish the modified ClearColi® acyl chain). The buffer (denoted as B) was 30 mM HEPES (pH 7.5), 500 mM NaCl, and 10% glycerol. SUMO protease purified from the T7 Express *E. coli* strain with an initial 30-40 CV 0.1% Triton X-114 wash during the IMAC step (**Figure 5.2A**) is denoted as SP, SUMO protease further purified with an additional 88 CV 0.1% Triton X-114 wash during the IMAC step is denoted as SPW, and SUMO protease purified from ClearColi® is denoted as SP. Error is standard error of the mean. The average endotoxin level of MilliQ water was statistically compared to the average endotoxin level of each protein sample using an one-way ANOVA followed by Dunnett's multiple comparisons test. \*\*\*\* $p \leq 0.0001$ , \*\*\* $p \leq 0.001$ , \*\* $p \leq 0.01$ , \* $p \leq 0.05$ .

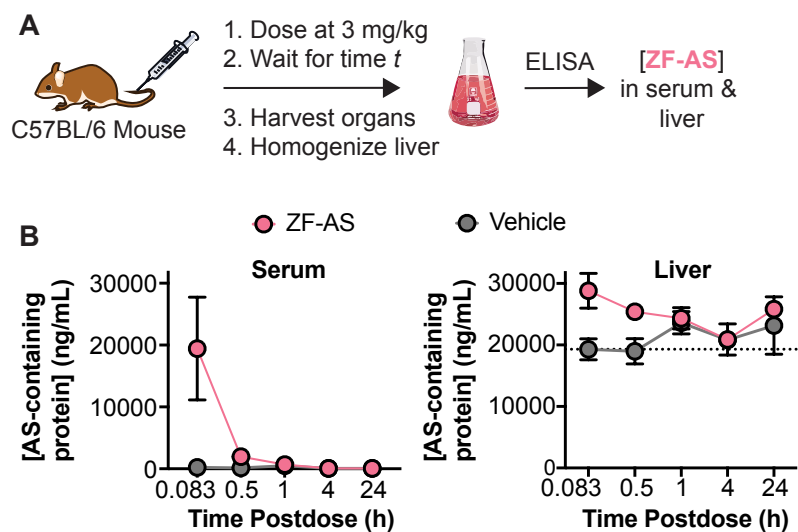


**Figure 5.19.** (A) Scheme for dosing of ZF-AS into C57BL/6 mice. Mice were injected with either 3 mg/kg ZF-AS (in DPBS) or vehicle (DPBS) into the tail vein. Three mice were sacrificed at each time point (0.083, 0.5, 1, 4, 24 h), their organs harvested, blood processed to serum, and liver processed to homogenate. The concentration of ZF-AS present in serum and liver samples was evaluated using an enzyme-linked immunosorbent assay (ELISA). (B) Concentration of AS-containing proteins detected in serum or liver over time.

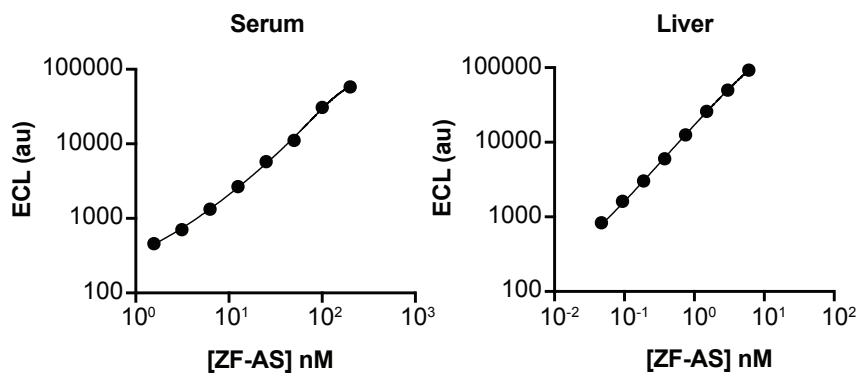


**Figure 5.20.** Linearity of ZF-AS in serum and liver homogenate (as detected in assay buffer) detected by electrochemiluminescence (ECL) of the SULFO-TAG™ after ELISA. ZF-AS was added to C57BL/6 serum or assay buffer (Superblock) and the signal produced was monitored as a function of ZF-AS concentration. The curve produced for assay buffer was used in liver determination during animal dosing. Data were fit to a 4-PL regression function ( $y = \frac{(A-D)}{1+(x/C)^B} + D$ ). For serum, relative weighting was used and  $A=261$ ,  $B=1.20$ ,  $C=1258$ , and  $D=5.97e+5$ ;  $R^2=0.99$ . For liver,  $A=123.9$ ,  $B=1.27$ ,  $C=18.39$ , and  $D=3.97e+5$ ;  $R^2=1.00$ .

## 5.7 Tables

**Table 5.1.** Mass identities of products obtained from AS and ZF-AS Rho labeling reactions determined by electrospray mass spectrometry.

Observed Mass (m/z)	Protein Product	Expected Mass (m/z)
47813	AS <sup>Rho</sup>	47810
51191	ZF-AS <sup>Rho</sup>	51188
46973	AS-LPET	46971
47047	AS-LPETG with a phosphorylation <sup>80</sup> potentially at T219 of AS <sup>81</sup>	47051
50352	ZF-AS-LPET	50348
50428	ZF-AS-LPET with a phosphorylation <sup>80</sup> potentially at T219 of AS <sup>81</sup>	50428
50504	ZF-AS-LPETG with a phosphorylation <sup>80</sup> potentially at T219 of AS <sup>81</sup>	50503
50538	ZF-AS-LPETGG with a phosphorylation <sup>80</sup> potentially at T219 of AS <sup>81</sup>	50542

**Table 5.2.** Comparison of catalytic constants determined for AS and ZF-AS variants purified from BL21-Gold (DE3) *E. coli* or ClearColi™ alongside literature values. Where applicable, literature values were converted to  $k_{cat}$  by multiplying the reported specific activity (in  $\mu\text{mol}/(\text{h}\cdot\text{mg protein})$ ) by the molecular weight of AS (46.530 mg/ $\mu\text{mol}$ ).

Protein	Expression System	$k_{cat}$ ( $\text{s}^{-1}$ )	$K_M$ ( $\mu\text{M}$ )
AS	Beef liver	0.1-0.6 <sup>38</sup>	46 <sup>43</sup>
AS (human)	BL21(DE3)pLysS	0.98 <sup>39</sup>	56-112 <sup>39,40</sup>
AS	Human liver	0.0006-1 <sup>33,41,42</sup>	0.01-30 <sup>33,41,42</sup>
AS	BL21-Gold (DE3)	0.39 $\pm$ 0.01	52 $\pm$ 5
AS	ClearColi™	0.40 $\pm$ 0.02	33 $\pm$ 6
AS <sup>Rho</sup>	BL21-Gold (DE3)	0.44 $\pm$ 0.03	34 $\pm$ 8
ZF-AS	BL21-Gold (DE3)	0.16 $\pm$ 0.01	33 $\pm$ 10
ZF-AS	ClearColi™	0.19 $\pm$ 0.01	11 $\pm$ 3
ZF-AS <sup>Rho</sup>	BL21-Gold (DE3)	0.32 $\pm$ 0.05	6 $\pm$ 8

## 5.8 Acknowledgements

We are grateful to Charles River Laboratories for the large-scale preparation of AS and ZF-AS in ClearColi®, *in vivo* mouse work, and liver homogenate studies, Dr. Matthew Wright at Genentech for guidance on evaluating liver delivery, Dr. Angela Steinauer for FCS training, and Dr. Joseph Wolenski for managing the Science Hill Imaging Facility at Yale University. We are also grateful to Susan Marqusee, Miriam Hood, and Eva Gerber for obtaining CD data and to Anthony Iavarone at QB3/Chemistry Mass Spectrometry Facility at UC Berkeley for mass spectrometry analysis of AS<sup>Rho</sup> and ZF-AS<sup>Rho</sup>.

## 5.9 References

- (1) Mullard, A. 2019 FDA Drug Approvals. *Nat. Rev. Drug Discov.* **2020**, *19* (2), 79–84. <https://doi.org/10.1038/d41573-020-00001-7>.
- (2) Dimitrov, D. S. Therapeutic Proteins. *Methods Mol. Biol. Clifton NJ* **2012**, *899*, 1–26. [https://doi.org/10.1007/978-1-61779-921-1\\_1](https://doi.org/10.1007/978-1-61779-921-1_1).
- (3) Global pharmaceutical revenue by technology 2012-2026 <https://www-statista-com.libproxy.berkeley.edu/statistics/309450/pharma-revenues-worldwide-prescription-drug-and-otc-by-technology/> (accessed Nov 7, 2020).
- (4) Frankel, A. D.; Pabo, C. O. Cellular Uptake of the Tat Protein from Human Immunodeficiency Virus. *Cell* **1988**, *55* (6), 1189–1193. [https://doi.org/10.1016/0092-8674\(88\)90263-2](https://doi.org/10.1016/0092-8674(88)90263-2).
- (5) Green, M.; Loewenstein, P. M. Autonomous Functional Domains of Chemically Synthesized Human Immunodeficiency Virus Tat Trans-Activator Protein. *Cell* **1988**, *55* (6), 1179–1188. [https://doi.org/10.1016/0092-8674\(88\)90262-0](https://doi.org/10.1016/0092-8674(88)90262-0).
- (6) LeCher, J. C.; Nowak, S. J.; McMurry, J. L. Breaking in and Busting out: Cell-Penetrating Peptides and the Endosomal Escape Problem. *Biomol. Concepts* **2017**, *8* (3–4), 131–141. <https://doi.org/10.1515/bmc-2017-0023>.
- (7) Bolhassani, A.; Jafarzade, B. S.; Mardani, G. In Vitro and in Vivo Delivery of Therapeutic Proteins Using Cell Penetrating Peptides. *Peptides* **2017**, *87*, 50–63. <https://doi.org/10.1016/j.peptides.2016.11.011>.
- (8) Steinauer, A.; LaRochelle, J. R.; Knox, S. L.; Wissner, R. F.; Berry, S.; Schepartz, A. HOPS-Dependent Endosomal Fusion Required for Efficient Cytosolic Delivery of Therapeutic Peptides and Small Proteins. *Proc. Natl. Acad. Sci.* **2019**, *116* (2), 512–521. <https://doi.org/10.1073/pnas.1812044116>.
- (9) Wissner, R. F.; Steinauer, A.; Knox, S. L.; Thompson, A. D.; Schepartz, A. Fluorescence Correlation Spectroscopy Reveals Efficient Cytosolic Delivery of Protein Cargo by Cell-Permeant Miniature Proteins. *ACS Cent. Sci.* **2018**, *4* (10), 1379–1393. <https://doi.org/10.1021/acscentsci.8b00446>.
- (10) Appelbaum, J. S.; LaRochelle, J. R.; Smith, B. A.; Balkin, D. M.; Holub, J. M.; Schepartz, A. Arginine Topology Controls Escape of Minimally Cationic Proteins from Early Endosomes to the Cytoplasm. *Chem. Biol.* **2012**, *19* (7), 819–830. <https://doi.org/10.1016/j.chembiol.2012.05.022>.
- (11) LaRochelle, J. R.; Cobb, G. B.; Steinauer, A.; Rhoades, E.; Schepartz, A. Fluorescence Correlation Spectroscopy Reveals Highly Efficient Cytosolic

- Delivery of Certain Penta-Arg Proteins and Stapled Peptides. *J. Am. Chem. Soc.* **2015**, *137* (7), 2536–2541. <https://doi.org/10.1021/ja510391n>.
- (12) Qian, Z.; Liu, T.; Liu, Y.-Y.; Briesewitz, R.; Barrios, A. M.; Jhiang, S. M.; Pei, D. Efficient Delivery of Cyclic Peptides into Mammalian Cells with Short Sequence Motifs. *ACS Chem. Biol.* **2013**, *8* (2), 423–431. <https://doi.org/10.1021/cb3005275>.
- (13) Husson, A.; Brasse-Lagnel, C.; Fairand, A.; Renouf, S.; Lavoinne, A. Argininosuccinate Synthetase from the Urea Cycle to the Citrulline–NO Cycle. *Eur. J. Biochem.* **2003**, *270* (9), 1887–1899. <https://doi.org/10.1046/j.1432-1033.2003.03559.x>.
- (14) Haines, R. J.; Pendleton, L. C.; Eichler, D. C. Argininosuccinate Synthase: At the Center of Arginine Metabolism. *Int. J. Biochem. Mol. Biol.* **2010**, *2* (1), 8–23.
- (15) Diez-Fernandez, C.; Rüfenacht, V.; Häberle, J. Mutations in the Human Argininosuccinate Synthetase (ASS1) Gene, Impact on Patients, Common Changes, and Structural Considerations. *Hum. Mutat.* **2017**, *38* (5), 471–484. <https://doi.org/10.1002/humu.23184>.
- (16) Kok, C. Y.; Cunningham, S. C.; Carpenter, K. H.; Dane, A. P.; Siew, S. M.; Logan, G. J.; Kuchel, P. W.; Alexander, I. E. Adeno-Associated Virus-Mediated Rescue of Neonatal Lethality in Argininosuccinate Synthetase-Deficient Mice. *Mol. Ther.* **2013**, *21* (10), 1823–1831. <http://dx.doi.org/10.1038/mt.2013.139>.
- (17) Herrera Sanchez, M. B.; Previdi, S.; Bruno, S.; Fonsato, V.; Deregibus, M. C.; Kholia, S.; Petrillo, S.; Tolosano, E.; Critelli, R.; Spada, M.; Romagnoli, R.; Salizzoni, M.; Tetta, C.; Camussi, G. Extracellular Vesicles from Human Liver Stem Cells Restore Argininosuccinate Synthase Deficiency. *Stem Cell Res. Ther.* **2017**, *8*, 176. <https://doi.org/10.1186/s13287-017-0628-9>.
- (18) Mingozi, F.; High, K. A. Immune Responses to AAV Vectors: Overcoming Barriers to Successful Gene Therapy. *Blood* **2013**, *122* (1), 23–36. <https://doi.org/10.1182/blood-2013-01-306647>.
- (19) Masat, E.; Pavani, G.; Mingozi, F. Humoral Immunity to AAV Vectors in Gene Therapy: Challenges and Potential Solutions. *Discov. Med.* **2013**, *15* (85), 379–389.
- (20) Calcedo, R.; Wilson, J. Humoral Immune Response to AAV. *Front. Immunol.* **2013**, *4*, 341. <https://doi.org/10.3389/fimmu.2013.00341>.
- (21) Louis Jeune, V.; Joergensen, J. A.; Hajjar, R. J.; Weber, T. Pre-Existing Anti-Adeno-Associated Virus Antibodies as a Challenge in AAV Gene Therapy. *Hum. Gene Ther. Methods* **2013**, *24* (2), 59–67. <https://doi.org/10.1089/hgtb.2012.243>.
- (22) Naso, M. F.; Tomkowicz, B.; Perry, W. L.; Strohl, W. R. Adeno-Associated Virus (AAV) as a Vector for Gene Therapy. *BioDrugs* **2017**, *31* (4), 317–334. <https://doi.org/10.1007/s40259-017-0234-5>.
- (23) Thomas, C. E.; Ehrhardt, A.; Kay, M. A. Progress and Problems with the Use of Viral Vectors for Gene Therapy. *Nat Rev Genet* **2003**, *4* (5), 346–358.
- (24) Hromada, C.; Mühleder, S.; Grillari, J.; Redl, H.; Holnthoner, W. Endothelial Extracellular Vesicles—Promises and Challenges. *Front. Physiol.* **2017**, *8* (275). <https://doi.org/10.3389/fphys.2017.00275>.
- (25) Knox, S. L.; Steinauer, A.; Alpha-Cobb, G.; Trexler, A.; Rhoades, E.; Schepartz, A. Chapter Twenty-One - Quantification of Protein Delivery in Live Cells Using

- Fluorescence Correlation Spectroscopy. In *Methods in Enzymology*; Chenoweth, D. M., Ed.; Academic Press, 2020; Vol. 641, pp 477–505. <https://doi.org/10.1016/bs.mie.2020.05.007>.
- (26) Kuo, D.; Nie, M.; Courey, A. J. SUMO as a Solubility Tag and In Vivo Cleavage of SUMO Fusion Proteins with Ulp1. In *Protein Affinity Tags: Methods and Protocols*; Giannone, R. J., Dykstra, A. B., Eds.; Springer New York: New York, NY, 2014; pp 71–80. [https://doi.org/10.1007/978-1-4939-1034-2\\_6](https://doi.org/10.1007/978-1-4939-1034-2_6).
- (27) Karlberg, T.; Collins, R.; van den Berg, S.; Flores, A.; Hammarstrom, M.; Hogbom, M.; Holmberg Schiavone, L.; Uppenberg, J. Structure of Human Argininosuccinate Synthetase. *Acta Crystallogr. Sect. D* **2008**, *64* (3), 279–286. <https://doi.org/doi:10.1107/S0907444907067455>.
- (28) Diez-Fernandez, C.; Wellauer, O.; Gemperle, C.; Rüfenacht, V.; Fingerhut, R.; Häberle, J. Kinetic Mutations in Argininosuccinate Synthetase Deficiency: Characterisation and in Vitro Correction by Substrate Supplementation. *J. Med. Genet.* **2016**, *53* (10), 710. <https://doi.org/10.1136/jmedgenet-2016-103937>.
- (29) Theile, C. S.; Witte, M. D.; Blom, A. E. M.; Kundrat, L.; Ploegh, H. L.; Guimaraes, C. P. Site-Specific N-Terminal Labeling of Proteins Using Sortase-Mediated Reactions. *Nat. Protoc.* **2013**, *8* (9), 1800–1807. <https://doi.org/10.1038/nprot.2013.102>.
- (30) Guimaraes, C. P.; Witte, M. D.; Theile, C. S.; Bozkurt, G.; Kundrat, L.; Blom, A. E. M.; Ploegh, H. L. Site-Specific C-Terminal and Internal Loop Labeling of Proteins Using Sortase-Mediated Reactions. *Nat. Protoc.* **2013**, *8*, 1787. <https://doi.org/10.1038/nprot.2013.101>.
- (31) Popp, M. W.-L.; Antos, J. M.; Ploegh, H. L. Site-Specific Protein Labeling via Sortase-Mediated Transpeptidation. *Curr. Protoc. Protein Sci.* **2009**, *Chapter 15*, Unit-15.3. <https://doi.org/10.1002/0471140864.ps1503s56>.
- (32) Brusilow, S. W.; Horwich, A. L. Urea Cycle Enzymes. In *The Online Metabolic and Molecular Bases of Inherited Disease*; Beaudet, A. L., Vogelstein, B., Kinzler, K. W., Antonarakis, S. E., Ballabio, A., Gibson, K. M., Mitchell, G., Eds.; The McGraw-Hill Companies, Inc.: New York, NY, 2014.
- (33) Saheki, T.; Sase, M.; Nakano, K.; Azuma, F.; Katsunuma, T. Some Properties of Argininosuccinate Synthetase Purified from Human Liver and a Comparison with the Rat Liver Enzyme. *J. Biochem. (Tokyo)* **1983**, *93* (6), 1531–1537.
- (34) Schimke, R. T. [38] Micromethods for the Assay of Argininosuccinate Synthetase, Argininosuccinase, and Arginase. In *Methods in Enzymology*; Academic Press, 1970; Vol. 17, pp 324–329. [https://doi.org/10.1016/0076-6879\(71\)17205-9](https://doi.org/10.1016/0076-6879(71)17205-9).
- (35) Wixom, R. L.; Reddy, M. K.; Cohen, P. P. A Concerted Response of the Enzymes of Urea Biosynthesis during Thyroxine-Induced Metamorphosis of *Rana Catesbeiana*. *J. Biol. Chem.* **1972**, *247* (11), 3684–3692.
- (36) O'Brien, W. E. A Continuous Spectrophotometric Assay for Argininosuccinate Synthetase Based on Pyrophosphate Formation. *Anal. Biochem.* **1976**, *76* (2), 423–430. [http://dx.doi.org/10.1016/0003-2697\(76\)90337-7](http://dx.doi.org/10.1016/0003-2697(76)90337-7).
- (37) McMurry, J. L.; Chang, M. C. Y. Fluorothreonyl-TRNA Deacylase Prevents Mistranslation in the Organofluorine Producer *Streptomyces*

- Cattleya. *Proc. Natl. Acad. Sci.* **2017**.  
<https://doi.org/10.1073/pnas.1711482114>.
- (38) Ghose, C.; Raushel, F. M. Determination of the Mechanism of the Argininosuccinate Synthetase Reaction by Static and Dynamic Quench Experiments. *Biochemistry* **1985**, *24* (21), 5894–5898.  
<https://doi.org/10.1021/bi00342a031>.
- (39) Shaheen, N. K. Characterization of Human Wild-Type and Mutant Argininosuccinate Synthetase Proteins Expressed in Bacterial Cells. *Enzyme Protein* **1994**, *48*, 251–264.
- (40) Berning, C.; Bieger, I.; Pauli, S.; Vermeulen, T.; Vogl, T.; Rummel, T.; Höhne, W.; Koch, H. G.; Rolinski, B.; Gempel, K.; Häberle, J. Investigation of Citrullinemia Type I Variants by in Vitro Expression Studies. *Hum. Mutat.* **2008**, *29* (10), 1222–1227. <https://doi.org/10.1002/humu.20784>.
- (41) Kennaway, N. G.; Harwood, P. J.; Ramberg, D. A.; Koler, R. D.; Buist, N. R. M. Citrullinemia: Enzymatic Evidence for Genetic Heterogeneity. *Pediatr. Res.* **1975**, *9* (6), 554–558. <https://doi.org/10.1203/00006450-197506000-00008>.
- (42) Matsuda, Y.; Tsuji, A.; Katunuma, N. Qualitative Abnormality of Liver Argininosuccinate Synthetase in a Patient with Citrullinemia. In *Urea Cycle Diseases*; Lowenthal, A., Mori, A., Marescau, B., Eds.; Springer US: Boston, MA, 1982; pp 77–82. [https://doi.org/10.1007/978-1-4757-6903-6\\_10](https://doi.org/10.1007/978-1-4757-6903-6_10).
- (43) Rochovansky, O.; Ratner, S. Biosynthesis of Urea: XII. FURTHER STUDIES ON ARGININOSUCCINATE SYNTHETASE: SUBSTRATE AFFINITY AND MECHANISM OF ACTION. *J. Biol. Chem.* **1967**, *242* (17), 3839–3849.
- (44) Stanzl, E. G.; Trantow, B. M.; Vargas, J. R.; Wender, P. A. Fifteen Years of Cell-Penetrating, Guanidinium-Rich Molecular Transporters: Basic Science, Research Tools, and Clinical Applications. *Acc. Chem. Res.* **2013**, *46* (12), 2944–2954.  
<https://doi.org/10.1021/ar4000554>.
- (45) Thompson, D. B.; Cronican, J. J.; Liu, D. R. Engineering and Identifying Supercharged Proteins for Macromolecule Delivery into Mammalian Cells. *Methods Enzymol.* **2012**, *503*, 293–319. <https://doi.org/10.1016/B978-0-12-396962-0.00012-4>.
- (46) McNaughton, B. R.; Cronican, J. J.; Thompson, D. B.; Liu, D. R. Mammalian Cell Penetration, siRNA Transfection, and DNA Transfection by Supercharged Proteins. *Proc. Natl. Acad. Sci.* **2009**, *106* (15), 6111–6116.  
<https://doi.org/10.1073/pnas.0807883106>.
- (47) McAlpine, J. A.; Lu, H.-T.; Wu, K. C.; Knowles, S. K.; Thomson, J. A. Down-Regulation of Argininosuccinate Synthetase Is Associated with Cisplatin Resistance in Hepatocellular Carcinoma Cell Lines: Implications for PEGylated Arginine Deiminase Combination Therapy. *BMC Cancer* **2014**, *14* (1), 621.  
<https://doi.org/10.1186/1471-2407-14-621>.
- (48) Holub, J. M.; LaRochelle, J. R.; Appelbaum, J. S.; Schepartz, A. Improved Assays for Determining the Cytosolic Access of Peptides, Proteins, and Their Mimetics. *Biochemistry* **2013**, *52* (50), 9036–9046.  
<https://doi.org/10.1021/bi401069g>.

- (49) Raetz, C. R. H.; Whitfield, C. Lipopolysaccharide Endotoxins. *Annu. Rev. Biochem.* **2002**, *71* (1), 635–700.  
<https://doi.org/10.1146/annurev.biochem.71.110601.135414>.
- (50) Schmidt, F. R. Recombinant Expression Systems in the Pharmaceutical Industry. *Appl. Microbiol. Biotechnol.* **2004**, *65* (4), 363–372.  
<https://doi.org/10.1007/s00253-004-1656-9>.
- (51) Sandle, T. Removal of Endotoxin from Protein in Pharmaceutical Processes. *Am. Pharm. Rev.* **2016**, *19*, 1–5.
- (52) Dullah, E. C.; Ongkudon, C. M. Current Trends in Endotoxin Detection and Analysis of Endotoxin–Protein Interactions. *Crit. Rev. Biotechnol.* **2017**, *37* (2), 251–261. <https://doi.org/10.3109/07388551.2016.1141393>.
- (53) Mamat, U.; Wilke, K.; Bramhill, D.; Schromm, A. B.; Lindner, B.; Kohl, T. A.; Corchero, J. L.; Villaverde, A.; Schaffer, L.; Head, S. R.; Souvignier, C.; Meredith, T. C.; Woodard, R. W. Detoxifying Escherichia Coli for Endotoxin-Free Production of Recombinant Proteins. *Microb. Cell Factories* **2015**, *14* (1), 57.  
<https://doi.org/10.1186/s12934-015-0241-5>.
- (54) Morrison, D. C.; Ryan, J. L. Bacterial Endotoxins and Host Immune Responses. In *Advances in Immunology*; Dixon, F. J., Kunkel, H. G., Eds.; Academic Press, 1980; Vol. 28, pp 293–450. [https://doi.org/10.1016/S0065-2776\(08\)60802-0](https://doi.org/10.1016/S0065-2776(08)60802-0).
- (55) Teghanemt, A.; Zhang, D.; Levis, E. N.; Weiss, J. P.; Gioannini, T. L. Molecular Basis of Reduced Potency of Underacylated Endotoxins. *J. Immunol.* **2005**, *175* (7), 4669. <https://doi.org/10.4049/jimmunol.175.7.4669>.
- (56) Saitoh, S.; Akashi, S.; Yamada, T.; Tanimura, N.; Kobayashi, M.; Konno, K.; Matsumoto, F.; Fukase, K.; Kusumoto, S.; Nagai, Y.; Kusumoto, Y.; Kosugi, A.; Miyake, K. Lipid A Antagonist, Lipid IVA, Is Distinct from Lipid A in Interaction with Toll-like Receptor 4 (TLR4)-MD-2 and Ligand-induced TLR4 Oligomerization. *Int. Immunol.* **2004**, *16* (7), 961–969.  
<https://doi.org/10.1093/intimm/dxh097>.
- (57) Satoh, M.; Iwahori, T.; Sugawara, N.; Yamazaki, M. Liver Argininosuccinate Synthase Binds to Bacterial Lipopolysaccharides and Lipid A and Inactivates Their Biological Activities. *J. Endotoxin Res.* **2006**, *12* (1), 21–38.  
<https://doi.org/10.1179/096805106X89062>.
- (58) USP. Chapter <85>, Bacterial Endotoxins Test. 2011.
- (59) Dawson, M. Endotoxin Limits for Parenteral Drug Products. BET White Paper 2017.
- (60) Guidance for Industry Pyrogen and Endotoxins Testing: Questions and Answers. U.S. Department of Health and Human Services 2012.
- (61) Tsuji, K.; Steindler, K. A.; Harrison, S. J. Limulus Amoebocyte Lysate Assay for Detection and Quantitation of Endotoxin in a Small-Volume Parenteral Product. *Appl. Environ. Microbiol.* **1980**, *40* (3), 533–538.  
<https://doi.org/10.1128/AEM.40.3.533-538.1980>.
- (62) Rueda, F.; Cano-Garrido, O.; Mamat, U.; Wilke, K.; Seras-Franzoso, J.; García-Fruitós, E.; Villaverde, A. Production of Functional Inclusion Bodies in Endotoxin-Free Escherichia Coli. *Appl. Microbiol. Biotechnol.* **2014**, *98* (22), 9229–9238.  
<https://doi.org/10.1007/s00253-014-6008-9>.

- (63) Coats, S. R.; Pham, T.-T. T.; Bainbridge, B. W.; Reife, R. A.; Darveau, R. P. MD-2 Mediates the Ability of Tetra-Acylated and Penta-Acylated Lipopolysaccharides to Antagonize Escherichia Coli Lipopolysaccharide at the TLR4 Signaling Complex. *J. Immunol.* **2005**, *175* (7), 4490. <https://doi.org/10.4049/jimmunol.175.7.4490>.
- (64) Visintin, A.; Halmen, K. A.; Latz, E.; Monks, B. G.; Golenbock, D. T. Pharmacological Inhibition of Endotoxin Responses Is Achieved by Targeting the TLR4 Coreceptor, MD-2. *J. Immunol.* **2005**, *175* (10), 6465. <https://doi.org/10.4049/jimmunol.175.10.6465>.
- (65) Saheki, T.; Komorizono, K.; Miura, T.; Ichiki, H.; Yagi, Y.; Hashimoto, S. Clearance of Argininosuccinate Synthetase from the Circulation in Acute Liver Disease. *Clin. Biochem.* **1990**, *23* (2), 139–141. [https://doi.org/10.1016/0009-9120\(90\)80026-F](https://doi.org/10.1016/0009-9120(90)80026-F).
- (66) Perez, C. J.; Jaubert, J.; Guénet, J.-L.; Barnhart, K. F.; Ross-Inta, C. M.; Quintanilla, V. C.; Aubin, I.; Brandon, J. L.; Otto, N. W.; DiGiovanni, J.; Gimenez-Conti, I.; Giulivi, C.; Kusewitt, D. F.; Conti, C. J.; Benavides, F. Two Hypomorphic Alleles of Mouse Ass1 as a New Animal Model of Citrullinemia Type I and Other Hyperammonemic Syndromes. *Am. J. Pathol.* **2010**, *177* (4), 1958–1968. <https://doi.org/10.2353/ajpath.2010.100118>.
- (67) Greenfield, N. J. Using Circular Dichroism Spectra to Estimate Protein Secondary Structure. *Nat. Protoc.* **2006**, *1* (6), 2876–2890. <https://doi.org/10.1038/nprot.2006.202>.
- (68) Geueke, B.; Kohler, H.-P. E. Enzyme Assays, Substrate Specificities, Kinetic Parameters: Measurement of Enzyme Activities. In *Handbook of Hydrocarbon and Lipid Microbiology*; Timmis, K. N., Ed.; Springer Berlin Heidelberg: Berlin, Heidelberg, 2010; pp 4195–4202. [https://doi.org/10.1007/978-3-540-77587-4\\_327](https://doi.org/10.1007/978-3-540-77587-4_327).
- (69) Lineweaver, H.; Burk, D. The Determination of Enzyme Dissociation Constants. *J. Am. Chem. Soc.* **1934**, *56* (3), 658–666. <https://doi.org/10.1021/ja01318a036>.
- (70) Ratner, S. A Radiochemical Assay for Argininosuccinate Synthetase with [U-<sup>14</sup>C]Aspartate. *Anal. Biochem.* **1983**, *135* (2), 479–488. [https://doi.org/10.1016/0003-2697\(83\)90716-9](https://doi.org/10.1016/0003-2697(83)90716-9).
- (71) Tochio, N., Tomizawa, T., Abe, H., Saito, K., Li, H., Sato, M., Koshiba, S., Kobayashi, N., Kigawa, T., Yokoyama, S., RIKEN Structural Genomics/Proteomics Initiative (RSGI). PDB ID: 2EOZ. Solution Structure of the C2H2 Type Zinc Finger (Region 809-841) of Human Zinc Finger Protein 473. **2007**. <https://doi.org/10.2210/pdb2EOZ/pdb>.
- (72) Krizek, B. A.; Amann, B. T.; Kilfoil, V. J.; Merkle, D. L.; Berg, J. M. A Consensus Zinc Finger Peptide: Design, High-Affinity Metal Binding, a PH-Dependent Structure, and a His to Cys Sequence Variant. *J. Am. Chem. Soc.* **1991**, *113* (12), 4518–4523. <https://doi.org/10.1021/ja00012a021>.
- (73) Krishna, S. S.; Majumdar, I.; Grishin, N. V. Structural Classification of Zinc Fingers: SURVEY AND SUMMARY. *Nucleic Acids Res.* **2003**, *31* (2), 532–550. <https://doi.org/10.1093/nar/gkg161>.

- (74) Krizek, B. A.; Merkle, D. L.; Berg, J. M. Ligand Variation and Metal Ion Binding Specificity in Zinc Finger Peptides. *Inorg. Chem.* **1993**, *32* (6), 937–940. <https://doi.org/10.1021/ic00058a030>.
- (75) Rich, A. M.; Bombarda, E.; Schenk, A. D.; Lee, P. E.; Cox, E. H.; Spuches, A. M.; Hudson, L. D.; Kieffer, B.; Wilcox, D. E. Thermodynamics of Zn<sup>2+</sup> Binding to Cys2His2 and Cys2HisCys Zinc Fingers and a Cys4 Transcription Factor Site. *J. Am. Chem. Soc.* **2012**, *134* (25), 10405–10418. <https://doi.org/10.1021/ja211417g>.
- (76) ClearColi® BL21(DE3) Electrocompetent Cells, MA018. Lucigen 2016.
- (77) Gottschalk, P. G.; Dunn, J. R. The Five-Parameter Logistic: A Characterization and Comparison with the Four-Parameter Logistic. *Anal. Biochem.* **2005**, *343* (1), 54–65. <https://doi.org/10.1016/j.ab.2005.04.035>.
- (78) Hoofnagle, A. N.; Wener, M. H. The Fundamental Flaws of Immunoassays and Potential Solutions Using Tandem Mass Spectrometry. *J. Immunol. Methods* **2009**, *347* (1), 3–11. <https://doi.org/10.1016/j.jim.2009.06.003>.
- (79) Xiang, Y.; Donley, J.; Seletskaja, E.; Shingare, S.; Kamerud, J.; Gorovits, B. A Simple Approach to Determine a Curve Fitting Model with a Correct Weighting Function for Calibration Curves in Quantitative Ligand Binding Assays. *AAPS J.* **2018**, *20* (3), 45. <https://doi.org/10.1208/s12248-018-0208-7>.
- (80) Macek, B.; Forchhammer, K.; Hardouin, J.; Weber-Ban, E.; Grangeasse, C.; Mijakovic, I. Protein Post-Translational Modifications in Bacteria. *Nat. Rev. Microbiol.* **2019**, *17* (11), 651–664. <https://doi.org/10.1038/s41579-019-0243-0>.
- (81) Bian, Y.; Song, C.; Cheng, K.; Dong, M.; Wang, F.; Huang, J.; Sun, D.; Wang, L.; Ye, M.; Zou, H. An Enzyme Assisted RP-RPLC Approach for in-Depth Analysis of Human Liver Phosphoproteome. *J. Proteomics* **2014**, *96*, 253–262. <https://doi.org/10.1016/j.jprot.2013.11.014>.

## **CHAPTER 6**

Cellular Delivery of Cas9 using ZF5.3

## 6.1 Abstract

Next-generation therapeutics demand delivery tools that move proteins from outside of the cell into the cytosol or nucleus. Cas9 has proven to be one of the foci of next-generation therapeutics, but its large size limits its potential use when delivered as a translated enzyme. Recently reported cell-permeant miniature proteins, including ZF5.3, provide a pathway for material that can access the interior of cells. The experiments described herein illustrate that N- and C-terminally labeled Cas9 remains active *in vitro* and can access the interior of cells at higher levels than wild-type Cas9 alone. Even in the presence of sgRNA, the Cas9 protein containing a C-terminal ZF5.3 exhibited the highest cellular uptake in all conditions evaluated. The use of a non-specific fluorophore label inhibited fluorescence correlation spectroscopy studies, and this observation was applied to future protein designs in the lab.

## 6.2 Introduction

CRISPR-Cas technology has transformed genome-based therapies. First described for its use in the bacterial adaptive immune system in 2007,<sup>1</sup> CRISPR-Cas systems have proven to be revolutionary technologies, leading to Jennifer Doudna and Emmanuelle Charpentier winning the Nobel Prize in Chemistry in 2020.<sup>2</sup> Although Cas9 is just one of many base editing proteins, it is the most widely used of the Cas proteins.<sup>3</sup> This RNA-programmable DNA endonuclease is a 160 kD monomer and classified as a class 2 type II CRISPR system.<sup>3,4</sup> Type II systems only require one protein for DNA recognition and cleavage, beneficial for targeting genome manipulation.<sup>4</sup> CRISPR-Cas technology, upon nuclear localization, allows for insertions, deletions, and mutations of the genome through nonhomologous end joining and homology directed repair.<sup>3</sup>

Cas9 is a useful biochemical and biomedical tool. An engineered version of Cas9 known as dCas9 is not catalytically active, but its ability for DNA recognition allows for spatio- and temporal-control using optogenetics and chemical induction methods.<sup>3</sup> Not only have Cas9 gene therapy applications been promising, but so have applications in translational medicine, providing adoptive T cell immunotherapy creating chimeric antigen receptors and universal cell donors.<sup>3</sup> Current delivery methods of this next generation therapeutic include both viral and nonviral strategies. Viral strategies include lentivirus, associated-adenovirus, adenovirus, and extracellular vesicles.<sup>5</sup> Physical nonviral strategies of microinjection and electroporation provide spatio-control; however, these techniques are limited to *in vitro* studies.<sup>5</sup> Chemical means to deliver Cas9 include utilizing cell-penetrating peptides, lipid nanoparticles, and gold nanoparticles. These chemical, nonviral strategies are beneficial as they pose no risk of viral incorporation into the genome as the viral methods do.<sup>5</sup>

The challenges with current delivery methods include random integration of viral fragments into the host genome, immune response, and limited quantification.<sup>5,6</sup> Development of a protein-based method for the delivery of Cas9 would eliminate the need for transfection reagents and mitigate the chance that a plasmid containing Cas9 would integrate into the genome. Even the chemical, nonviral methods suffer from

variable efficiencies and extensive optimization prior to use.<sup>5</sup> The use of a reliably efficient chemical method would transform Cas9 delivery. Previous cell-penetrating peptide (CPPs) efforts include utilization of a more traditional amphiphilic peptide<sup>7</sup> to deliver Cas9 to airway epithelial cells and usage of endosmolytic peptides.<sup>8,9</sup>

There have been a number of strategies employed to move proteins into cells, including the use of the endosmolytic peptide ppTG21. Endosmolytic peptides may cause damage to the endosome<sup>10,11</sup> and when codelivered with cargo such as Cas9, allow the protein to escape from endosomes.<sup>12</sup> This poses the question of whether the integrity of endosomes remain intact with use of an endosmolytic peptide and how that may affect normal cellular functions. An alternative strategy uses a delivery tool that does not cause major or minimal damage of the endosomal membrane. ZF5.3 provides a solution to this concern as it has been shown that at low micromolar concentrations, this cell-permeant miniature protein (CPMP) does not disrupt endosomes.<sup>13</sup> While the pI of Cas9 is 9.0<sup>14</sup>, it is anionic when complexed with guide RNA.<sup>15</sup> Wissner *et al.* described delivery of ZF5.3 conjugated to a protein exhibiting a low pI (SNAP-tag, pI = 6.5<sup>14</sup>), providing precedence that ZF5.3 can deliver anionic proteins. In addition to the aforementioned benefits, ZF5.3 can reach the nucleus.<sup>13,16</sup> A nuclear localization sequence (NLS) can deliver Cas9 into cells,<sup>9,17,18</sup> but it might be possible to circumnavigate the use of an NLS by using a CPMP. ZF5.3 provides a means for (1) cellular uptake, (2) endosomal escape, and (3) nuclear localization. These three properties prevent the need for individual molecules to complete each of these three necessary steps to exhibit the biological function of Cas9. These reasons provide precedent that ZF5.3 will be able to deliver Cas9 to achieve protein-based DNA therapy.

Here, we appended the CPMP ZF5.3 to either the N- or C-terminus of Cas9 and non-specifically labeled with Alexa Fluor™ 568 NHS ester to tag surface exposed amines. Not only is ZF5.3 expected to enhance endosomal escape of Cas9, but it is also predicted to eliminate the need for a nuclear localization sequence commonly appended with RNP delivery.<sup>9</sup> Preliminary flow cytometry data indicated that even in the presence of sgRNA, Cas9-ZF5.3 exhibited higher cellular uptake compared to Cas9 alone. Enzyme conjugates of Cas9 with ZF5.3 were active as determined using an *in vitro* DNA cleavage assay.

## 6.3 Materials and Methods

### 6.3.1 Sequences of Proteins

#### Cas9-His<sub>6</sub>

MDKKYSIGLDIGTNSVGVAVITDEYKVPSSKFKVLGNTDRHSIKKNLIGALLFDSGETAE  
ATRLKRTARRRYTRRKNRICYLQEIFSNEMAKVDDSSFFHRLEESFLVEEDKKHERHPIF  
GNIVDEVAYHEKYPTIYHLRKKLVDSTDKADLRLIYLALAHMIKFRGHFLIEGDLNPDNS  
DVDKLFIQLVQTYNQLFEENPINASGVDAKAILSARLSKSRLENLIAQLPGEKKNGLFG  
NLIALSLGLTPNFKSNFDLAEDAKLQLSKDYYDDLDNLLAQIGDQYADLFLAAKNLSDA  
ILLSDILRVNTEITKAPLSASMIKRYDEHHQDLTLLKALVRQQLPEKYKEIFFDQSKNGYA  
GYIDGGASQEEFYKFIKPILEKMDGTEELLVKLNREDLLRKQRTFDNGSIPHQIHLGELH  
AILRRQEDFYFPLKDNREKIEKILTFRIPYYYVGPLARGNSRFAMTRKSEETITPWNFEE

VVDKGASAQSFIERMTNFDKNLPNEKVLPKHSLLYEYFTVYNELTKVKYVTEGMRKPA  
FLSGEQKKAIVDLLFKTNRKVTVKQLKEDYFKKIECFDSVEISGVEDRFNASLGTYHDLL  
KIIKDKDFLDNEENEDILEDIVLTLTLFEDREMIEERLKTIAHLFDDKVMKQLKRRRYTG  
WGRLSRKLINGIRDKQSGKTILDFLKSDGFANRNFMQLIHDDSLTFKEDIQKAQVSGQG  
DSLHEHIANLAGSPAIKKGILQTVKVVDELVKVMGRHKPENIVIAMARENQTTQKGQKN  
SRERMKRIEEGIKELGSQILKEHPVENTQLQNEKLYLYYLQNGRDMYVDQELDINRLSD  
YDVDHIVPQSFLKDDSIDNKVLTRSDKNRGKSDNVPSEEVVKKMKNYWRQLLNAKLIT  
QRKFDNLTAKAERGGLSELDKAGFIKRQLVETRQITKHVAQILDSRMNTKYDENDKLIRE  
VKVITLKSCLVSDFRKDFQFYKVVREINNYHHAHDAYLNAVVGTAIIKKYPKLESEFVYGD  
YKVYDVRKMIKSEQEIGKATAKYFFYSNIMNFFKTEITLANGEIRKRPLIETNGETGEIV  
WDKGRDFATVRKVL SMPQVNIVKKTEVQTGGFSKESILPKRNSDKLIARKKDWDPKKY  
GGFDSPTVAYSVLVAKVEKKGSKKLSVKELLGITIMERSSSFENPIDFLEAKGYKEVK  
KDLIIKLPKYSLFELENGRKRMLASAGELQKGNELALPSKYVNFLYLASHYEKLGKSPE  
DNEQKQLFVEQHKHYLDEIIIEQISEFSKRVILADANLDKVL SAYNKHRDKPIREQAENIIH  
LFTLTNLGAPAAFKYFDTTIDRKRYTSTKEVL DATLIHQ SITGLYETRIDLSQLGGDHHH  
HHH

Cas9-ZF5.3-His<sub>6</sub>

MDKKYSIGLDIGTNSVGWAVITDEYKVPSKKFKVLGNTDRHSIKKNLIGALLFDSGETAE  
ATRLKRTARRRYTRRKNRICYLQEIFS NEMAKVDDSFHRL EESFLVEEDKKHERHPIF  
GNIVDEVAYHEKYPTIYHLRKKLVDSTDKADLR LIYLALAHMIKFRGHFLIEGDLNPDNS  
DVKLFIQLVQTYNQLFEENPINASGVDAKAILSARLSKSRLENLIAQLPGEKKNGLFG  
NLIALSLGLTPNFKSNFDLAEDAKLQLSKDTYDDDLDNLLAQIGDQYADFLAAKNLSDA  
ILLSDILRVNTEITKAPLSASMIKRYDEHHQDLTLLKALVRQQLPEKYKEIFFDQSKNGYA  
GYIDGGASQEEFYKFIKPILEKMDGTEELLVKNLREDLLRKQRTFDNGSIPHQIHLGELH  
AILRRQEDFYFPLKDNREKIEKILTFRIPYYYVGPLARGNSRF AWMTRKSEETITPWNFEE  
VVDKGASAQSFIERMTNFDKNLPNEKVLPKHSLLYEYFTVYNELTKVKYVTEGMRKPA  
FLSGEQKKAIVDLLFKTNRKVTVKQLKEDYFKKIECFDSVEISGVEDRFNASLGTYHDLL  
KIIKDKDFLDNEENEDILEDIVLTLTLFEDREMIEERLKTIAHLFDDKVMKQLKRRRYTG  
WGRLSRKLINGIRDKQSGKTILDFLKSDGFANRNFMQLIHDDSLTFKEDIQKAQVSGQG  
DSLHEHIANLAGSPAIKKGILQTVKVVDELVKVMGRHKPENIVIAMARENQTTQKGQKN  
SRERMKRIEEGIKELGSQILKEHPVENTQLQNEKLYLYYLQNGRDMYVDQELDINRLSD  
YDVDHIVPQSFLKDDSIDNKVLTRSDKNRGKSDNVPSEEVVKKMKNYWRQLLNAKLIT  
QRKFDNLTAKAERGGLSELDKAGFIKRQLVETRQITKHVAQILDSRMNTKYDENDKLIRE  
VKVITLKSCLVSDFRKDFQFYKVVREINNYHHAHDAYLNAVVGTAIIKKYPKLESEFVYGD  
YKVYDVRKMIKSEQEIGKATAKYFFYSNIMNFFKTEITLANGEIRKRPLIETNGETGEIV  
WDKGRDFATVRKVL SMPQVNIVKKTEVQTGGFSKESILPKRNSDKLIARKKDWDPKKY  
GGFDSPTVAYSVLVAKVEKKGSKKLSVKELLGITIMERSSSFENPIDFLEAKGYKEVK  
KDLIIKLPKYSLFELENGRKRMLASAGELQKGNELALPSKYVNFLYLASHYEKLGKSPE  
DNEQKQLFVEQHKHYLDEIIIEQISEFSKRVILADANLDKVL SAYNKHRDKPIREQAENIIH  
LFTLTNLGAPAAFKYFDTTIDRKRYTSTKEVL DATLIHQ SITGLYETRIDLSQLGGDYSCN  
VCGKAFVLSRHLNRHLRVHRRATHHHHHH

ZF5.3-Cas9-His<sub>6</sub>

MYSCNVCGKAFVLSRHLNRHLRVHRRATDKKYSIGLDIGTNSVGWAVITDEYKVPSKK  
FKVLGNTDRHSIKKNLIGALLFDSGETAEATRLKRTARRRYTRRKNRICYLQEIFS NEMA

KVDDSFHRLLEESFLVEEDKKHERHPIFGNIVDEVAYHEKYPTIYHLRKKLVDSTDKADL  
RLIYLALAHMIKFRGHFLIEGDLNPDNSVDKLFQILVQTYNQLFEENPINASGVDAKAIL  
SARLSKSRLENLIAQLPGEKKNLFGNLIASLGLTPNFKSNFDLAEDAQLQSKDQTYD  
DDLNDLLAQIGDQYADLFLAAKNLSDAILSDILRVNTEITKAPLSASMIKRYDEHHQDLT  
LLKALVRQQLPEKYKEIFFDQSKNGYAGYIDGGASQEEFYKFIKPILEKMDGTEELLVKL  
NREDLLRKQRTFDNGSIPHQIHLGELHAILRRQEDFYFPLKDNREKIEKILTFRIPPYYVGP  
LARGNSRFAMTRKSEETITPWNFEEVVDKGGASAQSFIERMTNFDKNLPNEKVLPHK  
SLLYEYFTVYNELTKVKYVTEGMRKPAFLSGEQKKAIVDLLFKTNRKVTVKQLKEDYFK  
KIECFDSVEISGVEDRFNASLGTYHDLLKIIKDKDFLDNEENEDILEDIVLTLTLFEDREMI  
EERLKTYAHLFDDKVMKQLKRRRYTGWGRLSRKLINGIRDKQSGKTILDFLKSDGFAN  
RNFMLIHDDSLTFKEDIQKAQVSGQGDSLHEHIANLAGSPAIKKGILQTVKVVDELVKV  
MGRHKPENIVIAMARENQTTQKGQKNSRERMKRIEEGKELGSQILKEHPVENTQLQN  
EKLYLYYLQNGRDMYVDQELDINRLSDYDVDHIVPQSFLKDDSIDNKVLTRSDKNRGK  
SDNVPSEEVVKKMKNYWRQLLNAKLITQRKFDNLTKAERGGLSELDKAGFIKRQLVET  
RQITKHVAQILDSRMNTKYDENDKLIREVKVITLKSCLVSDFRKDFQFYKVINNYHHA  
HDAYLNAVVGTAALIKKYPKLESEFVYGDYKVYDVRKMIKSEQEIGKATAKYFFYSNIM  
NFFKTEITLANGEIRKRPLIETNGETGEIVWDKGRDFATVRKVL SMPQVNIVKKTEVQTG  
GFSKESILPKRNSDKLIARKKDWDPKKGFFDSPTVAYSVLVAKVEKGGKSKKLKSVK  
ELLGITIMERSSEFKNPIDFLEAKGYKEVKKDLIILPKYSLFELENGRKRMLASAGELQK  
GNELALPSKYVNFYLYLASHYEKLGSPEDNEQKQLFVEQHKHYLDEIIEQISEFSKRVL  
ADANLDKVL SAYNKHRDKPIREQAENIIHLFTLTNLGAPAAFKYFDTTIDRKRYTSTKEV  
LDATLIHQ SITGLYETRIDLSQLGGDHHHHHH

### 6.3.2 Materials

*E. coli* BL21(DE3) pLysS cells were purchased from Agilent (Santa Clara, CA). Ni-NTA agarose resin was from Qiagen (Germantown, MD). LB Broth Powder (Lennox) were purchased from Thermo Fisher Scientific (Waltham, MA). Carbenicillin disodium salt, ampicillin sodium salt, Super Glycerol, 1M Tris HCl solution (pH 8), and dithiothreitol (DTT) were purchased from AmericanBio (Canton, MA). Super Optimal broth with Catabolite repression (SOC) outgrowth media, PvuII HF (20,000 U/mL), EcoRI HF, and 10X CutSmart buffer were purchased from New England BioLabs (Ipswich, MA). Any kD™ Mini-PROTEAN® TGX™ Precast Protein Gels (10- or 15-well) were purchased from Bio-Rad Laboratories (Hercules, CA). Saos-2 cells were purchased from American Type Culture Collection (ATCC, Manassas, VA). McCoy's 5A medium (with and without phenol red), cOmplete mini EDTA free protease inhibitor tablets, PD-10 desalting columns, and fibronectin were purchased from MilliporeSigma (Burlington, MA). Nunc™ Lab-Tek™ I Chambered Coverglass slides (8 Well, 0.8 cm<sup>2</sup>), TrypLE, fetal bovine serum (FBS), Dulbecco's modified eagle medium (DMEM, with and without phenol red), Hoescht 33342 stain, GlutaMAX, sodium pyruvate, Alexa Fluor™ 568 NHS ester, SYBR Safe DNA Gel Stain, Pierce™ 660 nm reagent, and TrypLE were purchased from Thermo Fisher Scientific (Waltham, MA). Penicillin/streptomycin and Dulbecco's phosphate-buffered saline (DPBS) were from Life Technologies (Carlsbad, CA). All other reagents were obtained from commercial sources and used without further purification, unless otherwise stated.

### 6.3.3 Expression and Purification of Cas9, ZF5.3-Cas9, Cas9-ZF5.3

#### *Plasmid Construction*

Cas9-His<sub>6</sub>, ZF5.3-Cas9-His<sub>6</sub>, and Cas9-ZF5.3-His<sub>6</sub> were cloned into a pET32a plasmid for expression in *E. coli*.

#### *Transformation into BL21(DE3)pLysS Competent E. coli Cells*

BL21(DE3)pLysS competent *E. coli* cells thawed on ice for 10 min. 2  $\mu$ L of the respective Cas9 conjugate plasmid (containing >100 ng/ $\mu$ L of either pET32a\_Cas9, pET32a\_Cas9-ZF5.3-His<sub>6</sub>, or pET32a\_ZF5.3-Cas9-His<sub>6</sub>) were added to cells. The cells incubated on ice for 15 min. Cells were heat shocked at 42 °C for 30 s followed by a 2 min recovery on ice. 450  $\mu$ L of SOC outgrowth media were added to the tube. The tube incubated with 200 RPM shaking at 37 °C for 1 h. 200  $\mu$ L of the cells were added to an ampicillin-containing plate and incubated at 37 °C overnight.

#### *Expression of Cas9 Conjugates*

Starter cultures were prepared with 5 mL of LB Lennox, 5  $\mu$ L of 1000X carbenicillin, and 1 colony of bacteria containing the respective construct. After 3.5 h, 1 L of LB Lennox was added to a 2 L flask. 100 mg of ampicillin were added to the flask. The starter culture was added to the flask and incubated at 37°C and 200 RPM. When the OD<sub>600</sub> reached 0.6-0.8, IPTG was added for a final concentration of 0.2 mM (48 mg). The temperature was reduced to 18 °C and the flask shook at 200 RPM overnight.

#### *Purification of Cas9 Conjugates*

The following buffers were used for purification: wash buffer (20 mM Tris pH 8.0, 1 M KCl, 20% glycerol, 1 mM DTT), elution buffer (20 mM Tris, 0.1 M KCl, 20% glycerol, 250 mM imidazole, 1 mM DTT), and dialysis buffer (20 mM Tris pH 8.0, 0.1 M KCl, 20% glycerol, 1 mM DTT, with 100  $\mu$ M ZnCl<sub>2</sub> for ZF5.3-containing proteins). Overnight cultures were spun down at 4100 RPM for 30 min at 4 °C. The cell pellet was resuspended in 10 mL of wash buffer (1 tablet cOComplete, mini EDTA-free protease inhibitor cocktail (Sigma-Aldrich, St. Louis, MO) was added per L of culture). The lysate sonicated for 8 min (30 s on, 30 s off). Lysate was cleared by centrifugation for 30 min at 4 °C and 4100 RPM. 2x1 mL fractions of Ni-NTA agarose beads were added to Eppendorf tubes (2 mL Ni-NTA agarose beads per L culture). These were centrifuged at max speed for 5 min and the supernatant was removed. The beads were washed 3 times with 1 mL wash buffer (centrifuged at max speed for 5 min). This was to pre-equilibrate the beads with the wash buffer. The lysate was combined with 2 mL of pre-equilibrated Ni-NTA agarose beads and added to a 50 mL Falcon tube. The tube was rotated on a rotisserie at 4 °C for 1 h. The slurry was added to an empty column tube and the flow through was drained by gravity. The resin was washed with 20 mL of wash buffer 3X. The protein was eluted by 9X1 mL fractions of elution buffer (collected each mL in a separate Eppendorf tube). SDS-PAGE samples were prepared of the elution fractions as well as for other steps of the purification (20  $\mu$ L sample + 5  $\mu$ L 5X loading

dye). SDS-PAGE was completed (200 V for 30 min). WT Cas9 had 20  $\mu\text{L}$  loaded onto the gel. ZF5.3-Cas9 had 15  $\mu\text{L}$  loaded onto the gel. Any fractions containing the protein of interest were combined and dialyzed overnight into dialysis buffer at 4 °C. The next day, the protein was added to a 15 mL Falcon tube and centrifuged for 5 min at 4100 RPM and 4°C. Any precipitation was discarded and the supernatant was aliquoted, protein concentration was determined using Pierce 660 nm reagent, and stored at -80 °C until subsequent use.

### **6.3.4 In Vitro Activity Assay**

#### *Linearization of dTomato Plasmid*

5  $\mu\text{g}$  of dTomato circular plasmid (1330 ng/ $\mu\text{L}$ ) were combined with 5  $\mu\text{L}$  10X CutSmart buffer, 1  $\mu\text{L}$  of EcoRI HF or PvuI HF, and diluted to a final reaction volume of 50  $\mu\text{L}$  with nuclease-free water. The reaction occurred for 2 h at room temperature. The sample was spun down and supernatant was transferred into new Eppendorf tubes. The enzyme pellet was discarded. Samples were analyzed using a 1% agarose gel (390 mg agarose, 40 mL 1X agarose gel running buffer, 10  $\mu\text{L}$  10,000X SYBR Safe). 5  $\mu\text{L}$  of the sample (and dTomato circular plasmid at 100 ng/ $\mu\text{L}$ ) was mixed with 3  $\mu\text{L}$  of DNA gel loading dye (6X). All 8  $\mu\text{L}$  were added to the lanes. 2  $\mu\text{L}$  of 1 kb ladder was used. The gel ran at 130 V for approximately 40 min. The gel was imaged using a ChemiDoc XRS+ transilluminator. The concentration of the linearized dTomato plasmid was 68.6 ng/ $\mu\text{L}$ , determined using a NanoDrop.

#### *Cas9 Activity Assay*

Cas9, ZF5.3-Cas9, and Cas9-ZF5.3 were thawed on ice and centrifuged for 3 min at maximum RPM and 4 °C. If a pellet was observed, the supernatant was removed and transferred into a separate Eppendorf tube. 20  $\mu\text{L}$  of a 10  $\mu\text{M}$  solution of sgRNA (5'-GGGGCCACTAGGGACAGGAT-3') was prepared from a 50  $\mu\text{M}$  stock. The reaction for each enzyme was set up on a 25  $\mu\text{L}$  scale. First, 4.2  $\mu\text{L}$  of 9  $\mu\text{M}$  Cas9, ZF5.3-Cas9, or Cas9-ZF5.3 or 1.9  $\mu\text{L}$  of 20  $\mu\text{M}$  commercial Cas9 incubated with 5  $\mu\text{L}$  of the 10  $\mu\text{M}$  sgRNA stock for 20 min at room temperature. Next, 5  $\mu\text{L}$  of 5X cleavage buffer (100 mM HEPES pH 7.5, 500 mM KCl, 25% glycerol, 2.5 mM EDTA, and 10 mM  $\text{MgCl}_2$ ) were added, followed by addition of 0.5  $\mu\text{M}$  50 mM DTT. 250 ng of linearized dTomato plasmid (68.6 ng/ $\mu\text{L}$ ) were added and nuclease free water was added for a final reaction volume of 25  $\mu\text{L}$ . The mixture was flicked several times and then spun down gently to ensure mixing. The reaction incubated at 37 °C for 2–17 h (17 h = overnight). Samples were stored at -20 °C until analysis. Samples were analyzed using a 1% agarose gel (390 mg agarose, 40 mL 1X agarose gel running buffer, 10  $\mu\text{L}$  10,000X SYBR Safe). 8  $\mu\text{L}$  of the samples (and dTomato linear plasmid at 10 ng/ $\mu\text{L}$ ) were mixed with 4  $\mu\text{L}$  of DNA gel loading dye (6X). All 12  $\mu\text{L}$  were added to the lanes. 2  $\mu\text{L}$  of 1 kb ladder was used. The gel ran at 130 V for approximately 60 min. The gel was imaged using a ChemiDoc XRS+ transilluminator.

### **6.3.5 Non-Specific Labeling of Cas9 Proteins**

#### *Buffer Exchange*

Prior to labeling, dithiothreitol (DTT) in the dialysis buffer needed to be removed from the proteins so that it did not compete with the Alexa Fluor™ 568 NHS ester reaction with primary amines. Tris was also not compatible with the labeling. Proteins dialyzed for 17 h in 20 mM HEPES pH 8.0, 100 mM KCl, and 20% glycerol, at 4 °C or were buffer exchanged into the same buffer using PD-10 desalting columns. After labeling, the total protein content was quantified using Pierce 660 nm reagent. The final concentration of Cas9 was 2.69 mg/mL, ZF5.3-Cas9 was 1.52 mg/mL, and Cas9-ZF5.3 was 2.75 mg/mL. Samples of both Cas9 and Cas9-ZF5.3 were prepared such that the final concentrations were 1.51 mg/mL in 500 µL total volume.

#### *Alexa Fluor™ 568 NHS Ester Labeling*

Alexa Fluor™ 568 NHS ester was resuspended in 200 µL of anhydrous DMSO and vortexed thoroughly (stock concentration 6.3 mM). 20 µL aliquots were stored in amber Eppendorfs at -80 °C until use. 1.51 mg/mL Cas9 (10.7 µM), ZF5.3-Cas9 (10.5 µM), and Cas9-ZF5.3 (10.5 µM) were thawed on ice. 1.99 µL of dye (3 equivalents) were added to the Cas9 proteins. The samples incubated at 4 °C for 4 h. A dye sample (for use in SDS-PAGE) was created with 1.9 µL of stock dye and 400 µL of Tris buffer (20 mM Tris pH 8.0, 1 mM DTT, 100 µM ZnCl<sub>2</sub>, 20% glycerol, 0.1 M KCl). A 10% SDS-PAGE gel was run with each sample (20 µL of sample and 5 µL of 5X SDS loading dye, 20 µL loaded onto gel). All proteins were dialyzed into 20 mM Tris pH 8.0, 1 mM DTT, 100 µM ZnCl<sub>2</sub>, 20% glycerol, 0.1 M KCl overnight at 4 °C. The following day, solutions from dialysis were transferred to Eppendorf tubes. The samples were spun down at 21100 RCF for 3 min. There was a small pellet for ZF5.3-Cas9 but none observed for Cas9 or Cas9-ZF5.3. The supernatant solutions were transferred into amber Eppendorf tubes (labeled appropriately). 1.9 µL of Alexa Fluor™ 568 NHS ester stock and 400 µL of Tris buffer were mixed. 20 µL samples from the fluorescently labeled proteins and dye were combined with 5 µL of SDS-PAGE loading dye. Samples were heated at 100 °C for 5 min and then spun down. 8 µL of ladder and 20 µL of each sample were added to a 10% SDS-PAGE gel. The gel ran at 200 mV for approximately 27 min. Samples were stored at -80 °C until subsequent use.

### **6.3.6 Cell Culture and Assays**

#### *Cell Culture Information*

Saos-2 cells were cultured in McCoy's 5A medium supplemented with 15% fetal bovine serum (FBS), sodium pyruvate (1 mM), penicillin (100 units/mL), and streptomycin (100 µg/mL). Cell cultures were maintained at 37 °C in a humidified atmosphere at 5% CO<sub>2</sub>. Procedures for flow cytometry and fluorescence correlation spectroscopy (FCS) were performed using the method described by Knox *et al.*<sup>19</sup>

#### *Flow Cytometry and Fluorescence Correlation Spectroscopy of Cas9 Proteins*

40,000 Saos-2 cells were plated on a 12-well dish in clear McCoy's media. The next day, cells were washed twice with clear McCoy's 5A. Cells incubated with 0.5–1 µM

of Cas9, ZF5.3-Cas9, and Cas9-ZF5.3 (or RNPs: 0.5  $\mu$ M of Cas9, ZF5.3-Cas9, or Cas9-ZF5.3 with 0.5  $\mu$ M sgRNA pre-incubated for 15 min at room temperature) for 30 min. After 25 min, Hoechst 3342 was added to the wells for a 5 min incubation and final concentration of 300 nM. During incubation, a fibronectin-coated slide was prepared using a 1:100 dilution of fibronectin by adding 10  $\mu$ L of 1 mg/mL fibronectin to 990  $\mu$ L DPBS (final concentration 0.1 mg/mL). This microscopy slide incubated at 37 °C until use. After incubation, cells were washed three times with DPBS, and lifted with 1 mL clear trypsin (TrypLE) to remove surface-bound peptide. Cells were transferred into a 15-mL Falcon tube containing 2 mL FBS-containing clear McCoy's 5A. Cells were centrifuged at 200 *g* for 3 min. The media was aspirated and cells were washed once with 1 mL clear DMEM, and then sedimented at 200 *g* for 3 min. Cells were resuspended in 100  $\mu$ L of DPBS and analyzed by flow cytometry on an Attune NxT flow cytometer. 10,000 cells were analyzed for each sample. Data was analyzed using FlowJo and the median fluorescence values with standard error of the mean were reported. Cells were resuspended in 300  $\mu$ L clear DMEM and plated onto the microscopy dish. Cells adhered at 37 °C for 20 min. Confocal microscopy was completed to analyze cell morphology and preliminary uptake. FCS measurements were obtained on an LSM 880 using ZEN software and previously published methods.<sup>13,16,19,20</sup> Traces were analyzed using various diffusion models in MatLab.

## 6.4 Results

### 6.4.1 Purification of Cas9 Conjugates

Cas9 has tolerated modifications at both C- and N-termini such that it retains its catalytic activity,<sup>9,21–23</sup> so we assessed appendage of ZF5.3 at both ends (**Figure 6.1A**). We expressed fusion proteins with a C-terminal His<sub>6</sub>-tag in BL21(DE3)pLysS competent *E. coli* and purified the desired proteins from cell lysate using immobilized metal affinity chromatography (**Figure 6.1B and C**). All protein constructs expressed in moderate yields (>5 mg protein/L culture): Cas9-His<sub>6</sub> (hereby referred to as Cas9, 159.3 kD) resulted in 9 mg/L culture and was >99% pure. ZF5.3-Cas9-His<sub>6</sub> (hereby referred to as ZF5.3-Cas9, 162.4 kD) was >99% pure and produced 6 mg/L culture. Interestingly, the C-terminal construct Cas9-ZF5.3-His<sub>6</sub> (hereby referred to as Cas9-ZF5.3, 162.4 kD) produced about twice as much protein per L culture as the wild-type or ZF5.3-Cas9, with a yield of 15 mg/L culture and 95.8% pure material.

### 6.4.2 *In Vitro* Cleavage Assay

With purified Cas9 proteins in hand, we next assessed their *in vitro* activity. Cas9 complexes with sgRNA to locate DNA sequences that are complementary to the sgRNA. Once the correct sequence base pairs, Cas9 engages its nuclease function to cleave the DNA.<sup>4</sup> The dTomato reporter plasmid (8960 bp) has been used in the literature for readout of Cas9 activity both *in vitro* and *in cellulo*.<sup>24</sup>

*In vitro* Cas9 activity was assessed by forming ribonucleoproteins (RNPs) containing both the Cas9 protein and sgRNA, incubating RNPs with linearized dTomato plasmid, and assessing cleavage activity by standard DNA electrophoresis. Our first

step was to generate a linear plasmid using a restriction enzyme. The dTomato plasmid (5 µg) incubated with 1 µL EcoRI HF for 2 h and was evaluated by gel electrophoresis. Results of the EcoRI HF digest indicated minimal linearization; the linear product could not be distinguished from the supercoiled DNA at the top of the gel of the uncut plasmid (**Figure 6.2A**). We moved on and used PvuI HF (20 units) for the linearization, which showed distinct band separation between the uncut and cut plasmid (**Figure 6.2B**). Next, we incubated the linearized dTomato plasmid (246 ng) with an RNP of Cas9 and sgRNA (1.33 ratio sgRNA:Cas9, incubated for 20 min at room temperature prior to reaction) at 37 °C for either 2 h or overnight (**Figure 6.2C and D**). The product was expected to produce fragments at 3474 bp and 5486 bp. While some of the 2 h reactions worked, there was clear separation of the product bands near 5500 bp and 3500 bp for all overnight reactions with Cas9, ZF5.3-Cas9, and Cas9-ZF5.3. Since there was a band between 8 and 9 kbp, not all of the linearized plasmid was cleaved by the Cas9 enzymes (linearized plasmid expected at 8.96 kbp). Part of the limited cleavage could be explained by the excess sgRNA added to the reaction; however, it would be expected that Cas9 act catalytically to cleave additional sgRNA molecules. We compared cleavage of our purified enzymes with commercial Cas9 and found the commercial Cas9 activity was comparable to that of our enzymes. This study indicated successful cleavage of dTomato plasmids with the Cas9 enzyme, indicating activity of all enzymes *in vitro*.

#### 6.4.3 Non-specific Labeling of Cas9 Conjugates

Confocal microscopy, flow cytometry, and fluorescence correlation spectroscopy require the installation of a fluorophore.<sup>19</sup> We chose to introduce a rhodamine-based fluorophore (Alexa Fluor™ 568 NHS ester) to Cas9 conjugates using a non-specific labeling approach. Alexa Fluor™ 568 NHS ester reacts with surface exposed amines. Prior to labeling with an NHS ester, the reducing agent dithiothreitol (DTT) required removal from the protein buffer so as to not compete with the Cas9 during the labeling reaction. Of the 150 Lys residues and the N-terminus in Cas9, there are at least 6 surface exposed amines.<sup>25</sup> Cas9, ZF5.3-Cas9, and Cas9-ZF5.3 were labeled with Alexa Fluor™ 568 NHS ester for 4 h at 4 °C (**Figure 6.3A**) and excess dye was removed via overnight dialysis at 4 °C. Fluorescence and SDS-PAGE analyses indicated the presence of Alexa Fluor™ 568 at the expected molecular weights for the respective fusion proteins (**Figure 6.3B**). The average number of labels per protein was calculated by dividing the concentration of the Alexa Fluor™ 568 determined by NanoDrop at 560 nm by the concentration of the protein determined by Pierce 660 nm Reagent (Cas9 = 2.0, ZF5.3-Cas9 = 1.5, Cas9-ZF5.3 = 1.8), which confirmed there were surface exposed amines for non-specific labeling to occur.

#### 6.4.4 Evaluation of Overall Uptake via Confocal Microscopy and Flow Cytometry

With active enzymes in hand, we wanted to assess the total cellular uptake of the various constructs. First, we assessed the enzymes alone. Saos-2 cells were treated with 0.5 or 1 µM of Cas9, ZF5.3-Cas9, or Cas9-ZF5.3 for 30 min at 37 °C (**Figure 6.4A**). After washing the cells, cells were lifted with trypsin (also used to remove surface-bound

protein), washed, and either resuspended in DPBS for flow cytometry analysis or re-plated in DMEM onto a dish for confocal microscopy. Confocal microscopy images indicated that only the cells incubated with fluorescently-tagged proteins had fluorescence present in the Alexa Fluor™ 568 (Rho) channel (**Figure 6.4B**). 1  $\mu\text{M}$  of Cas9 proteins containing ZF5.3 exhibited increased punctate fluorescence (representative of endosomes) in comparison to cells treated with Cas9 alone, but it is difficult to distinguish between uptake of the N- and C-terminally labeled proteins. Flow cytometry experiments with 0.5  $\mu\text{M}$  of these constructs in Saos-2 cells indicated that Cas9-ZF5.3 resulted in a greater than 2-fold increase in total cell uptake in comparison to Cas9 alone (**Figure 6.4C**). N-terminal ZF5.3-Cas9 also resulted in approximately a two-fold uptake in comparison to Cas9. At 1  $\mu\text{M}$ , Cas9-ZF5.3 had the highest cellular uptake and was 1.8-fold higher than Cas9 alone. Slight decreases between 0.5 and 1  $\mu\text{M}$  treatment conditions may be due to older protein samples from the second trial of 1  $\mu\text{M}$ , but at both concentrations analyzed, the C-terminal ZF5.3 resulted in the highest total cellular uptake.

Next, Cas9 proteins incubated with sgRNA for 30 min at room temperature to generate RNPs (1:1 ratio of Cas9:sgRNA) to determine the effects of sgRNA on total cellular uptake. Saos-2 cells were treated with RNPs (0.5  $\mu\text{M}$  of Cas9, ZF5.3-Cas9, or Cas9-ZF5.3 with 0.5  $\mu\text{M}$  sgRNA pre-incubated for 15 min at room temperature) for 30 min at 37 °C. The total cellular uptake of each Cas9 protein when in the presence of sgRNA decreased (**Figure 6.4C**). Interestingly, the only sample in which addition of sgRNA did not significantly impact total cellular uptake was in cells treated with wild-type Cas9. Similar to the results without sgRNA present, there was an approximate 2-fold increase in total cellular uptake with the C-terminal ZF5.3 conjugate. The cellular uptake may decrease so dramatically because of the changes in surface charge properties when Cas9 is bound to RNA (**Figure 6.4D**). Other groups have not been able to show uptake of Cas9 alone,<sup>18</sup> which may illustrate the possibility of cell line dependencies. Nonetheless, these experiments provide evidence that non-specifically labeled proteins can be used to determine total cellular uptake and that ZF5.3 increases the amount of Cas9 that reaches the interior of the cell.

#### 6.4.5 Evaluation of Cas9 via FCS

The final goal of this project was to quantify the amount of Cas9 that reaches either the cytosol or nucleus using FCS. Saos-2 cells were treated with 0.5 or 1  $\mu\text{M}$  of Cas9, ZF5.3-Cas9, or Cas9-ZF5.3 for 30 min at 37 °C (**Figure 6.4A**). After washing, the cells were lifted with trypsin (also used to remove surface-bound protein), washed, resuspended in DMEM, and re-plated onto a dish for FCS analysis. FCS methods were completed as previously published.<sup>13,16,19,20</sup> Unexpectedly, the *in vitro* standards (in DMEM) for Cas9, ZF5.3-Cas9, and Cas9-ZF5.3 produced diffusion times that were greater than those calculated for *in cellulo* measurements (~0.2 ms compared to >0.1 ms). For reference, most SNAP-tag proteins conjugated to various CPPs and CPMPs exhibited diffusion times <1 ms *in vitro*.<sup>20</sup> Since Cas9 (160 kD) is much larger than SNAP-tag, it is expected to have a larger diffusion time than SNAP-tag (20 kD); a smaller *in vitro* diffusion time indicates the protein is likely free-dye or digested. With this

observation and no traces that passed FCS analysis, it was concluded that non-specific labeling for FCS purposes is not ideal. Indeed, others have shown for quantification purposes there needs to be a homogenous protein mixture for FCS.<sup>19,26</sup>

## 6.5 Conclusions

The studies described herein illustrate that Cas9 labeled with N- or C-terminal ZF5.3 remains active *in vitro* and can access the interior of cells at higher levels than Cas9 alone. Using Alexa Fluor™ 568 NHS ester, Cas9, ZF5.3-Cas9, and Cas9-ZF5.3 were non-specifically labeled to produce fluorophore-labeled products for use with confocal microscopy and flow cytometry. The Cas9 protein containing a C-terminal ZF5.3 exhibited the highest cellular uptake in all conditions evaluated, even in the presence of sgRNA. The non-specific label inhibited compatibility with FCS as it generated a heterogeneous mixture of protein material. While the average protein contains a certain number of labels, each individual protein may contain more or less. Since FCS is such a quantitative technique, the use of a heterogeneous mixture is not compatible. This observation continues to inform protein design strategies in the Schepartz Laboratory.

Improvements for this project include the use of TALON resin and additional cation column purification. A recent paper from the Doudna lab used *Streptococcus progenies* Cas9 M1C/C80S for ASGPr ligand labeling (the protein contains two cysteine residues for conjugation), which allows for cell-specific studies.<sup>9</sup> Future work includes completing *in cellulo* studies to evaluate the ability of Cas9-ZF5.3 to turn off EGFP expression in U2OS cells.<sup>15</sup> To improve nuclear access, nuclear localization tags, such as that of SV40 large T antigen (PKKKRKV),<sup>27</sup> may be appended if necessary.

## 6.6 Figures

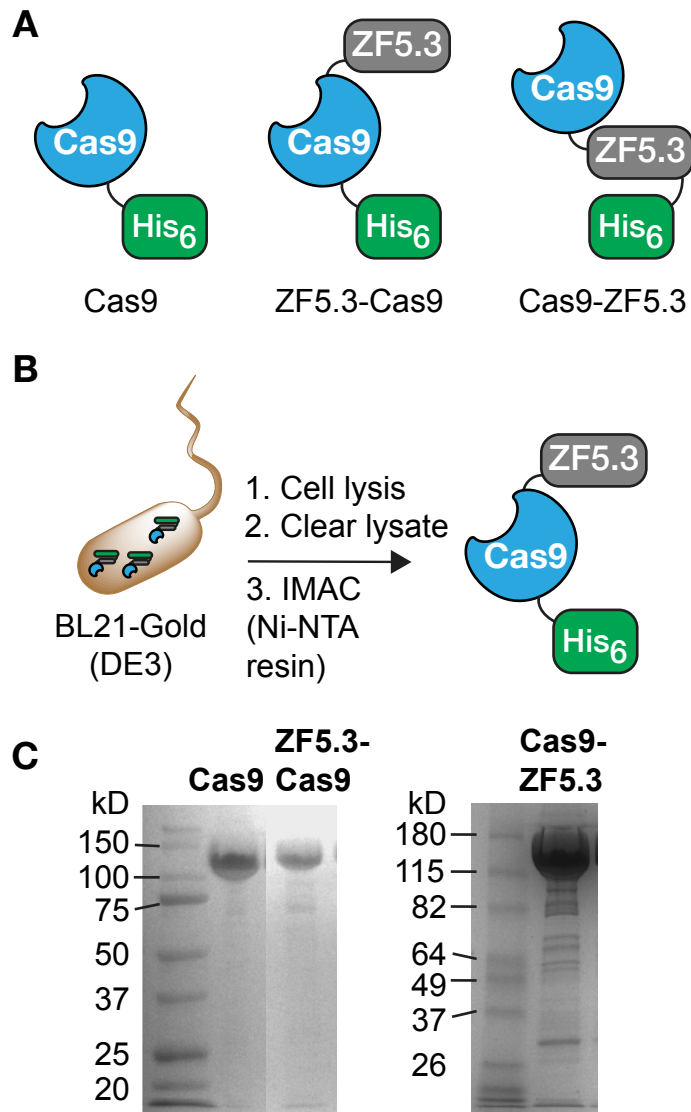


**Figure 6.1.** (A) Protein constructs evaluated in this chapter. (B) Example purification scheme of Cas9 fusion protein ZF5.3-Cas9. (C) SDS-PAGE analysis of Cas9, ZF5.3-Cas9, and Cas9-ZF5.3 after final dialysis into 20 mM Tris (pH 8.0), 100 mM KCl, 20% glycerol, and 1 mM DTT (with 100  $\mu$ M ZnCl<sub>2</sub> for ZF5.3-containing proteins).

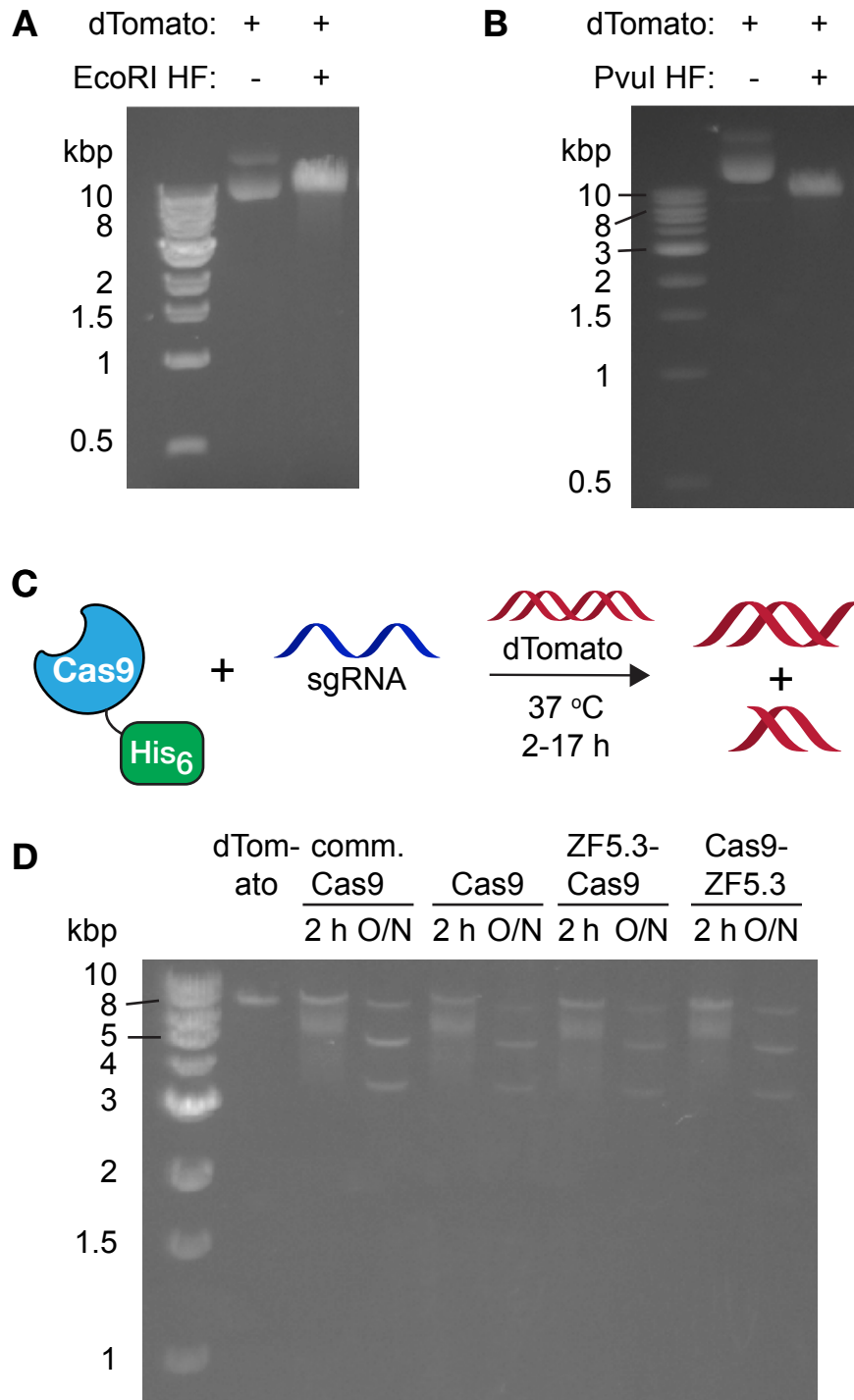


**Figure 6.2.** (A) Linearization of dTomato plasmid (5 µg) with EcoRI HF (1 µL) for 2 h at room temperature. (B) Linearization of dTomato plasmid (5 µg) with PvuI HF (20 units) for 2 h. (C) Scheme of *in vitro* cleavage assay using Cas9 enzymes. (D) Gel electrophoresis analysis of *in vitro* cleavage assay. O/N = overnight (17 h); comm. Cas9 = commercial Cas9.

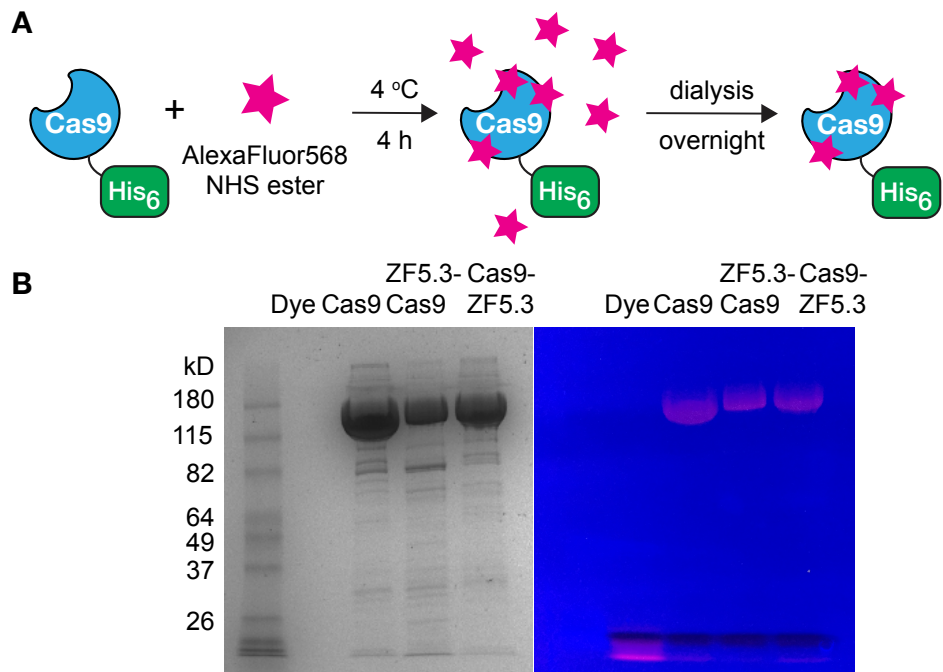


**Figure 6.3.** (A) Cas9 protein fluorophore labeling scheme. Excess dye is removed via overnight dialysis at 4 °C. (B) SDS-PAGE analysis of the fluorophore labeling reaction (Coomassie, left; UV, right). Dye = Alexa Fluor™ 568 NHS ester.

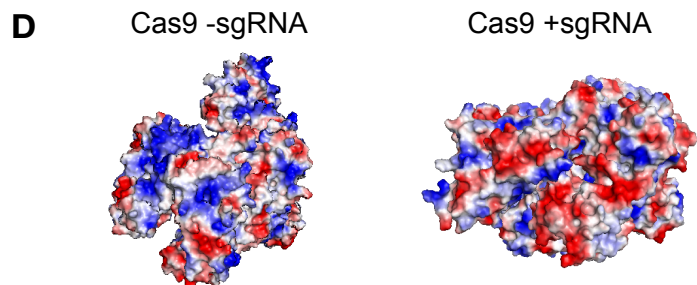
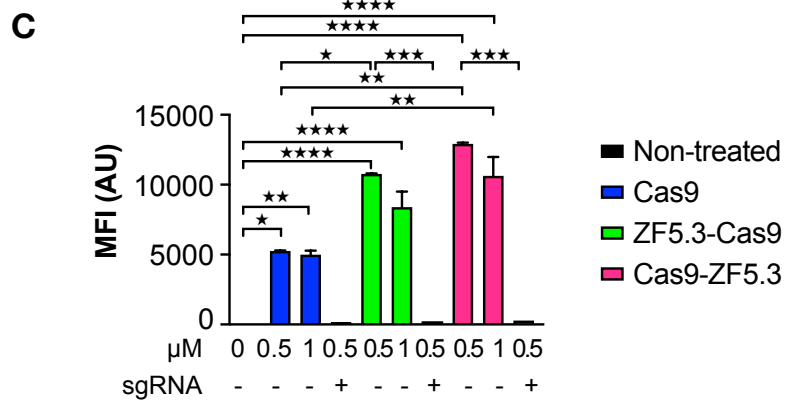
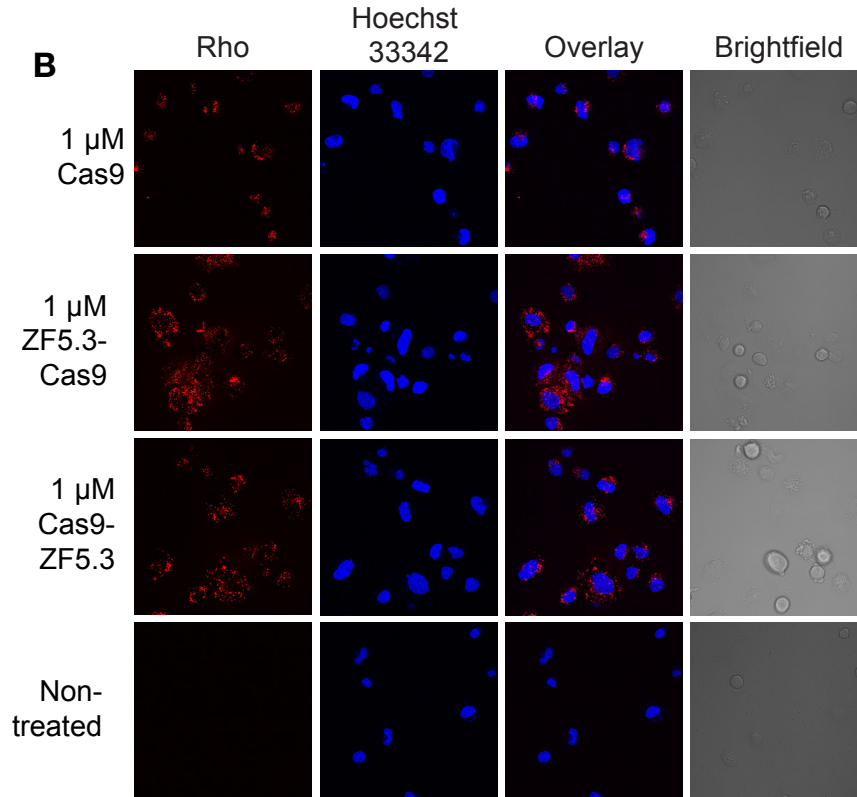
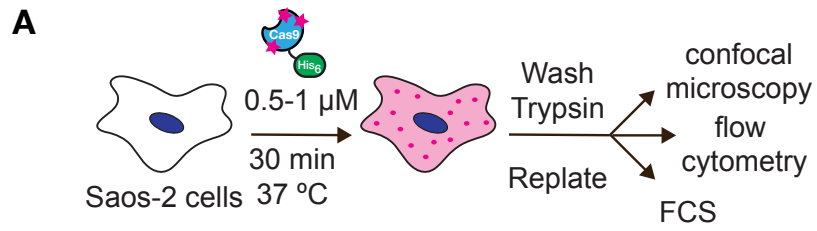


**Figure 6.4.** (A) Scheme illustrating confocal microscopy, flow cytometry, and fluorescence correlation spectroscopy (FCS) workflow. Saos-2 cells were treated with 0.5–1  $\mu\text{M}$  of Cas9, ZF5.3-Cas9, or Cas9-ZF5.3 for 30 min. Cells were washed, treated with trypsin, and either screened using flow cytometry or re-plated and imaged using confocal microscopy and FCS. (B) Total cellular uptake of Cas9 proteins assessed using confocal microscopy. Live cell images of Saos-2 cells treated with 1  $\mu\text{M}$  of the indicated protein for 30 min. (C) Histograms illustrating total cellular uptake of 0.5–1  $\mu\text{M}$  of Cas9, ZF5.3-Cas9, or Cas9-ZF5.3 during a 30 min incubation at 37 °C. MFI values represent the median fluorescence intensity of cells (10,000 cells each). Error bars represent the standard error of the mean. The MFI values of each Cas9 protein (at each treatment condition) were statistically compared. \*\*\*\* $p \leq 0.0001$ , \*\*\* $p \leq 0.001$ , \*\* $p \leq 0.01$ , \* $p \leq 0.05$ ; one-way analysis of variance (ANOVA) followed by Tukey's multiple comparisons test. (D) Surface charge analysis (blue = positive, red = negative) obtained with PyMol (Version 2.4.1) of Cas9 without sgRNA (PDB 4cmp) and in the presence of sgRNA (PDB 4un3).

## 6.7 References

- (1) Barrangou, R.; Fremaux, C.; Deveau, H.; Richards, M.; Boyaval, P.; Moineau, S.; Romero, D. A.; Horvath, P. CRISPR Provides Acquired Resistance Against Viruses in Prokaryotes. *Science* **2007**, *315* (5819), 1709. <https://doi.org/10.1126/science.1138140>.
- (2) The Nobel Prize in Chemistry 2020 <https://www.nobelprize.org/prizes/chemistry/2020/press-release/> (accessed Nov 3, 2020).
- (3) Pickar-Oliver, A.; Gersbach, C. A. The next Generation of CRISPR–Cas Technologies and Applications. *Nat. Rev. Mol. Cell Biol.* **2019**, *20* (8), 490–507. <https://doi.org/10.1038/s41580-019-0131-5>.
- (4) Doudna, J. A.; Charpentier, E. The New Frontier of Genome Engineering with CRISPR-Cas9. *Science* **2014**, *346* (6213), 1258096. <https://doi.org/10.1126/science.1258096>.
- (5) Yip, B. H. Recent Advances in CRISPR/Cas9 Delivery Strategies. *Biomolecules* **2020**, *10* (6). <https://doi.org/10.3390/biom10060839>.
- (6) Sun, W.; Ji, W.; Hall, J. M.; Hu, Q.; Wang, C.; Beisel, C. L.; Gu, Z. Self-Assembled DNA Nanoclews for the Efficient Delivery of CRISPR-Cas9 for Genome Editing. *Angew. Chem. Int. Ed Engl.* **2015**, *54* (41), 12029–12033. <https://doi.org/10.1002/anie.201506030>.
- (7) Krishnamurthy, S.; Wohlford-Lenane, C.; Kandimalla, S.; Sartre, G.; Meyerholz, D. K.; Théberge, V.; Hallée, S.; Duperré, A.-M.; Del'Guidice, T.; Lepetit-Stoffaes, J.-P.; Barbeau, X.; Guay, D.; McCray, P. B. Engineered Amphiphilic Peptides Enable Delivery of Proteins and CRISPR-Associated Nucleases to Airway Epithelia. *Nat. Commun.* **2019**, *10* (1), 4906. <https://doi.org/10.1038/s41467-019-12922-y>.
- (8) Wang, H.-X.; Song, Z.; Lao, Y.-H.; Xu, X.; Gong, J.; Cheng, D.; Chakraborty, S.; Park, J. S.; Li, M.; Huang, D.; Yin, L.; Cheng, J.; Leong, K. W. Nonviral Gene Editing via CRISPR/Cas9 Delivery by Membrane-Disruptive and Endosomolytic

- Helical Polypeptide. *Proc. Natl. Acad. Sci.* **2018**, *115* (19), 4903. <https://doi.org/10.1073/pnas.1712963115>.
- (9) Rouet, R.; Thuma, B. A.; Roy, M. D.; Lintner, N. G.; Rubitski, D. M.; Finley, J. E.; Wisniewska, H. M.; Mendonsa, R.; Hirsh, A.; de Oñate, L.; Compte Barrón, J.; McLellan, T. J.; Bellenger, J.; Feng, X.; Varghese, A.; Chrnyk, B. A.; Borzilleri, K.; Hesp, K. D.; Zhou, K.; Ma, N.; Tu, M.; Dullea, R.; McClure, K. F.; Wilson, R. C.; Liras, S.; Mascitti, V.; Doudna, J. A. Receptor-Mediated Delivery of CRISPR-Cas9 Endonuclease for Cell-Type-Specific Gene Editing. *J. Am. Chem. Soc.* **2018**, *140* (21), 6596–6603. <https://doi.org/10.1021/jacs.8b01551>.
- (10) Akishiba, M.; Takeuchi, T.; Kawaguchi, Y.; Sakamoto, K.; Yu, H.-H.; Nakase, I.; Takatani-Nakase, T.; Madani, F.; Gräslund, A.; Futaki, S. Cytosolic Antibody Delivery by Lipid-Sensitive Endosomolytic Peptide. *Nat. Chem.* **2017**, *9* (8), 751–761. <https://doi.org/10.1038/nchem.2779>.
- (11) Ahmad, A.; Ranjan, S.; Zhang, W.; Zou, J.; Pyykkö, I.; Kinnunen, P. K. J. Novel Endosomolytic Peptides for Enhancing Gene Delivery in Nanoparticles. *Biochim. Biophys. Acta BBA - Biomembr.* **2015**, *1848* (2), 544–553. <https://doi.org/10.1016/j.bbamem.2014.11.008>.
- (12) Rouet, R.; Christ, D. Efficient Intracellular Delivery of CRISPR-Cas Ribonucleoproteins through Receptor Mediated Endocytosis. *ACS Chem. Biol.* **2019**, *14* (3), 554–561. <https://doi.org/10.1021/acscchembio.9b00116>.
- (13) Steinauer, A.; LaRoche, J. R.; Knox, S. L.; Wissner, R. F.; Berry, S.; Schepartz, A. HOPS-Dependent Endosomal Fusion Required for Efficient Cytosolic Delivery of Therapeutic Peptides and Small Proteins. *Proc. Natl. Acad. Sci.* **2019**, *116* (2), 512–521. <https://doi.org/10.1073/pnas.1812044116>.
- (14) Gasteiger, E.; Gattiker, A.; Hoogland, C.; Ivanyi, I.; Appel, R. D.; Bairoch, A. ExPASy: The Proteomics Server for in-Depth Protein Knowledge and Analysis. *Nucleic Acids Res.* **2003**, *31* (13), 3784–3788. <https://doi.org/10.1093/nar/gkg563>.
- (15) Zuris, J. A.; Thompson, D. B.; Shu, Y.; Guiling, J. P.; Bessen, J. L.; Hu, J. H.; Maeder, M. L.; Joung, J. K.; Chen, Z.-Y.; Liu, D. R. Cationic Lipid-Mediated Delivery of Proteins Enables Efficient Protein-Based Genome Editing in Vitro and in Vivo. *Nat. Biotechnol.* **2015**, *33* (1), 73–80. <https://doi.org/10.1038/nbt.3081>.
- (16) LaRoche, J. R.; Cobb, G. B.; Steinauer, A.; Rhoades, E.; Schepartz, A. Fluorescence Correlation Spectroscopy Reveals Highly Efficient Cytosolic Delivery of Certain Penta-Arg Proteins and Stapled Peptides. *J. Am. Chem. Soc.* **2015**, *137* (7), 2536–2541. <https://doi.org/10.1021/ja510391n>.
- (17) Kim, S. M.; Shin, S. C.; Kim, E. E.; Kim, S.-H.; Park, K.; Oh, S. J.; Jang, M. Simple in Vivo Gene Editing via Direct Self-Assembly of Cas9 Ribonucleoprotein Complexes for Cancer Treatment. *ACS Nano* **2018**, *12* (8), 7750–7760. <https://doi.org/10.1021/acsnano.8b01670>.
- (18) Staahl, B. T.; Benekareddy, M.; Coulon-Bainier, C.; Banfal, A. A.; Floor, S. N.; Sabo, J. K.; Urnes, C.; Munares, G. A.; Ghosh, A.; Doudna, J. A. Efficient Genome Editing in the Mouse Brain by Local Delivery of Engineered Cas9 Ribonucleoprotein Complexes. *Nat. Biotechnol.* **2017**, *35* (5), 431–434. <https://doi.org/10.1038/nbt.3806>.

- (19) Knox, S. L.; Steinauer, A.; Alpha-Cobb, G.; Trexler, A.; Rhoades, E.; Schepartz, A. Chapter Twenty-One - Quantification of Protein Delivery in Live Cells Using Fluorescence Correlation Spectroscopy. In *Methods in Enzymology*; Chenoweth, D. M., Ed.; Academic Press, 2020; Vol. 641, pp 477–505. <https://doi.org/10.1016/bs.mie.2020.05.007>.
- (20) Wissner, R. F.; Steinauer, A.; Knox, S. L.; Thompson, A. D.; Schepartz, A. Fluorescence Correlation Spectroscopy Reveals Efficient Cytosolic Delivery of Protein Cargo by Cell-Permeant Miniature Proteins. *ACS Cent. Sci.* **2018**, *4* (10), 1379–1393. <https://doi.org/10.1021/acscentsci.8b00446>.
- (21) Bikard, D.; Jiang, W.; Samai, P.; Hochschild, A.; Zhang, F.; Marraffini, L. A. Programmable Repression and Activation of Bacterial Gene Expression Using an Engineered CRISPR-Cas System. *Nucleic Acids Res.* **2013**, *41* (15), 7429–7437. <https://doi.org/10.1093/nar/gkt520>.
- (22) Guilinger, J. P.; Thompson, D. B.; Liu, D. R. Fusion of Catalytically Inactive Cas9 to FokI Nuclease Improves the Specificity of Genome Modification. *Nat. Biotechnol.* **2014**, *32* (6), 577–582. <https://doi.org/10.1038/nbt.2909>.
- (23) Tsai, S. Q.; Wyvekens, N.; Khayter, C.; Foden, J. A.; Thapar, V.; Reyon, D.; Goodwin, M. J.; Aryee, M. J.; Joung, J. K. Dimeric CRISPR RNA-Guided FokI Nucleases for Highly Specific Genome Editing. *Nat. Biotechnol.* **2014**, *32* (6), 569–576. <https://doi.org/10.1038/nbt.2908>.
- (24) D'Astolfo, D. S.; Pagliero, R. J.; Pras, A.; Karthaus, W. R.; Clevers, H.; Prasad, V.; Lebbink, R. J.; Rehmann, H.; Geijsen, N. Efficient Intracellular Delivery of Native Proteins. *Cell* **2015**, *161* (3), 674–690. <https://doi.org/10.1016/j.cell.2015.03.028>.
- (25) Hemphill, J.; Borchardt, E. K.; Brown, K.; Asokan, A.; Deiters, A. Optical Control of CRISPR/Cas9 Gene Editing. *J. Am. Chem. Soc.* **2015**, *137* (17), 5642–5645. <https://doi.org/10.1021/ja512664v>.
- (26) Kim, S. A.; Heinze, K. G.; Schwille, P. Fluorescence Correlation Spectroscopy in Living Cells. *Nat. Methods* **2007**, *4* (11), 963–973. <https://doi.org/10.1038/nmeth1104>.
- (27) Tiganis, T.; Flint, A. J.; Adam, S. A.; Tonks, N. K. Association of the T-Cell Protein Tyrosine Phosphatase with Nuclear Import Factor P97. *J. Biol. Chem.* **1997**, *272* (34), 21548–21557. <https://doi.org/10.1074/jbc.272.34.21548>.

## **CHAPTER 7**

Towards Cellular Delivery of Ras-Binding NS1 Using ZF5.3

## 7.1 Abstract

While 20% of cancers carry activating mutations in Ras proteins, no approved therapeutic directly targets Ras proteins. The Ras proteins provide challenges for both small molecules and protein-based drugs, as they contain smooth surfaces and are located within the cell. Previous studies identified a monobody, NS1, that binds to two isoforms of Ras (H-Ras and K-Ras) with high affinity (>100 nM) *in vitro*. We hypothesized that appending the cell-permeant miniature protein ZF5.3 to NS1 would convey cell-permeant properties, allowing cellular delivery of purified NS1 into mammalian cells. Since expression of a genetic fusion containing both ZF5.3 and NS1 proved to be non-trivial, we assessed tyrosinase-mediated oxidative coupling to generate NS1-ZF5.3. We observed that ZF5.3 can be appended to proteins carrying a surface accessible Cys via tyrosinase. This project was (and continues to be) completed with support by Angel Vázquez-Maldonado, a rotation student in the Schepartz Laboratory.

## 7.2 Introduction

The Ras family proteins are master regulators of cell proliferation and survival. These GTPases bind and hydrolyze GTP and are active in their GTP-bound state and inactive in their GDP-bound state.<sup>1</sup> There are four isoforms of this family of proteins: H-Ras, N-Ras, K-Ras4a, and K-Ras4b, which exhibit approximately 80% homology in their primary sequences.<sup>1,2</sup> Many of the differences between these enzymes result from varying C-terminal domains.<sup>1</sup> 20% of all cancers carry activating mutations in Ras proteins, which provides motivation to target this family of proteins for inhibitor design.<sup>3</sup> The most frequent mutation in Ras proteins results in the inhibition of GTP hydrolysis, which diminishes the GTPase activity and changes the rate of guanine nucleotide exchange.<sup>1</sup> H-Ras localizes to the cytosol where it can be found interacting with the Golgi, caveolae, lipid rafts, and disorganized membranes.<sup>1</sup> K-Ras splice variants K-Ras4a and K-Ras4b localize to the plasma membrane, and K-Ras4a specifically reaches the plasma membrane via a Golgi-independent cytosolic route.<sup>4</sup> As these Ras proteins can be found in the cytosol, inhibitors would need to reach the interior of the cell to exhibit their function.

Challenges in targeting Ras proteins include the lack of a small-molecule binding pocket on the surface for traditional small molecule inhibitors and the intracellular locale for protein-based therapeutics.<sup>5</sup> No approved treatment directly targets Ras,<sup>6</sup> providing motivation to generate protein-based therapeutics that contain a delivery tool to provide a means for the therapeutic to reach the cell interior.

NS1 is a monobody that binds Ras proteins, not differentiating between active (GTP-bound) and inactive (GDP-bound) states.<sup>7</sup> This antibody mimetic exhibits high affinity for H-RAS (~15 nM) and K-RAS (~70 nM) *in vitro*, but no affinity for N-RAS.<sup>7</sup> *In cellulo*, NS1 decreases downstream signaling, including the ERK signaling pathway.<sup>7</sup> The *in cellulo* studies were conducted in a cell line that expresses NS1 so that they are

already inside of the cell. To expand the druggable proteome, it is necessary to design a cell-permeant NS1 that retains Ras-binding for therapeutic applications.

The cell-permeant miniature protein (CPMP) ZF5.3 can deliver proteins to the cytosol of mammalian cells and the livers of healthy mice.<sup>8,9</sup> Additionally, among a panel of cell-penetrating peptides and CPMPs, ZF5.3-labeled proteins reached the cytosol at the highest cytosolic concentrations,<sup>8</sup> motivating its use as a therapeutic delivery vehicle. We hypothesize that ZF5.3 will convey cell-permeant properties to NS1 in order to inhibit intracellular Ras. In this chapter we begin developing strategies to generate NS1 and NS1-ZF5.3 that contain a site-specific fluorophore for flow cytometry, confocal microscopy, and fluorescence correlation spectroscopy. Our ultimate goal is to determine the effects that ZF5.3 has on NS1 cellular delivery and cytosolic localization.

## 7.3 Methods

### 7.3.1 Protein Sequences

#### NS1-His<sub>6</sub>-Cys

GSVSSVPTKLEVVAAATPTSLISWDAPAVTVDYYVITYGETGGNSPVQKFEVPGSKSTATISGLKPGVDYTITVYAWGWHGQVYYMGSPIINIRYRTGSG**HHHHHHC**

#### His<sub>7</sub>-AviTag-TEV-NS1-GSGC

MHHHHHHHGSGLNDIFEAQKIEWHEGDYDIPTTENLYFQGMGSVSSVPTKLEVVAAATPTSLISWDAPAVTVDYYVITYGETGGNSPVQKFEVPGSKSTATISGLKPGVDYTITVYAWGWHGQVYYMGSPIINIRYRTGSGC

#### His<sub>7</sub>-AviTag-TEV-NS1-ZF5.3-GSGC

MHHHHHHHGSGLNDIFEAQKIEWHEGDYDIPTTENLYFQGMGSVSSVPTKLEVVAAATPTSLISWDAPAVTVDYYVITYGETGGNSPVQKFEVPGSKSTATISGLKPGVDYTITVYAWGWHGQVYYMGSPIINIRYRTGSGYSCNVCVKAFVLSRHLNRHLRVHRRATGSGC

#### ZF5.3-SGGY

Ac-WTSCNVCVKAFVLSRHLNRHLRVHRRATSGGY-NH<sub>2</sub>

#### ZF5.3

Ac-WYSCNVCVKAFVLSRHLNRHLRVHRRAT-NH<sub>2</sub>

#### ZF5.3<sup>Rho</sup>

<sup>Rho</sup>KWYSCNVCVKAFVLSRHLNRHLRVHRRAT-NH<sub>2</sub>

### 7.3.2 Primers for pET32a Vector Linearization

The sequence of NS1 or NS1-GSGC with a N-terminal His<sub>7</sub>, followed by an AviTag and TEV protease site were codon optimized for *E. coli* expression, cloned into a linearized pET-32a vector, and expressed in the BL21-Gold (DE3) *E. coli* strain. Primers for linearization of commercial pET-32a for Gibson Assembly reactions:<sup>8</sup> 5'-ATGTATATCTCCTTCTTAAAGTTAAACAAAATTATT-3'

5'-TAACAAAGCCCCGAAAGGAAG-3'

Primers for ZF5.3 deletion from pET32a\_ZF5.3-NS1-His<sub>6</sub>-Cys

5'-GGATCCGTCTCCTCCGT-3'

5'-CATATGTATATCTCCTTCTTAAAGTTAAACAAAATTAT-3'

### 7.3.3 Polymerase Chain Reaction (PCR) to Delete ZF5.3 from pET32a\_ZF5.3-NS1-His<sub>6</sub>-Cys

10 µL of 5X Phusion HF Buffer, 200 µM dNTPs, 0.5 µM forward primer, 0.5 µM reverse primer, 112.1 ng of template DNA, 1.5 µL DMSO, and 0.5 µL Phusion DNA polymerase were added to a PCR tube. Nuclease-free water was added to a final volume of 50 µL. Four PCR reactions were set up, two containing the 1.5 µL of DMSO and two without. Both 62 and 63 °C were tested for annealing temperatures. Standard PCR conditions were used.

After PCR, 2.5 µL of KLD reaction mixture was added to a tube of NEB® 5-alpha F Iq Competent *E. coli* (High Efficiency) and a transformation was completed. The plate incubated at 37 °C overnight. The following day, starter cultures were prepared (5 mL LB Lennox media, 5 µL 1000X carbenicillin, 1 colony) and grew overnight at 37 °C. A miniprep was completed using Qiagen reagents and Sanger sequencing was submitted to Genewiz using T7 forward and reverse primers. Correct plasmids (pET32a\_NS1-His<sub>6</sub>-Cys) were stored at -20 °C until use.

### 7.3.4 Gibson Assembly

Gibson assembly was completed as described previously<sup>10,11</sup> using a pET32a backbone and gBlock™ gene fragment for insertion of His<sub>7</sub>-AviTag-TEV-NS1-GSGC or His<sub>7</sub>-AviTag-TEV-NS1-GSG-ZF5.3-GSGC.

### 7.3.5 Protein Expression and Purification

#### *Protein Expression*

After transformation of pET32a\_NS1-His<sub>6</sub>-Cys, pET32a\_His<sub>7</sub>-AviTag-TEV-NS1-GSGC, or pET32a\_His<sub>7</sub>-AviTag-TEV-NS1-ZF5.3-GSGC into BL21-Gold (DE3) competent *E. coli*, starter cultures were set up in the morning containing 5 mL LB Lennox media, 5 µL 1000X carbenicillin, and 1 colony. After 3.5 h, the starter culture inoculated 1 L of LB Lennox media and 100 mg of ampicillin. When the OD<sub>600</sub> was 0.6–0.8, IPTG was added for a final concentration of 0.5 mM. The flasks shook overnight at 18 °C to allow expression to occur. The following day, the cultures were spun down at 4300 RPM and 4 °C for 30 min to pellet the bacteria.

#### *Purification of NS1-His<sub>6</sub>-Cys and His<sub>7</sub>-AviTag-TEV-NS1-GSGC*

The following buffers were used for purification: stock buffer (20 mM Tris-HCl pH 7.5, 5 mM MgCl<sub>2</sub>), high salt wash buffer (20 mM Tris-HCl pH 7.5, 5 mM MgCl<sub>2</sub>, 150 mM NaCl), wash buffer (20 mM Tris-HCl pH 7.5, 5 mM MgCl<sub>2</sub>), elution buffer (20 mM Tris-

HCl pH 7.5, 5 mM MgCl<sub>2</sub>, 250 mM imidazole), and dialysis buffer (20 mM Tris-HCl pH 7.5, 5 mM MgCl<sub>2</sub>, 1 mM dithiothreitol (DTT)). The pellet was resuspended in approximately 20 mL of 20 mM Tris-HCl pH 7.5, 5 mM MgCl<sub>2</sub> containing 1 protease inhibitor (1 tablet cOmplete, mini EDTA-free protease inhibitor cocktail). The lysate was sonicated for a total of 8 min (30 s on, 30 s off) at 30% duty cycle. The lysate was cleared by centrifugation for 45 min at 4 °C and 10,000 RPM. The cleared lysate was combined with Talon resin (3 mL of Talon resin/L of culture) and added to a 50 mL Falcon tube. The tube rotated on a rotisserie at 4 °C for 1 h. The slurry was added to a column and the flowthrough was drained (flowthrough was collected in a 50 mL Falcon tube for SDS-PAGE). The resin was washed 2X with 25 mL high salt wash buffer and 3X with 25 mL wash buffer. Each wash step was collected for SDS-PAGE analysis. The protein was eluted with 9 X 1 mL fractions of elution buffer. SDS-PAGE samples were prepared of the elution fractions as well as for other steps of the purification (20 µL sample + 5 µL 5X SDS-PAGE loading dye). SDS-PAGE was completed (200 V for 25–30 min). Fractions containing protein were combined and dialyzed overnight at 4 °C. The following day, the protein was concentrated using Amicon spin filters (10 kDa MWCO) and subsequently quantified using Pierce™ 660 nm reagent. Protein was stored at -80 °C until further use. The yield for NS1-His<sub>6</sub>-Cys was 0.98 mg/L. The yield for His<sub>7</sub>-AviTag-TEV-NS1-GSGC was 4.5 mg/L. Protein identity was confirmed via MS.

### 7.3.6 Peptide Synthesis

ZF5.3-SGGY, ZF5.3, and ZF5.3<sup>Rho</sup> were synthesized and purified as described in Steinauer *et al.*<sup>12</sup> Briefly, peptides were synthesized on a 50 µmol scale with H-Rink amide resin (to generate a final product with a C-terminal amide). Resin was swelled in dimethylformamide (DMF, 4.5 mL) at 70 °C for 20 min followed by microwave-assisted (75 °C for 5 min) coupling of amino acids using standard Fmoc chemistry (4.5 mL DMF, 5 equivalents (equiv) N,N,N',N'-tetramethyl-O-(1H-benzotriazol-1-yl)uronium hexafluorophosphate (HBTU), 5 equiv 1-hydroxybenzotriazole hydrate (HOBt), 10 equiv N,N-diisopropylethylamine (DIEA), and 5 equiv Fmoc-protected amino acid). Arginine, cysteine, and histidine residues were coupled at 50 °C and arginine residues were coupled twice. Fmoc deprotections were performed using 20% piperidine in DMF (4.5 mL) with microwave assistance (70 °C for 3 min, twice). The resin was washed thoroughly with DMF (four times, 4.5 mL/wash) between each coupling and deprotection step. Following synthesis, the resin was transferred to a custom glass reaction vessel containing a stir bar. To prevent sticking of the resin to glass, both the reaction vessel and stir bar were coated with SigmaCote before the resin was added.

ZF5.3-SGGY and ZF5.3 were acetylated at the N-terminus. The N-terminal Fmoc group was deprotected in 4.5 mL 20% piperidine in DMF at room temperature for 20 min twice. The resin was washed with 4 mL DMF three times. A solution of acetic anhydride, DIEA, and DMF (2 mL, in a 85:315:1600 volumetric ratio) were added to the resin and stirred at room temperature for 45 min. The resin was washed with 4 mL DMF three times. Next, the resin was washed three times with alternating DMF (10 mL) and dichloromethane (DCM, 10 mL). After the final DCM rinse, the resin was washed with 5

mL methanol and dried overnight under nitrogen. The resin was stored at -20 °C until cleavage.

To generate ZF5.3<sup>Rho</sup>, the N-terminus of ZF5.3 (on resin in a glass reaction vessel) was deprotected with 20% piperidine in DMF (2X, 15 min, room temperature). Boc-Lys(Fmoc)-OH (5 equiv) was coupled with 7-azabenzotriazol-1-ylxy)trispyrrolidinophosphonium hexafluorophosphate (PyAOP) (5.0 equiv), HOAt (5.0 equiv), and DIEA (10.0 equiv) in DMF (4 mL) at RT for 45 min. The side chain of the N-terminal amino acid was deprotected with 20% piperidine in DMF (2X, 15 min, room temperature). Next, the resin was washed with alternating DMF (10 mL) and DCM (10 mL) three times and washed several times with DMF. The glass reaction vessel was purged with nitrogen and the resin was washed five times with 5 mL anhydrous DMF under nitrogen atmosphere. 10 equiv of Lissamine rhodamine B sulfonyl chloride were added to anhydrous DMF (3 mL) and added to the resin. 10 equiv of anhydrous DIEA were subsequently added to the vessel. The reaction proceeded under nitrogen atmosphere overnight at room temperature. The next day, the resin was washed with alternating DMF (10 mL) and DCM (10 mL) three times and washed with DMF until no excess Lissamine rhodamine B was observed in the wash solution. The resin was washed with 5 mL methanol to shrink the resin and then dried overnight under a stream of nitrogen.

Since all peptides contained cysteines, the cleavage cocktail was comprised of trifluoroacetic acid (TFA, 81.5%), thioanisole (5%), phenol (5%), water (5%), ethanedithiol (2.5%), and triisopropylsilane (TIPS, 1%). Peptides were cleaved in the described cocktail (4.5 mL) at room temperature for 3 h. (3 h, RT). Cleaved peptides were precipitated in diethyl ether (40 mL, chilled to -80 °C), sedimented, redissolved in a mixture of water and acetonitrile (ACN, max. 20%), frozen at -80 °C, lyophilized to dryness, and reconstituted in 1–1.5 mL dimethylsulfoxide (DMSO) prior to purification by HPLC.

For HPLC purification of peptides, the peptide stocks in DMSO were filtered through a 0.45 µm filter prior to application onto a semiprep Grace Vydac C18 (218TP) column. Peptides were detected at 214 and 280 nm. ZF5.3<sup>Rho</sup> was additionally detected at 560 nm. Samples were eluted using solvent gradients of water in ACN containing 0.1% TFA over 20–25 min. Peptide identities were confirmed using either an Agilent Infinity II LC/6530 Accurate-mass Q-TOF LC/MS or electrospray ionization mass spectrometry (QB3 Berkeley). Fractions containing the peptide of interest were frozen at -80 °C, lyophilized to dryness and stored at -20 °C until use.

To ensure proper zinc finger folding, lyophilized ZF5.3 peptides were dissolved in nitrogen-purged 10 mM Tris buffer, pH 7.44. 2 equivalents of DTT were added to reduce cysteine residues and the solution reacted at room temperature for 15 min. 2 equivalents of ZnCl<sub>2</sub> (using a 1 M ZnCl<sub>2</sub> solution) were added to induce folding. ZF5.3 peptides were stored at 4 °C. Reconstituted peptide identities were confirmed using an Infinity II LC/6530 Accurate-mass Q-TOF LC/MS.

### 7.3.7 Tyrosinase Reactions

Tyrosinase isolated from common button mushroom (*Agaricus bisporus*) was purchased from Sigma Aldrich. Stock tyrosinase solutions (2 mg/mL) were prepared with 50 mM phosphate buffer (sodium phosphate monobasic monohydrate), pH 6.5. 50  $\mu$ L aliquots were stored at -80 °C until use.

The control proteins<sup>13</sup> Y200C sfGFP and nanoluciferase (NanoLuc) containing a GGY tag (hereby referred to as Luc-GGY) were generously provided by Marco Lobba at UC Berkeley. SNAP-tag-His<sub>6</sub> was expressed and purified as previously described.<sup>8</sup>

For small scale (50  $\mu$ L) test reactions, 167 nM tyrosinase, 10  $\mu$ M Cys-containing protein (Y200C sfGFP, NS1 proteins, SNAP-tag), and 0–150  $\mu$ M Tyr-containing protein (Luc-GGY, ZF5.3-SGGY, ZF5.3, ZF5.3<sup>Rho</sup>) were reacted in 50 mM phosphate buffer (pH 6.5) at room temperature (or 30 °C) for 30 min. A positive control<sup>13</sup> testing conjugation of Y200C sfGFP to Luc-GGY via tyrosinase was conducted. 1.5 equiv of SNAP-Cell® TMR-Star were added to SNAP-tag containing reactions where indicated. To assess whether coupling occurred, SDS-PAGE analysis was conducted. SDS-PAGE samples were prepared using 20  $\mu$ L of reaction and 5  $\mu$ L of 5X loading dye. An AnyKD gel was run for 25-30 min at 200 V, stained, and destained. Coomassie staining was imaged using a ChemiDoc MP.

### 7.3.8 TEV Protease Cleavage

For small scale (50  $\mu$ L/aliquot) test reactions, a variety of conditions were screened, including buffer (20 mM Tris pH 7.5, 5 mM MgCl<sub>2</sub> or 20 mM Tris pH 7.5, 5 mM MgCl<sub>2</sub>, 1 mM DTT), molar ratio, time, and temperature (room temperature, 4 °C, or 30 °C). Molar ratios of 1:50, 2:50, and 4:50 of TEV protease:NS1 protein were evaluated. Reactions were set up with 20  $\mu$ M His<sub>7</sub>-AviTag-TEV-NS1-GSGC and the appropriate amount of TEV protease (QB3 Facility) depending on the molar ratio studied (diluted to final volume using 20 mM Tris pH 7.5, 5 mM MgCl<sub>2</sub> or 20 mM Tris pH 7.5, 5 mM MgCl<sub>2</sub>, 1 mM DTT). Aliquots (50  $\mu$ L) were removed at each time point (0–2.5 h or overnight) and frozen at -80 °C until SDS-PAGE analysis. SDS-PAGE samples were prepared using 20  $\mu$ L of reaction and 5  $\mu$ L of 5X loading dye. An AnyKD gel was run for 25-30 min at 200 V, stained, and destained. Coomassie staining was imaged using a ChemiDoc MP.

### 7.3.9 Maleimide Labeling

Reaction with maleimides requires the absence of DTT and a pH between 7 and 7.5. An aliquot of His<sub>7</sub>-AviTag-TEV-NS1-GSGC (in 20 mM Tris pH 7.5, 5 mM MgCl<sub>2</sub>, 1 mM DTT) was thawed on ice. 10 kDa Amicon spin filters were equilibrated with 20 mM Tris, 5 mM MgCl<sub>2</sub>, pH 7. 200  $\mu$ L of His<sub>7</sub>-AviTag-TEV-NS1-GSGC were added to the spin filter and the protein was washed with 5X sample volume (1000  $\mu$ L) 20 mM Tris, 5 mM MgCl<sub>2</sub>, pH 7. The sample was concentrated to approximately 200  $\mu$ L and quantified with Pierce™ 660 nm reagent. 50  $\mu$ M His<sub>7</sub>-AviTag-TEV-NS1-GSGC and 500  $\mu$ M Atto 550

maleimide in 20 mM Tris pH 7, 5 mM MgCl<sub>2</sub> (250 µL total volume) reacted for 2 h at room temperature (50 µL aliquots removed for each time point and frozen at -80 °C until further use). Precipitation was observed during the course of the reaction. SDS-PAGE samples were prepared using 20 µL of reaction and 5 µL of 5X loading dye. An AnyKD gel was run for 25-30 min at 200 V, fluorescence imaged using a ChemiDoc MP, stained, destained, and Coomassie staining imaged using a ChemiDoc MP.

## 7.4 Results and Discussion

Preliminary expression experiments indicated difficulty in purifying NS1 genetically fused to ZF5.3 (possibly due to interactions with the negative fibronectin scaffold) as the purification resulted in precipitation of the protein (ZF5.3-NS1-His<sub>6</sub>-Cys). We wanted to design a separate strategy that would allow conjugation of ZF5.3 to NS1 after expression and purification from *E. coli*. There have been multiple reports of *Agaricus bisporus* tyrosinase (abTyr)-mediated oxidative coupling that allows for a tyrosine-containing protein to be coupled to a cysteine residue on a partner protein.<sup>13,14</sup> The reactivities of the partner proteins suggest that the tyrosine and cysteine need to be solvent accessible for the reaction to proceed. This tyrosinase coupling strategy is attractive as tyrosinase is commercially available and would allow the generation of conjugates that may not favor genetic fusion.

To test the substrate scope of abTyr, we evaluated whether ZF5.3-SGGY could be used as a Tyr-containing protein partner. We synthesized ZF5.3-SGGY by solid phase peptide synthesis, where the second amino acid in ZF5.3 (Y) was mutated to a threonine (T) to prevent modification within the ZF5.3 CPMP itself (**Figure 7.1A and B**). The peptide was purified by reverse phase HPLC and brought up in a Zn<sup>2+</sup>-containing buffer to preserve the zinc finger fold. ZF5.3-SGGY (0–100 µM) reacted with abTyr (167 nM) and Y200C sfGFP (10 µM) for 30 min at room temperature or 30 °C and the mixture was analyzed by SDS-PAGE (**Figure 7.1C–E**). The reaction between Y200C sfGFP (27.5 kD) and Luc-GGY (20.9 kD) via abTyr served as a positive control (band present near 48 kD). In all cases, no coupling between ZF5.3-SGGY (3.7 kD) and Y200C sfGFP was observed, supported by the absence of Coomassie-stained bands near 31.2 kD. These reactions indicate that under these conditions, ZF5.3-SGGY is not a substrate for abTyr-mediated oxidative coupling.

Since ZF5.3 (3.4 kD) itself contains a tyrosine residue at the second position, we decided to evaluate whether it was accessible for abTyr-mediated oxidation and subsequent conjugation to the model protein Y200C sfGFP (**Figure 7.2A and B**). Again, the reaction between Y200C sfGFP and Luc-GGY via tyrosinase served as a positive control. In the reactions containing 25–100 µM ZF5.3, 10 µM Y200C sfGFP, and 167 nM abTyr, we observed the formation of a band near 30.9 kD that increased in intensity as the concentration of ZF5.3 increased. The dose-dependent increase in the higher molecular weight band suggests that ZF5.3 in fact can act as a substrate for abTyr in and of itself and that the tyrosine in the second position is likely surface accessible. To confirm whether ZF5.3 could be appended to additional proteins, we analyzed conjugation to SNAP-tag (**Figure 7.2C**). SNAP-tag (20.1 kD) contains three Cys

residues, with one of these present in the active site.<sup>15,16</sup> Indeed, we observed that ZF5.3 labeling occurred multiple times through SDS-PAGE analysis and the presence of two distinct product bands corresponded to molecular weights near 23.5 and 26.9 kD. At 50  $\mu$ M ZF5.3, there was a faint band near 30.3 kD that suggested at higher concentrations of electrophile, the third cysteine residue of SNAP-tag was modified. The presence of higher molecular weight products could be dimer formation, since the bands correspond to a molecular weight near 40 kD. Additionally, we observed that SNAP-tag can be appended to Luc-GGY.

To determine whether the ZF5.3 labeled the active site Cys, we evaluated reaction of abTyr, ZF5.3, and SNAP-tag in the presence of SNAP-Cell® TMR-Star, a benzylguanine dye that contains a rhodamine-based fluorophore and reacts with SNAP-tag. We observed that the presence of SNAP-Cell® TMR-Star inhibited the reaction since no conjugation product was observed with the Tyr-containing substrates, either by Coomassie staining or fluorescence (**Figure 7.2D**). Even though no abTyr-mediated oxidative coupling occurred, SNAP-Cell® TMR-Star still reacted with SNAP-tag, evidenced by the presence of fluorescent bands near 20 kD. One possibility is that ZF5.3 and Luc-GGY predominantly label the active site Cys and the addition of SNAP-Cell® TMR-Star precludes the cysteine reaction with the quinone derivative. Previous studies conclude that upon binding a benzylguanine substrate, SNAP-tag exhibits conformational changes.<sup>15</sup> It is also possible that upon binding SNAP-Cell® TMR-Star, the two additional Cys residues of SNAP-tag are no longer solvent accessible and prevent reaction from proceeding.

Together, the data provides evidence that ZF5.3 conjugates to Cys-containing proteins (if the Cys is solvent accessible) via tyrosinase-mediated oxidative coupling. With evidence that ZF5.3 could label Y200C sfGFP and SNAP-tag, we moved on to evaluating whether abTyr oxidative coupling could be used to append ZF5.3 to an NS1-containing protein.

In our construct design for NS1, we kept in mind that residues near the N-terminus are necessary for Ras binding, choosing to append ZF5.3 at the C-terminus of the monobody. To generate a substrate for tyrosinase-mediated oxidative coupling, a cysteine residue was placed at the C-terminus to generate NS1-His<sub>6</sub>-Cys (**Figure 7.3A**). The His<sub>6</sub> tag was incorporated for use in immobilized metal affinity chromatography (IMAC). While this construct expressed well, it did not participate in tyrosinase-mediated oxidative coupling with either the model Tyr-containing protein Luc-GGY or ZF5.3, illustrated by the lack of new band formation around 24.3 kD on an SDS-PAGE gel (**Figure 7.3B** and **C**). Additionally, heating the reaction to 30 °C did not result in product formation (data not shown).

A previous construct for expression and purification of NS1 for crystallization included an N-terminal His<sub>6</sub> tag followed by a biotin acceptor tag and TEV, allowing the cleaved tag to produce NS1.<sup>7</sup> We generated a second construct that contained a C-terminal Cys based on the previously described strategy: His<sub>7</sub>-AviTag-TEV-NS1-GSGC (15.6 kD). We selected an AviTag as the biotin acceptor tag; when biotin and biotin

ligase (BirA) are added, the Lys in AviTag reacts with the carboxylic acid on biotin.<sup>17</sup> We note that although there are commercially available biotin-fluorophores available, most fluorophores are attached via the same carboxylic acid necessary for biotin ligation such that the AviTag is not a viable option to append a small molecule fluorophore to the fusion protein. The Cys at the C-terminus would allow for tyrosinase labeling with ZF5.3 or the incorporation of a maleimide, for multiple avenues to reach fluorescence correlation spectroscopy studies (**Figure 7.4**). We inserted a gBlock™ gene fragment containing His<sub>7</sub>-AviTag-TEV-NS1-GSGC into a pET32a backbone using Gibson assembly, confirmed insertion using Sanger sequencing, expressed the protein in BL21-Gold (DE3) competent *E. coli*, and purified using IMAC. After dialysis, the yield of His<sub>7</sub>-AviTag-TEV-NS1-GSGC was 4.5 mg per L of culture.

With purified His<sub>7</sub>-AviTag-TEV-NS1-GSGC, we evaluated whether Luc-GGY and ZF5.3 treated with abTyr could react with the C-terminal Cys (**Figure 7.5**). We observed the presence of dose-dependent bands near 36.5 kD with the reaction mixture of 25–50 μM Luc-GGY, 10 μM His<sub>7</sub>-AviTag-TEV-NS1-GSGC, and 167 nM abTyr. The presence of bands near 30 kD could be a dimer of His<sub>7</sub>-AviTag-TEV-NS1-GSGC as the protein contains a series of tyrosine residues that may be surface accessible; however, this dimer is not observed in the presence of ZF5.3 instead of Luc-GGY. Reaction of tyrosinase-mediated oxidized ZF5.3 with His<sub>7</sub>-AviTag-TEV-NS1-GSGC resulted in a band near the expected conjugation product, 18 kD. The reaction containing ZF5.3 precipitated upon reaction initialization but at the end of the 30 min incubation, addition of base solubilized the precipitate. Ultimately, this experiment indicated that the C-terminal Cys in the newly designed NS1 construct was available to participate in reaction with an oxidized tyrosine residue.

To continue optimizing the workflow, we next evaluated TEV protease cleavage to ensure that the His<sub>7</sub>-AviTag could be removed from the N-terminus (**Figure 7.6A**). After cleavage, the construct design allowed for removal of any His-tagged proteins, including TEV protease, His<sub>7</sub>-AviTag, and any unreacted His<sub>7</sub>-AviTag-TEV-NS1-GSGC, using IMAC. TEV protease incubated with His<sub>7</sub>-AviTag-TEV-NS1-GSGC for up to 2.5 h at room temperature (**Figure 7.6B**). This initial optimization showed dose- and time-dependencies where more NS1-GSGC (10.8 kD) was generated at higher TEV protease concentrations and longer incubation times. A molecular weight band near 17 kD at increased TEV protease concentrations suggests higher order structures such as dimers may form. We observed that the presence of increased TEV protease, inclusion of DTT, and higher temperature resulted in the best cleavage conditions (**Figure 7.6C**) in which all starting material cleanly converted to NS1-GSGC. We proceeded with larger scale reactions using a 2 h incubation at 30 °C in a DTT containing buffer.

As shown in **Figure 7.4**, the His<sub>7</sub>-AviTag-TEV-NS1-GSGC construct supports development of fluorophore conjugates either using tyrosinase oxidative coupling or maleimide chemistry. We assessed the reactivity of the C-terminal Cys residue to determine whether we could append a fluorophore containing a maleimide (**Figure 7.7A**). Atto 550 maleimide incubated in 10-fold molar excess of His<sub>7</sub>-AviTag-TEV-NS1-GSGC for up to 1 h at room temperature. SDS-PAGE analysis showed the presence of

a fluorescent band near the molecular weight of His<sub>7</sub>-AviTag-TEV-NS1-GSGC within the first 15 min of the reaction (**Figure 7.7B**). After 1 h, there were additional bands in both the Coomassie-stained as well as the fluorescence images. Maleimides can react with primary amines depending on the pH, so it may be favorable in the future to decrease the reaction pH slightly below 7. Additionally, since the maleimide was in 10-fold molar excess, the reaction might be tuned by decreased concentration of electrophile. While precipitation occurred during the reaction and additional optimization is necessary, SDS-PAGE indicated that Atto 550 maleimide can react with His<sub>7</sub>-AviTag-TEV-NS1-GSGC to form a fluorescent product.

## 7.5 Conclusions

The experiments described in this chapter detail initial development towards the generation of NS1 and NS1-ZF5.3 that contain a fluorophore compatible with FCS. We were surprised to learn that tyrosinase can oxidize the native Tyr in ZF5.3 for subsequent reaction with a Cys nucleophile on multiple proteins (Y200C sfGFP and SNAP-tag). While NS1-His<sub>6</sub>-Cys was unable to participate in tyrosinase-mediated oxidative coupling, modifying this construct to His<sub>7</sub>-AviTag-TEV-NS1-GSGC allowed reaction at the C-terminal Cys. Preliminary data (not shown) suggests that ZF5.3 containing a rhodamine fluorophore at the N-terminus (ZF5.3<sup>Rho</sup>) may not oxidize, perhaps due to steric effects with the bulky fluorophore near the Tyr required for oxidation. Additional ZF5.3 peptides containing Lissamine rhodamine B farther away from the Tyr will be synthesized in the future. TEV protease cleaved the parent construct to produce NS1-GSGC and the C-terminal Cys reacted with maleimides.

In addition to continuing to optimize tyrosinase labeling reactions, we generated a pET32a plasmid containing His<sub>7</sub>-AviTag-TEV-NS1-ZF5.3-GSGC, in hopes of purifying a genetic fusion containing ZF5.3. Similar to ZF5.3-NS1-His<sub>6</sub>-Cys, this construct ended up in the pellet after lysis at three different pHs (acidic, neutral, and basic). We are currently evaluating pellet extraction methods. Ultimately, a finalized purification strategy to NS1 and NS1-ZF5.3 will allow evaluation of the ZF5.3 benefit for delivering a monobody to mammalian cells.

## 7.6 Figures

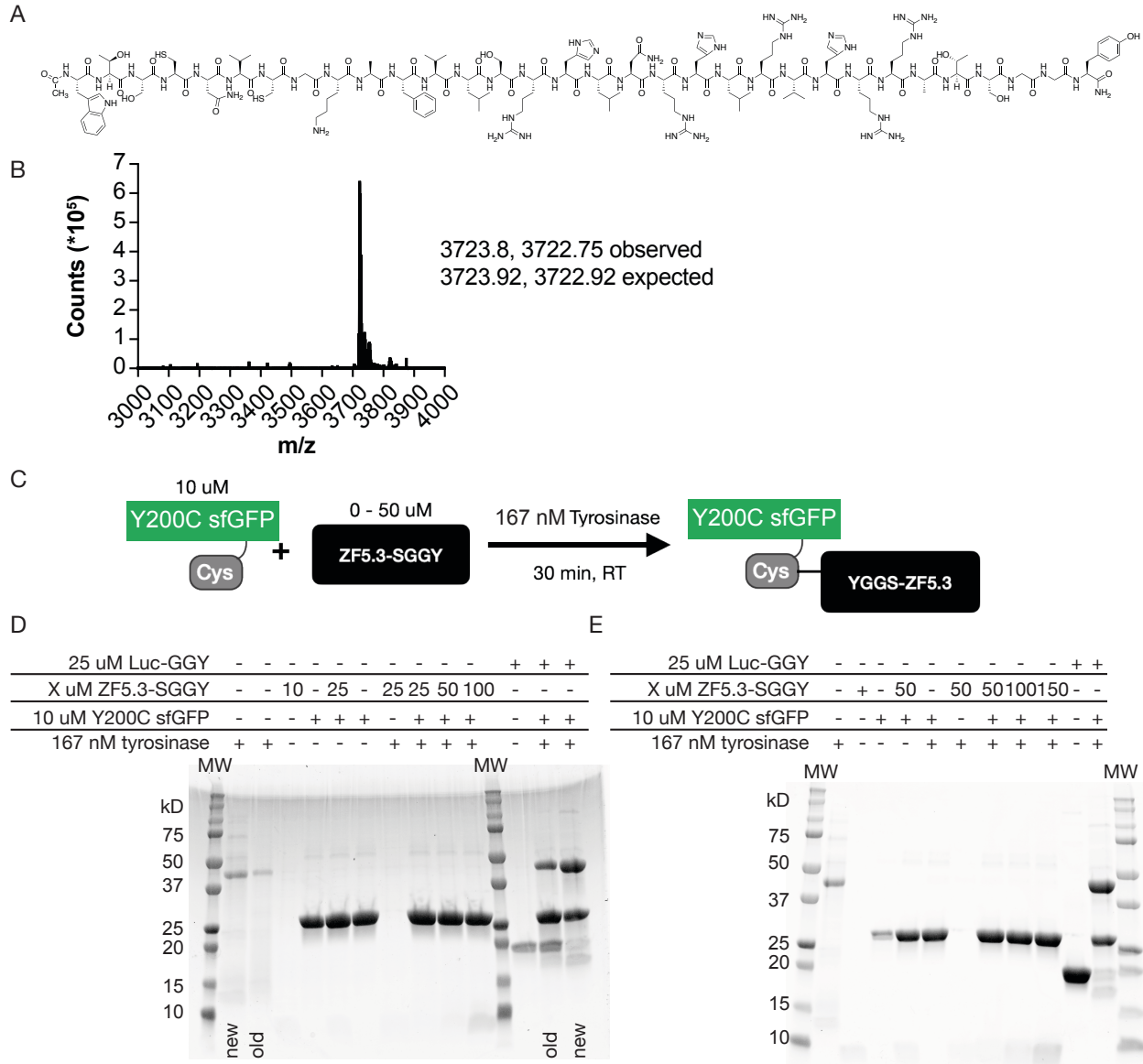


**Figure 7.1.** (A) Structure of ZF5.3-SGGY. (B) Mass spectrometry analysis of ZF5.3-SGGY using an Agilent Infinity II LC/6530 Accurate-mass Q-TOF LC/MS. (C) Reaction scheme for labeling of Y200C sfGFP with ZF5.3-SGGY via tyrosinase oxidative coupling. (D) Tyrosinase oxidative coupling reaction with Luc-GGY, ZF5.3-SGGY, Y200C sfGFP, and tyrosinase (either an old or new batch) at room temperature (RT) analyzed by SDS-PAGE. (E) Tyrosinase oxidative coupling reaction with Luc-GGY, ZF5.3-SGGY, Y200C sfGFP, and tyrosinase at 30 °C analyzed by SDS-PAGE.

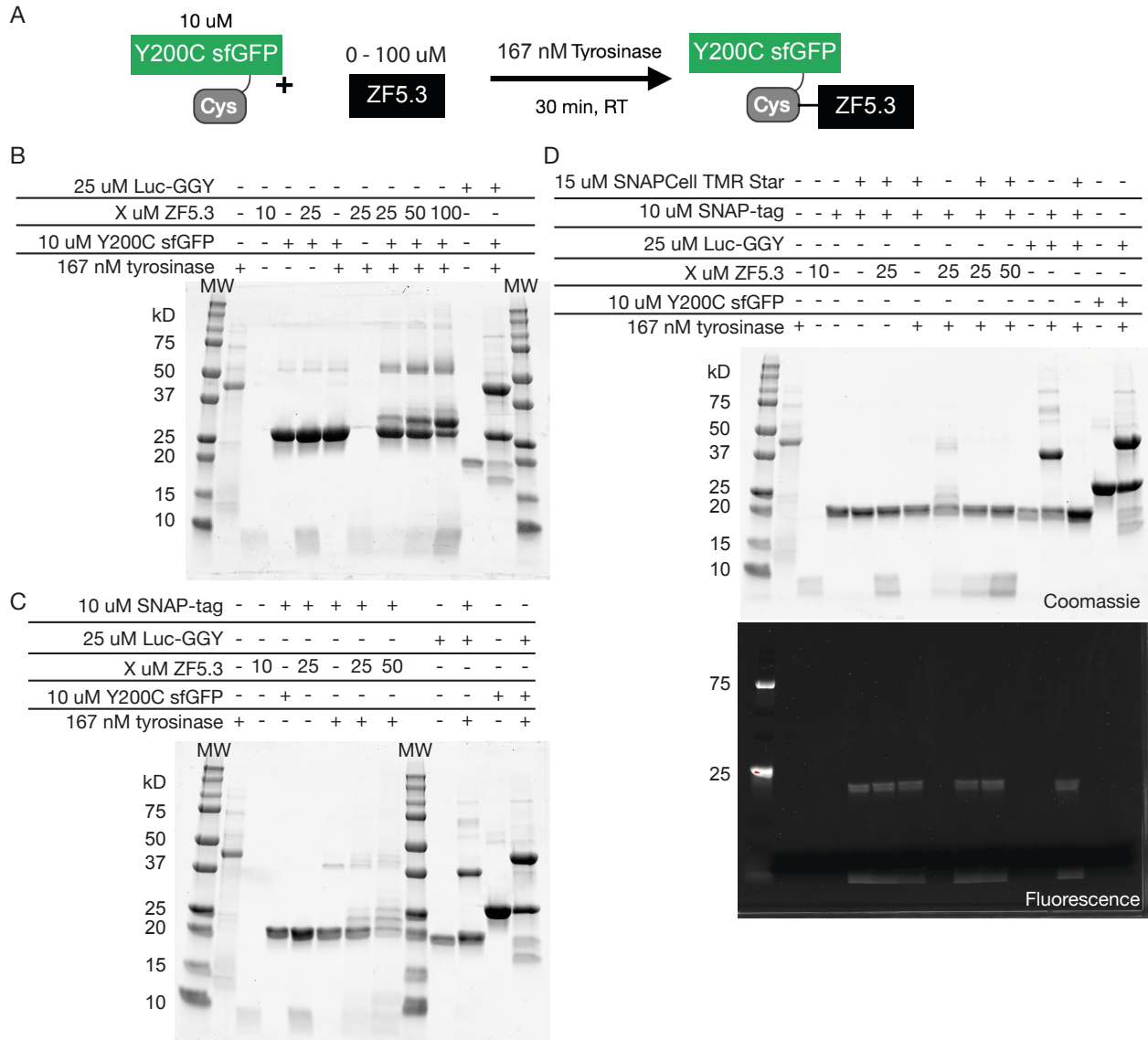


**Figure 7.2.** (A) Reaction scheme for labeling of Y200C sfGFP with ZF5.3 via tyrosinase oxidative coupling. (B) Tyrosinase oxidative coupling reaction with Luc-GGY, ZF5.3, Y200C sfGFP, and tyrosinase at room temperature (RT) analyzed by SDS-PAGE. (C) Tyrosinase oxidative coupling reaction with SNAP-tag, Luc-GGY, ZF5.3, Y200C sfGFP, and tyrosinase at room temperature (RT) analyzed by SDS-PAGE. (D) Tyrosinase oxidative coupling reaction with SNAP-tag (with or without the presence of 15  $\mu$ M SNAP-Cell<sup>®</sup> TMR-Star), Luc-GGY, ZF5.3, Y200C sfGFP, and tyrosinase at room temperature (RT) analyzed by SDS-PAGE.

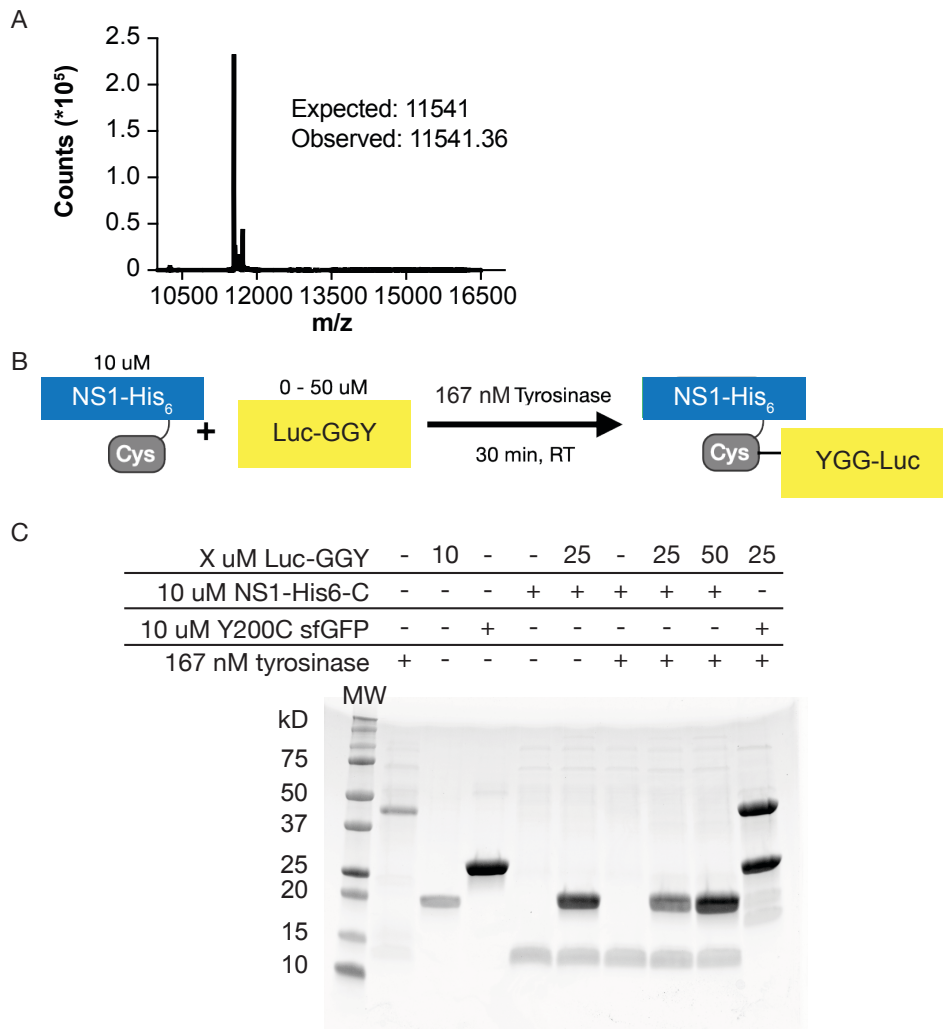


**Figure 7.3.** (A) Mass spectrometry analysis of NS1-His<sub>6</sub>-C using an Agilent Infinity II LC/6530 Accurate-mass Q-TOF LC/MS. Protein lacks the N-terminal Met residue. (B) Reaction scheme for labeling of NS1-His<sub>6</sub>-C with Luc-GGY via tyrosinase oxidative coupling. (C) Tyrosinase oxidative coupling reaction with Luc-GGY, NS1-His<sub>6</sub>-C, Y200C sfGFP, and tyrosinase at room temperature (RT) analyzed by SDS-PAGE.

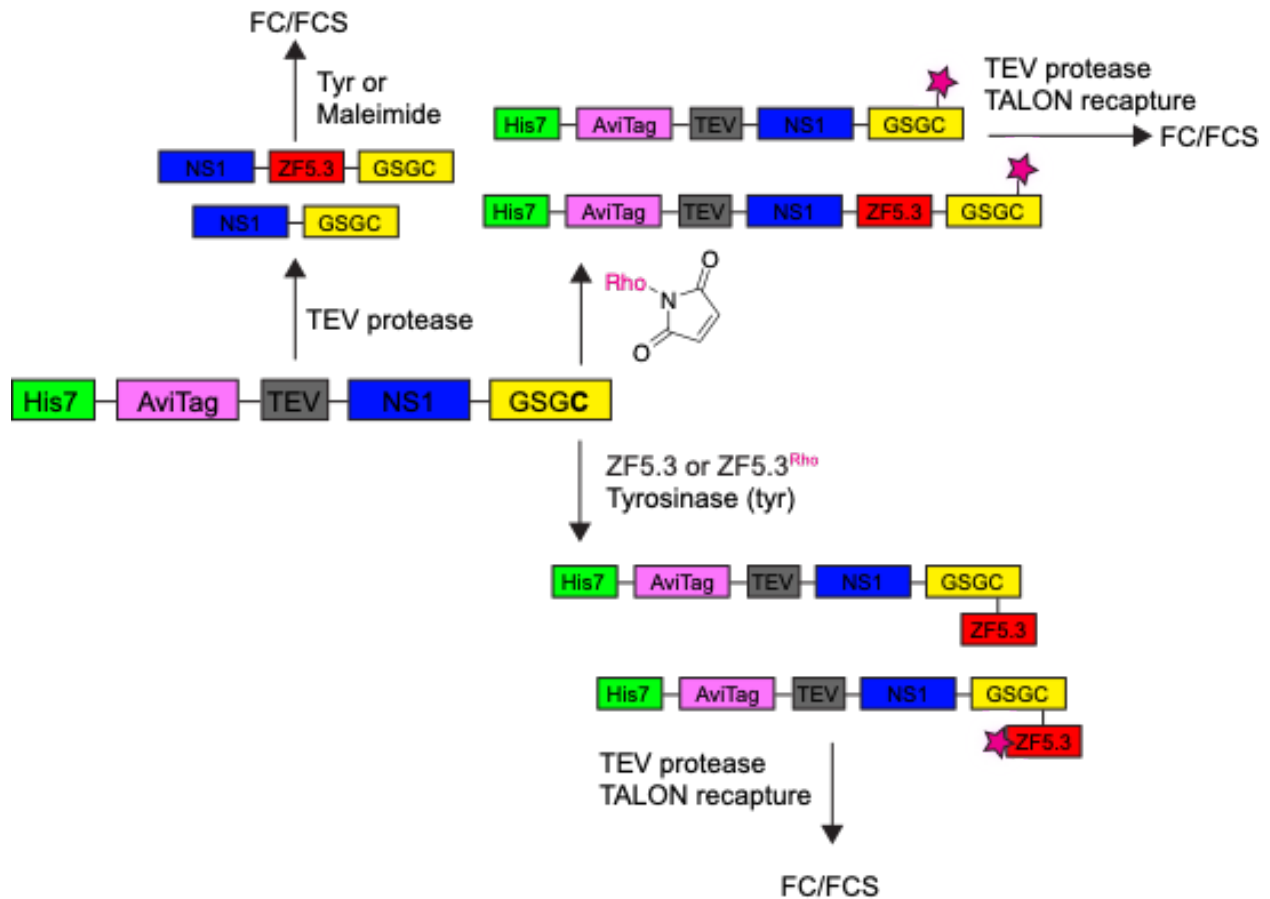


**Figure 7.4.** Strategies for generation of NS1 proteins containing ZF5.3 and a rhodamine (Rho) fluorophore for flow cytometry (FC) and fluorescence correlation spectroscopy (FCS). The parent construct His<sub>7</sub>-AviTag-TEV-NS1-GSGC (or His<sub>7</sub>-AviTag-TEV-NS1-ZF5.3-GSGC) contains a C-terminal Cys residue that can participate in tyrosinase (tyr) oxidative coupling or maleimide chemistry. The TEV cleavage site can be used to remove the His<sub>7</sub>-AviTag tag via TEV protease, resulting in NS1-GSGC or NS1-ZF5.3-GSGC. This material can then be used for Ras binding studies or reacted further using abTyr-mediated oxidative coupling or maleimide chemistry to install a Rho-based fluorophore. After TEV cleavage, TALON resin will capture any His<sub>7</sub>- or His<sub>6</sub>-tagged proteins (unreacted His<sub>7</sub>-AviTag-TEV-NS1-GSGC, His<sub>7</sub>-AviTag, TEV protease) and the products of interest will remain in the flowthrough (NS1-GSGC or NS1-ZF5.3-GSGC).

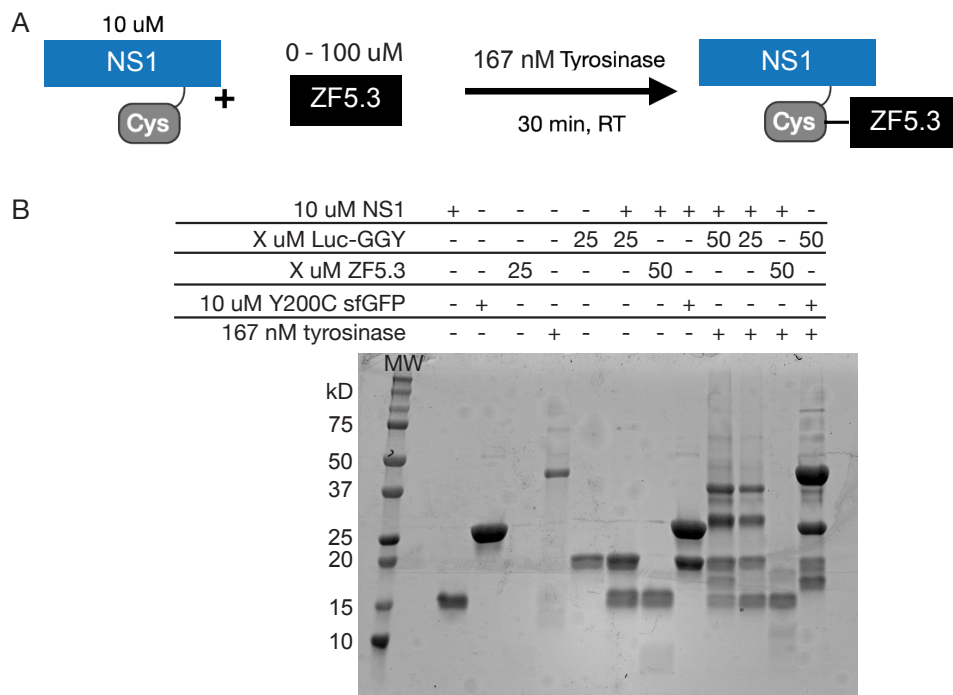


**Figure 7.5.** (A) Reaction scheme for labeling of His<sub>7</sub>-AviTag-TEV-NS1-GSGC (denoted as NS1) with Luc-GGY and ZF5.3 via tyrosinase oxidative coupling. (B) Tyrosinase oxidative coupling reaction with Luc-GGY, NS1, ZF5.3, Y200C sfGFP, and tyrosinase at room temperature (RT) analyzed by SDS-PAGE.

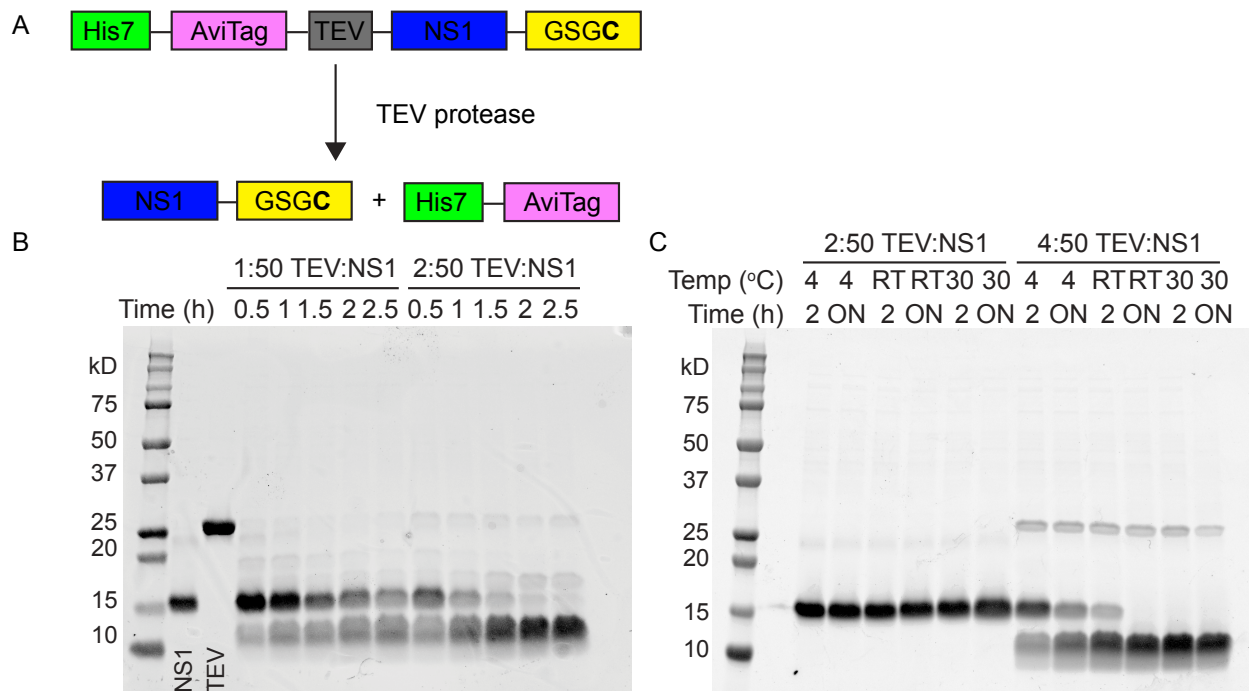


**Figure 7.6.** (A) Reaction scheme for TEV protease cleavage of His<sub>7</sub>-AviTag-TEV-NS1-GSGC. (B) TEV protease (TEV) cleavage of His<sub>7</sub>-AviTag-TEV-NS1-GSGC (NS1) at either 1:50 or 2:50 molar ratios in 20 mM Tris (pH 7.5), 5 mM MgCl<sub>2</sub>. Reactions incubated for a maximum of 2.5 h at room temperature and were analyzed by SDS-PAGE. (C) TEV protease cleavage of His<sub>7</sub>-AviTag-TEV-NS1-GSGC at either 2:50 or 4:50 molar ratios in 20 mM Tris (pH 7.5), 5 mM MgCl<sub>2</sub>, 1 mM DTT. Reactions incubated for a maximum of overnight (ON) at room temperature (RT) and were analyzed by SDS-PAGE.

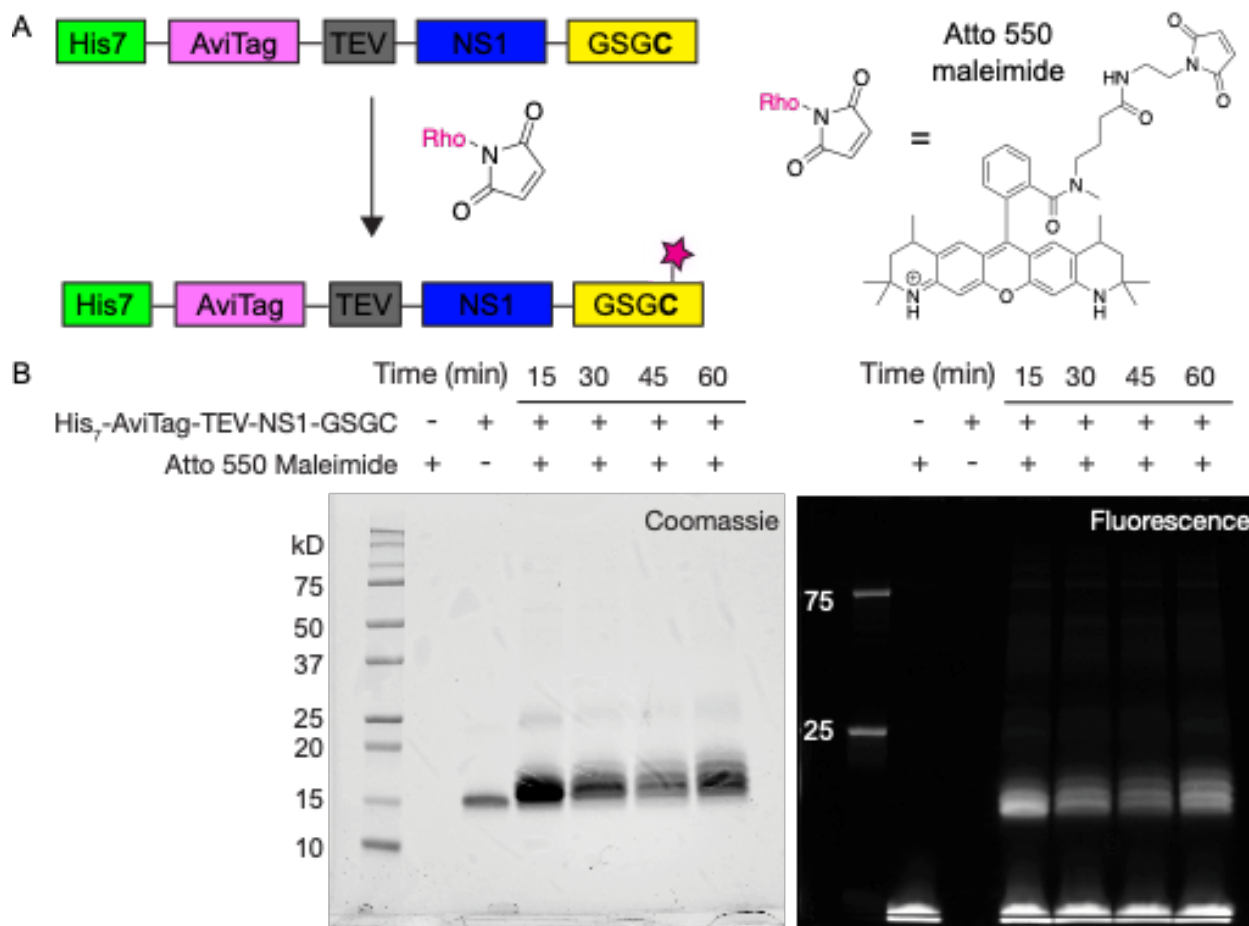


**Figure 7.7.** (A) Reaction scheme for Atto 550 maleimide labeling of His<sub>7</sub>-AviTag-TEV-NS1-GSGC. (B) SDS-PAGE analysis of 500  $\mu$ M maleimide labeling of 50  $\mu$ M His<sub>7</sub>-AviTag-TEV-NS1-GSGC for 1 h at room temperature in 20 mM Tris (pH 7), 5 mM MgCl<sub>2</sub>. Prior to SDS-PAGE, samples were diluted by half to produce clear bands on an AnykD gel.

## 7.7 References

- (1) Castellano, E.; Santos, E. Functional Specificity of Ras Isoforms: So Similar but So Different. *Genes Cancer* **2011**, 2 (3), 216–231. <https://doi.org/10.1177/1947601911408081>.
- (2) Prior, I. A.; Lewis, P. D.; Mattos, C. A Comprehensive Survey of Ras Mutations in Cancer. *Cancer Res.* **2012**, 72 (10), 2457. <https://doi.org/10.1158/0008-5472.CAN-11-2612>.
- (3) Downward, J. Targeting RAS Signalling Pathways in Cancer Therapy. *Nat. Rev. Cancer* **2003**, 3 (1), 11–22. <https://doi.org/10.1038/nrc969>.
- (4) Prior, I. A.; Hancock, J. F. Ras Trafficking, Localization and Compartmentalized Signalling. *Semin. Cell Dev. Biol.* **2012**, 23 (2), 145–153. <https://doi.org/10.1016/j.semcdb.2011.09.002>.
- (5) McGee, J. H.; Shim, S. Y.; Lee, S.-J.; Swanson, P. K.; Jiang, S. Y.; Durney, M. A.; Verdine, G. L. Exceptionally High-Affinity Ras Binders That Remodel Its

- Effector Domain. *J. Biol. Chem.* **2018**, 293 (9), 3265–3280.  
<https://doi.org/10.1074/jbc.M117.816348>.
- (6) Goebel, L.; Müller, M. P.; Goody, R. S.; Rauh, D. KRasG12C Inhibitors in Clinical Trials: A Short Historical Perspective. *RSC Med. Chem.* **2020**, 11 (7), 760–770.  
<https://doi.org/10.1039/D0MD00096E>.
  - (7) Spencer-Smith, R.; Koide, A.; Zhou, Y.; Eguchi, R. R.; Sha, F.; Gajwani, P.; Santana, D.; Gupta, A.; Jacobs, M.; Herrero-Garcia, E.; Cobbert, J.; Lavoie, H.; Smith, M.; Rajakulendran, T.; Dowdell, E.; Okur, M. N.; Dementieva, I.; Sicheri, F.; Therrien, M.; Hancock, J. F.; Ikura, M.; Koide, S.; O'Bryan, J. P. Inhibition of RAS Function through Targeting an Allosteric Regulatory Site. *Nat. Chem. Biol.* **2017**, 13 (1), 62–68. <https://doi.org/10.1038/nchembio.2231>.
  - (8) Wissner, R. F.; Steinauer, A.; Knox, S. L.; Thompson, A. D.; Schepartz, A. Fluorescence Correlation Spectroscopy Reveals Efficient Cytosolic Delivery of Protein Cargo by Cell-Permeant Miniature Proteins. *ACS Cent. Sci.* **2018**, 4 (10), 1379–1393. <https://doi.org/10.1021/acscentsci.8b00446>.
  - (9) Knox, S. L.; Wissner, R.; Piszkiwicz, S.; Schepartz, A. Cytosolic Delivery of Argininosuccinate Synthetase Using a Cell-Permeant Miniature Protein. *ACS Cent. Sci.* **2021**, 7 (4), 641–649. <https://doi.org/10.1021/acscentsci.0c01603>.
  - (10) Gibson, D. G.; Glass, J. I.; Lartigue, C.; Noskov, V. N.; Chuang, R.-Y.; Algire, M. A.; Benders, G. A.; Montague, M. G.; Ma, L.; Moodie, M. M.; Merryman, C.; Vashee, S.; Krishnakumar, R.; Assad-Garcia, N.; Andrews-Pfannkoch, C.; Denisova, E. A.; Young, L.; Qi, Z.-Q.; Segall-Shapiro, T. H.; Calvey, C. H.; Parmar, P. P.; Hutchison, C. A.; Smith, H. O.; Venter, J. C. Creation of a Bacterial Cell Controlled by a Chemically Synthesized Genome. *Science* **2010**, 329 (5987), 52. <https://doi.org/10.1126/science.1190719>.
  - (11) Gibson, D. G.; Young, L.; Chuang, R.-Y.; Venter, J. C.; Hutchison, C. A.; Smith, H. O. Enzymatic Assembly of DNA Molecules up to Several Hundred Kilobases. *Nat. Methods* **2009**, 6 (5), 343–345. <https://doi.org/10.1038/nmeth.1318>.
  - (12) Steinauer, A.; LaRoche, J. R.; Knox, S. L.; Wissner, R. F.; Berry, S.; Schepartz, A. HOPS-Dependent Endosomal Fusion Required for Efficient Cytosolic Delivery of Therapeutic Peptides and Small Proteins. *Proc. Natl. Acad. Sci.* **2019**, 116 (2), 512–521. <https://doi.org/10.1073/pnas.1812044116>.
  - (13) Lobba, M. J.; Fellmann, C.; Marmelstein, A. M.; Maza, J. C.; Kissman, E. N.; Robinson, S. A.; Staahl, B. T.; Urnes, C.; Lew, R. J.; Mogilevsky, C. S.; Doudna, J. A.; Francis, M. B. Site-Specific Bioconjugation through Enzyme-Catalyzed Tyrosine–Cysteine Bond Formation. *ACS Cent. Sci.* **2020**, 6 (9), 1564–1571. <https://doi.org/10.1021/acscentsci.0c00940>.
  - (14) Marmelstein, A. M.; Lobba, M. J.; Mogilevsky, C. S.; Maza, J. C.; Brauer, D. D.; Francis, M. B. Tyrosinase-Mediated Oxidative Coupling of Tyrosine Tags on Peptides and Proteins. *J. Am. Chem. Soc.* **2020**, 142 (11), 5078–5086. <https://doi.org/10.1021/jacs.9b12002>.
  - (15) Mollwitz, B.; Brunk, E.; Schmitt, S.; Pojer, F.; Bannwarth, M.; Schiltz, M.; Rothlisberger, U.; Johnsson, K. Directed Evolution of the Suicide Protein O6-Alkylguanine-DNA Alkyltransferase for Increased Reactivity Results in an Alkylated Protein with Exceptional Stability. *Biochemistry* **2012**, 51 (5), 986–994. <https://doi.org/10.1021/bi2016537>.

- (16) Gautier, A.; Juillerat, A.; Heinis, C.; Corrêa, I. R., Jr.; Kindermann, M.; Beaufils, F.; Johnsson, K. An Engineered Protein Tag for Multiprotein Labeling in Living Cells. *Chem. Biol.* **2008**, *15* (2), 128–136.  
<https://doi.org/10.1016/j.chembiol.2008.01.007>.
- (17) Fairhead, M.; Howarth, M. Site-Specific Biotinylation of Purified Proteins Using BirA. In *Site-Specific Protein Labeling: Methods and Protocols*; Gautier, A., Hinner, M. J., Eds.; Springer New York: New York, NY, 2015; pp 171–184.  
[https://doi.org/10.1007/978-1-4939-2272-7\\_12](https://doi.org/10.1007/978-1-4939-2272-7_12).

## **CHAPTER 8**

### Conclusions

Overcoming the challenges associated with cytosolic access would significantly expand the existing druggable proteome. Over the past fifteen years, the Schepartz Laboratory has continued to develop and employ cell-permeant miniature proteins (CPMPs). These delivery tools are based on the principle that structure would provide protease resistance and properly orient determinants of cell-permeability. Several generations of CPMPs resulted in the development of a penta-Arg motif within multiple CPMPs such as ZF5.3. CPMPs containing the penta-Arg motif reach the cytosol at concentrations higher than canonical cell-penetrating peptides (CPPs).<sup>1-3</sup> The experiments described within this text contribute to the body of knowledge of CPMPs in illustrating that ZF5.3 is an excellent protein delivery tool and has potential for clinical applications.

Despite the increasing number of reported methods for protein delivery,<sup>4</sup> most assays that assess trafficking into the cytosol are qualitative and indirect and can therefore be misleading. These limitations make evaluating progress in the field of protein delivery extremely challenging. In order to study endosomal escape and use a quantitative technique, we employ fluorescence correlation spectroscopy (FCS). The FCS and flow cytometry methodology described here established a protocol for laboratory members and new users to ensure consistency in experimentation and gain valuable insight from this direct and quantitative technique.

Using FCS, we confirmed that diffusion is temperature-dependent and observed that free dyes may interact with organelles due to diffusion coefficients that were smaller than expected. To provide evidence whether peptide degradation occurs in the cell, we chose to determine *in cellulo* diffusion coefficients of a panel of free dyes and compare them to the diffusion coefficients ( $D$ ) observed for CPMPs. Within the cell,  $D$  of SNAP-Cell TMR Star was approximately 2-fold higher compared to aPP5.3<sup>R</sup> and ZF5.3<sup>R</sup>, and supports the hypothesis that the fluorescent signal from CPMPs evaluated by FCS in Saos-2 cells is not simply free dye. The FCS experiments described in Chapter 3 established diffusion parameters for dyes and CPMPs both *in vitro* and *in cellulo*.

With a better understanding of CPMPs alone, the next chapters analyzed the delivery of three protein cargoes that ranged in size (20–160 kD) and surface charge (pI 6.5–9.0): SNAP-tag, argininosuccinate synthetase, and Cas9. We analyzed the relative efficiencies with which unstructured CPPs, CPMPs, and cyclic CPPs transport a model, self-labeled enzyme (SNAP-tag) into the cell using flow cytometry. We showed that SNAP-tag delivery is possible in multiple cell lines (HeLa, Saos-2, and SK-HEP-1), and that ZF5.3-SNAP-Rho achieves the highest total cellular uptake across all cell lines evaluated. ZF5.3 is also capable of delivering a large and complex urea cycle enzyme, argininosuccinate synthetase (AS), to the cytosol of cells in culture and the livers of healthy mice. The fusion protein ZF5.3-AS is catalytically active *in vitro*, stabilized in plasma, and traffics to the cytosol of cultured cells, achieving cytosolic concentrations greater than 100 nM. When injected into healthy C57BL/6 mice, ZF5.3-AS reaches the mouse liver at concentrations almost 200 nM above baseline. Finally, Cas9 labeled with N- or C-terminal ZF5.3 remains active *in vitro* and can access the interior of cells at higher levels than Cas9 alone. Using Alexa Fluor™ 568 NHS ester, Cas9, ZF5.3-Cas9,

and Cas9-ZF5.3 were non-specifically labeled to produce fluorophore-labeled products for use with confocal microscopy and flow cytometry. The Cas9 protein containing a C-terminal ZF5.3 exhibited the highest cellular uptake in all conditions evaluated, even in the presence of sgRNA. FCS studies of Cas9 delivery in live cells suggested that while compatible with flow cytometry, non-specific labeling is not suitable for FCS and alternative fluorophore-labeling strategies should be employed in future protein designs.

The final protein target described in this work is the fibronectin-based monobody NS1 that binds the Ras isomers H-Ras and K-Ras with high affinity. Initial optimization to develop methods to conjugate ZF5.3 with NS1 indicated that the endogenous tyrosine residue within ZF5.3 itself acts as a substrate for tyrosinase and through oxidation, can couple to cysteine residues on multiple proteins. Additionally, a construct containing NS1 with a C-terminal cysteine residue permits conjugation to the tyrosinase-mediated oxidized binding partners Luc-GGY and ZF5.3. Labeling of the C-terminal cysteine of NS1 with a maleimide indicated a secondary means of attaching maleimide-containing cargo.

Together, these projects demonstrate that the CPMP ZF5.3 is a superior delivery vehicle compared to canonical and cyclic CPPs, illustrate ZF5.3-mediated delivery of three protein cargos, and support further ZF5.3 clinical development as a tool for protein-based therapeutics.

Immediate future directions of the experiments described herein include appending Cas9 with a site-specific fluorophore for quantifying nuclear access via FCS. The site-specific fluorophore would allow comparisons between ZF5.3-containing Cas9 with wild-type protein alone. As site-specific incorporation of unnatural amino acids can decrease protein yield, optimizing tyrosinase oxidative coupling to be compatible with ZF5.3 and achieve high yields of conjugated protein would be beneficial. Finally, purifying NS1 containing ZF5.3 and a fluorophore would allow for confocal microscopy, flow cytometry, and FCS studies to evaluate the benefit of ZF5.3. Future work with NS1 provides preliminary conjugation methods and purification optimization for study of this monobody using FCS to provide information on the benefit of ZF5.3 for cellular delivery of NS1. These studies would demonstrate additional applications of ZF5.3 to establish it as a platform technology.

Longer term goals include determining the mechanism by which ZF5.3-containing proteins escape endosomes. Building upon the observations that ZF5.3 colocalizes with a marker for ILVs<sup>5</sup> and that ILVs are rich in a negatively charged lipid known as bis(monoacylglycero)phosphate (BMP)<sup>6</sup>, I evaluated ZF5.3-lipid interactions using commercially available lipid strips (**Appendix 1**). These initial studies support the hypothesis that ZF5.3 binds selectively to negatively charged lipids such as BMP and establish similar lipid interaction profiles of ZF5.3<sup>Rho</sup> and ZF5.3-SNAP. Understanding more about the role of lipids in endosomal escape mechanisms will benefit the design of a new generation of CPMPs and identification of additional targets to modulate for cytosolic access of protein therapeutics.

## References

- (1) Appelbaum, J. S.; LaRochelle, J. R.; Smith, B. A.; Balkin, D. M.; Holub, J. M.; Schepartz, A. Arginine Topology Controls Escape of Minimally Cationic Proteins from Early Endosomes to the Cytoplasm. *Chem. Biol.* **2012**, *19* (7), 819–830. <https://doi.org/10.1016/j.chembiol.2012.05.022>.
- (2) LaRochelle, J. R.; Cobb, G. B.; Steinauer, A.; Rhoades, E.; Schepartz, A. Fluorescence Correlation Spectroscopy Reveals Highly Efficient Cytosolic Delivery of Certain Penta-Arg Proteins and Stapled Peptides. *J. Am. Chem. Soc.* **2015**, *137* (7), 2536–2541. <https://doi.org/10.1021/ja510391n>.
- (3) Holub, J. M.; LaRochelle, J. R.; Appelbaum, J. S.; Schepartz, A. Improved Assays for Determining the Cytosolic Access of Peptides, Proteins, and Their Mimetics. *Biochemistry* **2013**, *52* (50), 9036–9046. <https://doi.org/10.1021/bi401069g>.
- (4) Lee, Y.-W.; Luther, D. C.; Kretzmann, J. A.; Burden, A.; Jeon, T.; Zhai, S.; Rotello, V. M. Protein Delivery into the Cell Cytosol Using Non-Viral Nanocarriers. *Theranostics* **2019**, *9* (11), 3280–3292. <https://doi.org/10.7150/thno.34412>.
- (5) Steinauer, A.; LaRochelle, J. R.; Knox, S. L.; Wissner, R. F.; Berry, S.; Schepartz, A. HOPS-Dependent Endosomal Fusion Required for Efficient Cytosolic Delivery of Therapeutic Peptides and Small Proteins. *Proc. Natl. Acad. Sci.* **2019**, *116* (2), 512–521. <https://doi.org/10.1073/pnas.1812044116>.
- (6) Matsuo, H.; Chevallier, J.; Mayran, N.; Le Blanc, I.; Ferguson, C.; Fauré, J.; Blanc, N. S.; Matile, S.; Dubochet, J.; Sadoul, R.; Parton, R. G.; Vilbois, F.; Gruenberg, J. Role of LBPA and Alix in Multivesicular Liposome Formation and Endosome Organization. *Science* **2004**, *303* (5657), 531. <https://doi.org/10.1126/science.1092425>.

## **APPENDIX 1**

### Probing ZF5.3-Lipid Interactions Using Lipid Strips

## Introduction

Endosomal escape is a process not well understood by the drug delivery field. While cellular uptake of cationic cell-penetrating peptides (CPPs) and cell-permeant miniature proteins (CPMPs) is known to be influenced by the presence of negatively charged proteoglycans on the surface of cells,<sup>1,2</sup> stimulating endocytosis, the process by which material traverses the endosomal pathway to reach the cytosol remains largely a mystery.

One of the challenges in designing next generation cell-permeant miniature proteins (CPMPs) includes determining the mechanism by which current CPMPs escape from endosomes. Previously, Steinauer *et al.* identified the homotypic fusion and protein-sorting (HOPS) complex as a required component for trafficking the CPMP ZF5.3 to the cytosol of cells.<sup>3</sup> While HOPS allows ZF5.3 to enter Lamp1+ late endosomes and lysosomes,<sup>3</sup> the actual mechanism by which ZF5.3 leaves these intracellular vesicles is unknown. Additional observations in Steinauer *et al.* noted the colocalization of ZF5.3 with rhodamine-labeled 1,2-dipalmitoyl-sn-glycero-3-phosphoethanolamine (*N*-Rh-PE),<sup>3</sup> a marker of intraluminal vesicles (ILVs) within late endosomes.<sup>4</sup> With the observation that ZF5.3 resides in ILVs, we explored the interactions ZF5.3 exhibits with biologically relevant lipids using commercially available lipid strips. We hypothesized that ZF5.3 would interact with negatively charged lipids, such as bis(monoacylglycero)phosphate (BMP), a major component in ILVs.

## Methods

Lipid strips were obtained from Echelon Biosciences (Membrane Lipid Strip™, P-6002) and Avanti® Polar Lipids (BMP Snoopers®, 330502). ZF5.3<sup>Rho</sup>, SNAP-tag, and ZF5.3-SNAP-tag were generated using previously described methods.<sup>3,5,6</sup> All incubation steps described were completed with gentle shaking. For fluorescence-based detection, lipid strips incubated with 3% bovine serum albumin (BSA) in TBST (3 g BSA/100 mL TBST) for 1 h at room temperature. 1 μM of fluorescent probes in TBST were added to the strips and incubated for 1 h at room temperature. The lipid strips were washed 4X with TBST (5 min per wash) at room temperature. Fluorescent signal was imaged using a ChemiDoc MP.

For chemiluminescence-based detection, lipid strips incubated with 3% bovine serum albumin (BSA) in TBST for 1 h at room temperature. 1 μM of SNAP-tag and ZF5.3-SNAP-tag in TBST were added to the strips and incubated for 1 h at room temperature. The lipid strips were washed 3X with TBST (5 min per wash) at room temperature. Anti-SNAP-tag antibody (NEB) (1:1000 dilution in TBST supplemented with 3% BSA) was added to the lipid strips and incubated for 1 h at room temperature. The lipid strips were washed 3X with TBST (5 min per wash) at room temperature. Next, the lipid strips incubated with anti-rabbit IgG horseradish peroxidase (HRP)-linked antibody (Cell Signaling Technology, at 1:1000 dilution in TBST) for 1 h at room temperature. The lipid strips were washed 3X with TBST (5 min per wash) at room temperature. The lipid strips incubated for 3 min with 4 mL total Clarity™ Western ECL

Substrate (Bio-Rad) at room temperature prior to imaging chemiluminescence using a ChemiDoc MP.

To quantify lipid interactions of Avanti lipid strips, images were analyzed using ImageJ (Version 2.0.0-rc-69/1.52p). A binary image was constructed after a background subtraction with rolling ball radius of 50 pixels. To generate the binary image, the threshold was adjusted so that only the signals (whether fluorescent or chemiluminescent) remained. The band intensities were quantified by densitometry analysis and normalized to the C11 TopFluor Fatty Acid reference molecule:

$$\frac{\text{lipid signal}}{\text{average C11 TopFluor signal}} - 1 \quad \text{Equation 1}$$

The subtraction of 1 allows more negative values to correspond to weaker interactions with a value of -1 indicating no interaction (due to no visible signal on the membrane). More positive interactions indicate stronger binding of proteins to lipids.

## Results and Discussion

As endocytosis progresses within the cell, the lipid content of endosomes changes.<sup>7</sup> Early and late endosomes are comprised primarily of phosphatidylcholine (PC) and phosphatidylethanolamine (PE), but late endosomes are characterized by the presence of 20% BMP (also known as lysobisphosphatidic acid, LBPA).<sup>8</sup> ILVs within these late endosomes have an even higher content of BMP, reaching 77% of the total lipid content.<sup>9–11</sup> Lipid strips contain a variety of biologically relevant lipids and can be used to probe protein interactions with lipids.<sup>12–14</sup> To evaluate whether ZF5.3 selectively associates with various lipids, we analyzed interactions of ZF5.3<sup>Rho</sup>, a rhodamine-tagged ZF5.3,<sup>3,6,15</sup> and ZF5.3-SNAP-tag<sup>5</sup> using commercially available lipid strips (**Figure 1A**).

With the observations that (1) ZF5.3 colocalizes with ILVs<sup>3</sup> and (2) ILVs are rich in BMP,<sup>11</sup> we probed ZF5.3-lipid interactions using Avanti® Polar Lipids BMP Snoopers®, which contain a number of BMP isomers and biosynthetic precursors (**Figure 1B–C**). As controls, we assessed GGGK<sup>Rho</sup> and *N*-Rh-PE, which should either bind to nothing or late endosomal lipids, respectively. GGGK<sup>Rho</sup> exhibited an interaction with 18:1 bis(diacylglycero)phosphate (BDP) (*S,S*), possibly due to its relatively hydrophobic structure. *N*-Rh-PE interacted with phosphatidylethanolamine (PE), a component of both early and late endosomes.<sup>8</sup> ZF5.3<sup>Rho</sup> associated with a number of BMP derived molecules, including 18:1 BMP (*R,R*), 18:1 BDP (*S,S*), 18:1 BMP (*S,R*), and 18:1 BMP (*S,S*). Additionally, interactions with PE but not PC were observed. Interestingly, ZF5.3<sup>Rho</sup> did not interact with synthetic precursors (hemi BMP) that contain three (versus two) oleoyl or alkyl chains. The fluorescent signal of each test compound is not strong, making it difficult to differentiate between interactions specific to GGGK<sup>Rho</sup> or ZF5.3<sup>Rho</sup> since GGGK<sup>Rho</sup> bound multiple lipids. At increased concentration (5 μM) for signal optimization, ZF5.3<sup>Rho</sup> exhibited a similar interaction profile to 1 μM treatment (**Figure 2**).

To improve signal through amplification, we moved to antibody-based detection of SNAP-tag proteins. Previous studies indicate that the presence of ZF5.3 significantly increases the amount of SNAP-tag protein that reaches the cytosol compared to SNAP-tag alone.<sup>5</sup> Comparing the differences between SNAP-tag and ZF5.3-SNAP-tag interactions would provide evidence of ZF5.3-specific interactions. Lipid strips were treated with 1  $\mu$ M of SNAP-tag proteins for 1 h, followed by 1 h incubation with an anti-SNAP-tag antibody, rigorous washing, and 1 h incubation with anti-rabbit IgG conjugated to horseradish peroxidase for chemiluminescent imaging (**Figure 1D–E**). Indeed, the amplified assay produced a better response than fluorescence-based detection. SNAP-tag alone exhibited minimal interactions with 14:0 hemi BMP (*S,R*) and 18:1 BDP (*S,S*). In addition to stronger associations with 14:0 hemi BMP (*S,R*) and 18:1 BDP (*S,S*), ZF5.3-SNAP-tag interacted with 18:1 BMP (*R,R*), 14:0 BMP (*S,R*), 18:1 Hemi BMP (*S,R*), 18:1 BMP (*S,R*), 18:1 BMP (*S,S*). ZF5.3-SNAP-tag exhibited approximately equal affinity for both the *S,R* and *S,S* isomers of 18:1 BMP. Similar to ZF5.3<sup>Rho</sup>, signal was observed for PE but there was no binding to positively charged PC. When analyzing the interactions of ZF5.3<sup>Rho</sup> and ZF5.3-SNAP-tag on the BMP Snoopers®, we see that both ZF5.3-containing proteins share similar lipid interactions. It is likely that ZF5.3 binds BMP derivatives due to favorable electrostatic interactions.

Among more general lipids present in the cell (**Figure 1F**), ZF5.3-SNAP-tag strongly bound to cardiolipin (**Figure 1G**). This lipid is involved in mitochondrial signaling, contains two phosphate groups, and may possess a -1 charge at physiological pH.<sup>16</sup> Thorén *et al.* observed that carboxyfluorescein-penetratin (a canonical CPP) could enter giant unilamellar vesicles that contained a small concentration of cardiolipin (4%).<sup>17</sup> Penetratin is a cationic peptide shown to adopt a helical structure in the presence of cardiolipin<sup>18,19</sup> and it is possible that the cardiolipin promotes charge-based interactions with ZF5.3-SNAP-tag. Additional signal was observed for the interaction between ZF5.3-SNAP-tag and phosphatidic acid (PA). Other arginine-rich motifs have been shown to bind to PA<sup>20</sup> so it is plausible that the penta-Arg motif of ZF5.3 supports similar PA interactions.

The remainder of the panel of lipids that produced no signal in the presence of ZF5.3-SNAP-tag include phosphatidylinositol (PI) and its phosphate derivatives (PIP molecules), sphingomyelin, and cholesterol. PI contains a negatively charged phosphate but its bulky inositol may preclude interactions with ZF5.3. Sphingomyelin, like many of the other lipids present on the Echelon lipid strip, exhibits an overall neutral charge. PIP derivatives contain increasing numbers of phosphates, but steric effects from inositol may play a role in the lack of binding of ZF5.3-SNAP-tag. We expected signal from the PE spot, but perhaps there are differences in the structures of the Egg PE from Avanti and the corresponding lipid from Echelon. Given the amount of each lipid spotted on the membrane, it is possible that a 1  $\mu$ M treatment is not enough for all lipids present so that only those in which the interactions are the strongest will produce a signal.

To quantify the signal from the BMP Snoopers®, signals were analyzed using densitometry, normalized to C11 TopFluor Fatty Acid, and plotted as a heat map (**Figure**

3), where a more negative value indicates less interactions and a more positive signal corresponds to stronger lipid interactions. ZF5.3-SNAP-tag exhibited the strongest interactions with 18:1 bis(diacylglycero)phosphate (BDP) (S,S). BDP contains four acyl chains and could promote hydrophobic interactions in addition to electrostatic ones. ZF5.3-SNAP-tag experienced similar interactions with the S,R and S,S isomers of 18:1 BMP, yet a decreased interaction with the R,R isomer, suggesting that while the ZF5.3-lipid interactions are driven predominantly by charge, stereochemistry may have minimal effects.

## Conclusions

The experiments described here indicate that ZF5.3 binds selectively to BMP derivatives and other negatively charged lipids present in membranes. Since the lipids that both ZF5.3<sup>Rho</sup> and ZF5.3-SNAP-tag bind to are similar, there may be similarities in the endosomal escape mechanisms of ZF5.3 alone and when conjugated to protein cargo. These findings will be used to inform experimental design for future *in vitro* lipid experiments.

## Figures

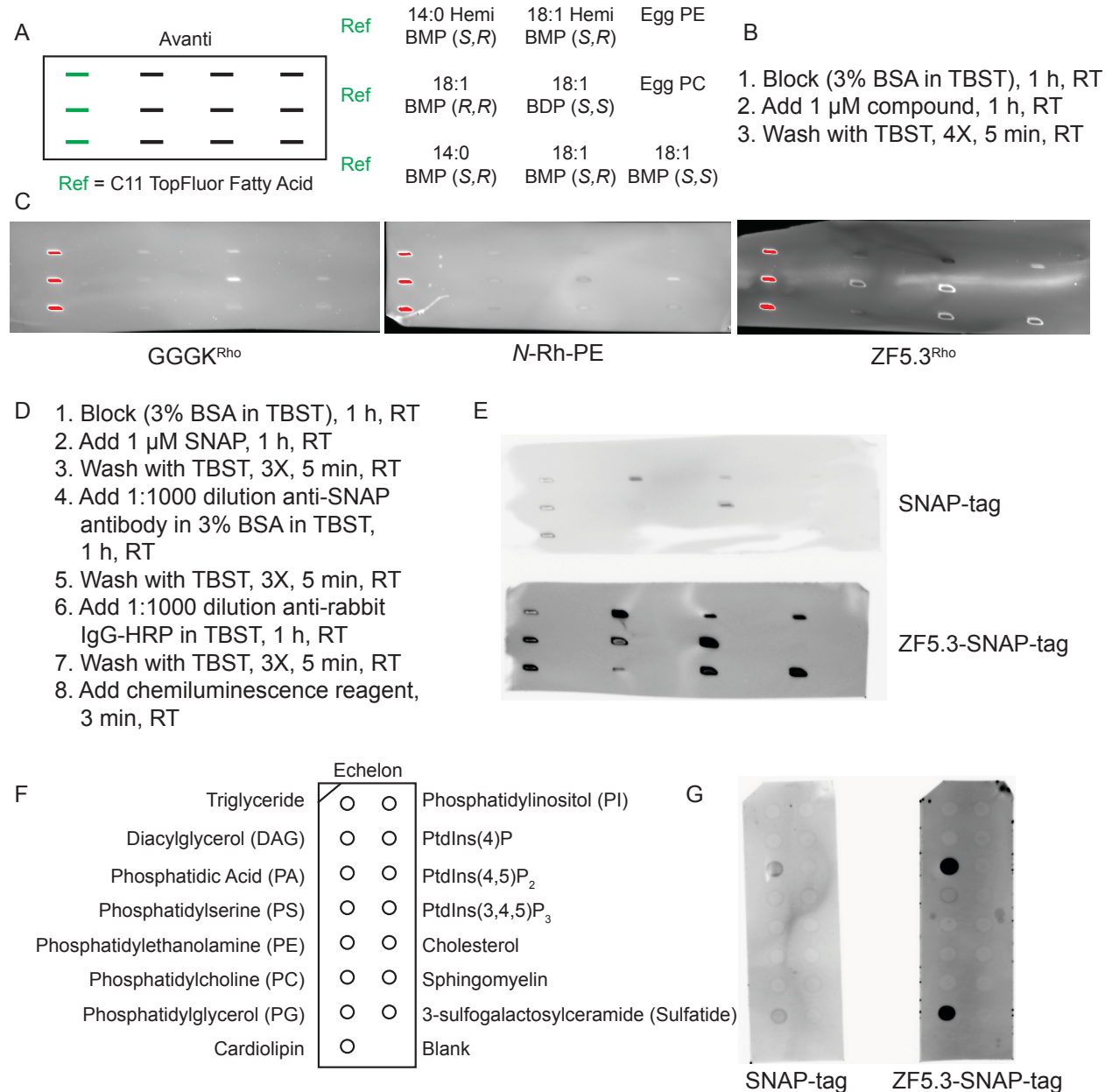


**Figure 1.** (A) Avanti® Polar Lipids BMP Snoopers® layout. Reference compound (ref) corresponds to C11 TopFluor fatty acid for strip orientation purposes and elicits a signal using epi-green (520–545 nm excitation) illumination and a 675–725 nm filter. (B) Workflow for fluorescence-based detection. (C) Avanti lipid strips treated with 1  $\mu$ M GGGK<sup>Rho</sup>, N-Rh-PE, or ZF5.3<sup>Rho</sup> and imaged using epi-green (520–545 nm excitation) illumination and a 675–725 nm filter on a ChemiDoc MP. (D) Workflow for chemiluminescence-based detection of SNAP-tag and ZF5.3-SNAP-tag. (E) Avanti lipid strips treated with 1  $\mu$ M SNAP-tag and ZF5.3-SNAP-tag and imaged using chemiluminescence. (F) Echelon Biosciences Membrane Lipid Strip™ layout. (G) Echelon lipid strips treated with 1  $\mu$ M SNAP-tag and ZF5.3-SNAP-tag and imaged using chemiluminescence.

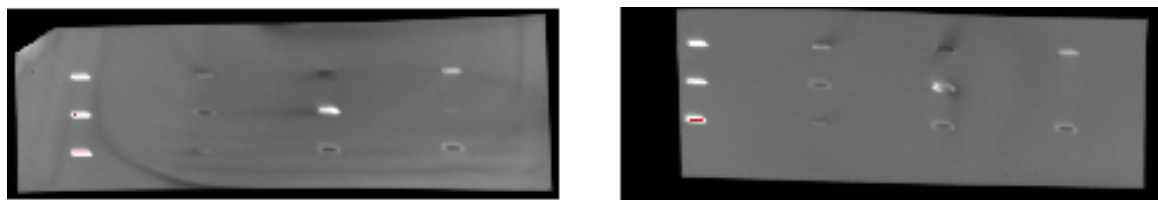


**Figure 2.** Avanti lipid strips treated with 5  $\mu\text{M}$  ZF5.3<sup>Rho</sup> and imaged using epi-green (520–545 nm excitation) illumination and a 675–725 nm filter on a ChemiDoc MP. Prior to imaging, lipid strips were blocked with 3% BSA in TBST for 1 h, incubated with 5  $\mu\text{M}$  ZF5.3<sup>Rho</sup> for 1 h at room temperature, and were washed with TBST 4X (5 min each wash).

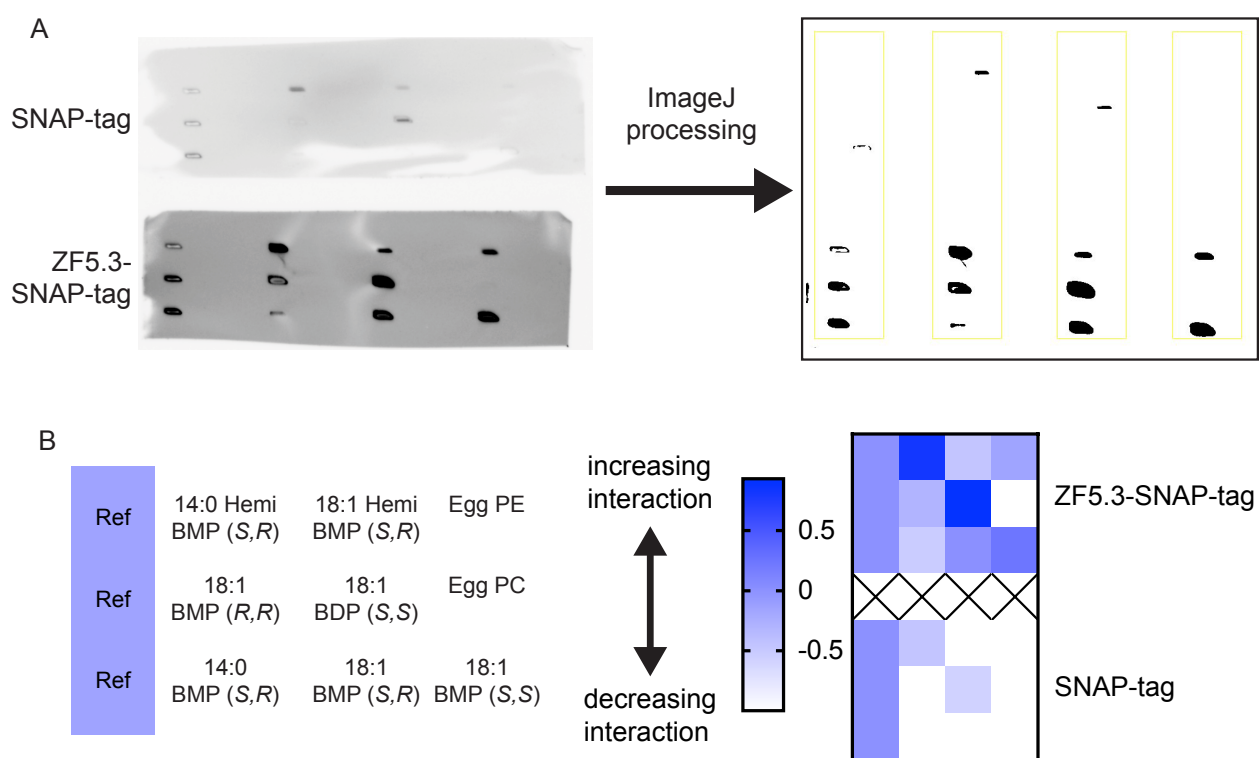


**Figure 3.** Quantification of lipid interactions using Avanti BMP Snoopers®. (A) The signal generated from imaging the membrane was analyzed in ImageJ as described in the Methods. (B) Normalized signal was plotted on a heat map, where the more positive the number, the stronger interaction and the more negative the number, the weaker interaction. Values at -1 indicate no signal observed on the membrane. ZF5.3-SNAP-tag and SNAP-tag were quantified together to ensure direct comparison. The line containing “X” is used as a spacer for the data. The interaction of the denoted protein with the respective lipid matches the layout of the lipid strip. Data represents the average of two trials.

## References

- (1) Åmand, H. L.; Rydberg, H. A.; Fornander, L. H.; Lincoln, P.; Nordén, B.; Esbjörner, E. K. Cell Surface Binding and Uptake of Arginine- and Lysine-Rich Penetratin Peptides in Absence and Presence of Proteoglycans. *Biochim. Biophys. Acta BBA - Biomembr.* **2012**, *1818* (11), 2669–2678. <https://doi.org/10.1016/j.bbamem.2012.06.006>.
- (2) Poon, G. M. K.; Gariépy, J. Cell-Surface Proteoglycans as Molecular Portals for Cationic Peptide and Polymer Entry into Cells. *Biochem. Soc. Trans.* **2007**, *35* (4), 788–793. <https://doi.org/10.1042/BST0350788>.
- (3) Steinauer, A.; LaRoche, J. R.; Knox, S. L.; Wissner, R. F.; Berry, S.; Schepartz, A. HOPS-Dependent Endosomal Fusion Required for Efficient Cytosolic Delivery of Therapeutic Peptides and Small Proteins. *Proc. Natl. Acad. Sci.* **2019**, *116* (2), 512–521. <https://doi.org/10.1073/pnas.1812044116>.
- (4) Savina, A.; Furlán, M.; Vidal, M.; Colombo, M. I. Exosome Release Is Regulated by a Calcium-Dependent Mechanism in K562 Cells\*. *J. Biol. Chem.* **2003**, *278* (22), 20083–20090. <https://doi.org/10.1074/jbc.M301642200>.
- (5) Wissner, R. F.; Steinauer, A.; Knox, S. L.; Thompson, A. D.; Schepartz, A. Fluorescence Correlation Spectroscopy Reveals Efficient Cytosolic Delivery of Protein Cargo by Cell-Permeant Miniature Proteins. *ACS Cent. Sci.* **2018**, *4* (10), 1379–1393. <https://doi.org/10.1021/acscentsci.8b00446>.
- (6) Appelbaum, J. S.; LaRoche, J. R.; Smith, B. A.; Balkin, D. M.; Holub, J. M.; Schepartz, A. Arginine Topology Controls Escape of Minimally Cationic Proteins from Early Endosomes to the Cytoplasm. *Chem. Biol.* **2012**, *19* (7), 819–830. <https://doi.org/10.1016/j.chembiol.2012.05.022>.
- (7) Doherty, G. J.; McMahon, H. T. Mechanisms of Endocytosis. *Annu. Rev. Biochem.* **2009**, *78* (1), 857–902. <https://doi.org/10.1146/annurev.biochem.78.081307.110540>.
- (8) Huotari, J.; Helenius, A. Endosome Maturation. *EMBO J.* **2011**, *30* (17), 3481–3500. <https://doi.org/10.1038/emboj.2011.286>.
- (9) Yang, S.-T.; Zaitseva, E.; Chernomordik, L. V.; Melikov, K. Cell-Penetrating Peptide Induces Leaky Fusion of Liposomes Containing Late Endosome-Specific Anionic Lipid. *Biophys. J.* **2010**, *99* (8), 2525–2533. <https://doi.org/10.1016/j.bpj.2010.08.029>.
- (10) Gruenberg, J. Life in the Lumen: The Multivesicular Endosome. *Traffic* **2020**, *21* (1), 76–93. <https://doi.org/10.1111/tra.12715>.
- (11) Matsuo, H.; Chevallier, J.; Mayran, N.; Le Blanc, I.; Ferguson, C.; Fauré, J.; Blanc, N. S.; Matile, S.; Dubochet, J.; Sadoul, R.; Parton, R. G.; Vilbois, F.; Gruenberg, J. Role of LBPA and Alix in Multivesicular Liposome Formation and Endosome Organization. *Science* **2004**, *303* (5657), 531. <https://doi.org/10.1126/science.1092425>.
- (12) Lu, B.; Benning, C. A 25-Amino Acid Sequence of the Arabidopsis TGD2 Protein Is Sufficient for Specific Binding of Phosphatidic Acid. *J. Biol. Chem.* **2009**, *284* (26), 17420–17427. <https://doi.org/10.1074/jbc.M109.016014>.

- (13) Sankarshanan, M.; Ma, Z.; Iype, T.; Lorenz, U. Identification of a Novel Lipid Raft-Targeting Motif in Src Homology 2-Containing Phosphatase 1. *J. Immunol.* **2007**, *179* (1), 483. <https://doi.org/10.4049/jimmunol.179.1.483>.
- (14) Hodel, A. W.; Rudd-Schmidt, J.; Trapani, J. A.; Voskoboinik, I.; Hoogenboom, B. Lipid Specificity of the Immune Effector Perforin. *Faraday Discuss.* **2020**. <https://doi.org/10.1039/D0FD00043D>.
- (15) LaRochelle, J. R.; Cobb, G. B.; Steinauer, A.; Rhoades, E.; Schepartz, A. Fluorescence Correlation Spectroscopy Reveals Highly Efficient Cytosolic Delivery of Certain Penta-Arg Proteins and Stapled Peptides. *J. Am. Chem. Soc.* **2015**, *137* (7), 2536–2541. <https://doi.org/10.1021/ja510391n>.
- (16) Dudek, J. Role of Cardiolipin in Mitochondrial Signaling Pathways. *Front. Cell Dev. Biol.* **2017**, *5*, 90. <https://doi.org/10.3389/fcell.2017.00090>.
- (17) Thorén, P. E. G.; Persson, D.; Karlsson, M.; Nordén, B. The Antennapedia Peptide Penetratin Translocates across Lipid Bilayers – the First Direct Observation. *FEBS Lett.* **2000**, *482* (3), 265–268. [https://doi.org/10.1016/S0014-5793\(00\)02072-X](https://doi.org/10.1016/S0014-5793(00)02072-X).
- (18) Trabulo, S.; Cardoso, A. L.; Mano, M.; De Lima, M. C. P. Cell-Penetrating Peptides—Mechanisms of Cellular Uptake and Generation of Delivery Systems. *Pharmaceuticals* **2010**, *3* (4). <https://doi.org/10.3390/ph3040961>.
- (19) Joanne, P.; Galanth, C.; Goasdoué, N.; Nicolas, P.; Sagan, S.; Lavielle, S.; Chassaing, G.; El Amri, C.; Alves, I. D. Lipid Reorganization Induced by Membrane-Active Peptides Probed Using Differential Scanning Calorimetry. *Biochim. Biophys. Acta BBA - Biomembr.* **2009**, *1788* (9), 1772–1781. <https://doi.org/10.1016/j.bbamem.2009.05.001>.
- (20) Sagaram, U. S.; El-Mounadi, K.; Buchko, G. W.; Berg, H. R.; Kaur, J.; Pandurangi, R. S.; Smith, T. J.; Shah, D. M. Structural and Functional Studies of a Phosphatidic Acid-Binding Antifungal Plant Defensin MtDef4: Identification of an RGFRRR Motif Governing Fungal Cell Entry. *PLOS ONE* **2013**, *8* (12), e82485. <https://doi.org/10.1371/journal.pone.0082485>.